

HIGH RESOLUTION TEMPORAL STUDIES OF CYGNUS X-1

by

ALAN B. GILES, B.Sc.

A thesis submitted to the  
UNIVERSITY OF LEICESTER  
for the degree of  
DOCTOR OF PHILOSOPHY.

MAY, 1978

X-Ray Astronomy Group  
Department of Physics  
University of Leicester.

UMI Number: U435646

All rights reserved

INFORMATION TO ALL USERS

The quality of this reproduction is dependent upon the quality of the copy submitted.

In the unlikely event that the author did not send a complete manuscript and there are missing pages, these will be noted. Also, if material had to be removed, a note will indicate the deletion.



UMI U435646

Published by ProQuest LLC 2015. Copyright in the Dissertation held by the Author.  
Microform Edition © ProQuest LLC.

All rights reserved. This work is protected against  
unauthorized copying under Title 17, United States Code.



ProQuest LLC  
789 East Eisenhower Parkway  
P.O. Box 1346  
Ann Arbor, MI 48106-1346



THESIS

556350

9 8 78

x753002352

TO  
MINKY

## CONTENTS

<u>Chapter</u>	<u>Page</u>
Abstract	i
Acknowledgements and Declaration	iii
1        An introduction to compact X-ray binary systems and the observational history of Cygnus X-1	1
2        The design and construction of a large area high time resolution detector system	48
3        Test equipment and data processing techniques	90
4        The calibration and expected performance of the experiment	110
5        The flight of SL-1306 and an analysis of the non-Cygnus X-1 data	136
6        The analysis of the Cygnus X-1 data	163
Appendix A    Honeycomb transmission	221
B    Detector field theory	223
C    FIFO tester	225
D    Energy fraction circuit	226
E    Check code circuit	230
F    Appleton PCM tape format	233
References	235

ABSTRACT

Rapid variability in X-ray sources implies a compact object such as a white dwarf, neutron star or black hole. Following a review of the best known examples and their associated models, the observational history of Cygnus X-1 is outlined. This source is generally believed to be a black hole since it appears to exhibit rapid variability (millisecond bursts) and has a mass above the theoretical neutron star limit.

This thesis is concerned with an attempt to study the rapid variability of the source using a multiwire array deploying detector system with a sensitive area of  $4,000 \text{ cm}^2$  (1.5 - 15 keV). The chance expectation value of millisecond bursts as seen by previous smaller experiments would be decreased from  $10^{-2}$  to  $10^{-9}$ .

The anticipated high count rate required the use of a data interactive electronics system together with a large buffer store to optimise use of the available telemetry data rate. This allowed timing of the X-ray events to  $2 \mu\text{S}$  together with a large transient handling capacity so that the system was no longer severely limited at the very moment that the information was of most interest.

The experiment was flown from Woomera in November 1976 and functioned correctly but the attitude control system failed providing only 6 seconds of Cygnus X-1 data at reduced sensitivity. No other interesting observations were made while the experiment's field of view drifted across the celestial sphere.

Investigations of the shot noise character of Cygnus X-1 are not inconsistent with previous observations, but the short data set is unsuitable for such studies.

A search for rapid bursts using the same analysis methods as

previous workers was also inconclusive, the presence of the calibration source flux possibly being crucial in limiting the probability of a number of borderline features.

The statistical interpretation of burst phenomena is discussed leading to the concept that the size of the features seen by SL-1306 are similar numerically to those reported by Rothschild et al. (1976) and therefore represent activity at approximately one-third the intensity. Such features occurring during the non-enhanced low states would not be detected with the customary analysis by previous smaller detectors. A frequency of  $\sim 1$  per sec is suggested for these mini bursts, the duration being 0.5 mS, the bursts appearing to be stronger in the latter 0.25 mS.

The author notes with considerable regret that two re-flight proposals were not approved.

ACKNOWLEDGEMENTS

My thanks are due, firstly, to Professor K.A. Pounds, Director of the X-ray Astronomy Group, who has been my supervisor during the course of this research.

The project described in this thesis has benefitted greatly from the assistance and advice of many members of the X-ray Astronomy Group, but I should like to acknowledge the assistance of two people in particular. Mr. C.H. Whitford was involved in almost all aspects of the work from design to data analysis and Mr. D.J. Watson provided invaluable experience and support in the design, testing and on-range preparation of the experiment. The Physics Department Workshop manufactured most of the mechanical components, the quality of which was due largely to the machining skills of Mr. H.C. Chapman. The Group Electronics Workshop also produced work of a high standard and Mr. R.D. Cooper carried out most of the detailed circuit design.

I should also like to thank the B.A.C. team who carried out the vehicle preparation and launch and the Science Research Council who provided a Research Studentship for the early part of this work.

My special thanks go to Julie for her encouragement and support throughout the project.

This thesis has been typed by Mrs. N. Corby and Mrs. M.G.M. Smith traced some of the figures.

Declaration

I, the undersigned, declare that the work described in this thesis has, except where indicated, been carried out by the author, during the period of registration for the degree of Ph.D. at Leicester. No part of it has been submitted for any other degree.

A. B. Giles

CHAPTER 1

An introduction to compact X-ray binary systems and the observational history of Cygnus X-1.

	Page
1.1 Introduction	2
1.2 The Properties of X-ray Binary Systems	6
1.3 X-ray Generation by Compact Objects	21
1.4 Observations of Cygnus X-1	33

## 1.1 Introduction

The early years of X-ray astronomy research were based on the observations of fairly simple experiments launched on sounding rockets that were spin stabilised or performed controlled scans of selected regions. A catalogue of these surveys was compiled by Friedman et al. (1967) which listed 30 sources including the Crab (Bowyer et al., 1964) and Sco X-1 (Gursky et al., 1966). This early work also indicated that Cygnus X-1 varied in intensity although the sporadic short observations did not allow detailed investigation.

The first high time resolution study of an X-ray source came in 1969 following the discovery of the radio pulsar in the Crab (NP 0532) (Staelin and Reifenstein, 1968) and the related optical pulses by Cocke et al. (1968). The M.I.T. group found NP 0532 to also be a pulsating X-ray source, at the same 33 ms period, and were able to produce a pulse profile in X-rays that agreed in phase with simultaneous optical data to within 1 ms (Bradt et al., 1969). This important result demonstrated that for compact objects a high time resolution capability was essential. Further survey flights discovered more X-ray sources and Seward (1970) lists some 60 objects that include a few more identifications with well known optical and radio sources such as M87, 3C273, NGC 4151, Cas A and the LMC. Balloons were used for energies greater than 30 KeV and sounding rockets for low energy work from 0.1 to 2 KeV. Specific sources were also studied in detail from sounding rockets at medium energies since the quick turn round allowed purpose built instruments of far greater power than those available on early satellites, such as OSO-3.

The launch of SAS A or Uhuru in December 1970 marked a turning point in permitting long observation times and a time resolution down to 0.096 seconds. The experiments on board have been described by

Giacconi et al. (1971) and discovered many new sources, confirmed previous identifications and produced reasonable error boxes. The third Uhuru catalogue published by Giacconi et al. (1974) contained 161 sources in the 2-6 KeV range with an intensity down to  $10^{-4}$  Sco X-1, some 20 of which had been identified. The production of a log N - log S curve by Matilinsky et al. (1974) showed three classes of object. About 60 sources of declination greater than  $\pm 20^\circ$  are interpreted as extragalactic and include the extended sources of the Virgo, Coma, Perseus and Centaurus clusters of galaxies. A group of 15 sources above 300 FU (Crab = 947 FU) are connected with the galactic centre and contain about 90% of the estimated  $3 \times 10^{39}$  ergs sec flux from our entire galaxy above 2 KeV. The remainder below 300 FU appear to lie in the spiral arms of our galaxy. The galactic sources fall into four groups - supernova remnants, binary sources, transient sources and the galactic centre objects which are difficult to identify optically probably due to absorbing matter. The binary sources include such objects as Cyg X-1, Her X-1 and Cen X-3. All these sources can be associated with compact objects since they show rapid variability in addition to any regular pulsar or binary periods, indeed sources such as Sco X-1 and Cyg X-1 appear to be variable on all time scales as section 1-4 shows for the latter. Selected objects such as the binaries Sco X-1 and Cyg X-1 have also been observed during this period by the OSO-7 satellite launched in September, 1971, and the Copernicus satellite launched in August, 1972.

The launch in October, 1974, of Ariel 5 enabled the incomplete sky coverage of Uhuru to be extended and fainter objects located down to 0.5 FU rather than 2-3 FU. A complete description of the six experiments on board and a summary of the first year's work can be found following Smith and Courtier (1976). Cooke et al. (1977) have

published the 2A catalogue of sources outside  $\pm 10^\circ$  of the galactic plane, the Leicester sky survey experiment (SSI) used to perform this task being described by Villa et al. (1976). These generally extragalactic objects have a distribution much the same as that in the 3U catalogue except that many weak high galactic latitude sources have been found. A 4U catalogue (Forman et al., 1977) has also been produced based on all the Uhuru data (January 1971 - March 1973) and is in substantial agreement with the 2A survey in the overlapping regions of similar sensitivity.

Most galactic X-ray sources appear to be variable with the exception of the SNR's and a number of objects have clearly disappeared or appeared since the earlier survey. Notable among Ariel 5's achievements are the discovery of several bright but transient sources such as A0620-00 (Elvis et al., 1975) and A0535+36 (Ricketts et al., 1975) and the observations of iron line emission (6.9 KeV) in several clusters of galaxies (Mitchell et al., 1976). In the extragalactic domain the 2A catalogue sources have been identified with some 16 Seyfert galaxies, 1 QSO (3C273) and about 35 clusters of galaxies.

The SAS-3 satellite launched in May, 1975, has been described by McIntock (1975) and is also completing a survey, though not to such a faint level as Ariel 5. This spacecraft however has a time resolution down to  $10^{-4}$  seconds compared to Ariel 5's minimum of 8 minutes, when not set to observe a known period. This feature has enabled an entirely new class of objects to be discovered known as X-ray bursters. A summary of the 12 known bursters has been given by Lewin (1976) a unique example being MXB 1730-335 (Lewin et al., 1976) since this has flares at several a minute rather than per hour or day as the rest do. This object unfortunately stopped bursting during May 1976, otherwise it would have been observed by the experiment

described in this thesis. It was subsequently re-discovered in mid-April, 1977, bursting as before, only to disappear again by May 31st (Lewin and Hoffman, IAU 3079). The Dutch satellite ANS launched in August, 1974, has also provided much time structure information.

The detailed time structure of several of the known binary sources has been examined using sounding rockets and Spada et al. (1974) describe observations of Her X-1, Vela X-1, Cir X-1, Cyg X-1 and 3U 1700-37 using a large detector ( $900 \text{ cm}^2$ ) and a time resolution of 1 mS. The most notable experiments of this type however are the two flights by Rothschild et al. (1974, 1976) which appear to have revealed one millisecond bursts from Cygnus X-1. More recently Toor (1977) has also observed millisecond variability from the somewhat similar X-ray source Circinus X-1. Observations of such rapid structure require the maximum possible detector area since observing for a long duration, although desirable, is not particularly beneficial when searching for non-periodic bursts.

The past generation of satellite experiments have had an observational and technical performance similar to that of the early rocket payloads and cannot compete at high time resolutions with specially designed rocket experiments such as the one above or SL-1306. Instruments of similar and even greater power are now becoming available such as HEAO-A, followed by Exosat and the Spacelab series in the early eighties. It is of interest to note however that if one considers all aspects of an experiment's performance for studying very rapid time structure the SL-1306 system is substantially superior to HEAO-A, neglecting of course the fact that only 4 minutes of observation on a single source is possible.

These massive experiments with huge bandwidth in the case of Spacelab will allow micro-second resolution routine observations of

many sources rather than the limited possibilities and brief durations available from sounding rockets. This kind of capability together with spectral and imaging devices should greatly increase our understanding of the emission mechanisms and physical properties of the astronomically speaking small and compact X-ray sources.

The remainder of this chapter discusses briefly the properties of binary star systems and then summarises the known X-ray sources of this type, together with emission mechanisms and models for compact objects. The detailed history of Cygnus X-1 observations is then reviewed leading to the conclusion that this system contains a black hole.

## 1.2 The Properties of X-ray Binary Systems

### 1.2.1 Classical Binaries

The study of binary systems has always been of fundamental importance to astronomy since they are the only stellar objects for which the masses of individual stars can be obtained. It has been estimated that perhaps 50% of stars are in multiple systems, 20% being in triplets or higher combinations (Batten, 1973), although only a few thousand spectroscopic doubles or eclipsing variables are actually known. The orbits have been determined for several hundred of these, the information we can obtain from the observed parameters being outlined below. We shall consider only close, i.e. non-visual, systems.

#### Spectroscopic Binaries

A series of measurements of the radial velocity in Km/sec allows us to produce the radial velocity curve.

### One Spectra Visible

In this case the companion is faint compared to the primary and we consider the absolute orbit of the brighter star around the centre of gravity. This type of system gives us only the mass function  $f(M)$  and  $a_1 \sin i$ , where  $a$  is the radius of the orbit and  $i$  the inclination. If we take units of  $a$  in  $10^6$  Km,  $P$  in days, and  $M$  in solar masses then

$$f(M) = \frac{(M_2 \sin i)^3}{(M_1 + M_2)^2} = (a_1 \sin i)^3 / 25P^2$$

A typical method for obtaining the parameters of the system is that of Schwarzschild (1920).

### Two Spectra Visible

When the components have comparable brightness the spectral lines will be seen periodically doubled. In this case we can find the mass ratio since

$$\frac{M_1}{M_2} = \frac{K_2}{K_1}$$

where  $K$  is the half amplitude of the radial velocity curve. If we use the same units as before we obtain

$$a \sin i = 0.01375 (K_1 + K_2) P \sqrt{1 - e^2}$$

where  $i$  is the inclination of the orbit and  $e$  the eccentricity and

$$M_1 \sin^3 i = (a_2 \sin i)(a \sin i)^2 / 25P^2$$

$$M_2 \sin^3 i = (a_1 \sin i)(a \sin i)^2 / 25P^2$$

The masses themselves or the sum of the masses can only be found in

combination with  $\sin^3 i$ ; however, if in addition the binary is an eclipsing system we can find  $i$  from the light curve and hence the individual masses.

### 1.2.2

#### Eclipsing Variables

A method for deriving the orbital elements from the light curve has been described by Kopal (1950) and Merrill (1953) has compiled extensive tables for various models. From the light curve we can derive  $i$ , the relative sizes and the relative intensities. The situation may be complex but we can identify three basic types of system.

#### Algol

Here we have circular orbits, spherical stars, uniform light and little reflection which produces two nearly flat maxima.

#### $\beta$ Lyrae

These close systems have oblate stars producing curved maxima. Oblateness observations are rarely more than  $\xi = 0.1$  at which point simple models are too crude since the stars become 'egg shaped'.

#### W Ursae Majoris

These oblate stars almost touch each other allowing determination of a density limit and the mean densities of each component. These very close systems do not have strictly constant periods.

### 1.2.3

The analysis of close binaries is greatly complicated by varying combinations of the following effects.

### Rotation

If the orbit is favourable then just before and after eclipse the radial velocity of the orbital motion will have superimposed on it a contribution from the edge of the spinning star. Rapid rotation also leads to an oblate star that no longer has a constant projected surface area.

### Gas Streams

As the stars orbit, any gas stream will periodically approach and recede causing a blurring of the apparent stellar velocity. This gas also affects the light curve of the system which results in poor orbit solutions.

### Reflection Effect

For objects of comparable luminosity the facing hemispheres may be brighter than the opposed ones causing the centre of light of the two discs to be displaced from the centre of mass to the centre of gravity of the system. Correction tables for this effect have been compiled by Kuiper (1938) since this underestimate of the orbit size enters to the third power producing appreciable changes in the computed masses.

### Limb Darkening

The theory of radiative transfer in stellar atmospheres leads to

$$I = I_0 (1 - x + x \cos \gamma)$$

where  $\gamma$  is the angle between the radius and line of sight. For the Sun  $x = 0.6$  giving an intensity only  $\frac{2}{3}$  of that for a uniform model.

Correction tables such as those compiled by Russell and Shapley (1912)

are particularly important in the case of oblate stars where the limb darkening contribution is 1.6 times greater. In every case the effect is to diminish the depth during mid-eclipse, produce unequal depths during occultation and transit and to produce curved minima during eclipse.

### Gravitational Darkening

This must be allowed for over a deformed surface because

$$F = \frac{GMm'}{d^2} = M'g \quad \text{and} \quad I \propto \frac{1}{d^2} \propto g \propto T^4$$

This effect can be written in a similar fashion to that of Limb Darkening as

$$I = I_0 (1 - y + y \cdot g/g_0)$$

if  $g = g_0$  then  $I = I_0$ .

The classical treatment is that of Von Zeipel (1924).

### Elliptical Orbits

In addition to causing minima of unequal duration the semi major axis of the orbit will precess if the bodies are oblate. The effect is for both minima to move equally in antiphase about the mean period,  $P$ , although in practice this period  $P'$  is very long since for normal binaries tidal distortion and rotation oblateness are small. An expression for the motion of the line of Apsides is that of Cowling (1938).

$$\frac{P}{P'} = C_1 \left[ \frac{r_1}{R} \right]^5 \left[ 1 + A \frac{M_2}{M_1} \right] + C_2 \left[ \frac{r_2}{R} \right]^5 \left[ 1 + A \frac{M_1}{M_2} \right]$$

where  $A = 16$  for low eccentricity orbits. The value of  $C$  is model dependent and for a homogeneous star  $C = \frac{3}{4}$ . Considering all the mass

at the centre (Roche model) however gives  $C = 0$  so by observing apsidal rotation we can infer details of the density gradient of the stars.

### Multiple Body Systems

Some eclipsing stars do not have a constant period and a third body can be inferred, the times of primary and secondary minima being identically affected since the gravity centre revolves around the common centre of gravity.

### Super Giant Binaries

A few cases are known where the primary is a super giant with an extended atmosphere in which the secondary disappears slowly. Observations of this type made at several wavelengths provide information on the structure of the atmosphere.

#### 1.2.4 X-ray Binaries

There are a number of possible models as discussed in a later section but in general the X-ray binaries are considered to consist of a collapsed object orbiting a normal star. In this case there will naturally only be one spectrum visible giving us the mass function of the system but there may also be some anomalous emission features. There may or may not be an eclipse depending on the geometry of the orbit but if there is we can estimate the mass of the individual components after determining the mass of the primary from its absolute magnitude. The analysis of the light curves has been discussed by Hutchings (1974) and by Wilson and Devinney (1971). The factors involved were outlined in the previous section but modern computers allow a treatment in which the primary fills its Roche lobe rather than

being an ellipsoid. A general expression for the light curve of an ellipsoidal model is that given by Russell and Merrill (1952) and Merrill (1970).

$$1) \quad I = I_{\text{MAX}} \left(1 - \frac{1}{2} Nz \cos^2 \theta\right)$$

where  $\theta$  is the phase angle,  $z$  the geometrical ellipticity which depends on the mass ratio, radius and inclination of the orbit, and

$$2) \quad N = (15 + x)(1 + y)/(15 - 5x)$$

where  $x$  is the limb darkening as determined by a non LTE model atmosphere with suitable temperature and gravity, and  $y$  is the gravity darkening.

Another technique is to estimate the masses from the X-ray data only. An equation relating the radius of the occulting object  $R_1$ , the separation  $a$ , the inclination  $i$  and the phase angle of the duration  $b$  is

$$3) \quad R_1^2/a^2 = \cos^2 i + \sin^2 b \sin^2 i$$

When combined with equation (4) which gives the size of the Roche lobe it is possible to tabulate the masses for a range of possible values of  $i$  and then place constraints on  $i$  from the properties of the eclipse.

The occurrence of simultaneous X-ray, optical, infrared or radio features has enabled a number of binary sources to be positively identified and investigated and these are listed in Table 1A. The number of known X-ray sources is only 1 in  $10^9$  of all the stars in the Galaxy but it appears likely that most galactic plane sources will have a binary nature. This is indicated by the short term variability and high X-ray luminosity (i.e. not SNR) in most sources and to a

Object	Optical	$L_x$ $36$ $\times 10^{36}$ erg/s	$M_x$ $M_\odot$	$M_p$	P DAYS	Variability	
						Short term	Long term
MER X-1 3U1653+35	H $\alpha$ Her 15m	10	1.3	2.2	1.7	1.24 sec Pulsar	35 day cycle 11 days on
CEN X-3 3U1113-60	Krz Star 13m	30	2.3	19.5	2.1	4.84 sec Pulsar	Accretion wake extended lows
CYG X-1 3U1956+35	HDE 226868 9m	3 - 10	>6	23	5.6	Quasi periodic down to mS 'mS BURSTS'	Low $\rightarrow$ High Transitions, several flares, absorption dips
VELA X-1 3U0900-40	HD 77581 6m	4	1.7	20	8.96	283 sec Pulsar	Occasional flaring accretion wake
CYG X-3 3U2030+40	Radio + I R 14m	60	-	-	0.2	No clear periodicities	17 day sinusoidal period transitions and flares
SMC X-1 3U0115-73	Sk 160 13m	300	1.4	8	3.9	Non periodic in minutes 0.715 sec Pulsar	Extended lows
SCO X-1 3U1617-15	12m	10	0.6	1.5	0.78	Non periodic	Flaring 10-30 minutes
X Per 3U0352+30	X Per 6m	0.005	>1	$\sim$ 10	0.9	13.9 min period + non periodic spectral and temporal variations	Spectroscopic binary 581 day period?
Am Her 3U1809+50	12m	-	0.4	1.0	0.13	Variable 5-10 minutes	Evidence for long term variations
3U1538-52	None 16m	<1.8	1.5	>12	3.7	Weak variable source	Changing eclipse width
3U1700-37	HD 153919 6m	3	2.4	33	3.4	Non periodic variable down to 0.1s	Accretion wake? 32 day period?
CYG X-2	Radio source 14m	0.3	-	-	13.6	Irregular variability over minutes	Variable
CIRC X-1 3U1516-56	-	-	-	-	12.3	'mS BURSTS' no rapid periodicities	Irregular fluctuations
LAC X-4	14m	100	1-3	>6	1.4	No periodicity flares on time scales of 10-20 min	Definite off states

TABLE 1A  
X-RAY BINARY SYSTEMS

lesser extent by the variable low energy cut offs which may be due to gas streams or discs. Only relatively few are known since the system must be close, contain a compact secondary and the X-ray lifetime is likely to be astronomically speaking fairly short.

#### 1.2.5 Evolution

The evolution of close binaries has been reviewed by Paczynski (1971) and the following general assumptions are made to aid the calculations:- Spherical stars, Circular orbits, Total mass and angular momentum conserved, Exchange occurs when the star exceeds the Roche lobe.

An expression for the Roche lobe radius is

$$4) \quad R_1/a = 0.38 + 0.2 \log(M_1/M_2)$$

Since most observed X-ray binaries are massive and have short periods the original systems must have been the same and Van den Heuvel and Heise (1972) have investigated the evolution of these types of systems.

The most massive of the two stars evolves faster and will reach its Roche surface some  $10^6 - 10^7$  years before helium burning occurs and will transfer mass rapidly to its companion on a time scale of  $10^3 - 10^4$  years becoming the less massive of the two. It will then lie near the helium burning main sequence and may resemble a Wolf Rayet system (Paczynski, 1967). Following this transfer the original primary can evolve in several different ways. If the mass  $M_1$  is less than about  $1.5 M_{\odot}$  it will become a degenerate dwarf but if  $M_1$  lies between  $1.5$  and  $3.5 M_{\odot}$  it evolves through the red giant stage again losing mass and eventually becomes a dwarf. If however after the first transfer the mass  $M_1$  is above  $3.5 M_{\odot}$  the star will explode leaving a neutron star or possibly a black hole. Kraft (1973) has noted that if less

than 1% of close binary systems become X-ray sources we can account for all the observed galactic objects. A serious problem here is to explain what happens after the explosion and McClusky and Kondo (1971) find that the few binaries that survived in their models ended up with large eccentricities for their orbits. Since the observed values are low we must assume either that the secondary is not a neutron star, that tidal forces produce co-rotation and circular orbits, or that some other factor such as mass loss is involved. It is interesting that the orbit of the binary pulsar PSR1913+16, in which mass exchange is not significant is highly eccentric.

The later stages of evolution have been speculated upon by Pringle (1973) who assumes that the new more massive companion will evolve and engulf its close collapsed companion. This will not sink towards the centre of the large star due to its large angular momentum unless there is high mass loss or magnetic braking and the two stars will have a common envelope. In this situation the large star may supernova halting further mass transfer or disrupting the system. It is also possible for the accretion to continue until the neutron star turns into a black hole which then gradually swallows the star, most of the angular momentum possible forming a massive disc. This Pringle suggests may be a model for Sco X-1 since no clear binary motion is observed.

#### 1.2.6 Possible Types

There seems to be a good case for differentiating between high and low mass systems, sources like Sco X-1 being low and sources like Cyg X-1 being massive and hence a younger type. X-ray models are discussed more fully in a later section but the low mass model would seem to have an accretion disc formed from Roche lobe overflow material

from the primary. The best observational evidence for a large disc comes from photometric observations of Hz Her, the optical companion of Her X-1. Deeter et al. (1976) have shown that the 35 day modulation is the result of eclipsing by a tilted accretion disc precessing around counter to the orbital motion since a 1.62 day period is seen ( $1.7^{-1} + 35^{-1}$ ).

Hensberge and Van den Heuvel (1974) have shown however that for masses above  $2.1 M_{\odot}$  an accretion rate  $\dot{M} > 10^{-6} M_{\odot} \text{ yr}^{-1}$  will extinguish the X-ray source. The massive OB stars with  $M > 15 M_{\odot}$  must therefore be accreting from a stellar wind which if we assume a typical loss rate of  $10^{-6} M_{\odot}/\text{yr}$  and an efficiency of capture at only 0.01 - 0.1% agrees with the observed luminosity.

OB stars are known to produce large stellar winds driven by radiation pressure via resonant line absorption or possibly by surface accoustical heating. The observations of Morton (1969) show that the velocity of flow increases outwards towards a terminal velocity of 500 - 2000 Km/sec at several stellar radii. This can be inferred from the width of optical lines which occur in dense parts of the wind while it is still accelerating but UV lines originating at greater distances give higher velocities. The most reliable rates are those determined from the microwave and infrared continuum which imply speeds only  $\frac{1}{4}$  of that predicted by Castor (1975) from the equation

$$V(r) = V_T (1 - R_*/r)^{\frac{1}{2}}$$

$$V_T = \text{terminal velocity} \quad R_* = \text{star radius}$$

Barlow and Cohen (1977) find that  $V$  at  $2R_*$  is only  $0.15 V_T$  and this is a very important parameter since it effects the accretion rate and the X-ray luminosity.

The assumption that neutron stars or black holes result from

a supernova leads to problems explaining the low orbit eccentricity observed but there is a curious coincidence here in that there are also two types of supernova. Recent work by Moore (1973) shows that type II ( $M_A = -13.6$ ) which only occur in spiral galaxies actually tend to be at the edge of the spiral arms implying that these types are young and massive. It seems possible that these objects are now seen as Cyg X-1 and Cen X-3. Type I ( $M_A = -16.5$ ) supernova however occur in all galaxy types predominantly in the discs and these may be linked to the lower mass sources. Type I have also been noted for the uniformity of their light curves and it is tempting to suppose that these distinct transitions may be a white dwarf collapsing to a neutron star due to mass increase from accretion.

#### 1.2.7 Types of X-ray Binaries

##### Transients

Lamb et al. (1977) have proposed a model for accretion in which the flow into the magnetosphere of a neutron star is regulated by radiative processes in the shocked gas so that thermal instabilities may be responsible for burst like behaviour. A whole series of models can be formulated in which material accumulates until it suddenly punches through the magnetosphere producing an X-ray flux and allowing the field to reform preventing further accretion. These relaxation oscillator models encompass both bursters and transients. Pringle (1973) notes that if accretion is too large the X-ray source will be smothered and emit about  $10^{38}$  ergs sec<sup>-1</sup> at optical and UV wavelengths. If mass transfer ceases the material will gradually disappear either by accretion or rejection through radiation pressure and when the line of sight becomes optically thin the source will appear briefly and slowly fade. Avni et al. (1976) have proposed an eccentric binary model

for transients in which material is accreted rapidly only during periastron but a problem here is that the high eccentricities required are not observed in known X-ray binaries. 3U1630-47 for instance appears to have a 600 day period (Jones et al., 1976). The bright transient A0620-00 (Elvis et al., 1975) rose to 12th magnitude accompanied by an X-ray flux increase of at least 5000 times. The many weaker transients seen are also probably accompanied by optical increases that will prove hard to detect since they may be initially very faint. Precise position measurements will make identification much easier.

#### Mini Transients

A number of short lived transits ( $T < 100$  minutes) have been reported such as those by Cooke (1976). Although the brief nature of the events does not allow identification these high galactic latitude sources may be connected with T Tauri or UV Ceti flare stars. Recently a single orbit transient observed with the SSI on Ariel 5 (Ricketts, 1977) has been found to coincide both in position and time with a  $\gamma$  ray burst observed by a VELA satellite.

#### Bursters

The discovery of the X-ray bursters by Lewin et al. (1976) prompted a search for further examples and Lewin (1977) lists some twelve objects of this type. Most burst only every few hours, however MXB 1730-335 is remarkable for the rapidity and pattern of its bursts. The available data on this source's ON-OFF states has been compiled by Grindley and Gursky (1978) and does not imply at present the presence of an underlying binary interaction. It is also of interest to note the similarity between the behaviour of MXB 1730-335 in its ON state

and the dwarf novae SS Cygni (Brecher et al., 1977).

### Dwarf novae

A complete review of dwarf novae can be found in Glasby's book (1970) and he points out that it is a generally accepted fact that recurrent and dwarf novae are in close binary systems. Of the several hundred known many such as SS Cygni have extensive gas discs and U Gem, EX Hydra and Z Cham show eclipses. The nova taken individually and together appear to show period luminosity laws, the typical  $M_v$  being 12 - 14 with a 3.5 increase. Warner (1974) has shown that 7 exhibit during maxima a roughly 30 sec period pure sinusoidal variation of 0.0001 - 0.1 magnitudes which is interpreted as radial oscillations of the white dwarf. From studying orbit period changes following flares Smak (1972) has inferred that there is extensive angular momentum exchange between the disc and secondary.

The dwarf novae binaries typified by U Gem have a period of 4 hrs - 100 days and masses of 1.1 - 2.4  $M_{\odot}$ . They are also similar in physical parameters spatial distribution and galactic kinematics to the close binary W Ursa Majoris variables. Bath (1973) expects many of these objects to be soft X-ray extreme UV emitters and U Gem itself has been detected by HEAO-A in the 2 - 8 keV range (Mason et al., 1977). SS Cygni the brightest of the dwarf novae has also recently been detected by the SSI on Ariel 5 (Ricketts, 1978).

### Novae

Several old novae such as DQ Herculis (1934) and T Auriga (1891) have been found to be in close eclipsing binary systems and Kraft (1963) has come to the conclusion that nearly 100% of novae and eruptive variables are also in binary systems. A search for Novae

Cygni has been reported by Hoffman et al. (1977) using the SAS-3 satellite but no source was detected. Novae are considerably less violent events than supernovae, their absolute magnitude being only -7.

### Pulsars

Many of the known binary sources contain a pulsar and the similarities in the profiles of 9 have been compared by Rappaport and Joss (1977a). An empirical fit for the rate of change of pulsation period based on 7 of these objects has been given by the same authors (1977b).

$$(-\dot{P}/P) \propto PL_x^{6/7}$$

The Crab is not included since it is clearly not a member of a binary system.

### Stars

Recently several stars all of which are in binary systems have been detected as X-ray sources. Sirius and Capella have been seen at low energies (Mewe et al., 1975) and one of the first imaging camera systems flown on a rocket has identified Algol itself as a weak low energy source (Harnden, 1977).

It seems likely that the range of X-ray sources leaving aside supernovae remnants and distant extragalactic objects simply reflects the great variety of possible binary systems and one can expect the forthcoming sensitive surveys to reveal many more sources of this type.

### 1.3 X-ray Generation by Compact Objects

#### 1.3.1 Generation of X-rays

Close binary systems provide a very efficient system for converting gravitational energy into radiation. If we take the mass loss rate  $\dot{M}$  and a velocity  $V$  the energy released will be

$$L = k\dot{M}V^2 \quad k = \text{constant}$$

where for a close system  $V$  will be near the free fall velocity

$$V_F = (GM_X/R)^{1/2}$$

$$1) \quad \therefore L = GM_X \dot{M}/R = 10^{33} \left[ \frac{M_X}{M_\odot} \right] \left[ \frac{R_\odot}{R} \right] \left[ \frac{\dot{M}}{M_\odot 10^{-8}} \right] \text{ ergs/sec}$$

and the temperature  $T$  produced by thermalisation of the flow is

$$T = \frac{\alpha \text{ mp } GM_X}{kR} = 10^7 \left[ \frac{M_X}{M_\odot} \right] \left[ \frac{R_\odot}{R} \right] \text{ }^\circ\text{K}$$

where  $\text{mp}$  = proton mass  $k$  = Boltzmann's constant

$$a) \quad \text{for adiabatic heating} \quad \alpha = 0.1$$

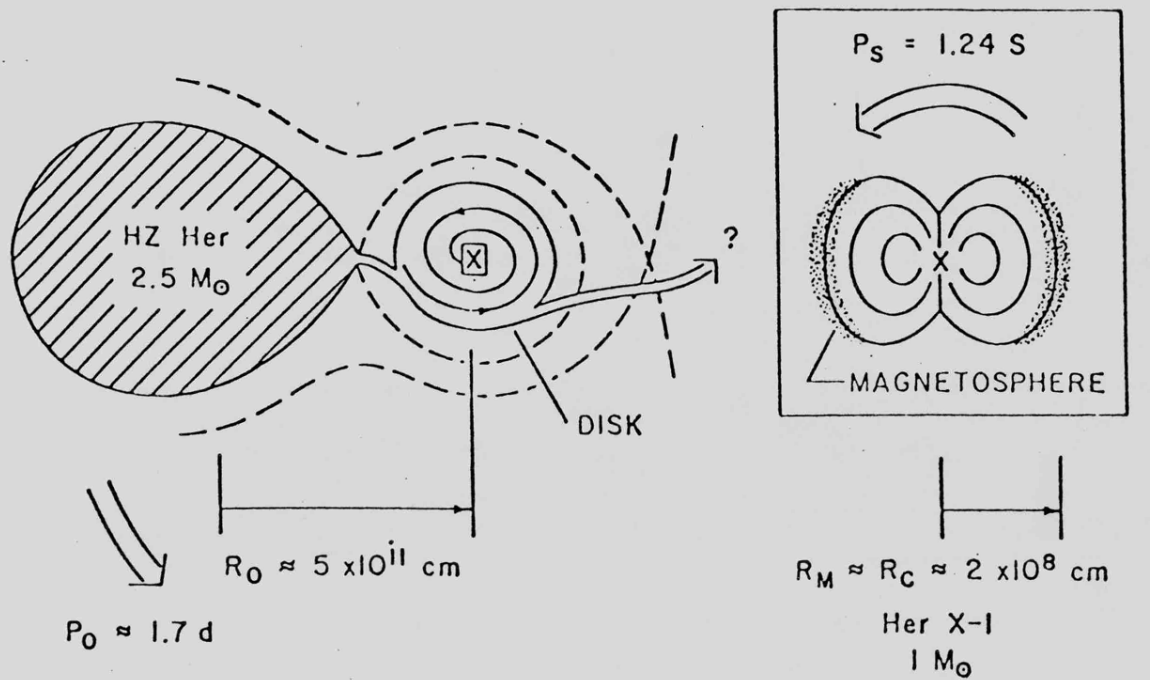
$$b) \quad \text{for slower processes} \quad \alpha \rightarrow 10^{-6}$$

To obtain temperatures of  $10^8$  K the masses and radii must satisfy

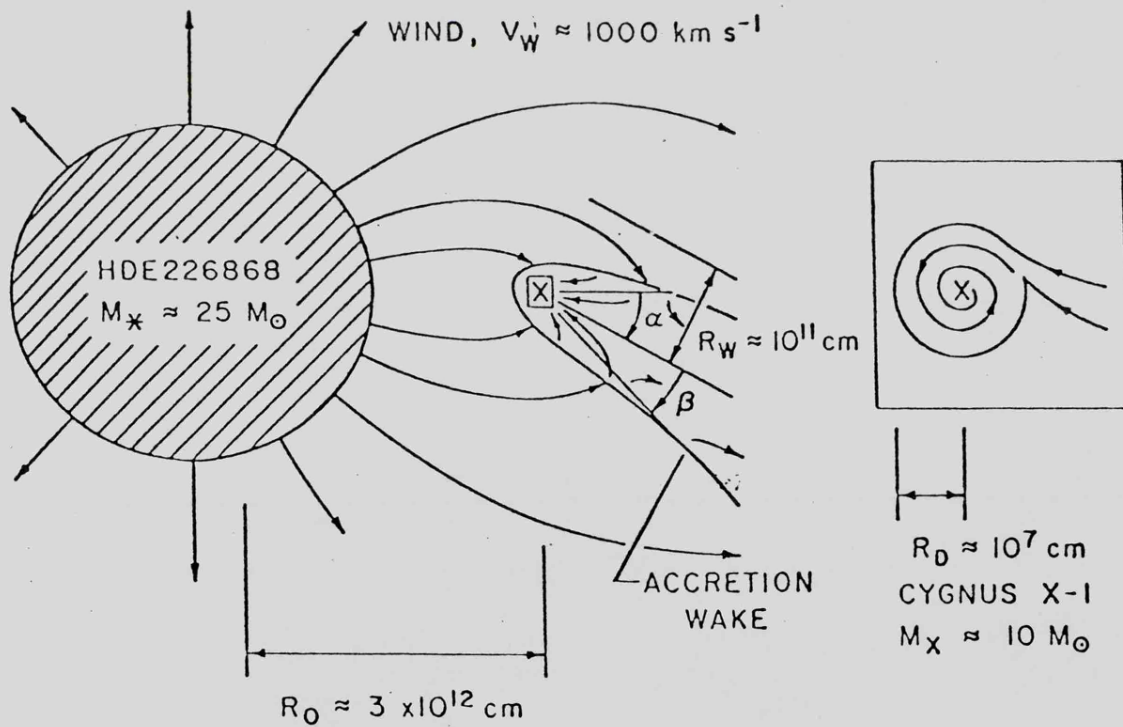
$$2) \quad \frac{M_X}{M_\odot} \cdot \frac{R_\odot}{R} = \frac{10}{\alpha} \gg 100$$

For main sequence stars this ratio is 3 and for giants 1, so neither of these will do to obtain the high temperatures required for the generation of X-rays. There are, however, 3 types of object that do satisfy this equation and we shall consider each of these in turn.

There are also two basic methods of accretion disc formation and these are shown in fig. 1.1. The top diagram is a model for the Hercules X-1 system in which the disc is created by Roche lobe overflow, the material then being funnelled onto the compact secondary, in this particular case a neutron star. The second model applies to Cygnus X-1 where the stellar wind from the massive primary forms a shock front



HER X-1



CYG X-1

FIG 1.1 X-RAY BINARY MODELS  
 ( Mc CRAY 1976 )

and then falls inwards to form a smaller disc.

### 1.3.2 White Dwarfs

The giant star will collapse after nuclear burning until the Pauli exclusion principle forms a state of equilibrium with gravity.

For  $M < 1.5 M_{\odot}$  stars this occurs at a radius given by Landau and Lifshitz (1958) as

$$R = 10^{-2} R_{\odot} \left[ \frac{M_{\odot}}{M_X} \right]^{1/3}$$

so for a dwarf equation (1) becomes

$$3) \quad \frac{M_X}{M_{\odot}} \cdot \frac{R_{\odot}}{R} = 100 \left[ \frac{M_X}{M_{\odot}} \right]^{4/3}$$

which satisfies equation (2) for case (a) but not for case (b). To have a luminosity of  $10^{36}$  erg sec<sup>-1</sup> the mass loss is  $10^{-7} M_{\odot}/\text{yr}$  and the X-rays can be emitted through direct radiation of accreted matter or by nuclear burning. If we imagine a body of radius  $10^9$  cm and density  $10^{16}$  gm cm<sup>-3</sup> the cooling time of the radiating plasma is around 0.1 sec which is short enough to explain fast time variations. Hoshi (1973) has considered accretion onto white dwarfs and this work has recently been extended by Fabian et al. (1976). They find the X-ray luminosities are unlikely to exceed  $10^{36}$  ergs and that the Bremsstrahlung temperatures are relatively high at  $kt = 50$  KeV with a substantial low energy cut off. A magnetic field channelling material towards the polar cap can also be important for cooling by cyclotron emission at optical or IR wavelengths and they suggest that many weak sources of this type await discovery. A further type of model in this class is the pulsating degenerate dwarf proposed by Burbidge (1972) in which nuclear burning of accreted material can cause oscillations. If  $g$  = gravity,  $v$  = escape velocity and pulsar period =

$t_p$  then if  $2v \approx g t_p$  large amplitude pulsations ( $\delta R/R \approx 0.1$ ) of the dwarf would produce shocks that could maintain an extended atmosphere. This model predicts a quasi thermal spectrum which is cut off at low energies and a luminosity

$$L \propto t_p^{-4/3} (\delta R/R)^4$$

although there is doubt about the stability of the atmosphere.

Another possibility concerning dwarfs is the differentially rotating degenerate dwarf or DRDD model which has been proposed by Lamb and Van Horn (1973) and Brecher and Morrison (1973). They picture a magnetised slowly collapsing degenerate core after the envelope is blown off or following normal collapse, that rotates so rapidly ( $P =$  several seconds) that the centripetal force plays a significant role in supporting the star. These objects would retain most of their original angular momentum in contrast to the typical value of  $10^{-5}$  that a pulsar is left with. In contrast to neutron stars rotational energy losses the accretion can cause this object to spin up, a direct consequence of the fact that rotation forms an essential role in supporting the star. These objects could emit through accretion onto the poles or by non thermal pulse-like emission of rotational energy.

### 1.3.3 Neutron Stars

In stars of heavier mass  $1.5 < M_{\odot} < 3.3$  the collapse continues until the degenerate pressure of the nucleus stabilises the star at a radius

$$R = 10^{-5} R_{\odot} \left[ \frac{M_{\odot}}{M_x} \right]^{1/3}$$

and therefore

$$4) \quad \frac{M_x}{M_{\odot}} \cdot \frac{R_{\odot}}{R} = 10^5 \left[ \frac{M_x}{M_{\odot}} \right]^{4/3}$$

easily satisfying case a and b and having a luminosity of  $10^{38}$  erg sec<sup>-1</sup> for a mass loss of  $10^{-8}$   $M_{\odot}$ /year. Many models have been put forward such as those of Lamb et al. (1973) and Pringle (1973) where accretion takes place onto a neutron star since this provides an explanation of the X-ray pulses. The material is channelled to the poles of a neutron star, whose magnetic and rotation axis are not aligned, from the stellar wind or from the inside of a surrounding disc. At the Alfvén surface the gas ram pressure equals the magnetic energy density and the infall becomes radial. The radius of this surface is given by

$$5) \quad R_A = 2.6 \times 10^8 \left[ \frac{B}{10^{12} \text{ Gauss}} \right] \left[ \frac{M_X}{M_{\odot}} \right]^{1/7} \left[ \frac{R}{10 \text{ km}} \right]^{10/7} \left[ \frac{L_X}{10^{37} \text{ erg}} \right]^{-2/7} \text{ cms}$$

The infalling material will flow towards the poles. Another important dimension is the corotation radius where the orbital velocity is equal to the surface rotation rate.

$$6) \quad R_c = 1.5 \times 10^8 \left[ \frac{M_X}{M_{\odot}} \right]^{1/3} (P_{\text{sec}})^{2/3} \text{ cms}$$

We can now consider three cases for the neutron star magnetosphere.

#### Slow rotators $R_A \ll R_c$

Examples of this case are those sources with periods greater than a few seconds such as Vela X-1 where centrifugal forces are unimportant at  $R_A$  and a spherically symmetric flow onto the magnetosphere is possible. Elsner and Lamb (1977) and others have determined that all lines of force of the dipole field are contained within  $R_A$ . The inflowing gas encounters a shock at the magnetopause and free falls in about 0.1 sec into the magnetosphere, the flow of material down the field lines exerting a torque, the direction depending on whether the star rotates in the same direction as the disc. Radiative cooling of the shocked gas is necessary to start instabilities but if  $P$  is very

small the pulsar-like emission will impede accretion resulting in a value of  $P > \frac{1}{2}$  second (Lamb et al., 1973). It has been pointed out by Gnedin and Sunyaev (1973) that estimates of an optical depth of 20 parallel to the flow and 3 across it will allow photons to escape preferentially in the latter direction. Considering cyclotron emission from an optically thin collisionless shock front at the neutron star surface they are able to produce a fan beam or if the electrons are relativistic and at small pitch angles to the magnetic field a pencil beam.

Intermediate rotators  $R_A \simeq R_C$

Examples of this case are Her X-1 and Cen X-3. The gas at  $R_A$  may now be supported by centrifugal force and an opaque shell will exist if the storage time is greater than 10 times the free fall time. This shell will absorb the high energy X-rays and re-emit soft X-rays (Basko and Sunyaev, 1976).

Fast rotators  $R_A \gg R_C$

Sco X-1 may be an example of this type in which centrifugal force is greater than gravity and accretion cannot occur. The gas will accumulate at  $R_A$  until it forces the magnetopause to a smaller value and when  $R_A \simeq R_C$  accretion will occur. Some matter may be ejected and this will have a braking effect on the neutron star. The surface area on which the infalling material collides will contain open field lines and have an area

$$\delta x = \pi R^3 / R_A \quad R = \text{radius of star}$$

and if it radiates like a black body a temperature at  $5 \times 10^7$  °K, (Davidson and Ostriker, 1973). The infalling gas interacts with the

neutron star magnetosphere causing the rotation period to approach an equilibrium of a few seconds and Lamb et al. (1973) note that  $P/\dot{P}$  for Cen X-3 and Her X-1 are in good agreement with the observed values of  $10^5$  for Her X-1 and  $10^4$  for Cen X-3, with the orbital motion in the same sense as the stellar rotation.

#### 1.3.4 Black Holes

For a black hole the Schwarzschild radius is

$$7) \quad R_g = 2 G M_x / C^2$$

the efficiency of energy release is  $0.1 mc^2$  for a non-rotating hole and  $0.4 mc^2$  for a rotating one (Novikov and Thorn, 1973).

$$8) \quad \therefore \frac{M_x}{M_\odot} \cdot \frac{R_\odot}{R} = 10^5 \cdot \frac{M_\odot}{M_x}$$

satisfying (a) and (b) and emitting  $10^{38}$  ergs second<sup>-1</sup> for a mass loss of  $10^{-8} M_\odot$ /year. Hot spots in the accreting disc can be created by turbulent convection or by magnetic field line closure giving rise to X-rays with a quasi periodic variability. Sunyaev (1973) has shown that the life time of a spot could exceed its orbit period stabilising the pulsations, the minimum period being 8 times less for a rotating hole than for the non-rotating case with the same mass. The formation of the disc and hot spots has been considered in detail by Lin and Pringle (1976).

If we assume that the bulk of the radiation is emitted beyond the Schwarzschild surface the characteristic period is  $(2 \times 10^{-3} \rightarrow 2 \times 10^{-2}) M_x/M_\odot$  seconds which is in general agreement for Cygnus X-1 if  $M_x = 10 M_\odot$ . Novikov and Thorn (1973) give a minimum period for the non-rotating case of  $0.5 (M_x/M_\odot)$  mS and  $0.06 (M_x/M_\odot)$  mS for the rotating case. This time scale results from general relativity considerations

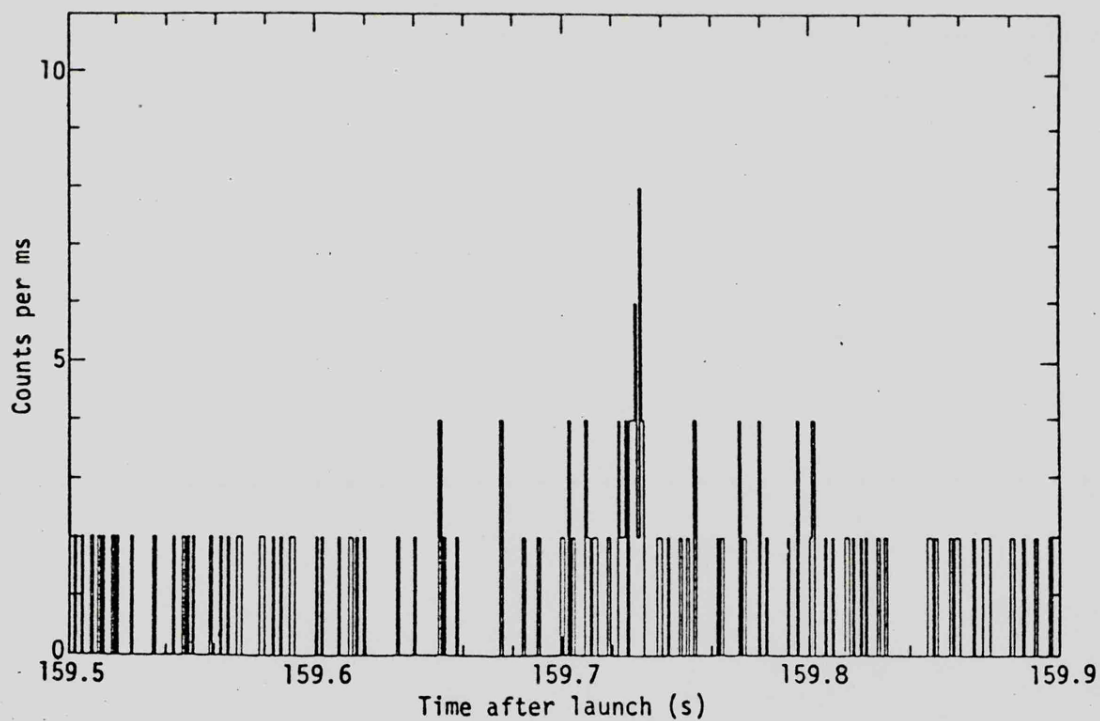
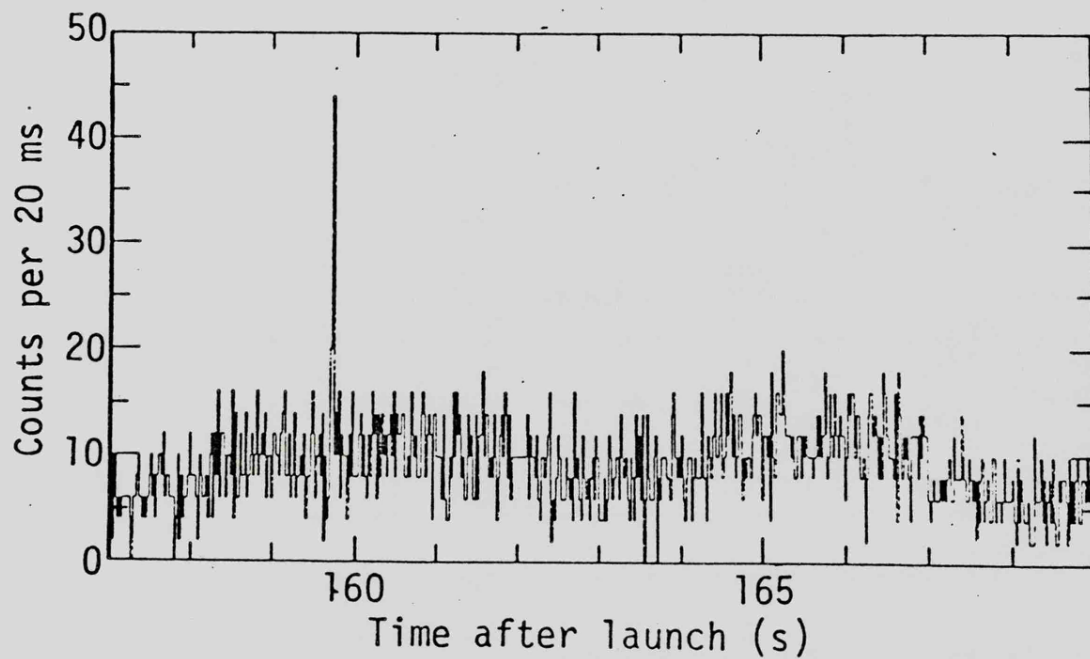


FIG 1.2 MILLISECOND BURST FROM  
CIR X-1 ( TOOR 1977 )

which show it is impossible for stable particle orbits to exist closer than  $3 R_g$  to a black hole. Only two X-ray sources are known to have such rapid structure namely Cir X-1 and Cyg X-1 so both are black hole candidates. Fig. 1.2 is an example of a 10 mS burst from Cir X-1 showing 1 mS structure. Shapiro and Lightman (1976) have shown that spherical accretion rather than disc accretion will lead to gas temperatures near  $10^{11}$  o K producing  $\gamma$  rays in the 1 - 10 MeV range (Shvartsman, 1971) and therefore this type of flow cannot supply the observed X-ray flux.

### 1.3.5 Stellar Wind Accretion

This has been considered by Davidson and Ostriker (1973) and appears to be a suitable method of mass transfer for Cygnus X-1 (fig. 1.1). If we consider an accretion disc around the black hole in a circular orbit about a primary that has a steady spherically symmetric wind a shock front will be produced since the flow is supersonic. The treatment of Hoyle and Lyttleton (1939) shows that gas will be captured inside a cylinder of radius

$$9) \quad R = \frac{\xi 2 G M_x}{v_{rel}^2} = 1.3 \times 10^{11} \left[ \frac{M_x}{10 M_\odot} \right] \left[ \frac{v_{rel}}{10^8 \text{ cm.s}} \right]^{-2} \text{ cm}$$

where  $V_{rel}$  is the relative velocity between the hole and wind and  $\xi$  is a correction factor near unity describing deviations from the Hoyle model. Due to the orbit motion the cylinder will form at an angle from the line joining the two stars in the direction of the relative wind velocity ( $V_{rel}$ )

$$\alpha = \tan^{-1} (v_x/v_w) \quad \begin{array}{l} v_x = \text{star velocity} \\ v_w = \text{wind velocity} \end{array}$$

and the mass gained is given by

$$10) \quad \dot{M}_x = \pi R^2 \rho_w v_w = \frac{G^2 M_x^2 \dot{M}_*}{R_o^2 v_w^2} \quad \begin{array}{l} \dot{M}_* = \text{mass loss of secondary} \\ R_o = \text{binary orbit radius} \end{array}$$

A powerful method to study this model is to observe the resulting accretion wakes which will cause absorption dips such as those in Cen X-3 (Jackson, 1975). The extended lows seen in this source and SMC X-1 have been interpreted as a temporary extinguishing of the X-ray flux due to too large an accretion rate.

### 1.3.6 Accretion Discs

Most theories start from the model developed by Pringle and Rees (1972) and have been reviewed extensively by Lightman et al. (1977, accretion flows) and by Shu (1976, accretion disks). It seems that the X-ray sources can be explained by combinations of inner and outer discs where inner means  $r < 10^7 M_x$  cms. A number of problems exist such as the viscosity parameters and attempts have been made to interpret these in terms of the better observed discs round dwarf novae. The models are also thermally unstable since the optically thin part of the discs radiate less effectively when hotter and vice-versa. Shu (1976) has pointed out that for the outer disc types such as Her X-1 the radius is so near the Roche lobe that this cannot be treated as a single force case. Davidson and Ostriker (1973) suggested that the  $\dot{M}_x$  of the captured wind may generate a sufficient luminosity  $L_x$  to continually drive the wind and Basko and Sunyaev (1977) have concluded that this self driven system may work for later type stars.

Continuing work by Shapiro and Lightman (1976) on the inner disc resulting from stellar wind accretion indicates that the radius is smaller than previous models such as those of Pringle and Rees (1972) or Eardley et al. (1975) and is only marginally stable. For a neutron star  $R_c$  is small compared to  $R_A$  and it is unlikely that a

disc can form from a steady stellar wind. Since the angular momentum resulting in accretion from a steady wind is low, random fluctuations or asymmetries in the geometry may compete with or dominate the current motion of the disc if  $\delta\rho/\rho > 1\%$ . This level of change across the face of the accretion cylinder results in random changes in the magnitude and sign of the disc on time scales

$$11) \quad \tau = \left[ \frac{M_X}{10 M_\odot} \right] \left[ \frac{V_w}{1000 \text{ km.s}} \right]^{-3} \text{ hrs}$$

This sudden change will be smeared out by the time a gas element takes to spiral down through the disc and so

$$12) \quad \tau \geq 10^3 \left[ \frac{V_\phi V_R}{10^5} \right] \left[ \frac{\delta\rho/\rho}{1\%} \right]^3 \text{ sec}$$

where  $V_\phi$  = orbital velocity,  $V_R$  = radial drift from viscosity.

Shapiro and Lightman (1976) suggest that the glitches in Cygnus X-1 were caused by reversals of this kind and the above indicates that  $\delta\rho/\rho$  of 5% gives a change in a few days. Longer changes in time scales of years may be due to fluctuations in the photosphere of the primary influencing the emitted wind. It is also suggested that  $\gamma$  ray bursts (1 - 100 MeV) lasting about one second may accompany reversal of the disc possibly being the events noted by Klebesade et al. (1973). The recent change noted by Canizares and Oda (1977) in the time structure of Cygnus X-1 may also support the hypothesis of large scale disc changes. This source has become even more active and now shows structure on all scales some 3 - 6 times longer than previously reported low state measurements.

### 1.3.7

A further possibility for X-ray generation is the model proposed by Bahcall and Rosenbluth (1973). This envisages a binary

system composed of two normal non-rotating stars that are linked by a large magnetic field. The idea is that the linked lines of force will be twisted up increasing the magnetic energy until instabilities set in and release the energy in the form of X-rays. There are two specific predictions involved here in that the stars rotate faster than the orbital period and that a large magnetic field of  $10^4$  gauss is required at the star's surface. The details of the X-ray generation are vague and Bachall points out the lack of understanding of the well observed solar flares to guard against over prediction, but the model does not require the existence of black holes. If  $T_e$  is the escape temperature the plasma will be at a temperature corresponding to

$$13) \quad k T_e = 2 \left[ \frac{M}{M_\odot} \right] \left[ \frac{R_\odot}{R} \right] \text{ keV}$$

for  $T \ll T_e$  little plasma supplied by mass loss

$T \gg T_e$  most plasma will escape.

The life time of such a source can be estimated to be

$$T = 1/2 I \omega^2 / L_X$$

which for Cyg X-1 gives an age of 3000 years. Assuming stars exist with the correct sort of magnetic field the life time estimate can give agreement with the number of sources in the Uhuru Catalogue.

### 1.3.8 X-ray Emission

The accretion process will not occur if the gas temperature is so high that the thermal velocity exceeds the escape velocity.

This Bondi radius is given by putting

$$14) \quad C_s = (kT/\mu m_H)^{1/2} = v_w \text{ in eqn 9}$$

$C_s$  = isothermal sound speed.

The Eddington limit is another important parameter obtained by equating gravity with the radiation force due to scattering. This gives a source a maximum luminosity of

$$15) \quad L_E = 1.2 \times 10^{38} \cdot \frac{M_x}{M_\odot} \text{ ergs/sec}$$

Hatchett et al. (1976) have shown that the radiation force may exceed electron scattering by a factor of  $10^3$ . Most X-ray sources are within a factor of 10 of  $L_E$  for  $M_x = M_\odot$  and Margon and Ostriker (1973) have suggested that the luminosity may be regulated by radiative pressure or heating. The luminosities obtained from these models are within observational and theoretical estimates for mass loss from stars due to tidal instability or radiation pressure driven winds.

The actual process of X-ray production has been investigated by Tarter and Salpeter (1969) who calculated models based on ionisation and recombination, heating and cooling, and absorption and emission. The calculations have been extended by Hatchett et al. (1976) and three facts emerge.

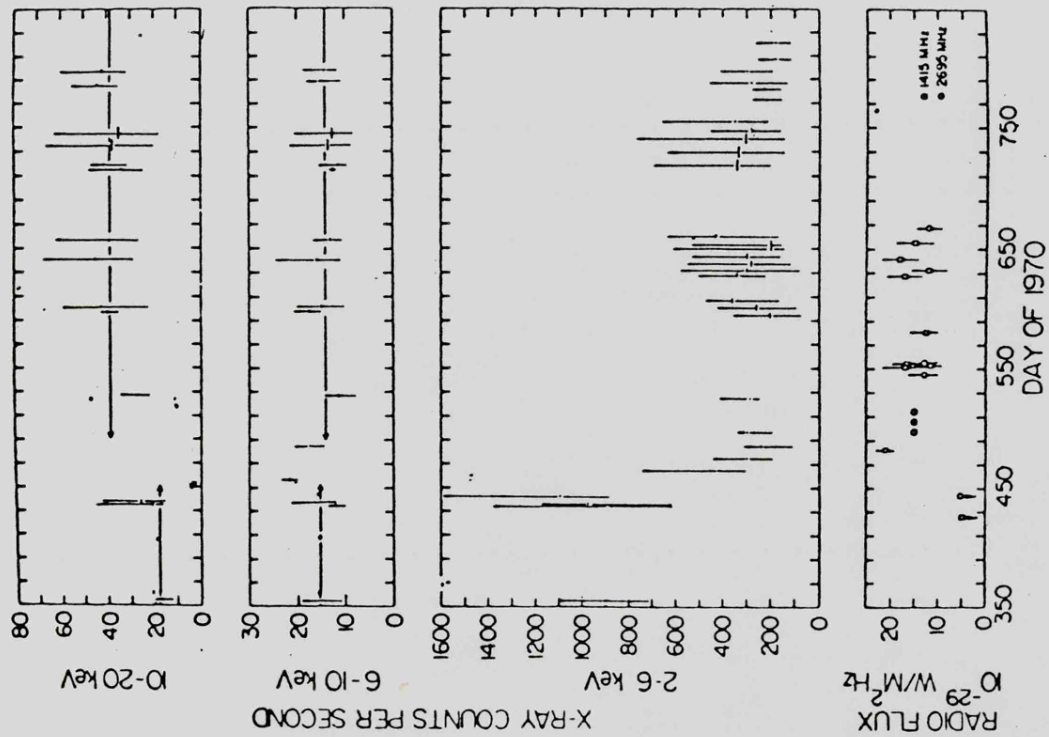
- a) The spectrum is rich in optical, UV and X-ray lines.
- b) Changing  $L_x$  leads to gas temperature changes and thermal instabilities in the flow.
- c) Radiation force can exceed that due to electron scattering. McCray (1976) has noted that further investigations of the detailed emission processes awaits good spectral measurements from powerful spacecraft such as HEAO-B.

#### 1.4 Observations of Cygnus X-1

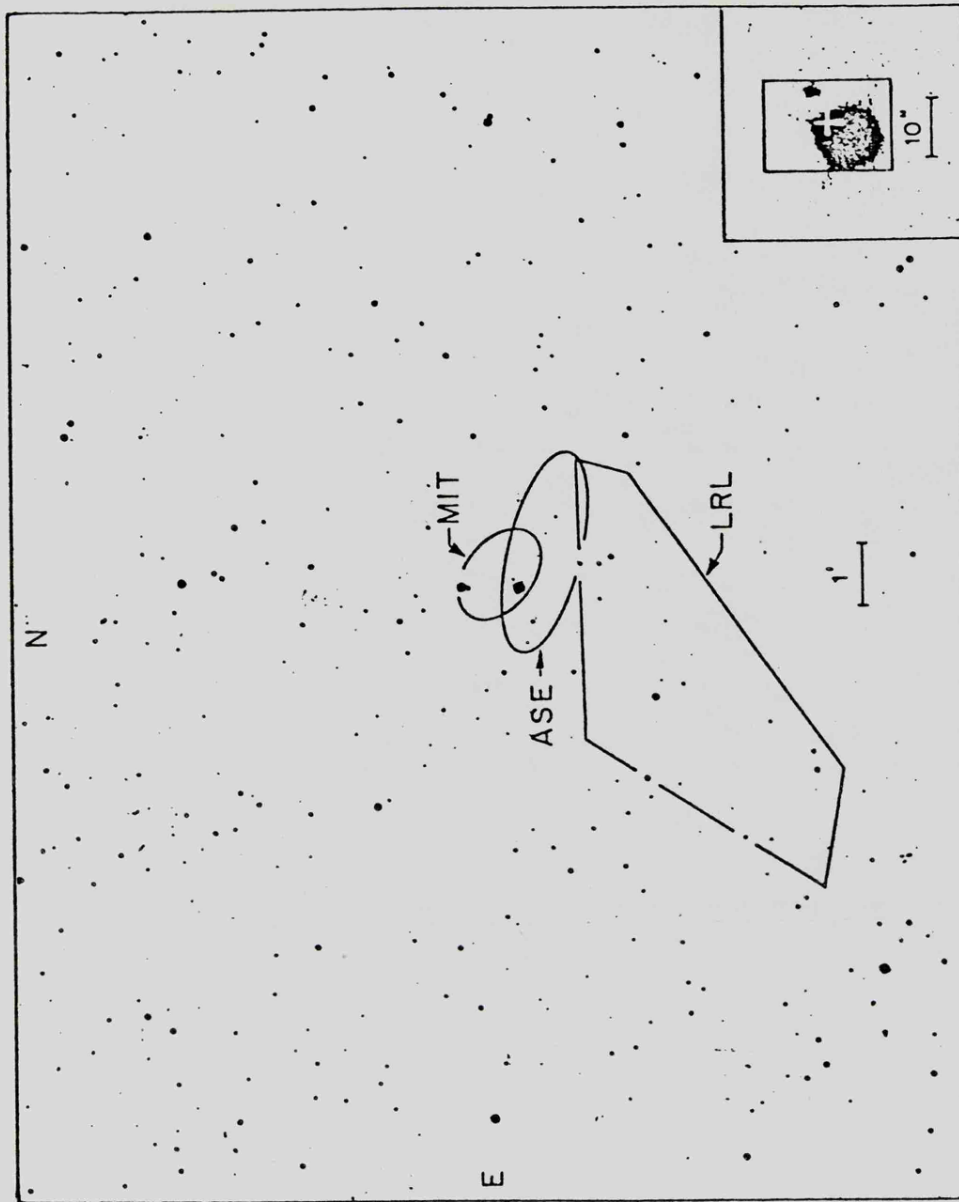
##### 1.4.1 Identification and Position

Cygnus X-1 was first detected as an X-ray source by Gursky (1963) and has been observed by many instruments since then. A

modulation collimator flown by Floyd et al. (1969) gave an early size limit in the 25-100 KeV band of 1.4' and early results by Byram et al. (1966) indicated a four fold increase in flux between June, 1964, and April, 1965, in the 1-10 KeV range. Uhuru observations produced a 15 square arc min error box (Tananbaum et al., 1971) but no suitable optical candidate was found due to the high density of field stars. A similar error box was produced by Toor et al. (1971) but much more accurate positions were obtained by a Japanese balloon flight by Miyamoto et al. (1971) and a rocket flight by Rappaport et al. (1971) both of which employed modulation collimators. The error boxes are shown in fig. 1.1, Rappaport giving the source position as RA 19h 56m 27.6s DEC +35° 04' 07" with only a 30" error. A radio search by Braes and Miley (1971) failed to locate a source down to the limit of sensitivity of 5 milli flux units. ( $1 \text{ FU} = 10^{-26} \text{ Wm}^{-2} \text{ Hz}^{-1}$ ) but during March/April, 1972, a source appeared at  $21 \pm 4 \text{ mFU}$ . A simultaneous change was noted in the X-ray spectra by Uhuru and Tananbaum et al. (1972) reported a 2-6 KeV flux decrease by a factor of 4 and a 10-20 KeV flux increase by a factor of 2 (fig. 1.3). No clear structure was noted either in the radio or X-ray observations but using the aperture synthesis technique Hjellming and Wade (1971) located the new object to within 1" finding it consistent with a point source. There were, however, two possible optical star counterparts (fig. 1.3), the brighter one at 9th magnitude being BD + 34 3815 or HDE226868, the fainter one at magnitude 15.2 being 9" to the north-east. The optical spectra of HDE226868 was studied at high dispersion and the radial velocity curve produced revealed it to be a spectroscopic binary system with a period of about 5.6 days. Since there was nothing unusual about the absorption spectrum obtained Kristian and Brucato (1971) suggested the second fainter star as the X-ray source but subsequent correlated



RADIO/X-RAY EVENT  
 ( TANANBAUM et al 1972 )



ERROR BOX ( KRISTIAN et al 1971 )

FIG 1.3 IDENTIFICATION OF CYG X-1

X-ray and radio flares have confirmed the belief that the HDE226868 system is responsible for the emission. This brief X-ray enhancement to something like the pre-1971 state occurred in May/June, 1975, and using Uhuru data Parsignault et al. (1976) reported a decay over several weeks that again matched radio data taken at 2695 and 8085 MHz.

#### 1.4.2 Time Structure

Several rocket flights had shown Cygnus X-1 was variable but Uhuru enabled a detailed study to be made. Oda et al. (1971) reported observations that indicated a 73 mS period but as the minimum bin size was 0.096 sec they could not rule out multiples up to 292 mS. Following this Holt et al. (1971) analysed an 8 sec observation with  $320 \mu\text{S}$  resolution finding several peaks in the Fourier spectrum at 0.29 and 1.1 sec. Rappaport et al. (1971) however found flaring on time scales of 50 mS with 1 mS resolution over a 75 second observation and from a power density spectrum found a few peaks between 1 and 5 seconds but no periodicity between 0.01 and 1 second. Shulman et al. (1971) re-analysing 40 seconds of 1967 data with 4.5 mS resolution found no periodicities between 0.01 and 4 seconds but had indications of significant intensity variations and Schreier et al. (1971) found evidence for pulse trains of 0.3 - 10 sec duration occurring at several tens per second. A further study over 6 months of Uhuru data led to the following conclusions.

- 1) Large fluctuations of intensity occur on time scales from 50 mS to 10 seconds containing up to 50% of the power.
- 2) Periodic pulse trains with periods 0.3 - 10 seconds exist containing 10 - 25% of the power but persist for only 10's of seconds.
- 3) No single period is present.

They also note that the energy spectrum is best fitted by a power law with a highly variable index with an excess at higher energies.

$$\frac{dN}{dE} = A_e^{-\alpha}$$

$\alpha = 3.8$	2-10 KeV
$\alpha = 1.5$	10-20 KeV

Terrell (1972) has explained these patterns in terms of a shot noise model which consists of random pulses having effective lengths of  $0.3 \pm 0.1$  seconds and occurring at several hundred Hertz, the actual shot profile not being very important. Computer generated data also looks similar to the Cygnus data and has a similar power spectra. Brinkman et al. (1974) has considered the Uhuru data in two energy channels, 2-5 KeV and 5-12 KeV and found using autocorrelation and cross correlation techniques that the higher energy pulses are typically narrower and appear to contain more power than the low energy data. This has, however, recently been criticised by Weisskopf et al. (1977) who have repeated the analysis using a more thorough mathematical technique. The shot noise has also been correlated with the binary period by Weisskopf (1976). Oda et al. (1975) have reviewed most of the early observations and have repeated the analysis of rocket flight data using sonographs and histograms rather than Fourier analysis in an attempt to gain more insight into the confusing patterns.

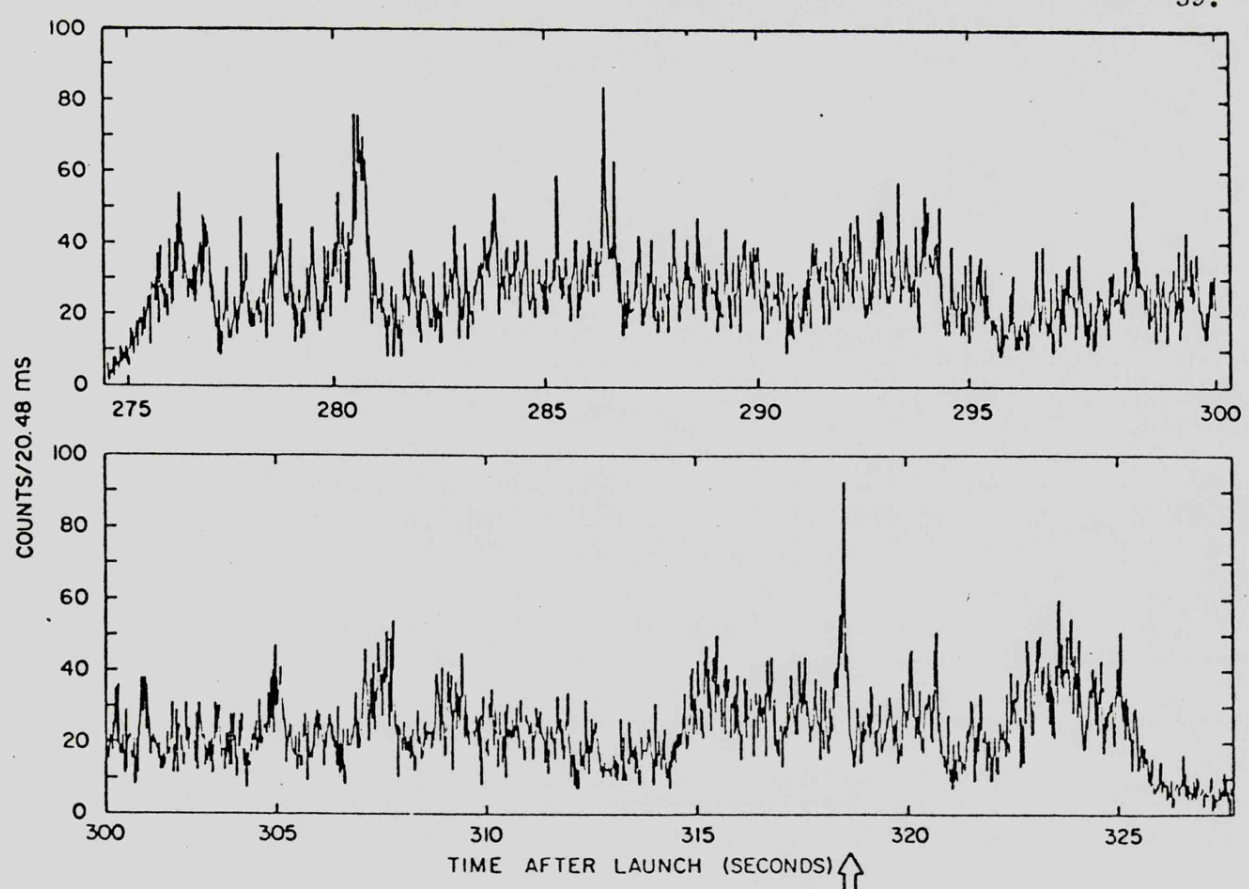
Recent observations from SAS-3 by Canizares and Oda (1977) made during October, 1976, only a few weeks before the launch of SL-1306 show Cygnus to be in a highly active state with flares on a time scale 3-6 times longer than previously observed. These frequent rapid flares lasting 1-10 seconds were not observed by the same instrument during earlier observations. Shot noise parameters for this observation have a time scale of 1.5-2 seconds with a repetition rate of 5-10 a second compared to 10-40 a second on a time scale of

0.2-0.5 seconds. This change has been interpreted as a variation in the accretion disc structure and implies that there are at least two distinct phases for Cygnus X-1 while in its current low state. Flares of approximately 1 second appear to occur predominantly below 5 KeV while those lasting up to 10 seconds are both hard and soft without any obvious recurrent pattern. A few observations made using 0.12 mS resolution show significant narrow peaks within the flares indicating temporal structure down to 40 mS. A characteristic time scale of 20 mS previously noted by Canizares et al. (1976) based on earlier SAS-3 data was again detected and features on this time scale have also been reported by Ogawara et al. (1977).

#### 1.4.3 Millisecond Bursts

While analysing Rappaport's rocket data (1971) Oda et al. (1974) found evidence for the grouping of millisecond pulses into 200 mS intervals with an excess of 3 sigma of short intervals (0.2s) between adjacent one millisecond bins containing more than 5 counts. Of particular relevance to this thesis are the two flights by Rothschild et al. (1974, 1976) which apparently showed Cygnus X-1 to have clear millisecond structure flares, (fig. 1.4). The lower diagram contains an aligned burst profile obtained by combining all the pulses detected in each burst for the 1974 flight. This square profile is of great interest since possible substructure could yield a value for the angular momentum of the collapsed object (Leach and Ruffini, 1973).

During a total of 230 seconds of observation in the two flights some 13 significant bursts were found when  $1.7 \pm 0.8$  might have been expected based on the count rate alone. This gives a duty cycle for such bursts of  $6 \times 10^{-5}$ . A search on time scales of  $160 \mu\text{S}$  to 5 mS did not reveal any features that had not been seen at 1 mS and



SIZE OF  
CYG X-1

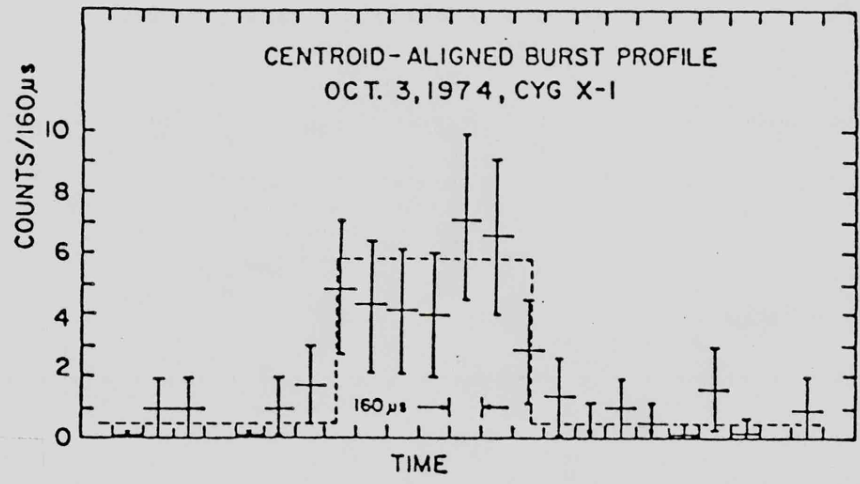
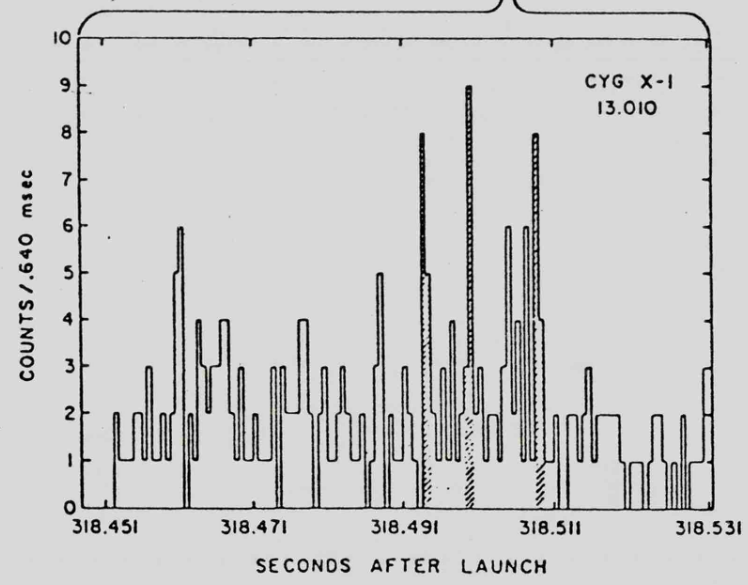


FIG 1.4 DATA FROM G.S.F.C (ROTHSCHILD et al 1974/76)

the limited PHA information indicated that the bursts may have had a somewhat harder spectrum than the overall source emission. The spectra for the two flights, October 1973 and 1974, were almost identical in contrast to earlier rocket results giving a power law fit with index  $-1.55$  and an upper limit of  $3 \times 10^{21}$  H atoms/cm<sup>2</sup> of interstellar material in the line of sight. A complete discussion of these two flights can be found in Rothschild et al. (1976).

The more recent flight reported by Ogawara et al. (1977) has found characteristic variability on time scales of 0.1-1.0 sec (1.5-25 KeV) which appears to be accompanied by spectral variations. A time scale of  $\leq 10$  mS is also indicated for their 10-25 KeV band. They have found 3 bursts each with greater than 13 counts in a 1.25 mS bin when less than  $2 \times 10^{-2}$  might have been expected.

The problems involved in using Poisson statistics for the probability of millisecond bursts has been discussed by Press and Scheckter (1974) but more recently the analysis of Rothschild et al. (1974) has been criticised by Weisskopf and Sutherland (1977) who created a computer simulation of the shot noise model. An analytic approach by Weisskopf et al. (1977) leads to similar conclusions but the 'harshness' of their model is open to debate. These problems are discussed more fully in chapter six when dealing with potential 'millisecond' bursts observed by SL-1306.

#### 1.4.4 Absorption Dips

Many searches have been made in satellite data for a correlation between the X-ray and optical light curves but without much success. Murdin (1976) however has found 4 correlated dips in Copernicus data (2-7 KeV) with an associated increase in the spectral hardness. Mason et al. (1974) has reported 4 similar events and Li

and Clark (1974) have found a further example using OSO-7 data. These dips occur preferentially near to superior conjunction and have no obvious systematic trend but Parsignault et al. (1976) has suggested that they may be semi-permanent since he finds similar correlations using November 1974 data from ANS. Various models have been proposed for these dips such as gas stream concentrations causing a partial eclipse, blobs in the ejected stellar wind, large prominences and eclipses by the B supergiants atmosphere. It is not clear yet which is more likely since all have problems in detail although the last case appears to be ruled out since the dips are not regular enough and can be too brief. The current inclination estimate would also place the line of sight too high above the B star's surface. Holt et al. (1976) using the All Sky Monitor (ASM) on Ariel 5, finds a modulation in the 3-6 KeV flux from October, 1974, to July, 1975, that is most pronounced just prior to the May flare. He also notes a second small flare on 8-16th September which was better observed by SAS-3 and Canizares et al. (1976) found the 1.5-6 KeV flux had increased by a factor of 4.

#### 1.4.5 Distance

There has been much discussion of the distance to Cygnus X-1 since this critically affects the derived mass of the secondary. An early estimate by Gursky and Gorenstein (1971) based on spectral absorption of X-rays was shown by Schreier et al. (1971) to be incorrect since the hard X-ray component was not constant. Since the star type is known we can assume an absolute magnitude of -6.5 but the error involved comes in estimating the amount of interstellar absorption to include with the visual magnitude. Several surveys have been carried out on surrounding star fields to determine this effect. Bregman et al. (1973) has observed 104 stars within 30' radius and gives HDE226868

a large colour excess of

$$E(B - V) = 1.12$$

considerably larger than the surrounding average figure of 0.3 (fig. 1.5). This yields a distance of 2.5 kpc. Fernice et al. (1968) have observed a nearby Cepheid variable V547 Cyg, known to be at 6.6 kpc from the period luminosity law, and obtains

$$E(B - V) = 1.1$$

which is far less than predicted by a uniform reddening extrapolation. This he interprets as a line of sight that emerges from the dust layer in our galaxy at a distance of 3 kpc, about 150 pc above the plane which implies that HDE226868 lies near the edge of the dust. A similar conclusion has been reached by Gursky and Gorenstein (1971) who examined a field of 50 stars within 50'. Another potential cause of reddening is a circumstellar shell but no IR excess has been noted by Becklin et al. (1972). This is also unlikely since the ratio of linear polarization to extinction agrees well with the other field stars (Hiltner, 1956). The open cluster NGC 6871 also lies nearby and has been examined by Crawford et al. (1974) who obtain  $E(B - V) = 0.38$  implying this association is nearer than Cyg X-1. A further indication of distance can be obtained by examining the widths of interstellar lines using very high dispersion and Smith et al. (1973) find an EW of  $0.49 \pm 0.05 \text{ \AA}$  for the K line giving a distance of 2 kpc if one uses the tables of Munch (1968). A recent addition to these classical methods is the UV observations from ANS between 1500 and 3300  $\text{\AA}$  by Chi-Chao Wu et al. (1976) which again give a distance of 2.5 kpc or more, to a higher degree of accuracy than conventional UBV since the extinction curve is sharply peaked at 2200  $\text{\AA}$ . The good agreement of all these methods each of which is not in itself precise does indicate

that HDE226868 lies beyond 2 kpc.

#### 1.4.6 Light Curve

Photoelectric observations by Lester et al. (1973) show light variations of 0.07 magnitudes in a double wave 2.8 day period with the minima in phase with the radial velocity curve, just the profile we would expect from a tidily distorted star. Walker (1976) reports that the curve has changed over the last three years but Liller (1976) having studied plates dating back to 1890 finds no gradual or sudden changes as reported in the X-ray and Radio regions in 1971 and 1975. A recent polarization measurement by Dolan (1976) finds the magnitude and position angle are correlated with the optical phase. Aureima et al. (1976) have found fast optical variations that appear for a few minutes and have a period very near 83 mS the period and duration not being constant.  $\Delta P/P$  is roughly  $10^{-4}$  with a typical duration of 10 minutes and several events per hour. These rapid variations have not been observed however by Robinson et al. (1978) in over 90 hours of observation.

The most complete light curve obtained so far is that of Walker and Quintanilla (1977) covering 349 nights between 1972 and 1977. The folded curve yields  $5.6015 \pm 0.0006$  days with an indication of a 0.1P period in addition to the double maxima and minima. There are also indications of a 150 day period during 1974/75 of 0.02 mag and some evidence for a 1.23 day period.

#### 1.4.7 Optical Spectra

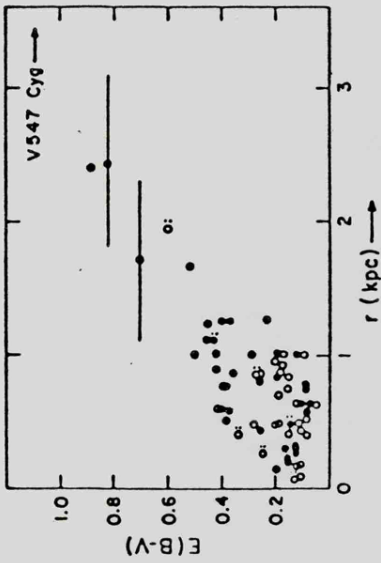
Initial observations of the newly identified optical star revealed it to be a B01b supergiant (Bolton, 1972; Webster and Murdin, 1972). A detailed spectral type of O9.7 Iab is given by Walbourn (1973)

who based this classification on the detailed study of two similar stars namely  $\xi$  ORI (BOIa) and 19 CEP (09.5 Iab). The actual difference is revealed by studying the Si IV lines at 4089 and 4116 Å relative to the line strengths of adjacent H and He I features, all these absorption lines being perfectly normal. There was also a highly unusual and variable emission feature at He II (4686 Å) which Smith et al. (1973) determine did not originate in the secondary star but was probably due to gas somewhere between the secondary and the inner Lagrangian point of the system. The asymmetry in this line can be explained by an approaching emission component arising from a gas stream plus receding absorption from the primary. This is similar to a well observed close binary known as HD47129 (Plasketts star). Hutchings et al. (1973) have also shown this emission to arise in a region close to the secondary but trailing it in its orbit and they interpret the H $\alpha$  emission as being due to a disc round the secondary.

#### 1.4.8 Mass Estimates

An early discussion of the secondaries mass by Brucato and Kristian (1973) led to  $M_1 = 22 M_{\odot}$  and  $M_x = 5.5 M_{\odot}$ , way above the neutron star limit at just under  $3 M_{\odot}$  (Ruffini, 1973). This prompted Trimble et al. (1973) to suggest a model in which the primary was a luminous undermassive B star due to mass exchange of the Hz 22 type but the distance measurements have ruled this out since the system needed to be only a few hundred parsecs away. Another possibility was proposed by Paczynski (1972) in which X-ray heating of the primary altered its spectrum but Mauder (1973) finds these effects to be small and also finds the optical variations consistent with tidal distortion alone enabling him to estimate the mass function as

$$F(M) = 0.22$$



RADIAL VELOCITY (BOLTON 1975)

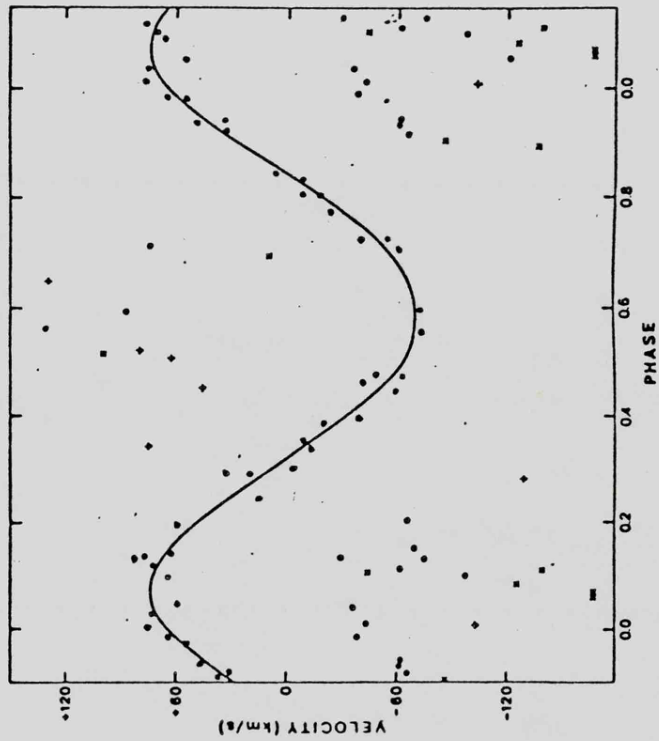
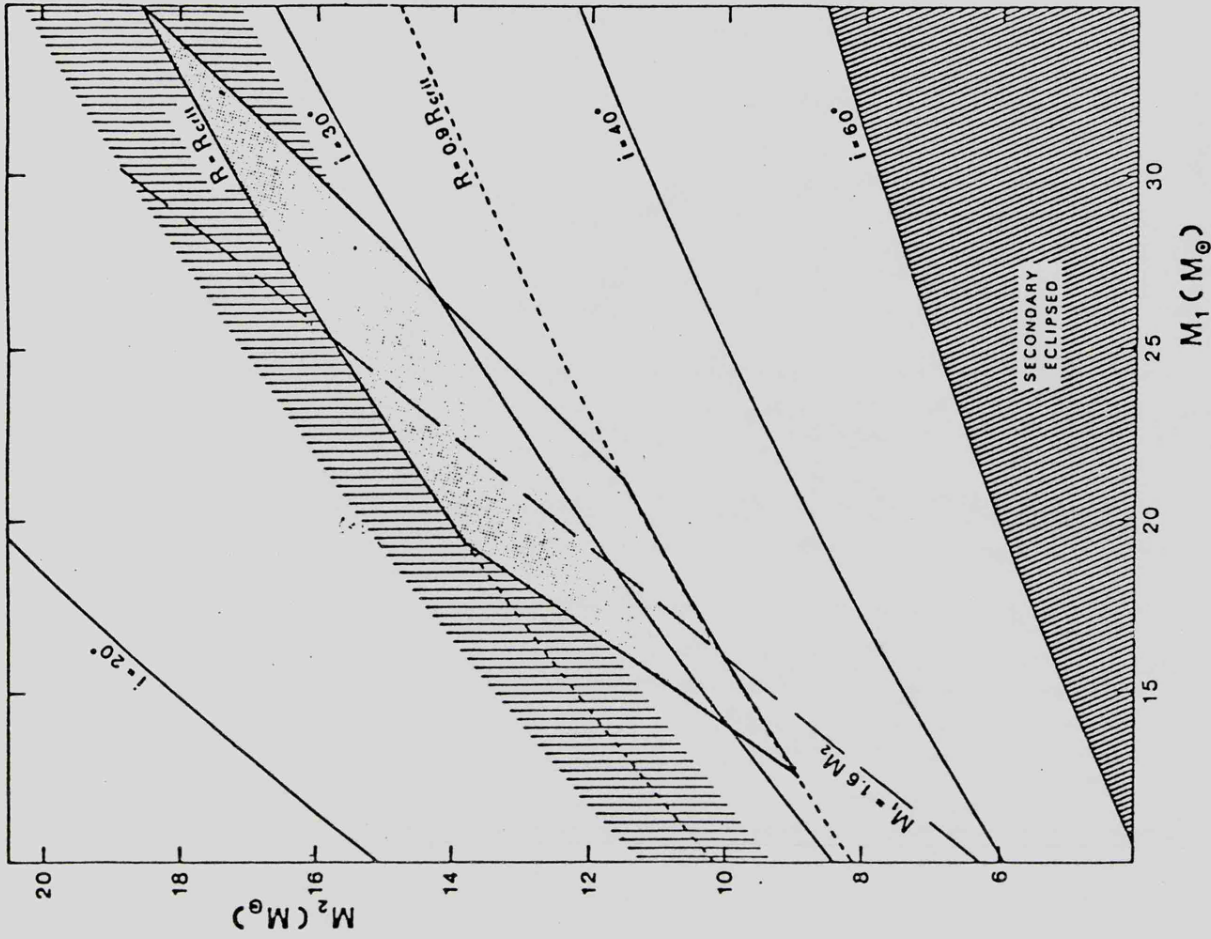


FIG 1.5 MASS OF CYG X-1



M1-M2 MASS PLANE  
(BOLTON 1975)

Bolton (1975) has obtained accurate radial velocity measurements and combined these with several other data sets to produce the radial velocity curve shown in fig. 1.5 and from it the following orbital parameters.

$$P = 5.599824 \pm 0.000037$$

$V_o$ (km/sec)	$-1.7 \pm 0.5$
$k$ (km/sec)	$72.2 \pm 0.8$
$e$	$0.06 \pm 0.01$
$\omega$	$330^\circ \pm 10$
$a_1 \sin i$ ( $10^6$ km)	$5.549 \pm 0.061$
$f(M/M_\odot)$	$0.217 \pm 0.007$
$\mathcal{E}$ (km/sec)	$\pm 4.38$
superior conjunction	
JD 240000	+ 1561.22
inferior conjunction	
JD 240000	+ 1558.24

The scattered points in fig. 1.3 occurring roughly in antiphase with the smooth curve are due to the emission feature described previously, the curve itself is not a perfect sine wave since the orbit is not quite circular. Mass estimates for the primary have ranged from  $35 M_\odot$  (Stothers, 1972) down to  $10 M_\odot$  (Van den Heuvel and Ostriker, 1973) and Bolton has used these together with a limit on the allowed  $i$ , since no eclipses are seen to produce the probable mass location diagram in fig. 1.5. This implies

$$8 M_\odot < M_x < 16 M_\odot$$

## 1.4.9

Several other types of model have been produced to avoid having a black hole secondary. The triple system proposed by Fabian et al. (1974) has difficulty with the phasing of the X-ray absorption dips and the large 4686 He II velocity deviations expected from an accretion disc bound to the third body neutron star. A differentially rotating degenerate dwarf proposed by Brecher and Morrison (1973) could work in principle but cannot explain the bursts seen by Rothschild et al. (1974) unless the accreted mass is channelled to a very small region of the surface. The model by Bahcall et al. (1973) containing two normal B stars linked by a magnetic field has vague predictions that are difficult to test. These alternative models are discussed in section 1.3.7. Alme and Wilson (1976) have proposed a model in which matter is transferred primarily by radiation driven density waves generated in the atmosphere of the primary, which fills only about 85% of its Roche lobe. Variations in transfer due to slight orbital eccentricity may then cause transitions of state as discussed in 1.3.6.

The evidence for Cygnus X-1 being a black hole rests on three basic points:

- 1) HDE226868 is the X-ray source (coincident X-ray and Radio events, fig. 1.3).
- 2) X-ray object is compact (1 mS bursts, fig. 1.4).
- 3) Total mass of system  $> 20 M_{\odot}$  implying  $M_x > 3 M_{\odot}$  (distance  $> 2$  kpc, fig. 1.5).

The 1 mS bursts have been questioned and the mass estimate is uncertain since this value is based on the distance as inferred from the absolute magnitude and interstellar absorption. The model in which an accretion disc surrounds a black hole appears however to be able to explain all the features so far observed and only requires a modest accretion rate of  $10^{-9} M_{\odot}/\text{year}$  to produce the observed X-ray luminosity.

CHAPTER 2

The design and construction of a large area high time resolution detector system

	Page
2.1 Basic Design Considerations	49
2.2 Mechanical Design and Testing	53
2.3 Collimator Design and Testing	61
2.4 Multi-wire Array Design	66
2.5 Experiment Electronic Design	76

## 2.1 Basic Design Considerations

### 2.1.1

The experiment and observations described by Rothschild et al. (1974) have been used as the basic reference points in designing this large detector system, the actual scaling up required being described in section 4.3 where the expected performance is reviewed. Our first concern was to obtain the largest possible effective area and it was immediately apparent that it was impossible to greatly exceed that of previous proportional counter detectors built at Leicester, such as those listed below.

<u>Date</u>	<u>Round</u>	<u>Area cm<sup>2</sup></u>	<u>Reference</u>
1970	SL-904	720	Cooke et al. (1969) ?
1971	SL-1002	860	Ricketts (1973)
1972	SL-972	1385	Adams, Ricketts (1973)
1974	SL-1304	800	Hoffman (1974)

The problem has always been the limited space beneath the standard Skylark type 1b split nose cone (B.A.C. 1972) which provides a parallel section 38 cm in diameter and 30 cm long surmounted by a cone tapering to a point 152 cm away. A simple analysis shows that the maximum cross section is roughly constant around a height to width ratio of 2:1 where the width is about 30 cm. Variations in the areas of the detectors listed can be explained by various special features such as shadowing, canted collimators, flat top collimators or simply less efficient mechanical design. Obviously a larger nose cone is required but a simpler solution appeared to be to create a two stage system, the lower sections being ejected a few seconds after the standard nose semi-cones.

B.A.C. were asked to look into the possibility of sawing a standard 20" bay (50 cm) in half and fitting it with the same set of gas

piston actuators as the nose cone assembly. It was envisaged that the split would be at 90 degrees to the nose cone join and that the electrical connections would be made through a second set of butting connections. B.A.C. were at once enthusiastic and it seemed that this special split bay could become a piece of standard hardware. This item was subsequently designed and produced and together with the nose cones and flight panels underwent a vibration test of 5g RMS in the longitudinal axis and 2.5g RMS in each lateral axis with a bandwidth of 20-2000 Hz. An ejection test was successfully carried out to gain confidence in the design and in all further tests and during the flight the system worked perfectly.

#### 2.1.2

The potential area of the detector was now over  $2,000 \text{ cm}^2$  but to increase this further required some sort of deploying system. The three possibilities considered were hinged panels, sliding panels or some sort of concertina arrangement but the first of these concepts appeared to provide the largest area and simplest mechanical solution. The basic design adopted is shown in fig. 2.1 and it can be seen that the panels have a very limited depth. The only potential problem lay in the large increase in the moment of inertia (MI) of the payload in roll once the panels had deployed. A weight estimate of 18 kg per panel indicated an MI increase from  $6 \text{ kg.m}^2$  to  $8 \text{ kg.m}^2$  which would have the effect of making the payload more sluggish responding to the roll jets. This was accepted by B.A.C., provided that the weight estimate was not greatly exceeded, the final value being only 2 kg over. The nett impulse to the round will hopefully be close to zero since the outer panels open in a symmetrical fashion.

The experiment was to be flown on a sun pointing Stage I ACU (B.A.C. 1972) the fine eye sensor being mounted on top of the centre panel

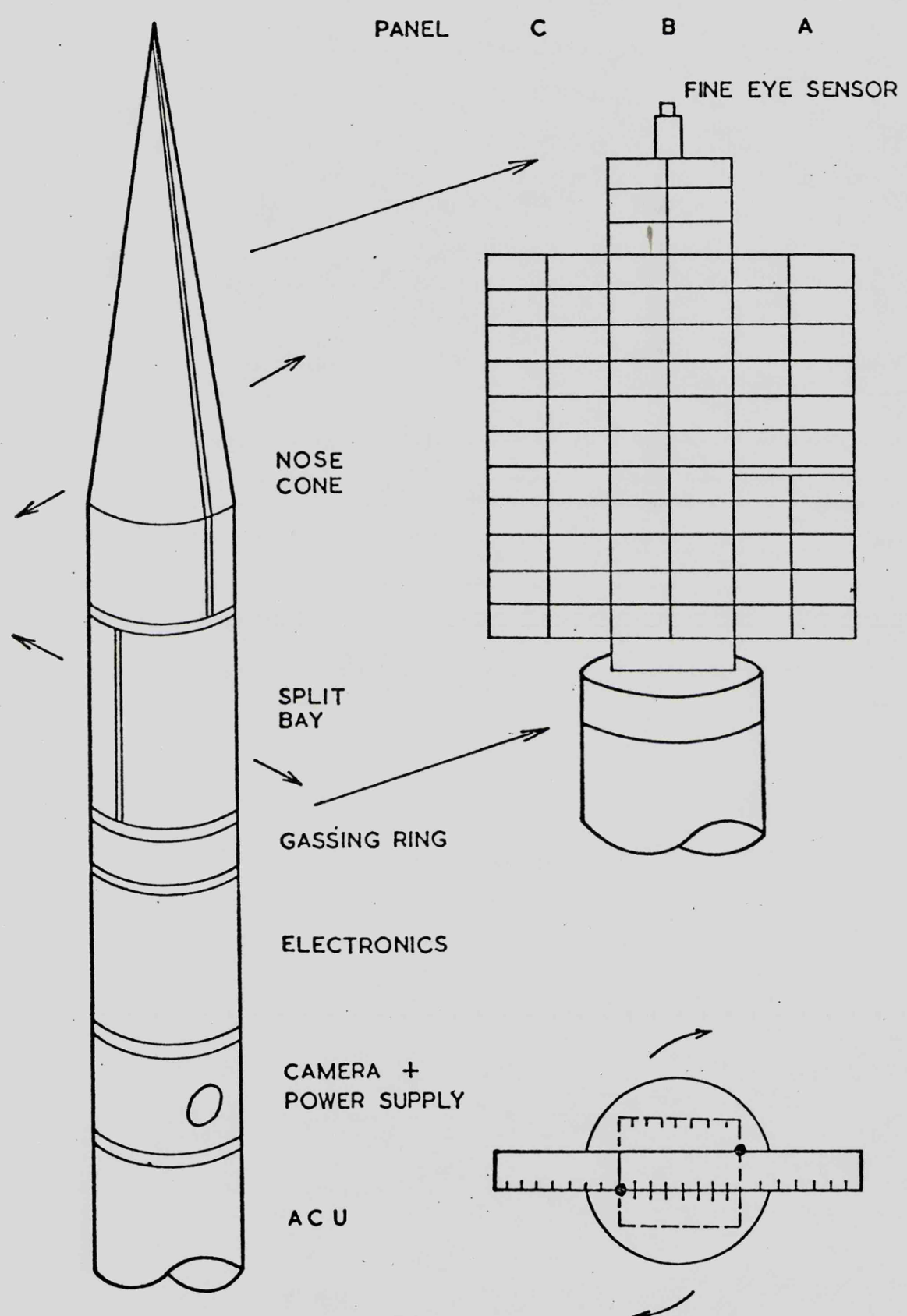


FIG. 2-1 SL 1306 EXPERIMENT DESIGN

for an unobstructed view with magnetic control in roll. The collimators were designed to look out at  $90^{\circ}$  to the roll axis since this minimises construction problems and maximises the effective area for a given panel size.

### 2.1.3

The high voltage units and pre-amps were mounted directly on each panel to avoid having weak signals in long cable looms. The background rejection problem was considered at an early stage and it was decided to operate the guard in anticoincidence with the main channel without rise time discrimination (RTD). The RTD method has been described by Mathieson and Harris (1970) and can in theory provide a very high efficiency but in practice requires a lot of care to set it up correctly. Since each panel would require its own RTD system, it was felt that a guard surrounding three sides of the signal array would provide sufficient rejection considering the bright source being observed and the fact that the time structure was the primary interest. Since all three panel outputs were merged into one processing unit it was necessary to devise a system that could inhibit any line that might fail due to RF pick-up or HT breakdown from swamping the PCM frames with false data. Another basic decision was to fly a star field camera to determine the error in pointing at the chosen object. This would, in the event of an ACU failure, determine where the detectors pointed as with an area estimated to be in excess of  $3,000 \text{ cm}^2$  it was felt that something of interest might well be observed.

It was apparent from the results of Rothschild et al. (1974) that to transmit complete time information alone for the millisecond bursts would require the use of a memory to buffer the information from the PCM frame. Similar features seen by our much larger detector could correspond

to instantaneous count rates as high as 30,000 c/sec so it was obviously necessary to have a very small dead time for the processing electronics.

In the following discussion on the design of the experiment each aspect is considered separately for clarity but many features are closely inter-related.

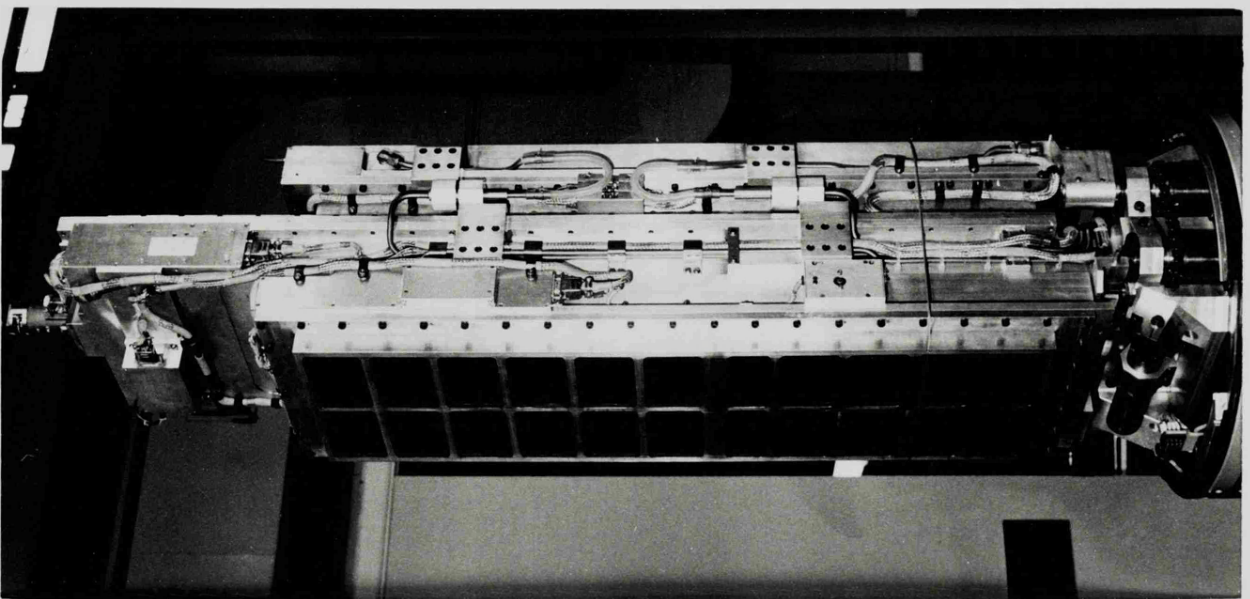
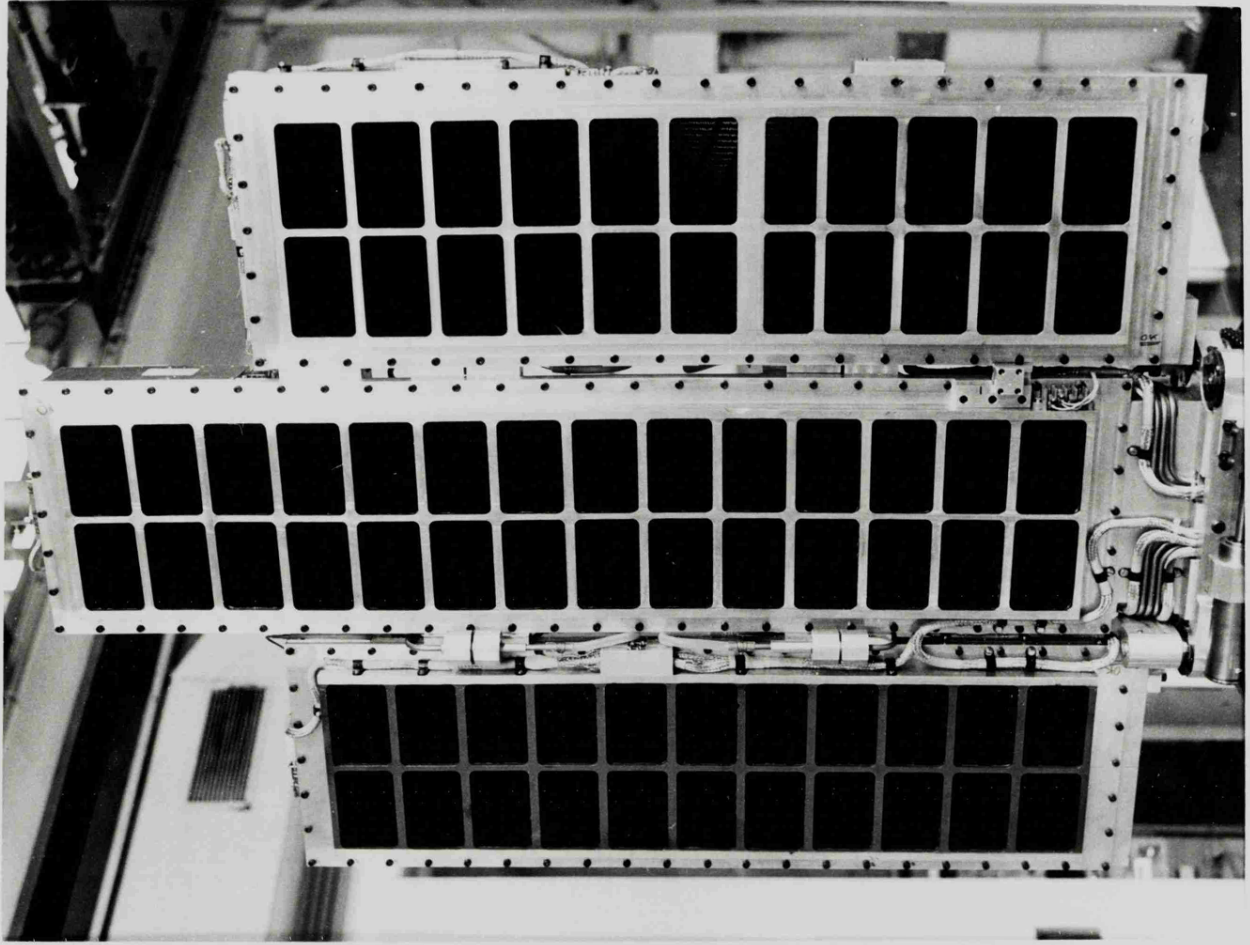
## 2.2 Mechanical Design and Testing

### 2.2.1

Having obtained the space available under the new nose cone assembly it was possible to fix the sizes of the panels with the limitation that the cross section of each had to be the same. The central panel which was rigidly bolted to the top bulkhead was made taller since the tapering of the cone ( $15^\circ$  included angle) is less severe for a central position. The outer panels are 87 cm by 27 cm with a depth of 9.5 cm, the centre panel being 30 cm taller. At the corners of the centre panel on the bulkhead are located 4 cylindrical hollow drums, each one containing bearings and a sprocket wheel shaft assembly that supports a loop of chain. One diagonally opposite pair are idler sprockets and the other pair contain springs that provide the force to open the panels. This last pair have heavier bearings and larger shafts to which the outer panels are connected. The chain is split into two lengths that are linked by an adjustable tensioning device to ensure that the panels open in unison and remain parallel during deploy. The outer panels were also supported on the side at the top and middle by needle roller bearing hinges to give better alignment and rigidity. To give further support during launch a block was attached to the inside of each split bay half. These could be packed out with shims to provide a light, firm clamp on the detector panels, the thicker bar on the right hand collimator frame, fig. 2.2, indicating where these were positioned. All the load during

FIG. 2.2

DETECTOR SYSTEM WITH NOSE CONES AND  
SPLIT BAY REMOVED SHOWING THE  
PANELS STOWED AND DEPLOYED



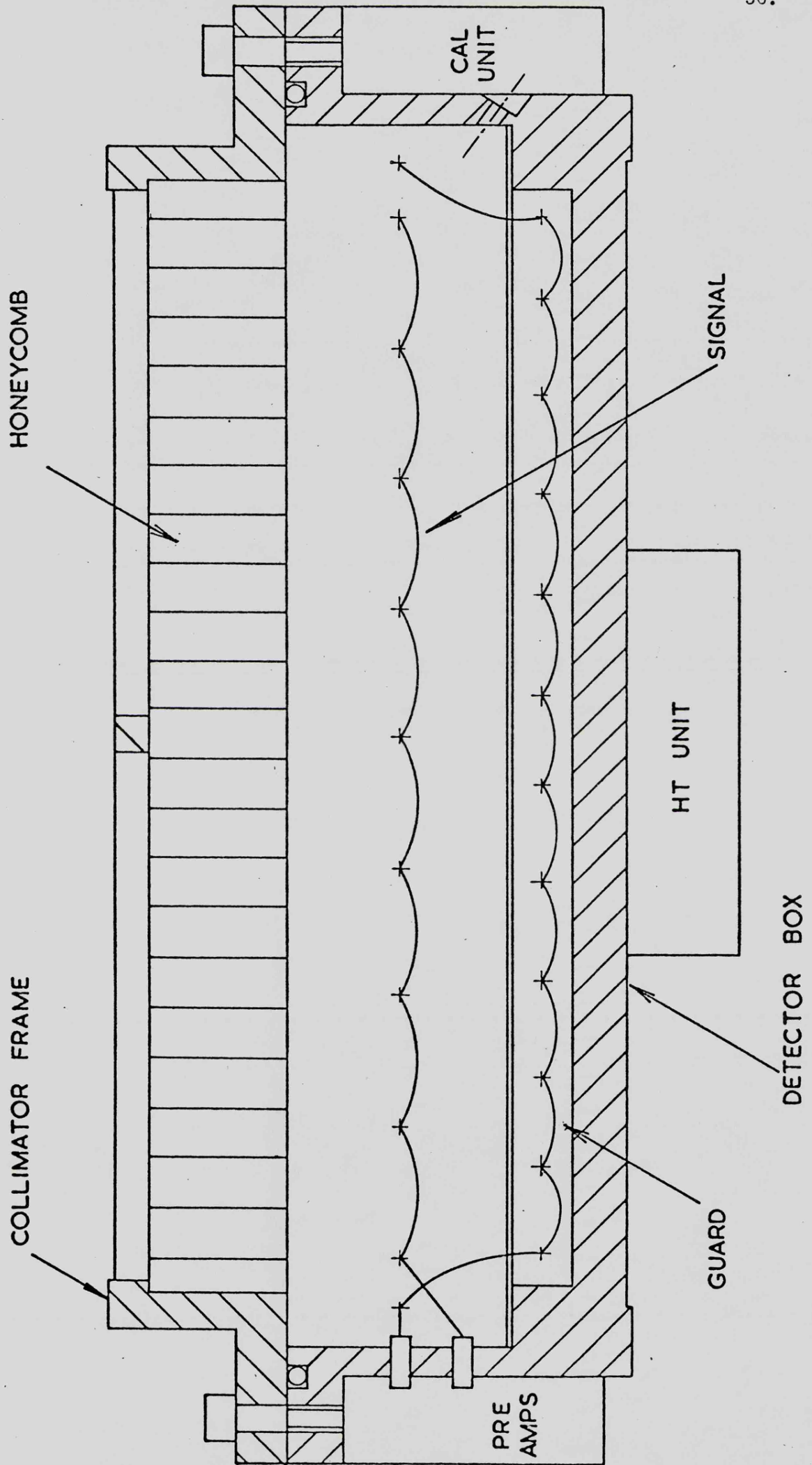
launch was taken by the end shaft and bearings which at the peak acceleration of 15g amounted to 300 kg.

The speed at which the panels opened could be adjusted by rotating and re-clamping the drum housing round each spring, effectively winding it up or down depending on the direction of rotation. An initial torque in excess of 0.35 kg.m was sufficient to completely open the panels against the force of two hydraulic dampers which brought them smoothly to rest. At this point an over centre catch was released which firmly locked the panels in the correctly aligned position. To prevent jamming, the panels could not be allowed to unfold until the split bay was well clear and to achieve this a wire loop was loosely tensioned round all 3 panels holding them together. This wire was then severed by a small guillotine pyro-technic device to initiate deploy. All this activity was monitored on two multiplexer channels, one coming from a micro switch indicating lock and the second indicating angular position from a calibrated potentiometer attached to one of the panel shafts. In tests, deploy lasted 3-4 sec and was delayed by 14 sec from the time during the acquire sequence that the ACU changed from coarse to fine eyes at a  $10^{\circ}$  offset from the sun. This delay was introduced in the hope that any position change caused by the opening panels would still leave the sun within the fine eye field of view since a recycle back to coarse eyes would have lost observing time.

### 2.2.2

Each panel had gas pipes attached to opposite corners which led down to the 3" gassing ring shown in fig. 2.1. The 6 valve sockets hidden beneath an access plate were self sealing upon removal of the respective plugs which was performed manually. As a safety feature for the actual flight there was also a manually operated valve in series with

FIG. 2-3. DETECTOR CROSS SECTION (FULL SIZE)



each socket that was accessed through another cover plate aperture by using a special spanner. On the two outer panels the gas pipes pass through the centres of the hinges so that only a 10 cm length of silicon rubber tubing was needed to provide the flexible coupling. During deploy this undergoes a torsional twist of  $180^\circ$  without resistance and with no tendency to become trapped preventing the panels from fully opening. Each panel has a  $\text{Fe}^{55}$  calibration source aligned with a small window in the box wall allowing irradiation of the signal array as shown in fig.

2.3. The source is mounted on a movable arm which positions it over the window when the cal is required. Most of the features described can be seen on the photographs in fig. 2.2.

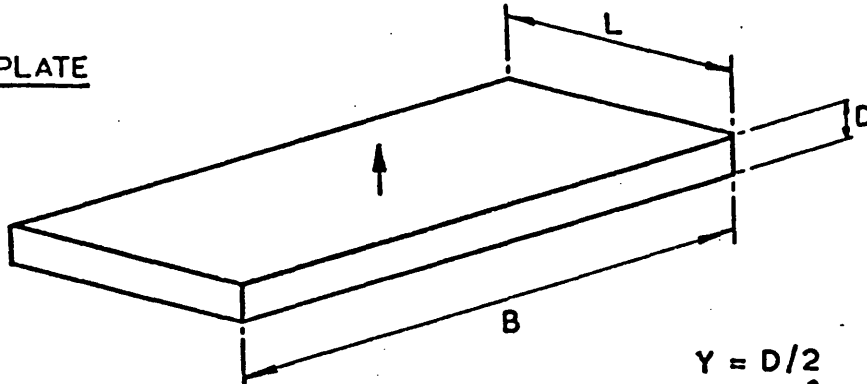
For identification, each panel and the signals derived from it were given a letter. The centre panel was called B, the outer panel with the thick bar on the collimator frame was called A and the other panel was called C (fig. 2.1).

### 2.2.3

The cross section of the panels is shown in fig. 2.3 and the depth can be divided into the following four regions - backplate, guard, main and collimator. With the guard set at 1 cm to produce reasonable cosmic particle track lengths (10 keV deposited per cm) every effort was made to maximise the detector depth to obtain the widest energy range possible. To save machine time the back plate was made with a constant thickness rather than some sort of complicated webbed structure. The theory behind deflections and stresses in plates is discussed in detail by Timoshenko (1959) and if the width to length ratio is 1:2 or greater the plate can be treated as a simple bending beam across the narrowest dimension. The deflection at this ratio is only 2% less than that for an infinitely long plate and in our detectors this ratio  $L/B$  is 1:4.

## FIG. 2-4 STRUCTURE ANALYSIS

### BACKPLATE

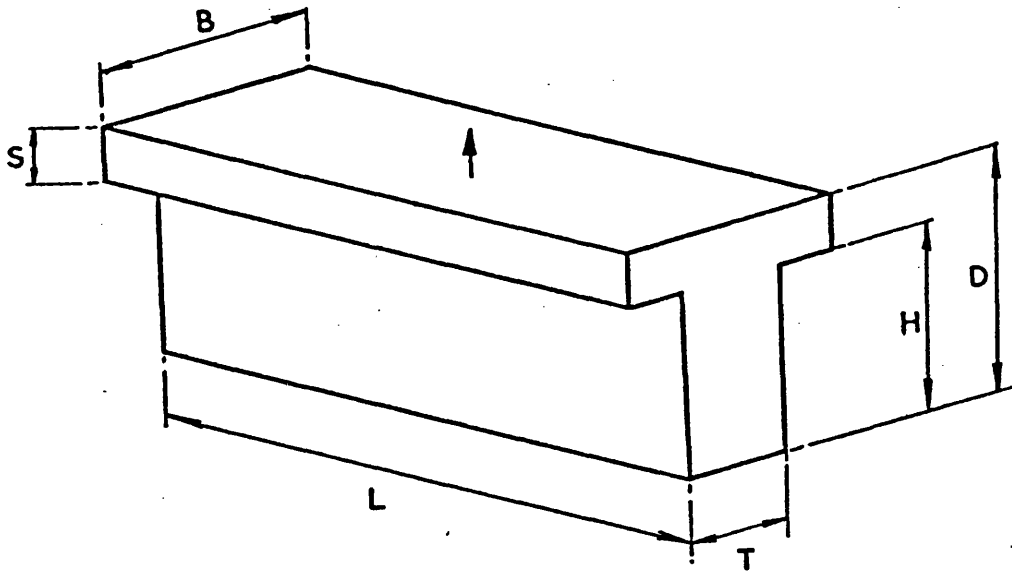


$$Y = D/2$$

$$I = BD^3 / 12$$

$$W = BLP$$

### T BEAM



$$Y = D - \frac{D^2 T + S^2 (B-T)}{2 (BS + HT)}$$

$$I = \frac{1}{3} [TY^3 + B (D-Y)^3 - (B-T)(D-Y-S)^3]$$

$$W = LP \times (\text{BAR SPACING})$$

### DEFLECTION

$$D = \frac{5}{384} \frac{L^3 W}{EI}$$

### STRESS

$$S = WLY / 8I$$

E = YOUNGS MODULUS

I = MOMENT OF INERTIA

Y = DISTANCE FROM AXIS  
TO EXTREME FIBRE

W = TOTAL LOAD

P = ATMOSPHERIC PRESSURE

The relevant equations are shown in fig. 2.4 and calculations showed that a thickness of 9 mm was sufficient to withstand 1 atmosphere, the deflection then amounting to 0.3 mm with a stress of  $310 \text{ kg/cm}^2$ , just within half the material yield point value. The actual deflection is critical however since sufficient clearance must be allowed between the panels to prevent excessive force from jamming the system when the panels expand as the rocket ascends through the atmosphere.

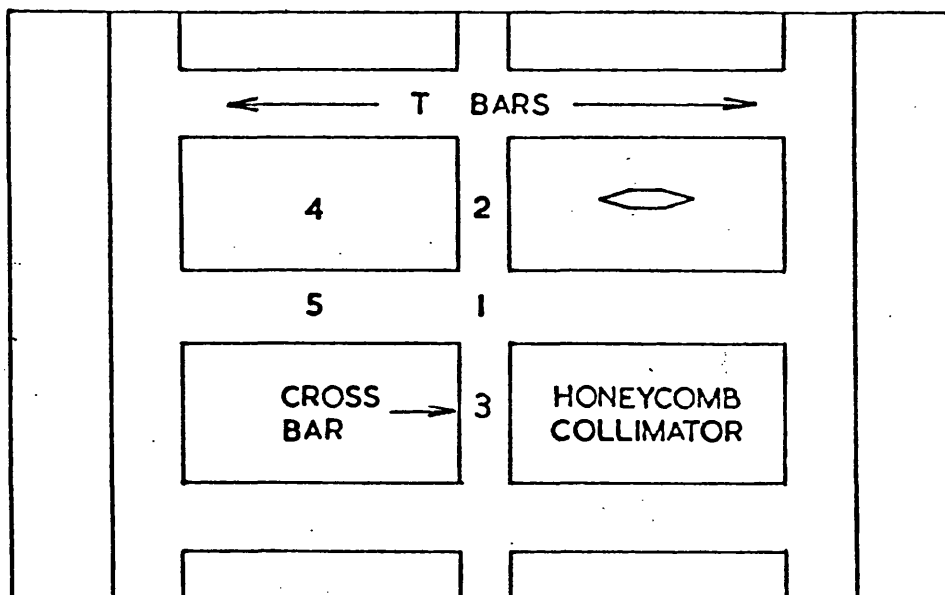
#### 2.2.4

The deflection of the collimator frame is equally important so a prototype box was constructed to check the calculations. To save time this was produced as a welded fabrication made from 4 side walls, a back plate and a top flange. The flight panels themselves might have been made this way rather than the usual time consuming method of machining from a solid block but the prototype contained numerous small cracks in the weld that leaked badly (100 torr/hour at 1 atmosphere). To achieve a leak-tight weld with argon arc equipment the workpiece must be at several hundred degrees centigrade to prevent differential cooling causing cracks as the gun moves on. Welding at this temperature would however result in large distortions when the box cooled down and re-welding over the leaks simply made them move a bit further along. In view of this the panels were machined from solid NPS aluminium blocks after the drawings were updated to allow for expansion and for all the fixing points required for the numerous gas pipes, cable looms and bolt-on extras. The type of aluminium used is very stable and has excellent machining qualities.

All the deflection measurements were obtained using an engineer's dial gauge and the results for a completed flight panel are listed in fig. 2.5 and agree fairly well with the simple beam calculations.

TORR	POSITION					
	1	2	3	4	5	6
260	0,055	0,065	0,050	0,055	0,025	0,065
520	0,100	0,125	0,115	0,100	0,050	0,140
780	0,165	0,205	0,190	0,150	0,100	0,230
780	0,28	← CALCULATED →				0,3
1040	0,230	0,255	0,250	0,230	0,180	0,320

DEFLECTIONS IN MM.



POSITION 6 CENTRE BACK PANEL

FIG. 2-5 BOX DEFLECTIONS

It can be seen that the deflection is proportional to the load as expected with no sign of permanent distortion being noted after repeated cycling to 1.25 atmospheres.

## 2.3 Collimator Design and Testing

### 2.3.1

The collimators presented another problem since for such a large area, the fabricated egg box type assemblies previously used would have taken too long to build. The pointing errors of the Stage I ACU are listed below and they show why it is customary to build an elongated field of view to allow for roll errors of up to several degrees.

Pointing bias lateral 2'                      Noise 10" RMS

Pointing bias roll 5 Cosec  $A^\circ$               Noise 10' RMS

Pointing drift lateral 5'/min

Pointing drift roll 0.25 Cosec  $A^\circ$ /min

where A is the sun vector, magnetic vector angle which was in our case a very favourable  $79^\circ$ .

Hexagonal honeycomb material (Aeroweb 1973) seemed a good idea but had only been used previously at Leicester to give a roughly circular field of view. The  $4^\circ \times 12^\circ$  FWHM field of view chosen was determined by the errors in pointing and the positions of the nearby sources around Cygnus X-1 (fig. 4.1). The  $4^\circ$  axis is larger than required from pointing errors alone because the angular offset from the sun could not be exactly matched. It was wide enough for offsets up to  $0.25^\circ$  to still give a transmission of 94% or more (see chapter 5).

A computer program written to examine the modulations introduced by the use of hexagonal honeycomb on the UK 5 experiment D crystal

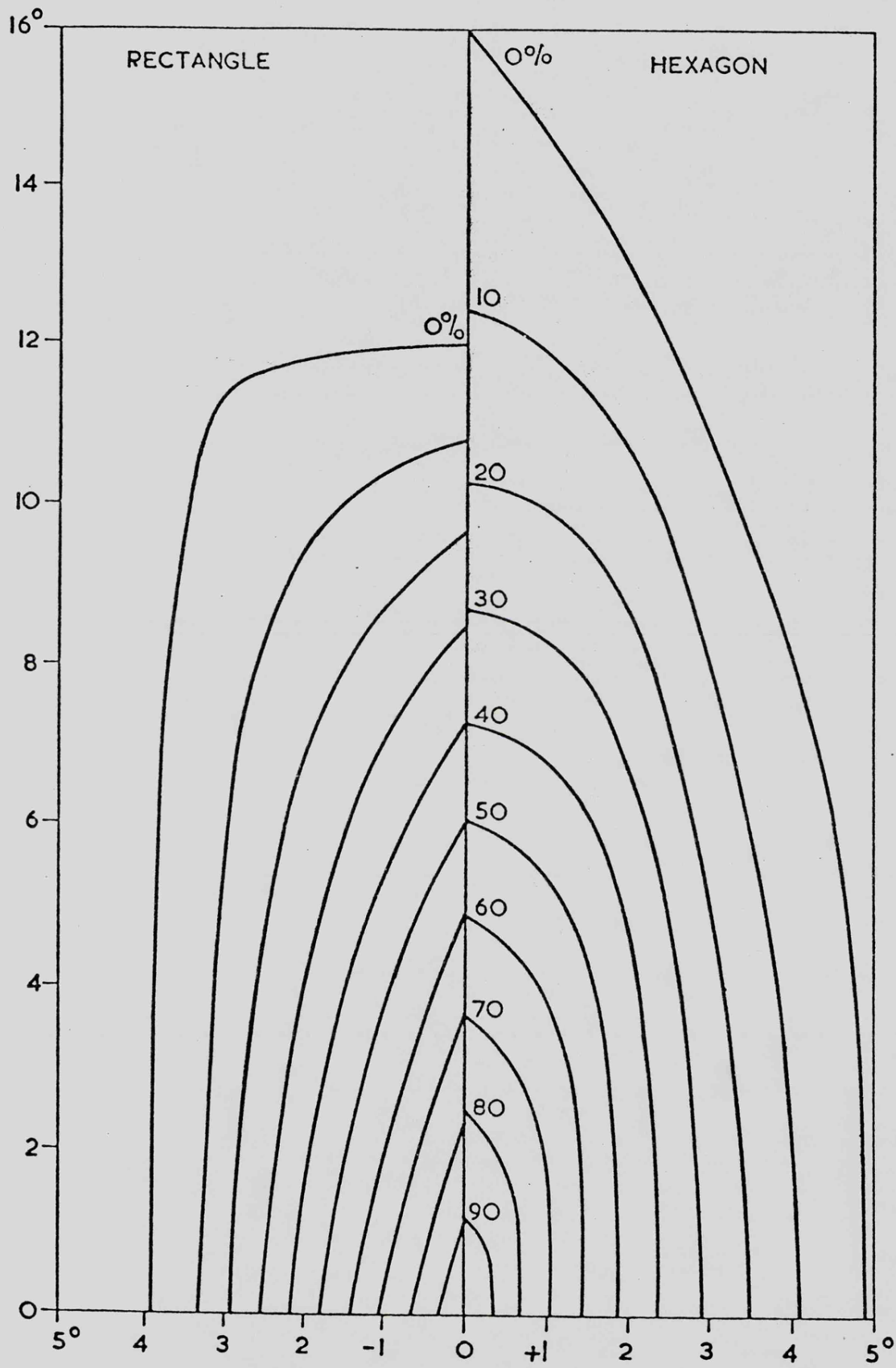


FIG. 2-6 COLLIMATOR TRANSMISSION

spectrometer was used to examine the difference in transmission between a squashed hexagonal cell and a conventional rectangular cell. This program described in appendix A produced the transmission map shown in fig. 2.6 and it can be seen that the hexagonal cell is an advantage when large errors may occur in roll combined with an inability to perfectly match the sun-source angle. The outer weak extension is unimportant unless there are strong nearby sources.

By special arrangement the sheet was obtained from the manufacturers in a half expanded state giving squashed hexagons with a width to length ratio of 1:2. The cells had a wall thickness of 0.05 mm, a depth of 2.5 cm and in the fully expanded mode a diameter of 4.8 mm across flats. It was proposed to squash this further to give the desired field of view at a width to length ratio of 1:4 but a test piece always produced a diagonal fault of completely squashed cells. It was realised that stretching the material in the other axis would produce the desired effect and so a special jig was built for this operation. Hardened silver steel pins were inserted through the cells across each end of an oversize block of material and frames positioned on the inner side of the protruding ends could then be pulled apart by a hydraulic crane. In addition to obtaining the desired shape the alignment between the cells was also greatly improved. Almost any field of view can be obtained by a suitable combination of cell size, depth and degree of stretching. The sides of the block were then stripped off by hand until there were 36 hexagons across the width. This was then eased into a frame of the required size and the ends sawn off leaving 22 hexagons down the length. Some 60 pieces were processed in this way and the best 36 selected for use in the flight collimator frames.

### 2.3.2

It was uncertain what area of unsupported honeycomb could safely withstand 1 atmosphere pressure but calculations based on the manufacturers' data indicated a width of about 7 cm. A test frame of 3 collimator sections was therefore inserted into the top plate of the prototype box and deflection measurements made. The honeycomb was glued into position with Araldite and sits on a lip round the inside of the frame which gives the main cross bars a T section. The analysis and deflections of these bars is shown in fig. 2.4 and they are designed to have a deflection equal in magnitude to that of the back plate. The centre of the honeycomb block bowed appreciably at 1 atmosphere pressure and so a thin cross support was added to the design of the frames to keep the field of view correct. These 3 collimator frames were also machined from solid blocks of NPS aluminium.

### 2.3.3

All previous detectors assembled at Leicester have had the window material separated from the collimator by an etched support grid but the normal manufacturer was unable to supply satisfactory grids of the required size in one piece. It had always been felt that these grids would prove unnecessary anyway since the small hexagons approximate to the normal grid size. These grids obstruct up to 20% of their area which does not necessarily coincide with the collimator support structure above, a typical combination may lose 20-25% of the collimator frame open area. The honeycomb however obstructs only 7% so leaving out the grid represents in our case a saving in area of about  $700 \text{ cm}^2$  giving a final total effective area of  $3980 \text{ cm}^2$ . Tests on the prototype showed that the window did not leak after repeated cycling to 1.25 atmospheres and so great care was taken to glue the blocks in the frames without

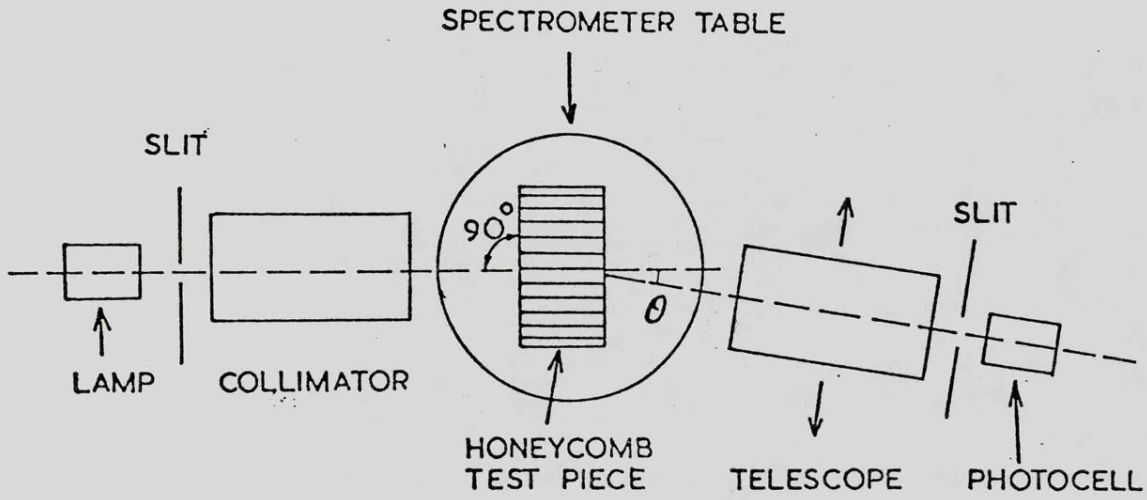
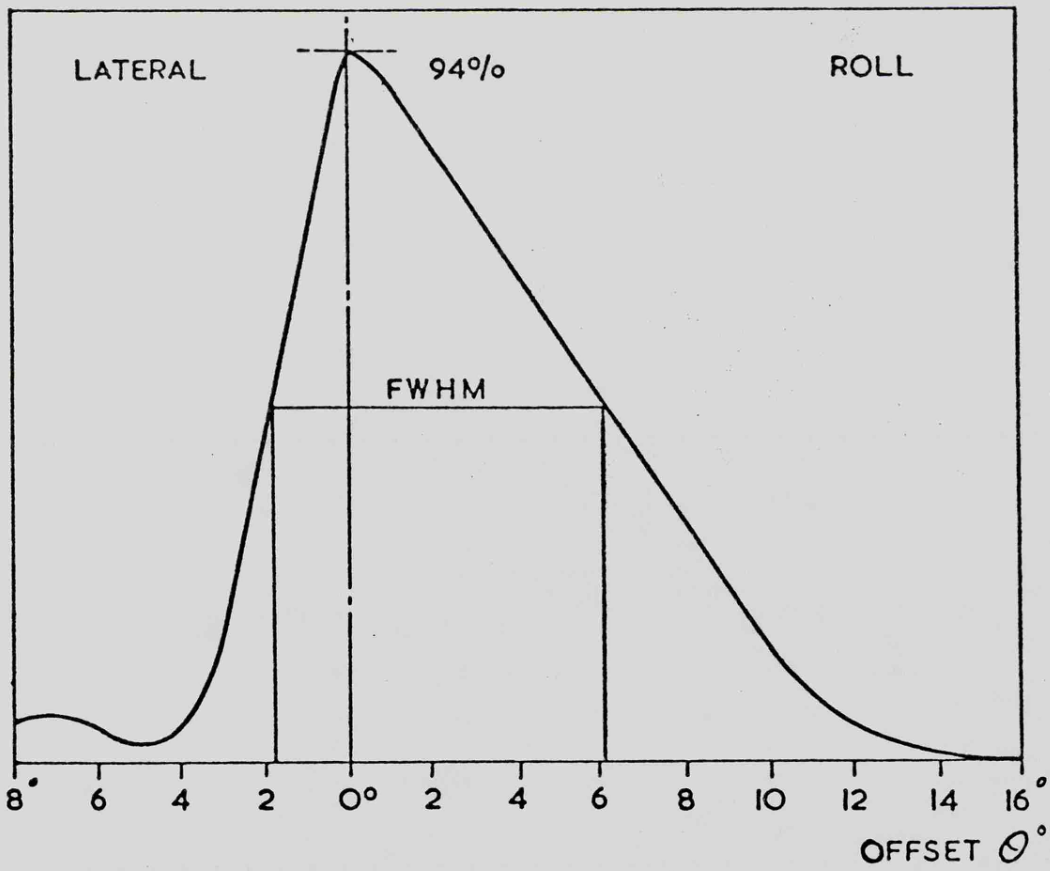


FIG.2-7 OPTICAL TRANSMISSION MEASUREMENTS



damaging the surfaces and to ensure that the lower face was perfectly flush. The window material used was 12 micron Melinex and if carefully chosen without pin holes did not leak noticeably over a 24 hour period when pressurised to one atmosphere.

#### 2.3.4

A test sample of honeycomb was used in a novel optical method to produce the transmission calibration curves in fig. 2.7. The collimator on the spectrometer produces parallel light, some of which passes straight through the cells and is focused by the telescope onto the photocell device. Any reflected light will be focused off axis and this scattered contribution can largely be excluded by having a slit at the focal plane. Angular rotations are easily measured using the table vernier graduations. An identical result was produced using a parallel beam of X-rays in the Leicester tunnel facility. This system has been described by Smith (1977). Finally, the inner faces of all the hexagonal blocks were sprayed with graphite to help eliminate UV reflections.

### 2.4 Multi-wire Array Design

#### 2.4.1

The cross-section available inside the detector box is 22.25 cm by 5 cm, the guard layer at the back having a depth of 1 cm leaving 4 cm for the signal layer. This gas depth allows a reasonable range in energy detection of 1.5 to 15 keV and the actual response to a Cygnus X-1 spectrum is described in section 4.2. The detector was operated at atmospheric pressure with the usual 90% Argon, 10% methane gas mixture. Since multi wire array technology was at the time being developed for the Leicester UK 6 satellite detectors it seemed the obvious choice for the interior structure to eliminate complicated machining.

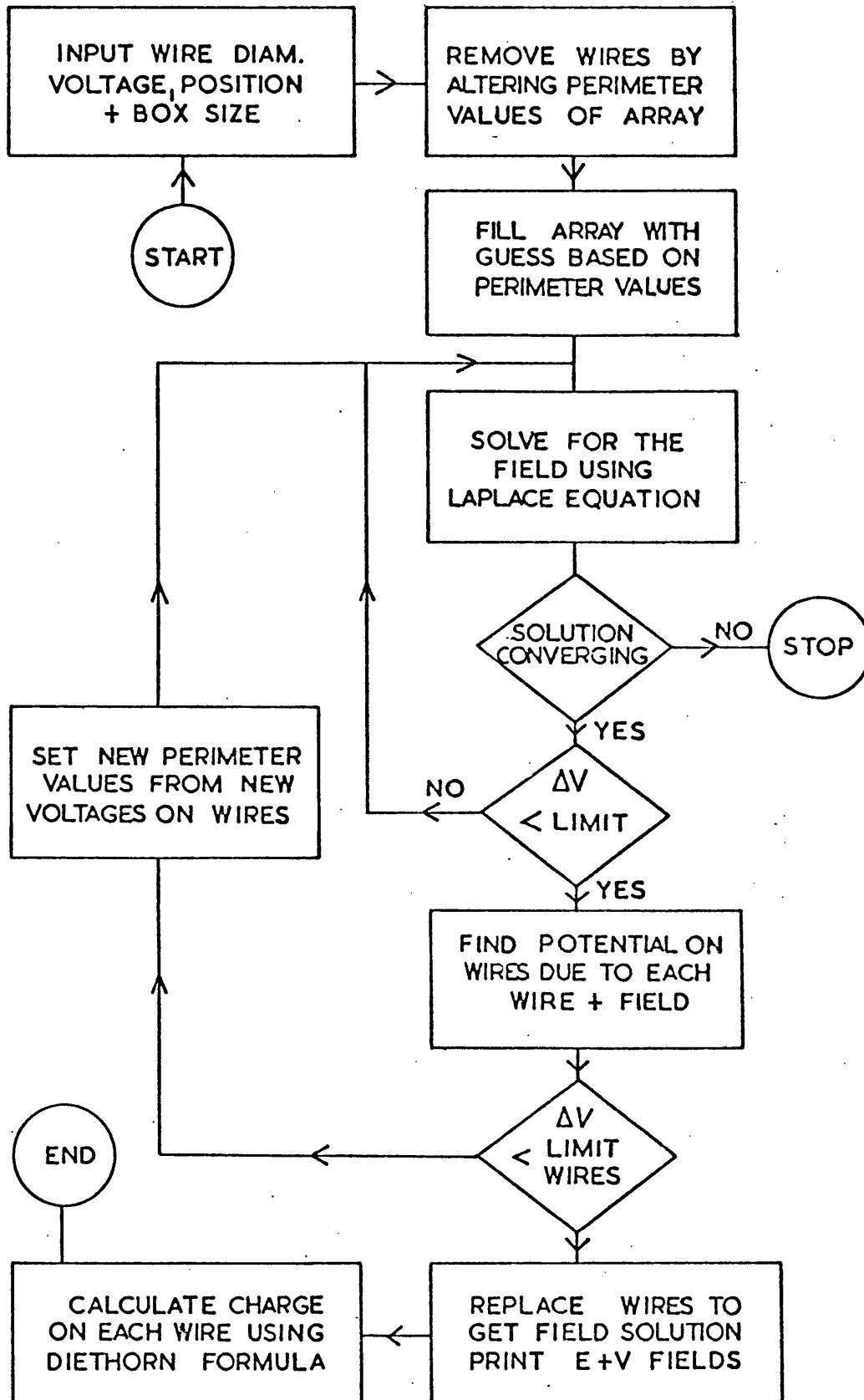


FIG.2-8 FIELD FITTING PROGRAM

#### 2.4.2

The analysis of electrical fields in a rectangular proportional counter has been described by Tomitani (1972) and reduces to a two dimensional problem if the counter approximates to infinite length in the other axis. General characteristics have been investigated and discussed by Charpak et al. (1970) with developments separating into two main types, one being closely spaced arrays used in various one or two dimensional position sensitive systems and the other having more open separations intended for large detecting areas which is our concern here. The guard and signal regions can be treated separately since they are divided by a mesh grid earth plane. The wires were placed as listed in fig. 2.9, their distribution about the centre line being symmetrical. Although the wire positioning is not too critical near the centre of the array where the electric field is very uniform, the gain becomes extremely sensitive on the wires near the side walls. To position these by trial and error would be impractical so use was made of a program being developed for the UK 6 detector design (Whitford, 1974). This program requires the box dimensions, wire positions, radii and voltage and then calculates the electric field within the box by solving Laplace's equation.

This technique has been described by Waligorski (1973) and consists of dividing the interior into a grid pattern and calculating the potential at each point of intersection. Since the boundary conditions are fixed the box being at earth and the wires at some constant voltage each point will have a residual inconsistent with Laplace's equation and after sufficient iteration using the point relaxation method the residuals are decreased until the voltages are internally consistent. The theory is outlined in appendix B and fig. 2.8 shows the basic flow chart. For improved accuracy the field in the box is treated in two parts, one being

a fairly uniform geometrical function  $U$  and the second part being the sum of logarithmic functions describing the strong fields surrounding each wire

$$V = U + \sum_{i=1}^N q_i \log r_i$$

The program was extended to convert the electric field to a charge output value for direct comparison with experimental results. A variety of gas models have been compared by Charles (1972) and based on his conclusions the Diethorn model (1956) was chosen to give the gas gain.

$$\frac{\ln G}{P_a S_a} = \psi = C(\ln A - \ln S_o) + K$$

where

- $C = 0.0228$  volts
- $P =$  atmospheric pressure
- $S_o = 28424.0$  V/cm/atm.
- $a =$  anode radius
- $G =$  gas gain
- $A =$  field strength V/cm
- $S_a = A/P$
- $K =$  gas constant dependent on  $S_o$

Having obtained the gas gain  $G$  we now calculate the charge out

$$Q = \frac{1000}{E} \times G \times 1.6 \times 10^{-19} \text{ Coulombs}$$

where  $E$  is the energy necessary to produce 1 ion pair which for the gas mixture used is 27 eV.

As the program was under development a test array was produced and the wire positions carefully measured. The charge on each wire was obtained by careful irradiation with a collimated  $Fe^{55}$  source and compared

MAIN DETECTOR										
Wire No.	diameter cm $\times 10^{-4}$	X-cm	Volts/cm $\times 10^5$	Gain $\times 10^4$	Charge/6kev $\times 10^{-13}$ C	Shaped $\times 10^{-13}$ C	Measured $\times 10^{-13}$ C			
1	45	0.7	1.26	1.56	5.56	1.23	1.70			
2	25	1.6	1.83	1.68	5.99	1.24	1.65			
3	30	4.0	1.63	1.71	6.07	1.28	1.50			
4	30	6.4	1.63	1.72	6.12	1.29	1.50			
5	30	8.8	1.63	1.72	6.11	1.29	1.50			
6	30	11.1	1.63	1.69	6.02	1.27	1.50			
7	30	13.5	1.63	1.71	6.08	1.28	1.50			
8	30	15.9	1.63	1.73	6.14	1.30	1.50			
9	30	18.2	1.26	1.70	6.05	1.28	1.50			
10	25	20.6	1.83	1.68	5.97	1.23	1.65			
11	45	21.5	1.26	1.56	5.54	1.23	1.70			
GUARD DETECTOR										
Wire No.	diameter cm $\times 10^{-4}$	X-cm	Volts/cm $\times 10^5$	Gain $\times 10^4$	Charge/6kev $\times 10^{-13}$ C	Shaped $\times 10^{-13}$ C	Measured $\times 10^{-13}$ C			
1	105	0.6	8.03	2.17	7.71	1.90	2.10			
2	100	2.3	8.22	2.12	7.54	1.84	2.05			
3	100	3.9	8.23	2.15	7.63	1.87	2.10			
4	100	5.7	8.23	2.17	7.72	1.89	2.10			
5	100	7.5	8.23	2.16	7.69	1.88	2.10			
6	100	9.3	8.23	2.17	7.72	1.89	2.10			
7	100	11.1	8.23	2.17	7.72	1.89	2.10			
8	100	12.8	8.23	2.16	7.68	1.88	2.10			
9	100	14.6	8.23	2.17	7.71	1.88	2.10			
10	100	16.4	8.23	2.14	7.62	1.86	2.10			
11	100	18.1	8.23	2.12	7.54	1.84	2.05			
12	105	19.8	8.03	2.17	7.70	1.90	2.10			

FIG 2.9 DETECTOR WIRE DETAILS (  $1\mu$ S TIME CONSTANTS )

with the program prediction. The agreement was satisfactory for the limited accuracy of construction and so the program was used to design the flight configuration. A correction must be applied to the measurements as the integrating and differentiating time constants in the pre-amps alter the value obtained. The program produced a corrected charge output corresponding to a 6 keV X-ray ( $\text{Fe}^{55}$ ) input pulse using the same time constants as those of the flight pre-amps. This correction has been described by Mathieson and Charles (1969) and Gott and Charles (1969).

Measured charge = Calculated charge/F

where  $F = 0.087 + 0.797 \log_{10} (2TcA(Va\mu)/R_a)$

where Tc = time constants

$R_a$  = anode radius

A = electric field V/cm

Va = wire voltage

$\mu$  = mobility of positive ions ( $\text{cm}^2/\text{v.s}$ )

The details of the wire positions together with both the charge predicted and measured is shown in fig. 2.9 for both the guard and signal channels.

#### 2.4.4

When the first panel was checked an unexpected effect was found on the outer signal wire. Charpak (1970) has noted that irradiating a wire produces a pulse that is largely due to the drift of the positive ions away from the wire rather than the actual collection of electrons. The negative pulse on the wire irradiated therefore induced a positive pulse on the neighbouring electrodes with a very slight effect on the next pair. Over the centre of the array all the wires are connected together but when irradiating the outer signal wire the adjacent guard is naturally not connected to the signal anodes. A small positive charge

therefore flows to the guard pre-amp becoming a negative pulse into the discriminator which actually in this case only detects positive pulses. This charge however is lost from the signal array which consequently produces a larger pulse from the pre-amp than when the source irradiates the other wires. This effect also alters the gain of the outer top guard from that predicted by the program.

#### 2.4.5

The outer bushes had been produced with eccentrically located field tubes for fine adjustment of field uniformity and these were simply rotated to diminish this effect. The excess gain on the end signal anode amounted to 10% but was reduced to 5% by adjustment, the measured values being shown in fig. 2.9.

The work of Tomitani (1972) has shown that for a uniform gain the ratio of wire spacing to cell depth should not be much greater than 1:2. The reason for this is that the region of low field between the wires and near the window becomes so large that the increased electron drift times lead to loss of resolution and gain. This effect has been discussed by Brown and Jenson (1964) and is not very significant for our gases and geometry, but is particularly severe for Xenon based mixtures.

#### 2.4.6

A further possible effect in arrays having long unsupported wires is a displacement caused by the mutual repulsion between the wires, this force being opposed by the tension in the wire. Trippe (1969) has considered this problem and for our detector there is no solution of the wave equation.

$$\text{for } T < \frac{C^2 v^2 L^2}{S^2 4 \pi \epsilon_0} \left[ 1 + \frac{S^2}{4a^2} \right]$$

where  $T$  = wire tension provided by springs  
 $V$  = anode voltage  
 $L$  = anode length  
 $S$  = separation of wire  
 $\epsilon_0 = 8.85 \times 10^{-12}$  F/M permittivity constant  
 $C$  = capacitance for unit length of anode  
 $a$  = cathode anode separation

The capacitance of each wire can be obtained from the output of the field fitting program

$$Ea = \frac{Q}{2\pi r \epsilon_0}$$

where  $Ea$  is the field strength at the wire and  $r$  is its radius.

Using  $Q = CV$

we have

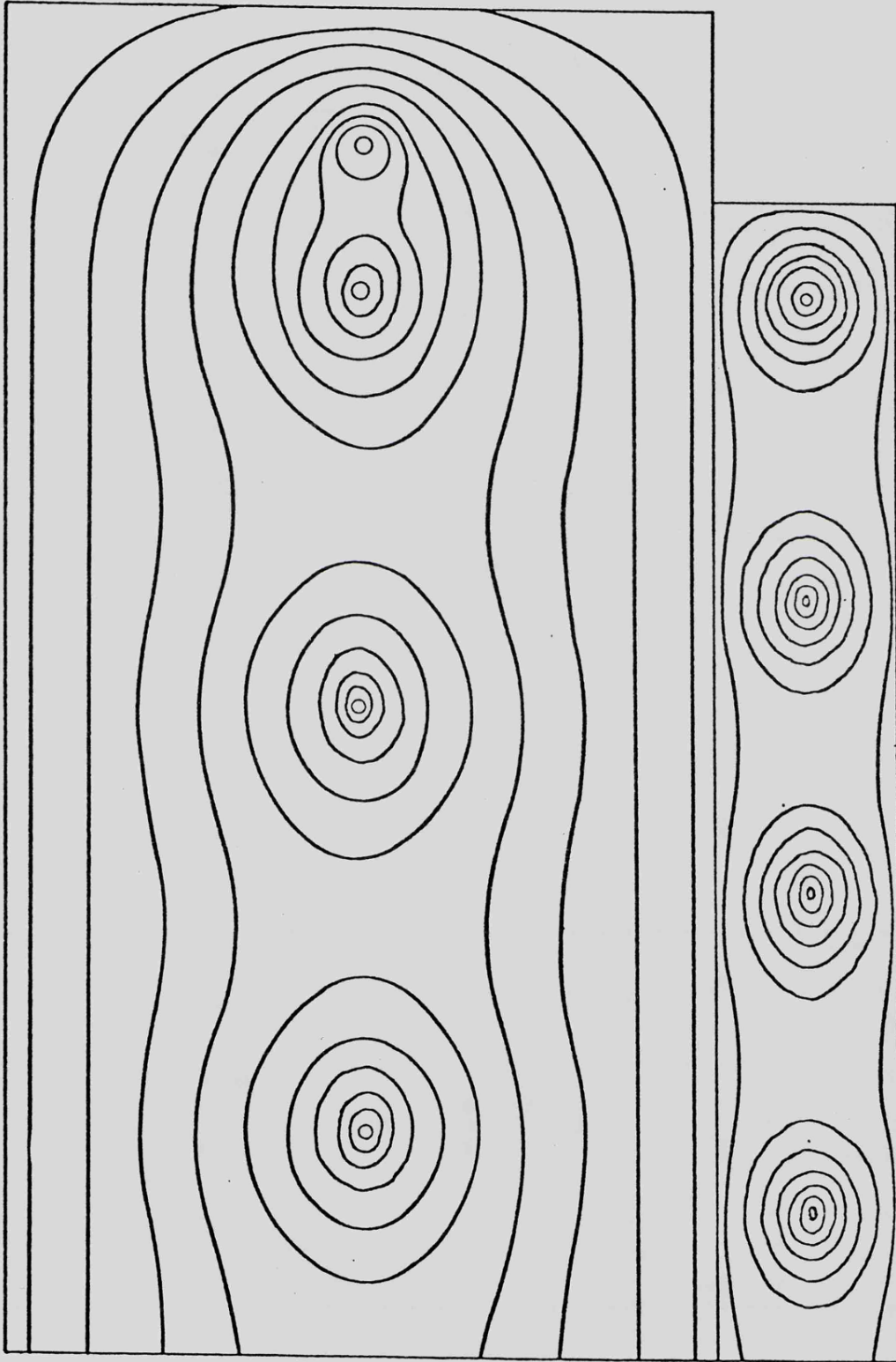
$$C = \frac{2\pi r Ea \epsilon_0}{V} \quad \text{per unit length}$$

The capacitance of a guard wire is therefore 11.5 pF per metre and for the main anode 6.6 pF. This leads to a minimum tension requirement of 3.5 gms for the signal and a considerably greater value of 60 gms for the guard wires.

The gains from multi wire arrays are always much lower than for an equivalent set of rectangular pods but this is compensated by an exceedingly good and constant resolution over the entire area, the performance of the flight detectors being described in chapter 4. Reference has been made earlier to the deflection of the back panel and collimator frame being 0.3 mm. Since most amplification occurs immediately around the wire itself the gain in the signal channel is relatively unaffected for medium energy X-rays. Fig. 2.10 shows the equipotential surfaces within the box, the contours being linearly scaled between the

FIG. 2-10 DETECTOR ELECTRIC FIELD  
(2.5x FULL SIZE)

( CONTOURS 0-2000 VOLTS, 200 VOLT INTERVALS )



lowest and highest voltage grid points within the array. The figure is 2/5 full size and only shows a few wires since the box interior is regular and symmetrical.

#### 2.4.7

The solid material left running lengthwise down the bottom corners of each panel were used to attach the grid divider. This consisted of a stainless steel mesh of 0.05 mm diameter strands with a transmission of 70%, carefully stretched and glued on a frame that was securely screwed to the box. The signal anode wires were strung between PTCFE bushes located on a metal end card that was bolted to the box, the end effect being minimised in the usual way by adjusting the field tube length. This material is a very good insulator and has stable mechanical properties. The guard end walls were made from a solid rectangular bar of this material, the field tubes not projecting beyond the side since the surface is non conducting.

The remaining problem is that the wires are extremely long, 70 cm for panels A and C and 90 cm for panel B, so some interior supports were required to limit their vibrational energy even though the HT was off during the launch. The use of nylon threads as described by Charpak et al. (1970) was felt to be unsuitable and so it was decided to have a single solid insulating wall across the middle of the main detector and 3 equally spaced sections across the guard detector. These also served as spacers to enable the grid frames to be bolted to the back panel eliminating flapping during launch. The wires passed through large clearance holes in the divider, the theory being that when the amplitude of vibration reached the diameter of the hole further energy input would be lost in collisions with the edge of the hole. A test rig was built to confirm that the wire would not break and observation with a stroboscopic

lamp confirmed that the amplitude of the harmonics on opposite sides of the divider did not greatly exceed the hole diameter. Tests were done to find the optimum size of the holes for each detector and noticeable change in gain was confined to within 2 cm on each side of the support.

Since the breakage of any of the 69 anode wires would be inconvenient to fix on the ground or catastrophic during the flight a new technique of crimping and spot welding the terminations was developed. The old method had always been suspect since the welds were known to become brittle after a few months. In tests of the new type it was the wire itself that broke rather than a failure at the weld point.

## 2.5 Experiment Electronic Design

### 2.5.1

The electronics can be split into an analog section and a digital section and it is proposed to deal with the analog side first. Each detector panel had 3 insulated lead throughs to its interior, one being the HT input and the other two being the guard and signal channel outputs, these emerging into recesses that had been left in the sides of the boxes to provide locations for the pre-amps and RC networks. There were slight differences between each panel but basically the RC network was connected to the terminal from inside the box and then a further lead through took the signal into the pre-amp compartment. Each pre-amp contained a voltage stabiliser chip to convert  $\pm 17$  volts input from the power supply to  $\pm 12$  volts. The noise in the pre-amp was principally due to power supply ripple and was 30 mV corresponding to  $10^{-15}$  C. Each pre-amp had variable gain and also an overshoot adjust control since the base line restorers (BLR) on the analog board did not like negative pulses. The output pulses from the pre-amps were linear up to the 5 volt HI level on the pulse height analyser (PHA) and had  $1\mu$ S rise time

and a  $1.5\mu\text{S}$  decay time.

The high voltage generators used have been described by Cooper (1977) and were mounted on the back of panels B and C and on the side of panel A. Each unit contained a variable oscillator that powered a specially made transformer with a 1000:1 ratio. This then drove a voltage doubler to produce a nominal 2000v with the adjustment potentiometer in its mean position. A remove adjustment of  $\pm 200$  volts was available on each unit by controlling a motorised potentiometer that affected the oscillator circuit. This independent control of each detector was used for final positioning of the gains from the block house just prior to launch. These units were switched off at -18 sec and on at +57 sec by the program motor in the ACU. Earlier designs of HT units had proved unreliable to repeated operation so launches had previously occurred with the HT live at some risk to the charge sensitive pre-amp although the anode wires were generally shorter and at a greater distance from the cathode walls than in the guard detector.

### 2.5.2

The long cable looms clearly visible in fig. 2.2 were completely screened as the threat of RF interference was a major one. It proved necessary to attach the screen to the boxes with a metal P clip since with plastic ones it was possible for a significant length to be unconnected to earth creating a small aerial. Great care was also taken with the earthing to avoid loops since there were so many different returns. To facilitate removal of the panels the wiring from the HT, pre-amp and calibration units were taken to a common 25 way connector.

An explanation of the processing of the 6 detector outputs can best be achieved by considering a single main channel and guard channel pair. A block diagram for this is shown in fig. 2.11 and an indication is



given where the other two channels merge in to form a common function.

### 2.5.3

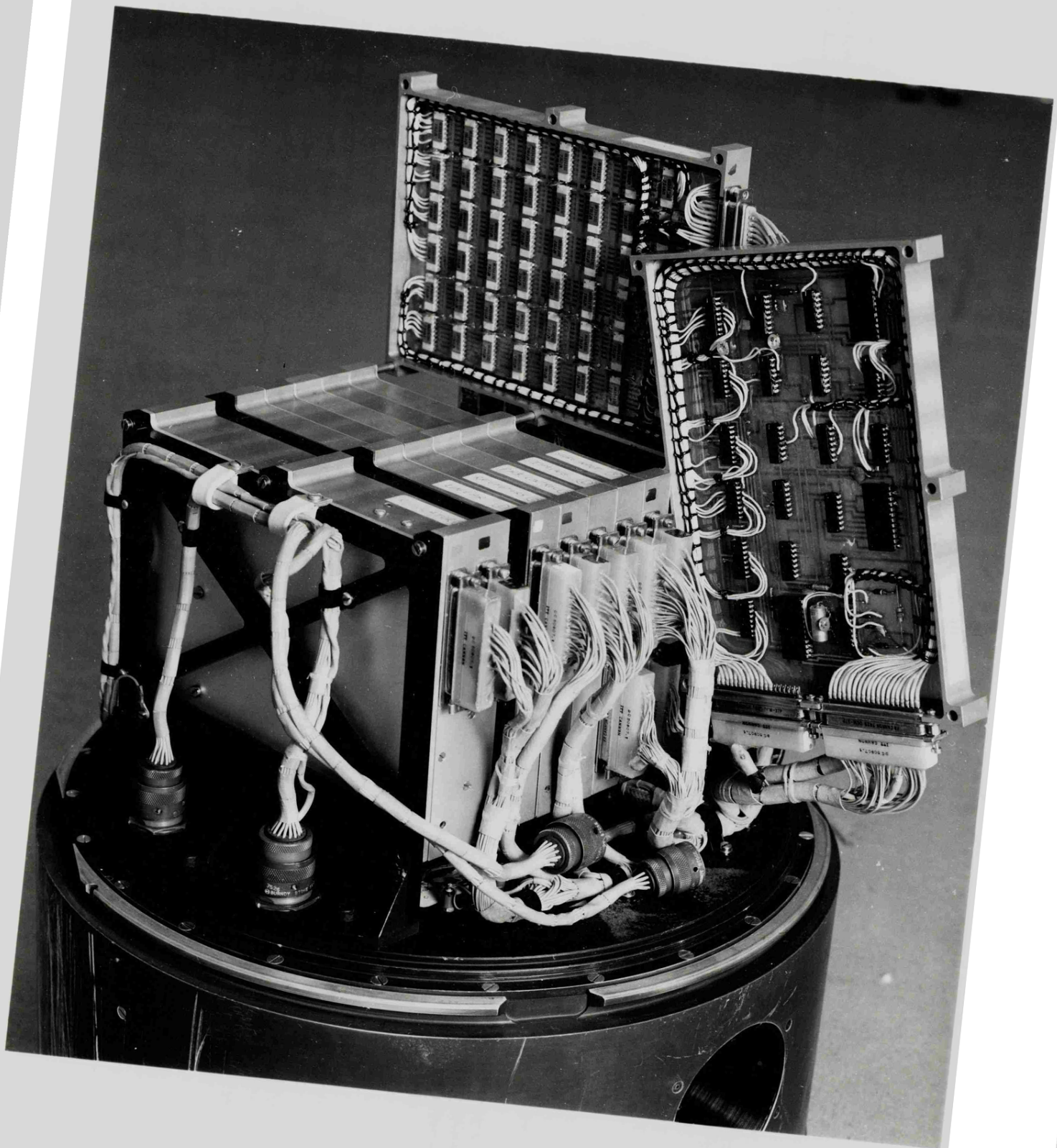
The signal pulse from the BLR is fed through a  $2\mu\text{S}$  delay which allows the logic to operate and gate the correct channel to the PHA if the pulse is valid. If a guard pulse has arrived during the previous  $3\mu\text{S}$  the A flip flop is not set, the PHA not enabled and EVENT never generated. If, however, A is set, the priority gate selects the correct channel to send through to the PHA, and the PHA BUSY prevents pulses from other channels interfering until the pulse has been analysed and PHA DONE is indicated. Should two signal pulses arrive simultaneously SA has priority over SB and SC, and SB has priority over SC. The setting of the A flip flop also fires a  $3\mu\text{S}$  monostable. If a guard pulse GA arrives during this time a coincidence is detected and the generation of EVENT is inhibited. EVENT is also inhibited if the PHA indicates a HI corresponding to a peak voltage of 5 volts. A further device that can inhibit the generation of EVENT by holding the flip flop off is the count rate integrator (CRI). This circuit consists of an integrating amplifier the output drifting up and down with a time constant of 0.01 sec in response to the input rate tripping the signal channel lower level threshold. When the output exceeds a pre-set level a discriminator forces the flip flop to the permanently off position for 2 seconds. After this time an attempt is made to re-allow this channel but if the CRI level is still high there will be no EVENTS from this channel. Each channel has this device so that HT breakdown in any unit will not corrupt the data from the remaining good detectors.

The PHA itself is a stack of 8 discriminators to achieve a fast response and the eight output lines are considered as an eight bit binary word that is retained until PHA DONE occurs. This is actually

FIG. 2.12

ELECTRONICS PACKAGE BOARDS FROM FRONT TO BACK

1. POWER REGULATOR + GAIN REMOTE ADJUST
2. LINEAR BOARD
3. RATEMETERS FOR SENDER 2
4. PHA CONTROL + VETO LOGIC
5. TIMING + ENERGY FRACTION CIRCUIT
6. STORE INPUT CONTROL
7. P.C.M. FORMATING BOARD (DISPLAYED)
8. FIFO MEMORY BOARD (DISPLAYED)



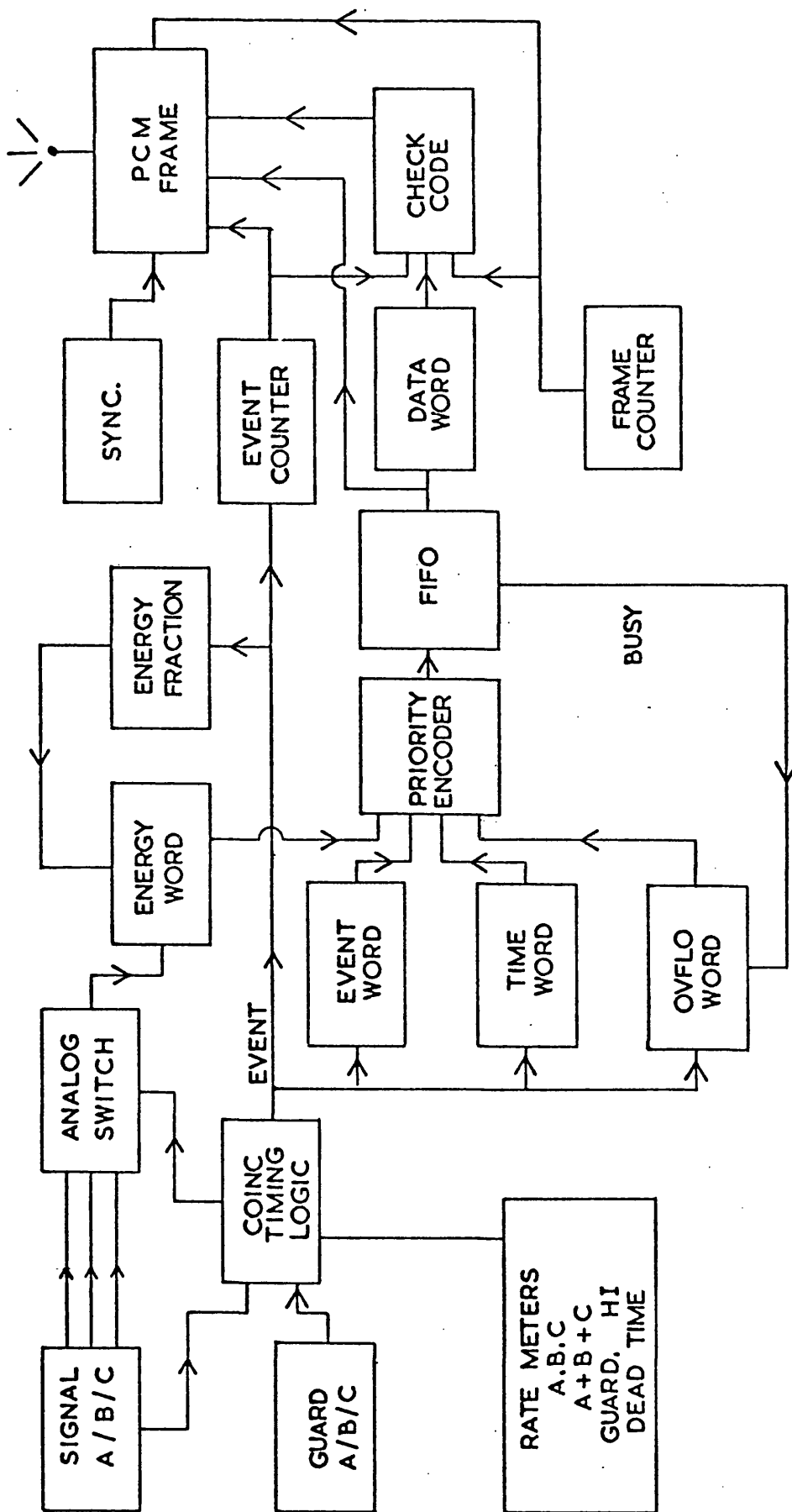


FIG.2-13 ELECTRONICS SYSTEM BLOCK DIAGRAM

encoded as a 3 bit BCD word and this can be combined with a further 2 bits describing the identity of the detector for possible insertion into the memory. These 2 bits are derived from the outputs of the A, B and C flip flops, the code used being det A (01), det B (10) and det C (11). Each PHA level is independently adjustable and the setting up and values used are described further in chapter 4. The 7 monitors indicated in fig. 2.11 were passed to digital to analog converters for inserting onto sender 2 as described in chapter 4. The rest of the electronics is purely digital and responds to the generation of EVENT. All the data required including the PHA word can be loaded into the memory before the generation of the next EVENT pulse which cannot occur until PHA DONE is indicated. The actual dead time of the system was measured to be  $6.5\mu\text{S}$ .

#### 2.5.4

The random EVENT time was then synchronised to the next positive going 4 MHz pulse edge in order to simplify the timing of the digital processing. All the clock pulses were derived from an 8 MHz crystal oscillator which was divided down to a slowest rate of one cycle every 50 seconds. The digital system is outlined in the block diagram, fig. 2.13, and a photograph of the complete package is shown in fig. 2.12. Having obtained the large area and hence a high count rate from a bright source like Cygnus X-1 there is a problem in how to transmit all this information. An analysis of the planned system indicated a basic time resolution of  $2\mu\text{S}$  which is also similar to the pre-amp pulse time scale. To deal with 5 - 10,000 pulses a second with complete time and energy information is beyond the capacity of the 125K bit data rate allowed by the bandwidth of the standard PCM system. The best compromise was to devise circuits that could automatically insert more information when room was available and to this end a variable sequence, non regular chain of

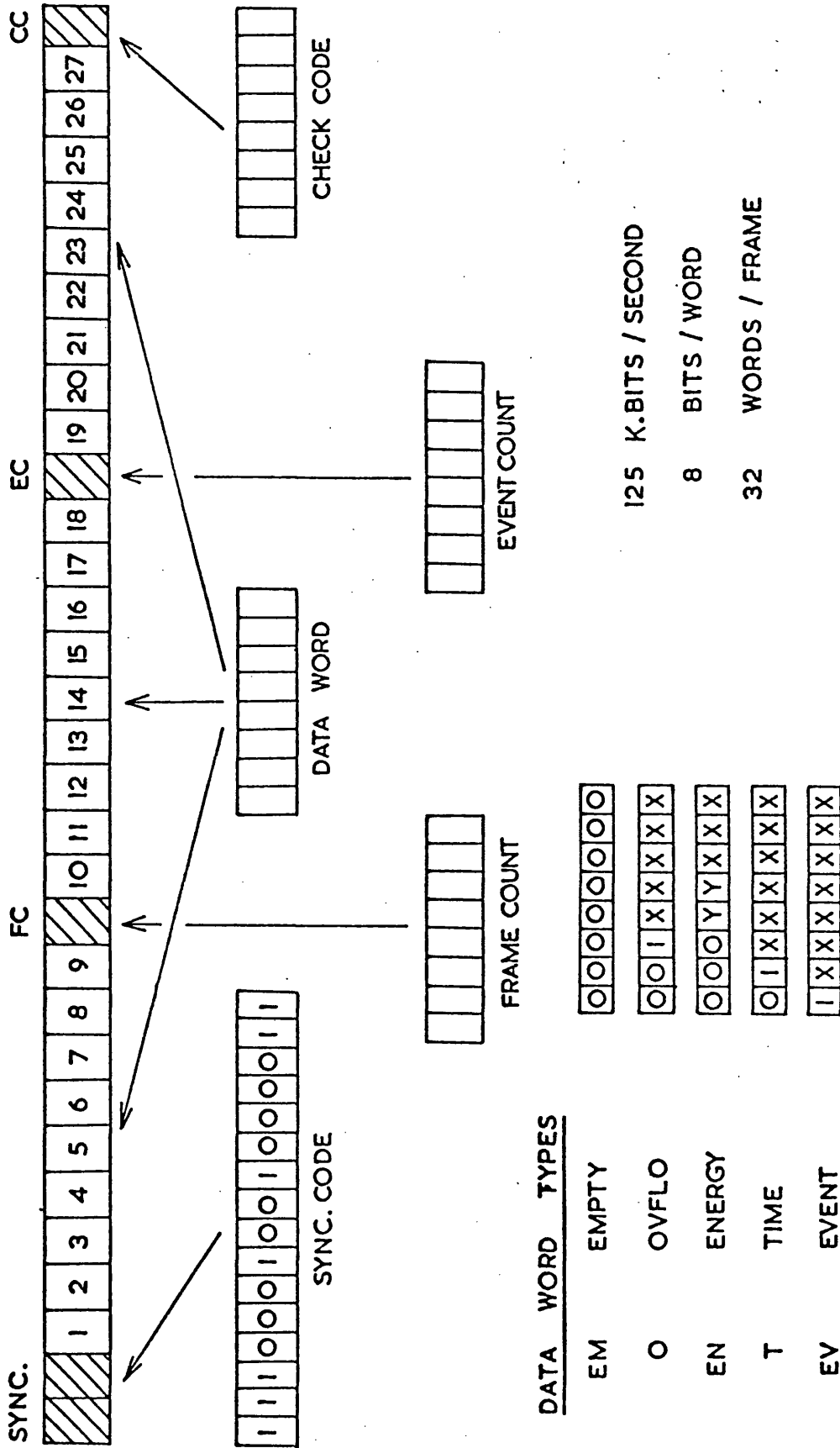


FIG. 2-14 PCM FORMAT

data words was inserted into the PCM fixed format (fig. 2.14).

The time information was split into two parts since continual transmission of unchanging bits is very wasteful and beyond here these are referred to as the TIME update word and EVENT time. Every EVENT allowed by the analog circuits and logic set a flag indicating that the EVENT time should be loaded into the store. This word contains 7 bits of the clock chain representing  $2\mu\text{S}$  to  $128\mu\text{S}$ . A continuous monitor was kept of the interval between EVENTS and if this was greater than  $256\mu\text{S}$  the TIME word flag was set, this word containing the next 6 bits of the clock chain representing  $256\mu\text{S}$  to  $8192\mu\text{S}$ . A check was also carried out to see if a TIME word had been flagged in the previous  $8192\mu\text{S}$  and if not the flag was set. This ensured that these bits could never complete one cycle before being sent again avoiding any ambiguity in timing.

Since the experiment was primarily concerned with timing it was the ENERGY information words that were sacrificed at high count rates. To achieve this a circuit was devised (appendix D) that flagged a variable percentage of energy words depending on the sum of the current mean rate observed by all three panels. At very high count rates the memory could become full, a STORE BUSY signal causing an OVERFLOW word to be flagged. When EVENT is generated a priority circuit loads data words into the memory corresponding to the following sequence of flags if set OVERFLOW, ENERGY, TIME, EVENT. The overflow condition if flagged will continue until the current sequence has been completed and a following EVENT has arrived thus identifying the number of excess counts detected between the two EVENT times. Each of these word types is identified by a unique code which is described in fig. 2.14. The memory or FIFO (first in, first out) is considered separately at the end of this section. Since a word is removed from the memory every  $74\mu\text{S}$  it is possible for

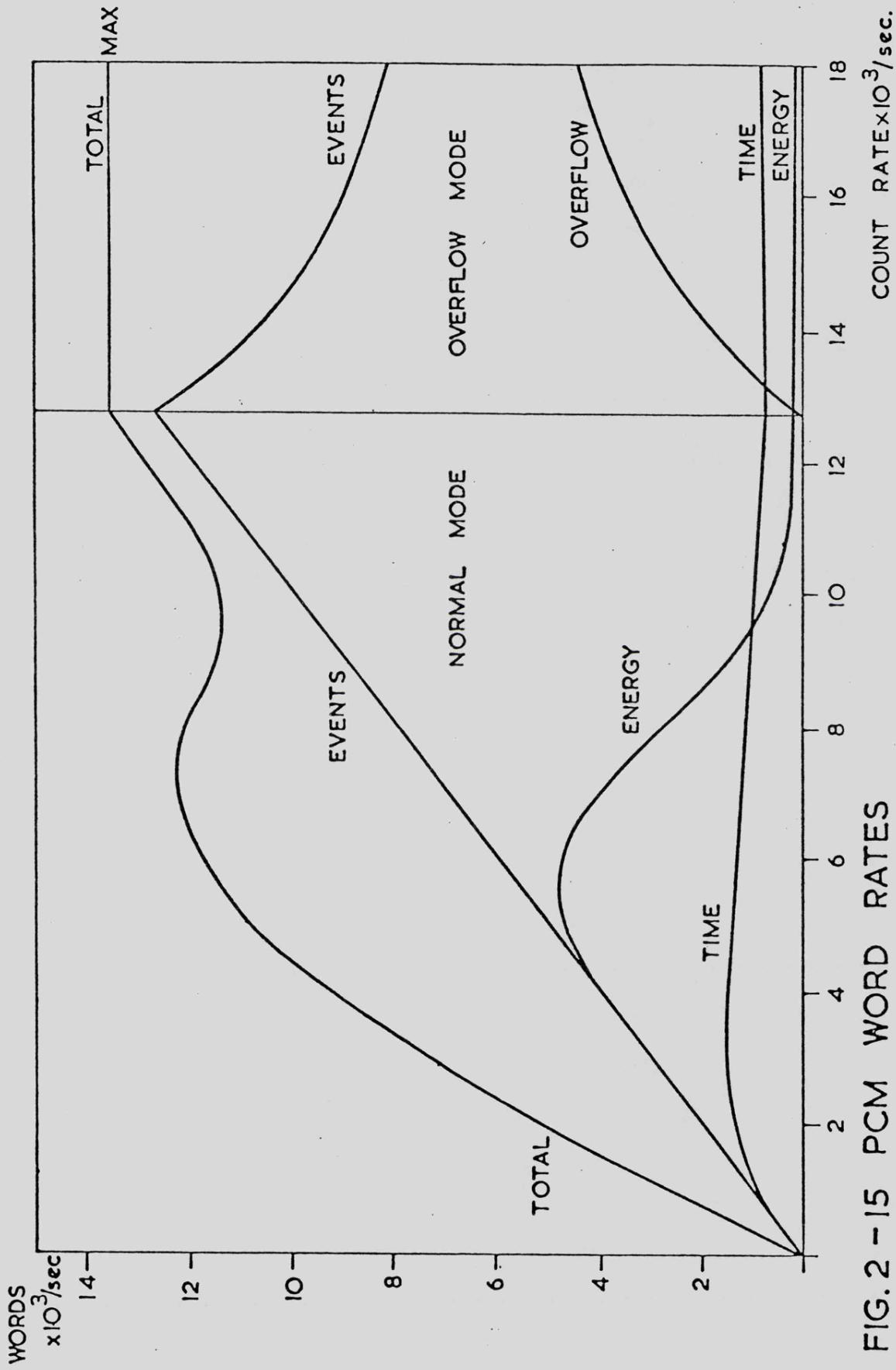


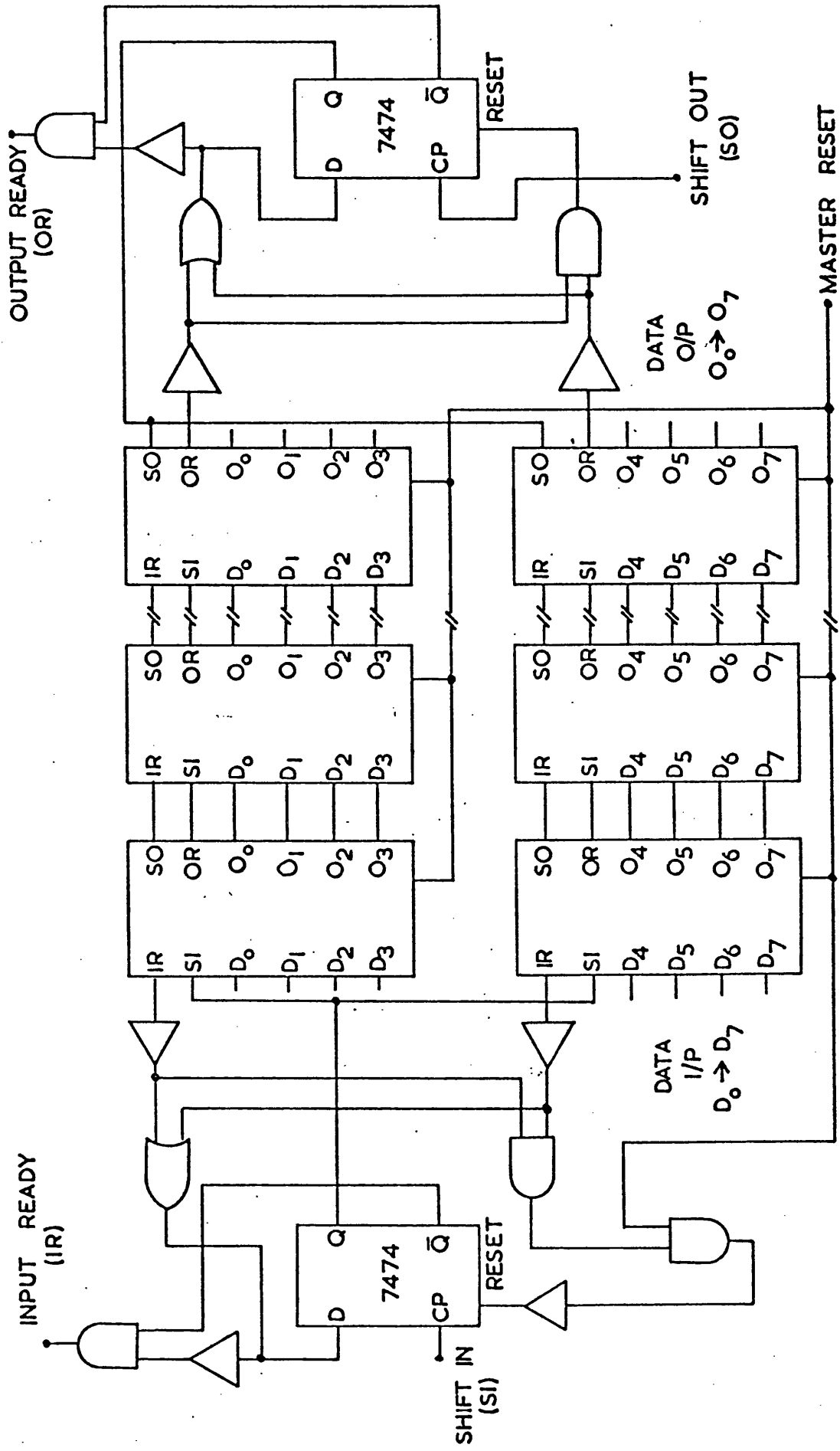
FIG. 2-15 PCM WORD RATES

the overflow counter to have operated for a minimum time of two words or  $148\mu\text{S}$  since an EVENT will accompany every OVERFLOW. As the overflow counter has five bits the overflow mode is valid up to 100,000 counts per second which is approaching the dead time limit of the analog pulse analysis. If the memory is empty when a word is read out it will naturally have eight zero's and is therefore called an EMPTY word. To identify this as a 5th type of word is valid since EMPTY words may or may not precede any of the 4 other types but they certainly should not occur within the sequence. The relative ratios of word types transmitted was checked by using a random pulse generator of precisely controlled mean rate, the results being shown in fig. 2.15. This applies to a steady state situation rather than the rapidly varying combinations caused by the large variations to be expected from Cygnus X-1 but it does explain the possibilities. The energy fraction circuit was programmable with wire links to optimise the entire system's response to expected variations. Since the system is complicated a computer program was produced to investigate all aspects of the response and this is discussed in section 4.4.

#### 2.5.5

The actual PCM format shown in fig. 2.14 is obtained by suitable gating of pulses from the clock chain. The SYNC pattern was chosen to be compatible with the Appleton PCM system described in appendix F, but any pattern that occurs infrequently within the frame is suitable. The event counter is a back up system that bypasses the memory by displaying the number of EVENTS detected in real time during the previous frame. This corresponds to a  $2.048\text{ms}$  time interval but the total displayed bears no relation to the number of EVENT words within the frame. The frame counter is derived from the 8 bits in the clock chain beyond those used in the

FIG.2-16 FIFO MEMORY CONSTRUCTION



TIME update word giving the most significant bit a period of 0.5 seconds. The 8 bit check code was introduced because the timing information is very interdependent and although a correcting update would eventually occur a fast sequence of EVENT times might well contain errors. The circuit described in appendix E operates on all previous bits in the frame and allows identification and correction of single errors introduced during transmission and reception. Multiple errors although detected cannot be corrected. The 27 eight bit gaps within the fixed format are filled at a regular rate with words from the memory as previously described.

#### 2.5.6

The memory unit was contained on a separate board and was built from 48 integrated circuits of a type known as AM 3341. Each chip has a 64x4 bit memory that acted on a first in first out basis (FIFO) so that a word of 4 bits entered in parallel ripples through to appear at the output in a typical time of  $10\mu\text{S}$ . The IC's can be cascaded serially since the control and data lines match up for adjacent chips. Parallel extension to obtain the 8 bit word required is obtained by using appropriate control logic to ensure that both lines remain locked since the measured difference in ripple time down each line of 24 chips amounted to  $8\mu\text{S}$ . The arrangement used is shown in fig. 2.16 and it is apparent that treated as a black box it resembles a single integrated circuit. This board was checked thoroughly using a test box described in appendix C and operated without errors up to 2 MHz drawing up to 1.7 amps from the power supply.

The memory can be considered as a queue with words entered at the top automatically falling down the stack of 1536 positions until prevented from going further by existing data. These words then drop

down one position every  $74\mu\text{S}$  when a word is inserted into the PCM frame. The STORE BUSY signal mentioned earlier is derived from the input ready (IR) control line of the FIFO. If the word entered at the top of the stack has not moved before another arrives the IR line will stay low inhibiting the next shift in (SI) attempt and setting the OVERFLOW flag. The queue will continually vary in length with many EMPTY words occurring until the observed count rate reaches a certain value (fig. 2.15) at which point it will rapidly fill up and overflow. The interaction of this queue with the other variables in the system is discussed further in chapters 3 and 4. Since the security of the FIFO is vital to the experiment it was tested exhaustively and found to be prone to switch on lock up due to various supply rails coming on in different time scales. To overcome this a small circuit held the master reset (MR) on for several milliseconds at switch on and every 50 seconds causing the loss of an insignificant amount of data. Any variation in the rails as seen on previous experiments during launch could not now produce a permanent failure mode.

## CHAPTER 3

## Test equipment and data processing techniques

	Page
3.1 Test Gear System	91
3.2 Electronic Test Box Design and Function	98
3.3 Data Tape Processing Techniques	102

### 3.1 Test Gear System

#### 3.1.1

From the previous chapter it is apparent that the complete testing of this experiment both in the launcher and in the more casual atmosphere of preparation requires an extensive system of equipment. A fast mini computer would have been ideal but was not available so it was decided to construct a complex box of electronics that would decode the PCM data stream and interface to a number of standard pieces of laboratory equipment.

#### 3.1.2

With this approach in mind the following list of test requirements was drawn up and these can be divided into two groups.

##### Fixed format data:

- 1) Detection of SYNC and display indicating lock.
- 2) Check that successive frame counts increment by 1.
- 3) Continuous verification of the check code word with error indicating lamp.
- 4) Display of current word number as defined in fig. 2.14 showing the PCM format.
- 5) Display of number of EMPTY words during a set interval as defined in test no. 13. With no data words there will be approximately 13500 in one second.

##### Data word checks:

- 6) Display of contents of event counter when stimulated by an external pulse generator.
- 7) Continuous checking of word sequence with display of previous type, current type and an error indication.
- 8) Continuous checking, with error lamp display, that 8 bit words

not one of the 4 main types were indeed EMPTY words.

- 9) A decoded ENERGY word displaying the 8 PHA channels for use with a variable height pulse generator.
- 10) The ability to select any combination of detectors for test 9.
- 11) To check that the time difference between consecutive EVENTS is constant or varies correctly when using a pulse generator.
- 12) To check that the time difference between consecutive TIME words is correct as in test 11.
- 13) To display the number of any selected word type during
  - A) 100 SYNC's
  - B) 500 SYNC's (approximately 1 second)
  - C) 10,000 EVENTS.
- 14) Verification of the different word ratios as shown in fig. 2.15 at varying count rates using a random pulse generator. A constant rate pulse generator if used here gives a 1:1 relation of TIME and EVENT words up to the point where EVENTS are  $256\mu\text{S}$  apart at which point the TIME word rate will drop to 122 Hz.
- 15) Display of the contents of the OVERFLOW word when using a high pulse rate.

Tests mentioned above that are not performed continuously are selected by a rotary switch that also routes the chosen information to a suitable display. Any sequence, check code or empty errors could be made to latch all the displays to aid exact identification of the fault, this feature being made optional since for some of the check out tests odd stoppages were unacceptable. All aspects of the experiment can easily be checked with the monitoring system shown in fig. 3.1 but once the electronics package is inside the bay a few tests cannot be done using an external pulse generator. These include the trip levels of the 3 CRI units, the guard veto circuits for detectors B and C and the testing of the PHA

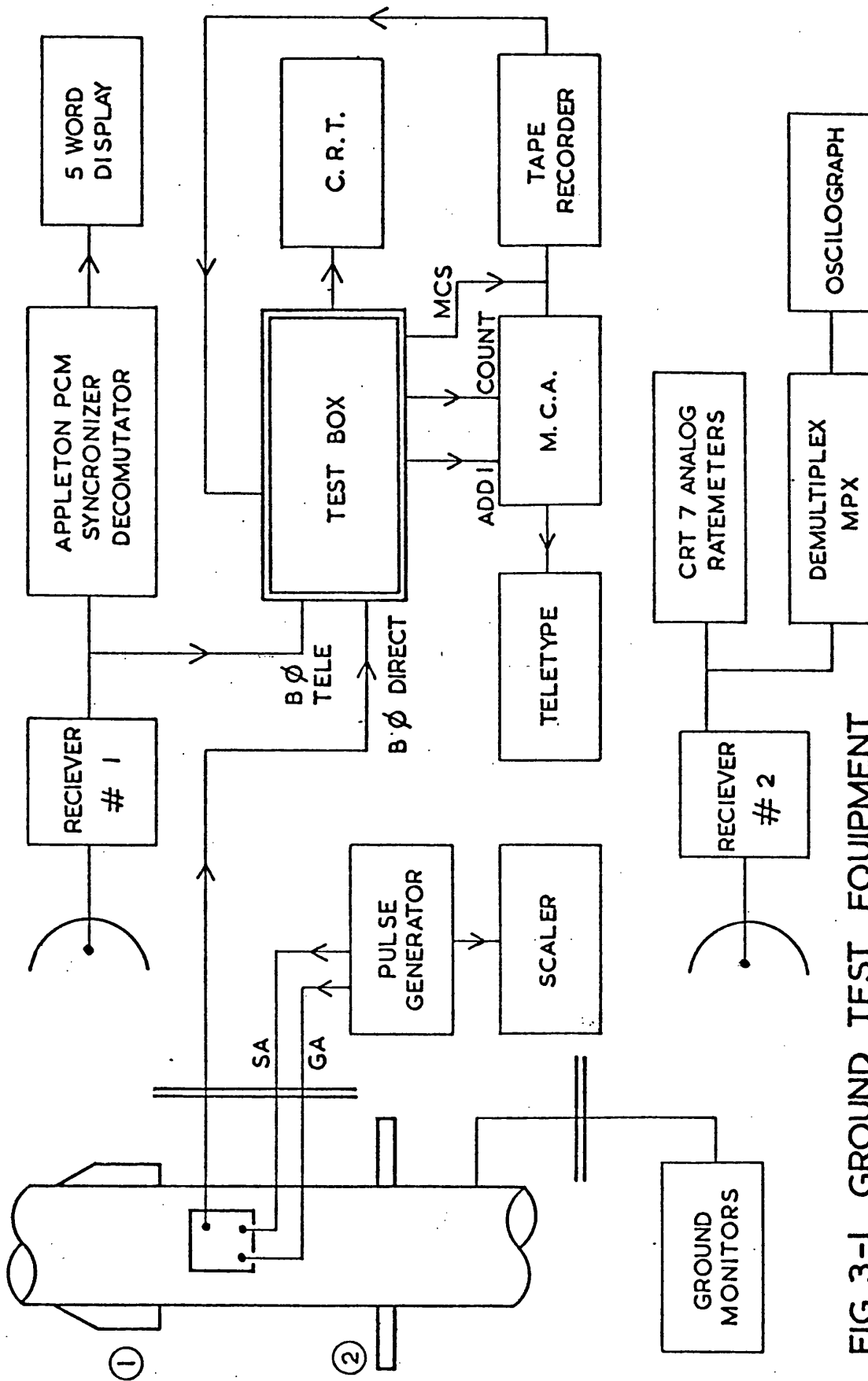


FIG. 3-1 GROUND TEST EQUIPMENT

levels. These 3 items can, however, be monitored by comparison with previous data when the detectors are operating and the cal or an external  $\text{Fe}^{55}$  source is used.

### 3.1.3

A number of the features shown in the block diagram are worthy of further explanation. The pulse generator mentioned in the tests can be used to trigger the A guard and the A signal channels through 2 BNC snatch connectors on the side of the round enabling the  $3\mu\text{S}$  overlap vetoes to be checked out. A further BNC lead provided a direct Bi-phase (BØ) PCM data stream so that the transmitter receiver loop could be by-passed. All three BNC socket leads pass through relays, switchable from the blockhouse to isolate them from the electronics prior to launch to ensure that heating of the skin cannot cause short circuits.

Since BØ signals are impossible to read by eye, an oscilloscope (CRT) was used to display the reconstituted bit stream for visual inspection of the frame fixed format data. By careful adjustment of frequency, the pulse generator can be made to beat with the PCM frame frequency which holds the data words at fixed positions in the frame. At a low enough EVENT rate, say 2 KHz, there will be an ENERGY, TIME, EVENT sequence occurring 4 times in each frame of 27 words so that the word identities and contents can be checked by eye based on experience.

### 3.1.4

The multi-channel analyser (MCA) can be used in two modes since some modifications had been made internally for a previous experiment. The decoded 8 bit data words can be treated as an address 0-255 which is transferred serially down the COUNT line from the test box, this location in the MCA store then being incremented by a pulse down the ADD 1 line.

In this way locations 1, 2, 4, 8, 16, 32, 64 and 128 in the MCA memory acted as an 8 channel analyser. This mode also tested the frame counter (test 1) since this would have a cycling value addressing all locations in the MCA if operating correctly producing a straight line that slowly moved up the display.

The MCA could also be used in the multi-channel scaling mode (MCS) if suitable pulses were provided from the test box. If, for example, EVENT was selected, a short pulse was sent down the MCS line coincident with every EVENT detected. Up to 250 seconds worth of data could then be stored in the MCA in 1 second time bins as a histogram showing intensity variations. Shorter intervals can be analysed in finer time bins but for the flight itself a 250 second interval was required. Unfortunately the tape recorder was unable to record reliably the 125 K bit data stream but could easily record the MCS output since it is impossible to get more than 13500/second corresponding to a selection of EMPTY words and an empty frame. During the flight EVENT words were selected so that the tape could be replayed and interesting sections examined in more detail.

### 3.1.5

Since the main unit can only display one word type at a time a useful addition was to link in part of the Appleton PCM test rack allowing any five words from the frame of 32 to be selected and displayed. The ground monitor signals came down the round umbilical connections and were used for testing the experiment rail voltages and HT monitors when in the non-flight mode.

### 3.1.6

The second sender flown was the standard 465 Mcs system that has been used for many years to transmit analog information. Its main use



on this payload was to provide all the ACU monitors during flight but 8 of the 24 available channels were used by the experiment since there was no room for housekeeping data on the PCM sender. One of the eight channels was used for a 32-way electronic multiplexer and the other seven provided a data back-up to the primary system. Each of the channels is sampled 80 times a second so to ensure that none of the multiplexer levels were missed this unit was given a sync frequency of 2.5 Hz. This is rather a slow rate to view on an oscilloscope and so an oscillograph was used when testing this channel during integration and check out. The channel allocations on the multiplexer are shown in fig. 3.2 and several of these features are worthy of further explanation.

The EHT monitors were derived from a potential divider on the HT side of the circuit prior to the R-C network and therefore provided a positive indication that the unit had switched on. The three CRI monitors are derived from the analog levels mentioned in section 2.5.3 and as the preset figure is approached the monitor voltage drops rapidly indicating that the veto pulse should be inhabiting that particular channel. The camera operated monitor is obtained from a micro switch that is operated by the same mechanism that depresses the shutter release and with each exposure lasting two seconds the monitor should be on for four frames.

### 3.1.7

The other seven channels on sender 2 were used for the following rate monitors: detectors A, B, C, A+B+C, and HI, GUARD, DEAD TIME. These signals are derived from the points indicated in fig. 2.11 after passing through some divider circuits allowing adjustment to the expected rates, division by up to  $2^4$  being possible simply by moving wire links on the divider chip. The D/A converters had 64 bit resolution with an output range of  $\pm 3$  volts and since each channel was sampled 80 times a second,

the input rate to each unit had to be kept below 5120 Hz to prevent ambiguous cycling of the counter. The setting up of these units is described in section 4.3.2. With the experiment in the flight mode, channels A, B and C were free to cycle and the other four were reset after each sample pulse. For ground testing, all seven were allowed to cycle since odd noise or RF interference would be more conspicuous because the level would build up rather than hover around the zero mark.

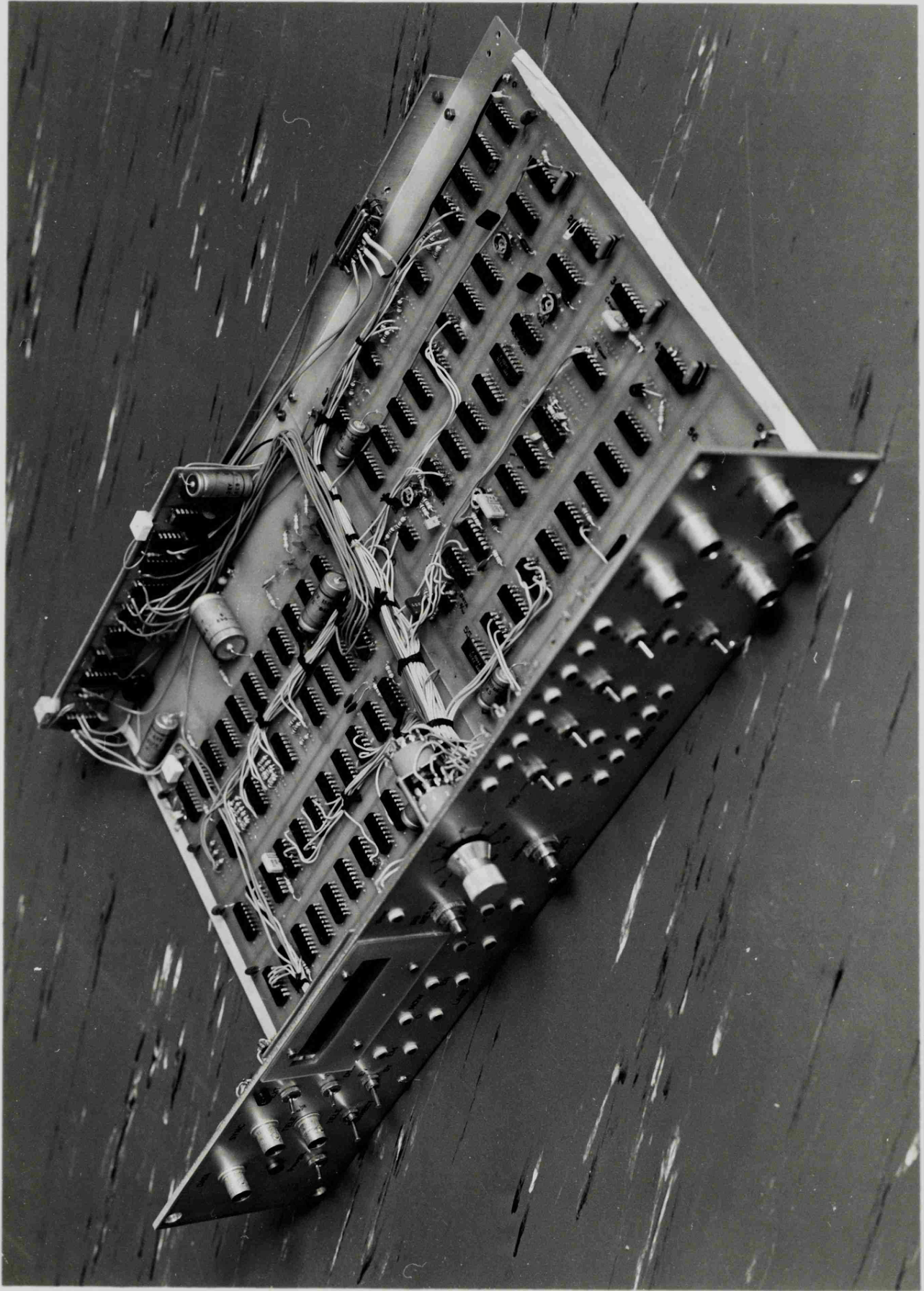
## 3.2 Electronic Test Box Design and Function

### 3.2.1

The construction of the electronic test box is best understood with reference to the electronic block diagram, fig. 3.4, and the photograph in fig. 3.3 which shows the unit with the cover removed. In general, word frequencies are displayed on a digital counter with word contents and other information being routed to LED lamps. The B $\emptyset$  bit stream is fed to a phase locked loop in order to provide the basic clock chain necessary for correct timing of the decoding circuits. The data is then reconstituted and a hard wired check carried out to identify the sync pattern (111000101000011) which together with the clock is used to convert the serial data to 8 bit parallel words. As mentioned in chapter two, and with reference to fig. 2.14, we can identify several possible causes of false sync detection. All these can be eliminated by checking that the SYNC pulse occurs at the correct interval and ignoring rare matches in between. Naturally, once the system is in step it will stay that way but at switch-on or during a break in transmission the lock will be lost. The circuit will then treat the first occurrence of the sync pattern as being correct which if valid will cause it to remain in lock since another SYNC will occur at the correct interval. If, however, it was false, the circuit will miss a subsequent real SYNC, and after the correct time interval, will

FIG. 3.3

TEST BOX ELECTRONICS SHOWING FRONT PANEL  
FEATURES AS DESCRIBED IN THE TEXT



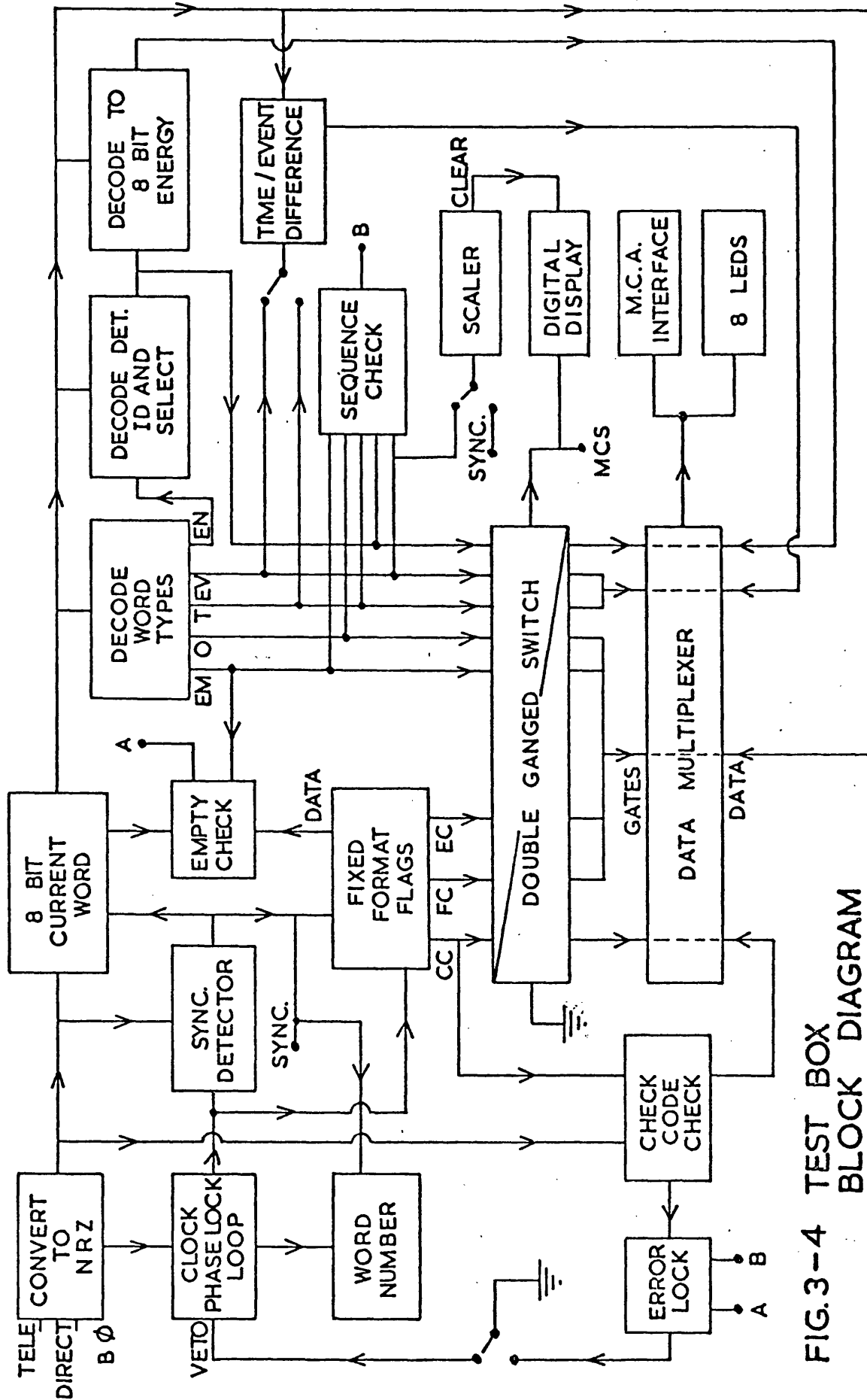


FIG.3-4 TEST BOX BLOCK DIAGRAM

search for and lock onto the next SYNC, the process repeating until the correct sequence is picked up.

### 3.2.2

The clock is used to construct the following flags indicating the word position in the fixed format of the Frame Counter (FC), Check Code (CC), Event Counter (EC) and DATA words. In addition, a counter indicates the position 1 - 32 of the word currently held in the 8 bit store. The current word is continually decoded to decide which of the 5 word types it is if a DATA word is indicated. The following flags may be set - EMPTY (E), ENERGY (EN), OVERFLOW (O), TIME (T) and EVENT (EV) and if EN is indicated this is further decoded to provide the detector origin and an 8 bit PHA word derived from the 3 bit BCD energy information. If the word is neither EN, O, T nor EV, and DATA is indicated, it must be an E word which can be compared with the 8 bit current word possibly giving an empty error. The word sequence display consists of two rows of five LED's, the top row being the current word and the bottom row the previous word, each lamp indicating a particular word type and glowing with a brightness corresponding to its relative frequency. Since only one word type can be processed at a time, these lamps are a good monitor of the general state of the experiment, features such as the sudden change to overflow mode at high rates being easily seen. The circuit checking for sequence errors works by comparing the previous and current word type flags according to the following truth table.

		LAST WORD					
		T	EN	O	E	EV	
CURRENT WORD	EV	1	1	1	1	1	
	T	0	1	1	1	1	1 allowed
	EN	0	0	1	1	1	0 not allowed
	E	0	0	0	1	1	
	O	0	0	0	0	1	

The check code circuit described more fully in appendix E is duplicated in the test box, and operates serially throughout the frame on words 3 - 31 of the reconstituted bit stream. At this point, it should have the same value as the contents of word 32 which it then operates on during the CC flag producing all zeros if no error was detected in the 30 processed words. Various types of operations are carried out on the 8 bit current word as indicated by the word type flags, the derived data being passed down 8 line channels to a data multiplexer. This "word content" information was gated by selection with a rotary switch which simultaneously allowed the frequency of the selected variable to be monitored by counting the flag pulses. In addition to the LED display, the output of the multiplexer was routed to a MCA interface circuit, providing the addressing system referred to in the previous chapter. The TIME difference and the EVENT difference circuit worked by storing the current and previous times and performing subtraction using two's complement arithmetic.

### 3.2.3

To operate all this test gear efficiently, especially during the launcher check-outs, necessitated the use of a quick set of tests to verify that everything looked right. The sequence followed is shown in fig. 3.5 and took approximately five minutes to complete.

## 3.3 Data Tape Processing Techniques

### 3.3.1

Until recently all Skylark telemetry was based on several analog systems (B.A.C. 1972) where the experimenter may possibly have shared some of the channels with the ACU data as done for sender 2 on this payload. Some of these systems have also used some PCM modulation but this experiment has been designed to use the new 125 K bit PCM equipment. Due to the

FUNCTION TESTED	TEST MODE
<p><u>HT off, CAL off, PULSER off</u></p> <ol style="list-style-type: none"> <li>1) Sync okay</li> <li>2) Frame count okay</li> <li>3) Correct number of empty words</li> <li>4) No errors</li> </ol>	<p>CRT inspection MCA inspection Test box display Error VETO on</p>
<p><u>HT off, CAL off, PULSER on CONSTANT</u></p> <ol style="list-style-type: none"> <li>5) Event counter correct</li> <li>6) Drop in time words at 4 KHz</li> <li>7) Change from empty to overflow</li> <li>8) Overflow counter correct</li> </ol>	<p>Pulse F up and down Monitor test box F around 13 kHz F above 13 kHz</p>
<p><u>HT off, CAL off, PULSER on RANDOM</u></p> <ol style="list-style-type: none"> <li>9) Energy fraction correct</li> </ol>	<p>Set F to expected value while monitoring EVENTS then switch to ENERGY words</p>
<p><u>HT on, CAL off, PULSER off</u></p> <ol style="list-style-type: none"> <li>10) Check background rates in A,B,C</li> <li>11) Monitor guard on sender 2</li> </ol>	<p>Energy words selected Telemetry # 2 CRT inspection</p>
<p><u>HT on, CAL on, PULSER off</u></p> <ol style="list-style-type: none"> <li>12) Check rates in all 3 detectors</li> <li>13) Check CAL-PHA distribution</li> <li>14) Monitor # 7 on sender 2</li> <li>15) Time difference correct</li> </ol>	<p>ENERGY and EVENT words ENERGY words + MCA Telemetry # 2 CRT inspection MCA should have exponential profile</p>

FIG 3.5 LAUNCHER CHECK-OUT SCHEDULE

complexity of the format required to achieve the necessary information rate, the electronics was designed to include its own PCM frame generator as described in chapter two, producing the format shown in fig. 2.14. This was made compatible with the Appleton PCM checkout equipment and data processing system by having the same data rate, sync pattern, frame length and word length.

### 3.3.2

During the actual flight, the instrumentation building at range E Woomera monitored the flight using a dual aerial receiver system and recorded in parallel two tape records to the following specifications:

#### Track Number

- 1) System information
- 2) NASA 36 bit time code
- 3) M36 Receiver A direct
- 4) Annotate (Voice channel)
- 5) TIM 1 50 kHz reference
- 6) M36 Receiver B direct

This tape could also be played back into our test gear for quick-look analysis after the flight since the tape recorders were of considerably higher quality than our own.

A copy of this tape was sent back to England to be digitised at the Appleton Laboratory where a computer compatible tape was produced. Two time references are included on the tape, the NASA 36 code being an international standard, and the TIM 1 code being local to the Woomera/WRE Salisbury system. The data from the second sender was recorded in a similar fashion but was not digitised. The type of signal transmitted was bi-phase (BØ) because this has a transition on every clock edge enabling the decoding

clock to lock onto the same frequency. An example is given below to show how the SYNC pattern is transmitted.

SYNC 1 1 1 0 0 0 1 0 0 1 0 0 0 0 1 1



TRANSMITTED



RECOVERED



The data tape provided by Appleton has a complicated format due to the merging of the time code and data tracks to produce a fully documented flight tape. This format is described in appendix F, and the densely packed tape must be unpacked and sorted to derive the group of 8 bit words that we require. Apart from providing various error flags, the main aspect about the production of this tape is that where data is missing, due to a break in reception, one or more dummy frames are inserted to keep the time code/frame relationship in step.

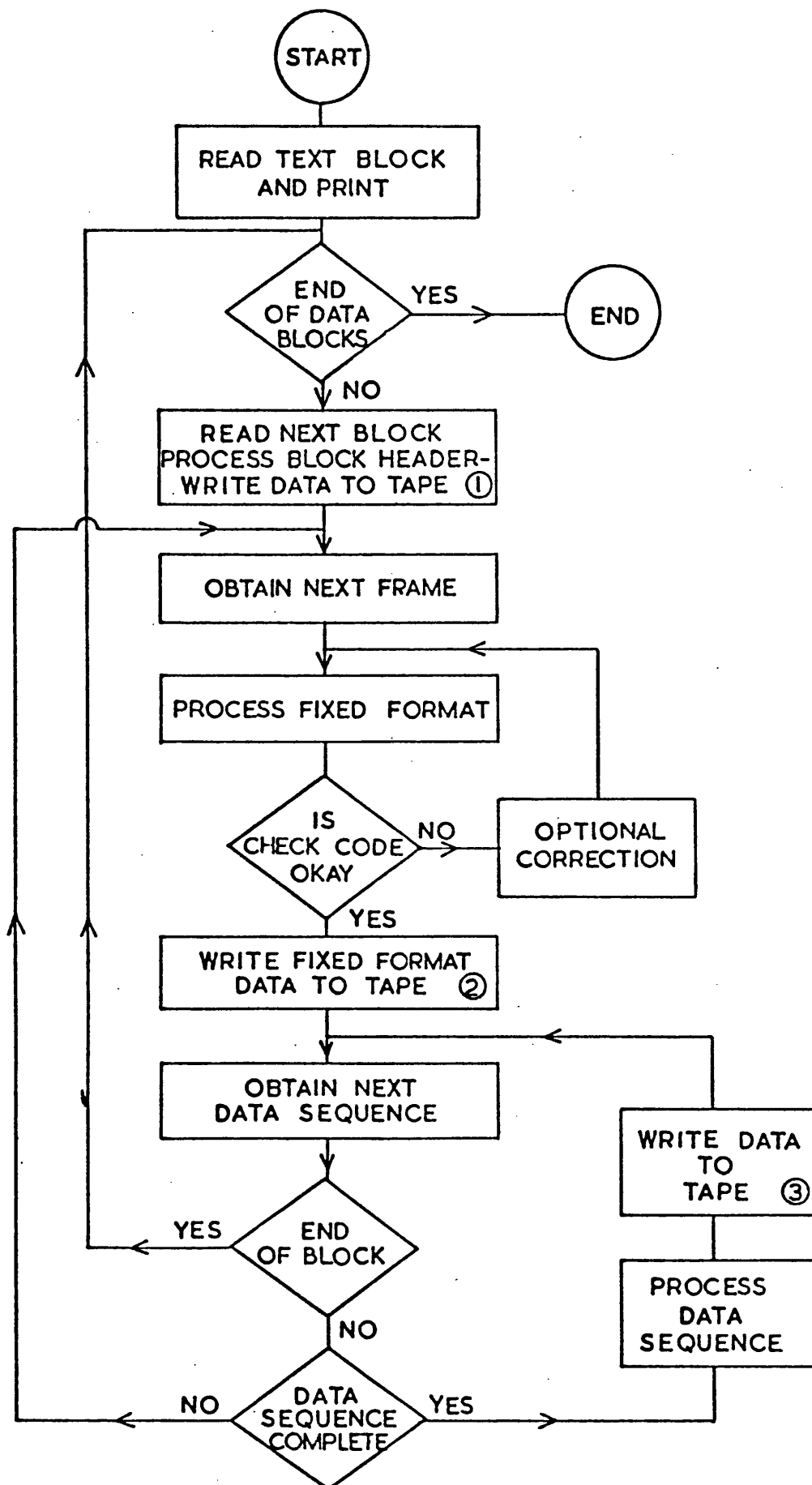


FIG.3-6 FLIGHT TAPE PROCESSING

### 3.3.3

In order to obtain scientific results, this cumbersome format must be reduced to an easily read and interpreted tape. This job need only be done once, but must be achieved with complete reliability, because all further reduction depends upon this first pass. The approach chosen was to split the operation into two parts and test each part separately, with suitably prepared simulation data, before trying to decode a real test tape. A flow chart for the computer program is shown in fig. 3.6 and shows that the logical steps for part 2 are equivalent to those built into the electronic test box.

The first section of the program deals with decoding the tape to simply present 30 word data frames to the second section. The way in which these words can be accessed is described in Appendix F. The routines to achieve this were made totally internally consistent so that problems such as packing and unpacking the computer words, block lengths and block types were all taken care of automatically. The second half of the program keeps calling new frames, processing them, and writing the derived data onto another magnetic tape in a new format. Various error messages can be output for the complete range of possible faults and an optional correction of the data frame can be made if a check code error is detected. Because this tape replaces the original, any suspect data must be tagged to indicate the detected fault and some time information must also be retained. Superfluous information on this tape can be ignored for routine processing since we basically only require the list of event times, the actual start time being arbitrary, but capable of precise location using the NASA 36 time code information. In writing this new tape, the University Cyber 72 computer system takes care of the block formats and lengths, greatly speeding up the subsequent processing since the tape is very easy to read, the new format being shown in fig. 3.7. There will be 64 FRAME

PASS 1

- BLOCK COUNT + DAY	- 10'S HRS	UNITS HRS	MILLI SEC	10'S MIN	UNITS MIN	10'S SEC	UNITS SEC
- FRAME COUNT (MASTER)	FRAME COUNT 100'S	FRAME COUNT 10'S + UNITS	EVENT COUNTER 0-255	DUMMY FRAME IF 1	SYNC LOCK CHECK 1 LOST 2	BAD CHECK CODE IF 1	BAD FRAME COUNT IF 1
+ EVENT TIME μS	DET IDENT 1 - 3	ENERGY 1 - 8	OVFLO COUNT 1 - 33	EMPTY ERROR IF 1	SEQ ERROR IF 1	TIME SUM ERROR IF 1	IDENT ERROR IF 1

PASS 2

- BLOCK COUNT (CHANGE ONLY)	ERRORS (OO-OKAY)
LAST EVENT μS AGO	+1 IF EMPTY +2 IF SEQ +4 IF TIME SUM +10 IF SYNC CHECK +20 IF CHECK CODE +40 IF FRAME COUNT
DET IDENT 1 - 3	ENERGY 1 - 8

PASS 3

- BLOCK COUNT (CHANGE ONLY)
EVENT COUNTER

FIG 3.7 PROCESSED TAPE FORMAT

words between every BLOCK word and a variable number of EVENT words between each FRAME word. This software was tested before launch by processing part of the tape recorded during the final test record run at B.A.C., Bristol, prior to shipping of the experiment to Australia.

The processing of the flight tape from  $T = 0$  to  $T = +400$  secs exceeded the maximum time limit available on the University Computer System, so a break was introduced at  $T = +284$ . This is just after the detectors view the horizon at the end of block number 2499 which does not have an unfinished data sequence in the last frame. This tape was used for preparing error summaries and investigating course details of the flight but much of the information was superfluous so a second pass was made to condense the data further. The format for this second pass is also shown in fig. 3.7 and consists of a time, identity, energy and brief error summary for each event, the code for a valid event being 00. Rather than record the event time from the arbitrary zero point, the time word is now simply the elapsed time in  $\mu S$  since the previous event, some coarse time calibration being included by the occasional block change number.

It was also found convenient to produce a third type of tape which contained only the Event Counter contents (2.048 mS bins) and block change numbers (fig. 3.7).

## CHAPTER 4

The calibration and expected performance of the  
experiment

	Page
4.1      Launch Slot Calculations	111
4.2      Internal, External and PHA calibrations	114
4.3      Expected Count Rates and Background Rejection Estimates	122
4.4      Performance of memory to bursts	127

## 4.1 Launch Slot Calculations

### 4.1.1

As described in chapter two, the experiment looks outwards at  $90^\circ$  to the sun vector and so it is an easy computation in spherical trigonometry to calculate the two occasions during the year at which the sun is  $90^\circ$  from Cygnus X-1. During 1976 this occurred on May 3rd and November 5th, the second date being selected as a realistic target requiring delivery of the experiment by early June at the latest. Reference to the collimator profile in fig. 2.6 shows that the effective area decreases from the maximum by 25% for each day either side of the most favourable moment. This was considered to be an unacceptable loss and so it was proposed to manufacture a set of precisely angled wedges at  $\frac{1}{2}^\circ$ ,  $1^\circ$  and  $2^\circ$  for insertion under the twin axis sun sensor to more nearly achieve normal incidence to the source. By using various combinations of these wedges the most unfavourable error possible was  $\frac{1}{4}^\circ$  which represents a loss of only 6% and this procedure was cleared by B.A.C., up to a maximum offset of  $3^\circ$ , giving a launch slot from October 31st to November 9th. The fine sensor can be electrically biased for small offsets but tilting the whole unit is not normally done since the control jets can no longer be considered to act in separate axes with the result that a coning motion is possible. A small correction must be applied to the roll angle offset which will also be subject to an increased error.

### 4.1.2

The projection of the field of view onto the celestial sphere can be seen in fig. 4.1, indicating that source confusion is not important. The 3U1953+31 source in the Uhuru catalogue is listed as having an intensity of 63 units but monitoring with the UK 5 B experiment showed it to have a much weaker mean flux of about 20 units. The table in fig. 4.1

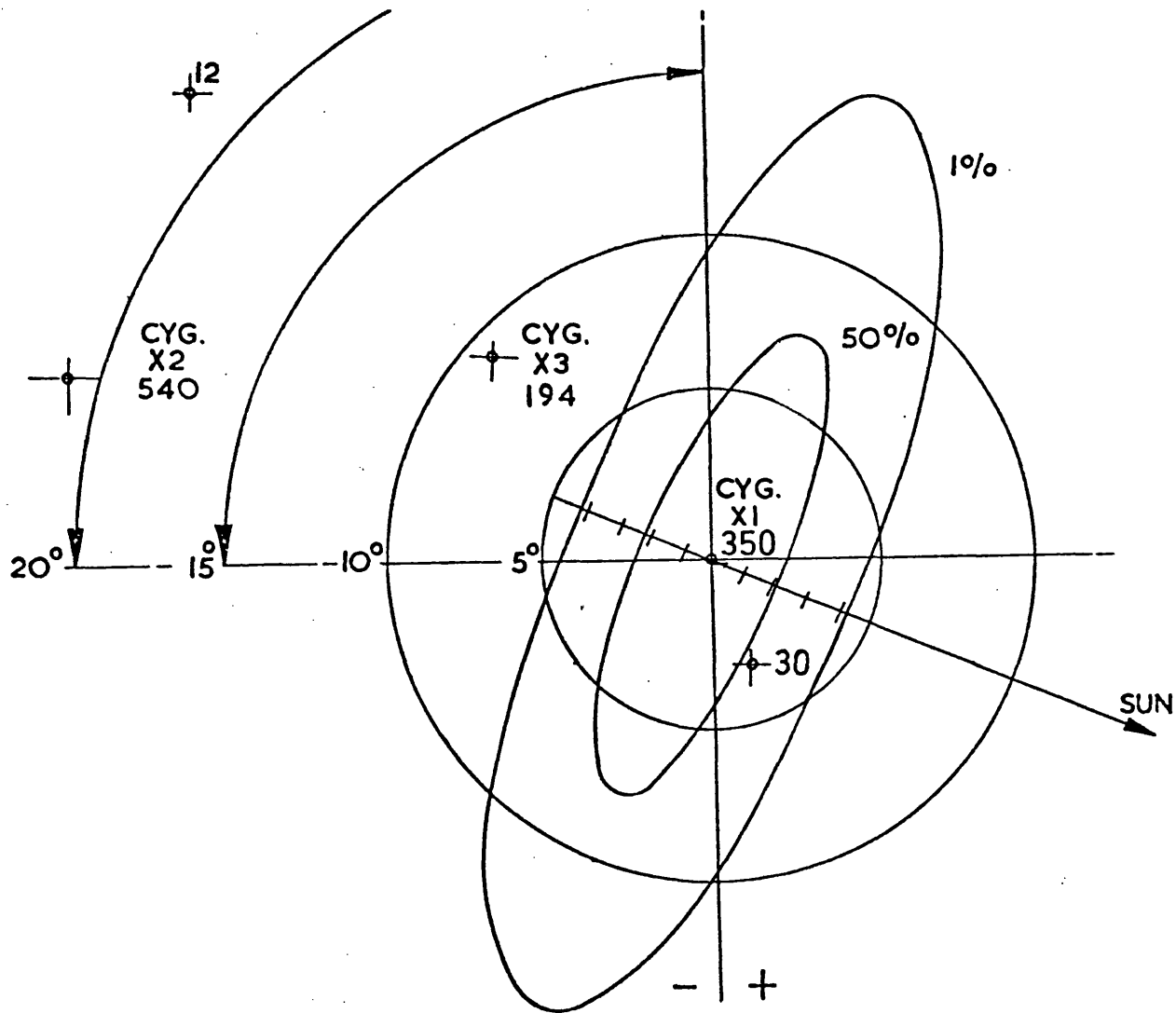
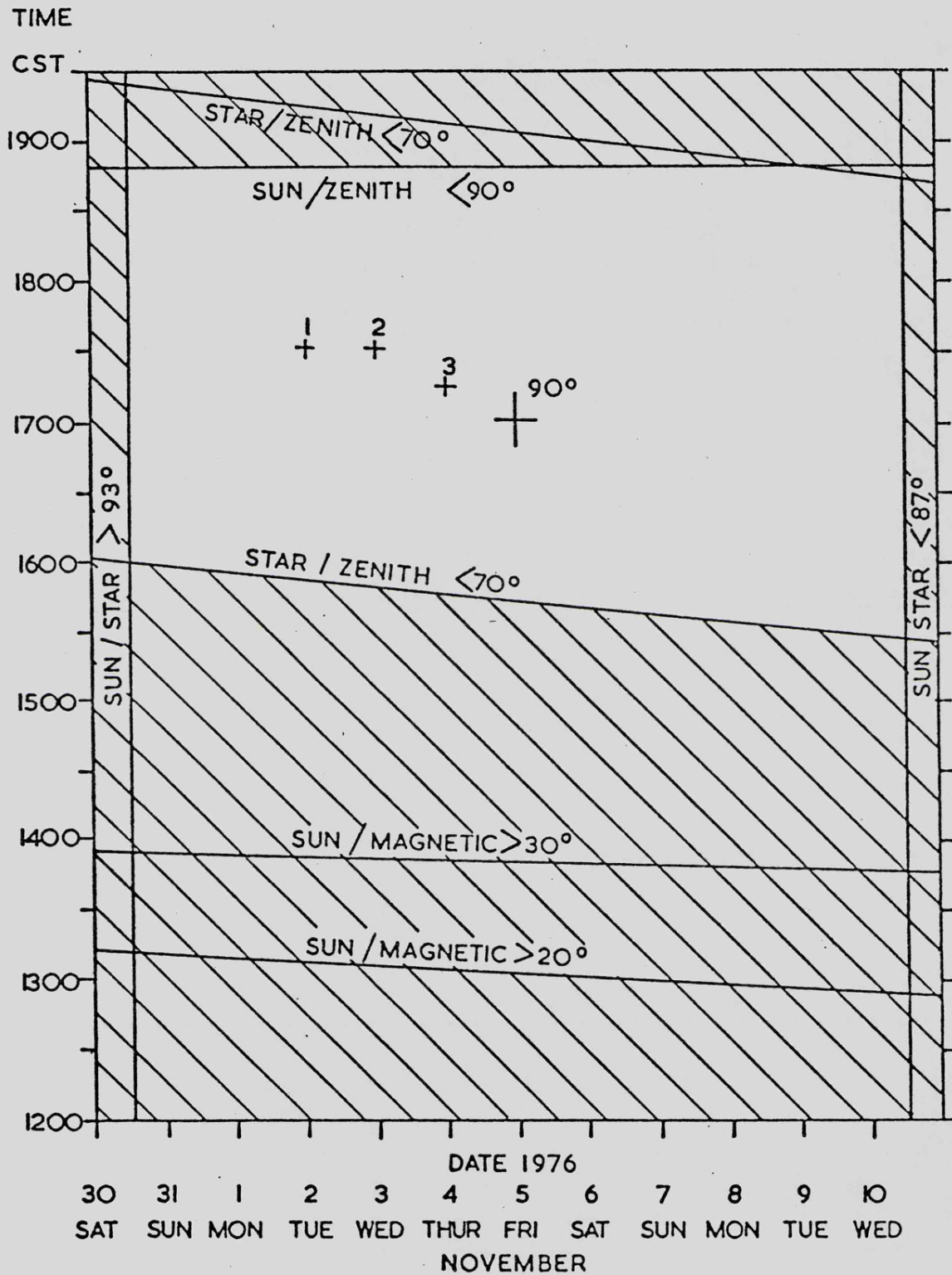


FIG. 4-1 FIELD OF VIEW

	DATE	ANGLE	BLOCKS	RESIDUAL	% AREA
	31	92.88	+ (B+C)	-0.25°	93.5
BLOCK A	1	92.29	+ C	+0.26	93.5
32'	2	91.71	+ (A+B)	+0.08	98.0
BLOCK B	3	91.12	+ B	+0.02	99.5
1° 6'	4	90.54	+ A	+0.01	99.8
BLOCK C	5	89.95		-0.05	98.7
2° 2'	6	89.37	- A	-0.10	97.5
	7	88.78	- B	-0.12	97.0
	8	88.19	- C	+0.22	94.5
	9	87.61	-(A+C)	+0.17	95.7
	10	87.02	-(B+C)	+0.15	46.2

AT 18,000 CST

FIG.4-2 LAUNCH SLOTS



ACTUAL LAUNCH TIME 17.15 CST = 7.45 UT  
18.15 LOCAL SUMMER TIME

shows for each day of the slot the offsets that must be introduced in order to bring the transmission pattern coincident with Cygnus X-1 together with the best combination of wedges and the residual error. The pointing errors of the stage 1 ACU have already been described in section 2.3.1, but for a favourable magnetic vector angle, the launch must occur in the few hours after sunrise or before sunset. In November both sun and source are only above the horizon together before sunset and so the daily slot was defined as 5 - 7 p.m. local time. The reason for this limit is that Cygnus X-1 has a declination of  $+35^{\circ}$  and so from Woomera at latitude  $-40^{\circ}$  it only executes a low arc across the northern horizon with a maximum elevation of  $24^{\circ}$ . The chart in fig. 4.2 indicates all the actual constraints as computed for an observer at ground level, the horizon being  $12^{\circ}$  lower from the mean observing altitude of 150 Km. The maximum elevation of the source produces a line of site well clear of the Earth's atmosphere and fortunately falls near the centre of the daily slots when the sun is still above the horizon.

## 4.2 Internal, External and PHA calibrations

### 4.2.1

The settings chosen for the PHA levels were based on the detector efficiency and its response to the best known spectrum for Cygnus X-1. This was investigated by modifying a spectral fitting program, described by Ricketts (1973), to work in reverse so that it produced the expected count rate for each of the eight energy channels. This program includes a model for interstellar absorption based on the cross-section of Brown and Gould (1970), and successively folds the chosen input spectrum with the following sequence of effects interstellar absorption, detector efficiency, fluorescence and resolution spreading. The resultant profile is then integrated between the chosen PHA levels and normalised to produce

the counts per channel. The principal factors in this case are discussed below, the detector efficiency and response to Cygnus being shown in fig. 4.3.

#### 4.2.2 Spectrum:-

As mentioned in section 1.3 Cygnus has been suspected of having a variable spectrum but the two flights of Rothschild et al. (1976) separated by one year found little variation. The best fit power law spectra is

$$\frac{dN}{dE} \propto e^{-1.55E}$$

with an upper limit of  $3 \times 10^{21}$  hydrogen atoms/cm<sup>2</sup> of cold interstellar material in the line of sight.

#### 4.2.3 Resolution:-

The resolution is dependent on the gas multiplication process occurring inside the detector. If E is the energy of an incident photon the number of ion pairs produced is

$$N = E/W$$

where W is the energy required to create an ion pair which for 90% Ar, 10% CH<sub>4</sub> is 26.3 eV. Since W is independent of the initial electron energy the mean number of ion pairs produced is proportional to E, and Fano (1947) has shown that the variance of N is given by

$$\left[ \frac{\sigma_N}{N} \right]^2 = \frac{F}{N}$$

where F = 0.19 for argon. Provided that the initial ionisation and multiplication processes are independent, the relative variance of the gain is  $\left[ \frac{\sigma_A}{A} \right]^2$  where A is the gas gain (section 2.4).

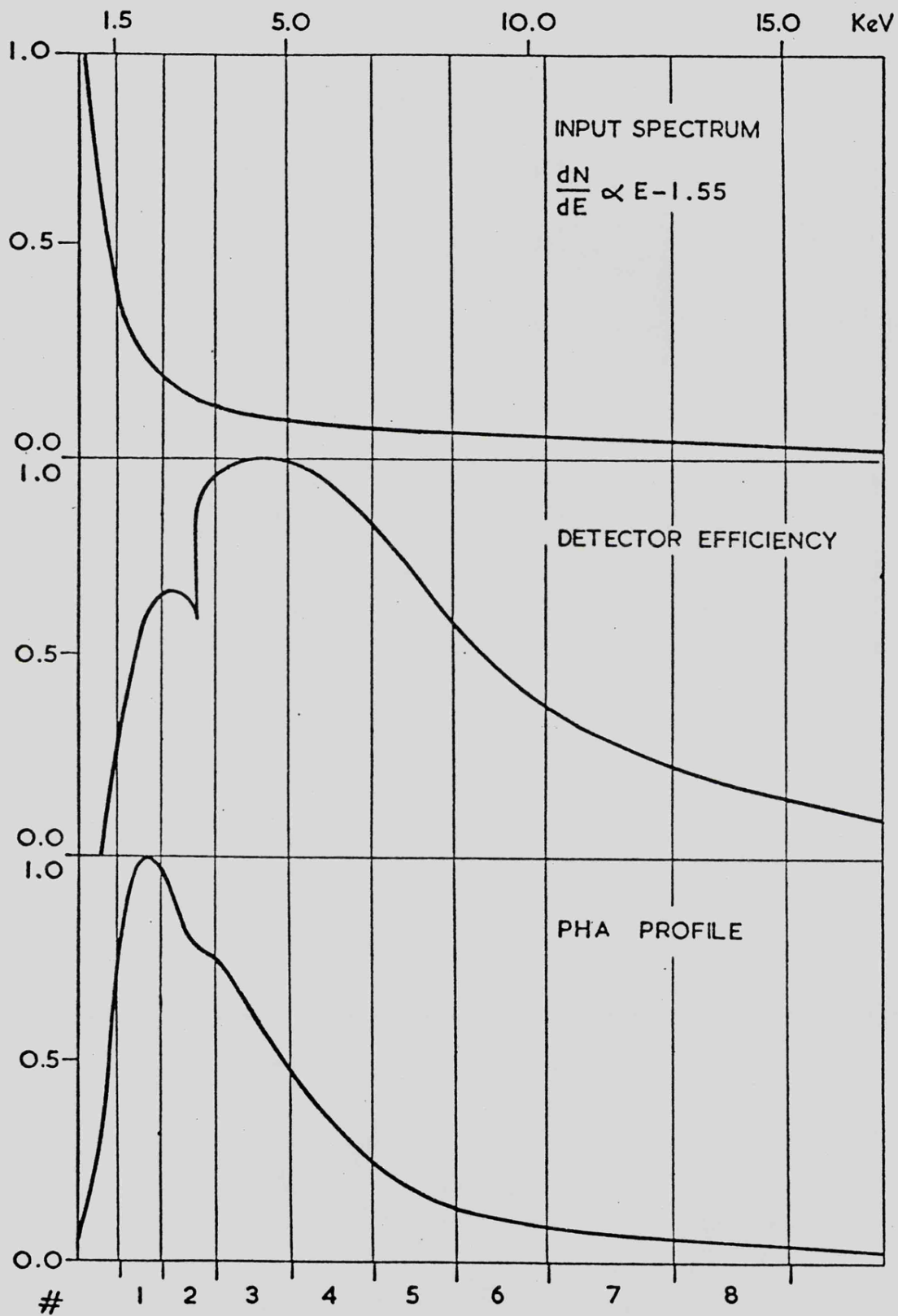


FIG.4-3 CYGNUS X-1 RESPONSE

The standard deviation of the output from the detector is

therefore

$$\frac{\sigma_P}{P} = \left[ \left[ \frac{\sigma_N}{N} \right]^2 + \frac{1}{N} \left[ \frac{\sigma_A}{A} \right]^2 \right]^{\frac{1}{2}}$$

which reduces to

$$\frac{\sigma_P}{P} = KE^{-\frac{1}{2}}$$

K having a minimum value of 0.15 (Charles and Cooke, 1968). For the 5.9 KeV radiation from the Fe<sup>55</sup> calibration sources, this corresponds to a best resolution of 14% FWHM. The actual resolution when irradiating a single anode wire was 16%, the difference being due to a combination of gas impurities, wire non-uniformity, field non-uniformity and noise effects. The array is inherently very uniform in gain and this resolution applies over about 90% of the detection area, the remainder having a gradual deterioration due to side, end and divider effects even though every effort was made to minimise them. The typical overall resolution was 18%, a very acceptable result since the energy information was of secondary importance. The overall resolution of the guard was found to be 20% FWHM.

#### 4.2.4 Detector Efficiency:-

This was computed using cross sections by MacMaster (1969) for the detector gases, mylar window and for its aluminium coating. The chemical formula for mylar is C<sub>10</sub>H<sub>8</sub>O<sub>4</sub>, the hydrogen component being ignored in this case.

#### 4.2.5

The PHA levels used to construct table 4.4 were decided upon on the following basis. The upper level was fixed at +5 volts (HI) due

OTHER SCALES			PULSE CALIBRATION				ENERGY CHANNELS		
POT	LIN	LOG KEV	V REF	# A	B	C	$\sqrt{\text{KEV}}$	#	%
LL	1.50	1.50	-0.432	0.16	0.17	0.17	1.50	1	22.5
1	3.19	2.00	+0.760	0.27	0.27	0.26	2.43	2	24.1
2	4.88	2.67	1.176	0.39	0.40	0.40	3.50	3	21.3
3	6.56	3.56	1.658	0.54	0.55	0.55	4.85	4	14.7
4	8.25	4.74	2.207	0.72	0.73	0.74	6.47	5	9.0
5	9.94	6.32	2.844	0.92	0.92	0.94	8.26	6	4.7
6	11.63	8.43	3.559	1.15	1.15	1.17	10.33	7	2.4
7	13.31	11.24	4.320	1.40	1.39	1.43	12.57	8	1.3
HI	15.00	15.00	4.999	1.67	1.66	1.72	15.00		

FIG 4.4 P.H.A. CALIBRATION

to the design of the analog board, and it was decided to set the lower level (LL) discriminator at 0.5 volts to ensure that noise or low RF pick up would not interfere with the signal channels. The guard LL was also set to 0.5 volts, the relative pre-amp gains being adjusted to trip the guard before the lowest signal channel for the same incident threshold cosmic ray event. Comparison of this dynamic range of 10 with the detector efficiency in fig. 4.3 indicates a LL at 1.5 KeV with a HI at 15 KeV and since each of the seven levels in between is independently adjustable some thought was given to the channel widths. For a typical X-ray power law spectrum, constant width channels give few counts in the upper bins and a logarithmic set-up will crowd the lower levels together. In view of this, it was decided to use a square root law, the actual calibration being performed using a precision pulse generator and accurate terminating capacitor feeding an identical pre-amp to those on the experiment. A comparison of the three different scales is shown in fig. 4.4 together with the adjusted reference voltages for the square root case and the energy values in KeV that these will correspond to when the gain is correctly set. The final column shows the relative count rate to be expected in each channel for the Cygnus spectrum expressed as a percentage of the total window rate.

For routine testing, the detector gains and resolutions can be monitored directly on a multi channel analyser but when the experiment is completely assembled and under the nose cones we only have access to the 8 channel PHA output from the test gear. The resolution and gain of the calibration sources are slightly different to those measured for an external source due to the window geometry and so it was necessary to establish a link between the two. The direct calibrations are shown in fig. 4.5 but of more relevance to gain adjustment are the normalised results tabulated in fig. 4.6. The procedure for setting up the system was as follows.

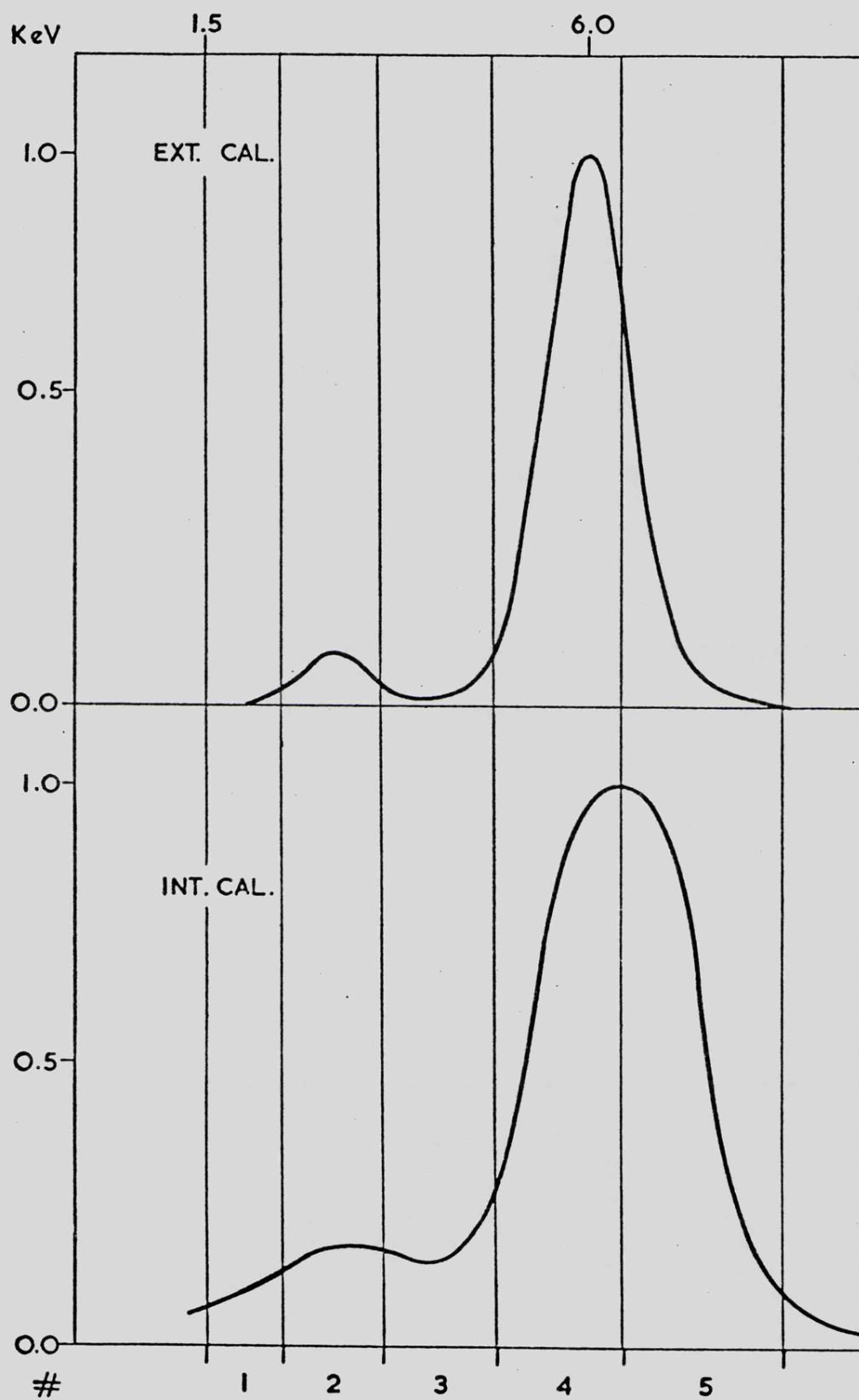


FIG. 4-5 DETECTOR A CALIBRATION Fe 55

PHA #	EXTERNAL AND INTERNAL $^{55}\text{Fe}$						RESOLUTION		BACKGROUND	
	A		B		C		A+B+C EXT	5.9 keV GAUSSIAN	A + B + C COSMIC	Co 60
	EXT	INT	EXT	INT	EXT	INT				
1	0.2	3.0	0.1	3.0	0.5	3.3	0.2	-	7.7	6.5
2	4.4	4.0	3.3	5.4	4.0	3.5	3.9	-	9.0	7.1
3	1.5	6.0	1.5	12.2	1.7	5.6	1.6	-	10.0	8.4
4	81.0	50.1	82.4	44.2	82.6	35.0	82.0	0.88	13.2	12.3
5	12.6	36.0	12.6	33.8	11.0	46.2	12.1	0.11	14.9	15.3
6	0.3	0.9	0.1	1.4	0.2	4.4	0.2	-	16.6	17.1
7	-	-	-	-	-	-	-	-	14.2	17.6
8	-	-	-	-	-	-	-	-	14.4	15.8

FIG 4.6 EXPERIMENT PRE-FLIGHT CALIBRATION

#### 4.2.6

After an extensive gassing period to remove most impurities each HT unit was set to 2 KV with the remote adjust in its central position. The pulse generator system referred to above was then used to trigger each channel in turn, the undershoot correction being set so that the base line restorer (BLR) was not retriggered since this adjustment also altered the pulse height. The pre-amp gain was then adjusted to give the 1.5 - 15 KeV range required using an external  $\text{Fe}^{55}$  source, the channel counts being compared with predictions based on the resolution, known channel boundaries and the  $\text{Fe}^{55}$  spectrum. These predictions are shown in column 9 of fig. 4.6 and can be compared with the external calcs for detectors A, B, C and the matching internal calcs. Any temperature or pressure-caused change of gain can be compensated for individually by the remote HT adjust until the internal calibration figures for that particular channel are reproduced. When this occurs we know the system is set correctly for incident radiation even though an external cal is not available. The actual count rates are determined by the source strengths and the geometry of the aperture in the detector wall, the rate being 200 c/sec for detector B and 180 c/sec for detectors A and C.

### 4.3 Expected Count Rate and Background Rejection Estimates

#### 4.3.1

Many of the parameters used in designing the experiment were based on the observations of Rothschild et al. (1974), the expected count rates being calculated simply on the relative areas of the two detectors. Fig. 4.7 shows a table of this comparison assuming that the source behaviour will be much the same in November 1976 as in October 1973 and 1974. Also shown for comparison are the early flight by Rappaport et al. (1971) and the more recent experiment by Ogawara et al. (1977). We can

	MIT	GSFC	ISAS	LEIC
DATE	1971 MAY 1	1973/74 OCT 4/3	1975 SEPT 24	1976 NOV 4
AREA cm <sup>2</sup>	500	1360	680	4000
TIME RESOLUTION $\mu$ S	1000	320/160	625/40	2
ENERGY KEV	1.5 - 10	1.5 - 30	1.5 - 25	1.5 - 15
FIELD FWHM	16 <sup>o</sup>	2 <sup>o</sup> x 8 <sup>o</sup>	-	4 <sup>o</sup> x 12 <sup>o</sup>
DURATION SEC	75	50/180	250	240 *
LOW MEAN C/SEC	500	1270	550	3800
HIGH MEAN C/SEC	750	2190	700	6560
BURST C/SEC	6000	9380	10000	28100
NO BURSTS	10 > 5/BIN BIN=1mS	13 > 12/BIN BIN=1.28mS	3 > 13/BIN BIN=1.25mS	-
REF	A	B	C	-

\* EXPECTED

A RAPPAPORT et al. 1971

B ROTHSCHILD et al. 1974/76

C OGAWARA et al. 1977

FIG 4.7 COMPARISON OF CYG X-1 HIGH TIME  
RESOLUTION EXPERIMENTS

now discuss the setting up of the various adjustable features that have previously been described.

#### 4.3.2 Energy Fraction

The performance of this circuit has been outlined in section 2.5.4 and was set up to suit variations in count rate from the low mean of 3800 c/sec to the high mean at 6560 c/sec. Based on this upper value and the profile of Cygnus X-1 in fig. 1.3 there should not be any overflow words.

CRI trip levels The maximum expected count rate from all three channels is 28100 c/sec so each unit was set up to trip at approximately 30,000 c/sec. This is way above the maximum of 9,400 c/sec expected from any one channel but in testing with purposely introduced RF noise was easily exceeded and the channel inhibited.

FIFO characteristics The performance of the memory can be examined in terms of the expected mean and burst rates and this is discussed in section 4.4.

Sender 2 dividers The D/A converters cycled at 5120 Hz and so the dividers were set according to the following table. The dead time counter registers a number of pulses, depending on the actual processing time, varying from 5 for a vetoed event to 10 for a valid one.

Channel No.	Function	÷ BY
8	A	2
9	B	2
10	C	2
11	A+B+C	8
12	Dead Time	128
17	Guard	4
20	HI	4

Table 4.1

As previously noted the signal channel and guard were operated in anti coincidence with no RTD. Mathieson and Harris (1971) have shown that up to 95% or more rejection of partical background is possible with only 5% or less reduction of Fe<sup>55</sup> at 6 KeV. This method can also reduce by a factor of 30 a simulated background from a Co<sup>60</sup> source, however, the usual circuits suffer from non-linearity and the small cross over times being measured mean that great care must be taken to ensure that very few X-ray events are rejected.

#### 4.3.3

In estimating the background there are three main constituents which we can consider in turn.

Cosmic Diffuse X-rays This contribution to the background is dependent on the field of view and effective area of the detectors. Adams and Ricketts (1973) have derived the following spectrum

$$\frac{dN}{dE} = 16E^{-1.8} \text{ photons cm}^{-2} \text{ s}^{-1} \text{ sr}^{-1} \text{ KeV}^{-1}$$

Their experiment area was 720 cm<sup>2</sup> and covered the 2 - 10 KeV range with a 6° x 23° FWHM field of view yielding 160 c/sec. Comparison with the parameters in fig. 4.7 leads to an expected flux of 330 c/sec.

The other two effects are cosmic ray primaries and electrons produced by Compton interactions of  $\gamma$ -rays with the walls and gas of the detector. Results published by Cooke (1973) based on the work of Griffiths (1971) conclude that for a smaller detector of similar cross section the non X-ray background events are 20% Compton electrons and 80% charged particles.

Cosmic Primaries Background If we consider the passage of minimum ionising protons and  $\alpha$  particles through the detector over an extended

energy range we can estimate the incident flux, however, the attitude of the experiment will alter the observed rate since the flux is not isotropic. A commonly quoted figure for the flux is

$$0.14 \text{ cm}^{-2} \text{ s}^{-1} \text{ sr}^{-1}$$

The cross section area of all three boxes is  $5500 \text{ cm}^2$  so this gives an incident flux of 2400 c/sec, most of them being detected by the guard.

#### 4.3.4 Background Rejection

The rejection efficiency of  $\gamma$ -rays can be estimated using a Cobalt 60 source that emits 1.17 and 1.13 MeV radiation but the rejection of cosmic primaries is more difficult since the spectrum at ground level is somewhat different to that during the flight. An estimate can be made however with the detector facing upwards since the flux falls off approximately as  $\text{Cos}^2 \theta$  where  $\theta$  is the offset from vertical. The observed spectra of both the background and  $\text{Co}^{60}$  are shown in fig. 4.6. A series of measurements were taken with the guard operating and disconnected to establish the rejection efficiencies shown in table 4.2, these values closely matching those of the SL 904 experiment (Ricketts, 1973). This detector also viewed a source with a lowish altitude and the transmission of veto information allowed him to note that above the atmosphere the guard efficiency had improved from 60% to 82%.

Table 4.2 Rejection Panel A

$\text{Co}^{60}$ c/sec		Background c/sec	
Guard ON	OFF	ON	OFF
450	1309	10.5	46
	65%		77%

Most of the rejected events will be simply protons passing

straight through both layers although due to detector geometry some can trigger the signal channel alone. The remainder are Compton electrons produced in the walls and not detected by the three-sided guard, the thin high transmission dividing grid being relatively unimportant. The Compton electrons that are not detected by the guard will be indistinguishable from real X-ray events if their energy falls within the PHA window. The actual background estimate is based on Ricketts' results at ground level of 55% rejection of  $\text{Co}^{60}$ , 59% of cosmic rays, and a flux of 130 c/sec over  $1300 \text{ cm}^2$ , during the flight with the nose cones still on. This leads to a rate of 550 c/sec in our detectors which because their guard rejection appears to be some 10 - 20% more efficient may reduce this to under 400 c/sec.

The total background will therefore be this rate plus the diffuse X-ray flux giving about 800 c/sec or 15% of the mean expected source intensity.

#### 4.4 Performance of memory to bursts

##### 4.4.1

The word type against count rate curves shown in fig. 2.15 are actual measured rates but these can be confirmed by predictions based on a computer program that exactly modelled the system. The effect of varying input rates on the queue length in the store can then be studied and one can then superimpose on this random, constant mean rate a sudden burst to simulate the 20 mS enhancements in which the 1 mS bursts are found (Rothschild, 1974).

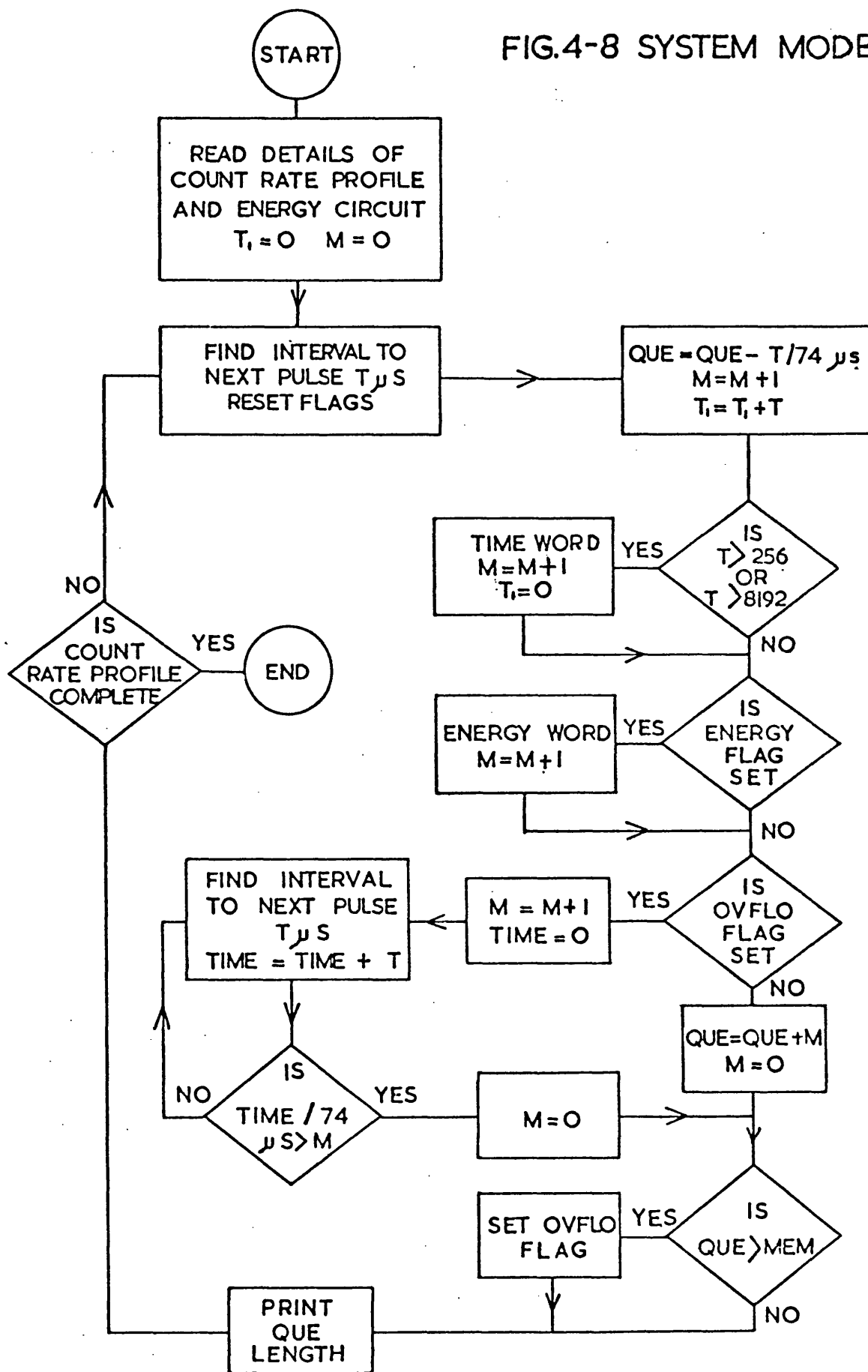
##### 4.4.2

In recent years a number of papers have been published dealing with Queueing theory that are relevant to this problem, most of them being concerned with multiplexed time sharing computer communication. The work

of Dor (1967) describes the relations between overflow probabilities and buffer length for Poisson distributed arrivals and constant output rates. This has been expanded to allow for batch Poisson arrivals of varying length by Chu (1970) but this does not really represent our case since the mean rate is not constant for Cygnus X-1 and this source also has the rapid 'delta function' bursts. A flow diagram for the program is shown in fig. 4.8 and its logical functions are identical to those shown in the electronic block diagram in fig. 2.13. Two burst profiles were tried, the first having an exponential shape with instantaneous rise time as used in the shot noise model explanation of Terrell (1972). The second profile used was a simple rectangular burst as indicated by Rothschild's data (1974). A typical set of curves for an exponential burst are shown in fig. 4.9 and these give some insight into how the store performs. Each curve represents the queue length for the mean rate indicated when a sudden input to 5 times this rate occurs with a time decay constant of 40 mS. Naturally, prior to the event the store is almost always empty but once the mean rate exceeds the extraction rate the queue will rapidly grow as happens above 13,000 c/sec. The sudden impulse causes a brief burst of words in the store which after the event decays linearly, the time taken to clear out the store taking longer for higher mean rates. The rise time is roughly proportional to the peak intensity and the effect of the energy rejection circuit is visible around the 7-9,000 c/sec. region. The system response is best treated in two parts:

4.4.3     Mean rate     The function of the energy rejection circuit is to adjust the mean word input rate to a roughly constant value for the expected variation in count rate from Cygnus X-1. The horizontal part and below of the curve in fig. 2.15 is the operating region required since this roughly allows for the variation by a factor of 2 in mean intensity

FIG.4-8 SYSTEM MODEL



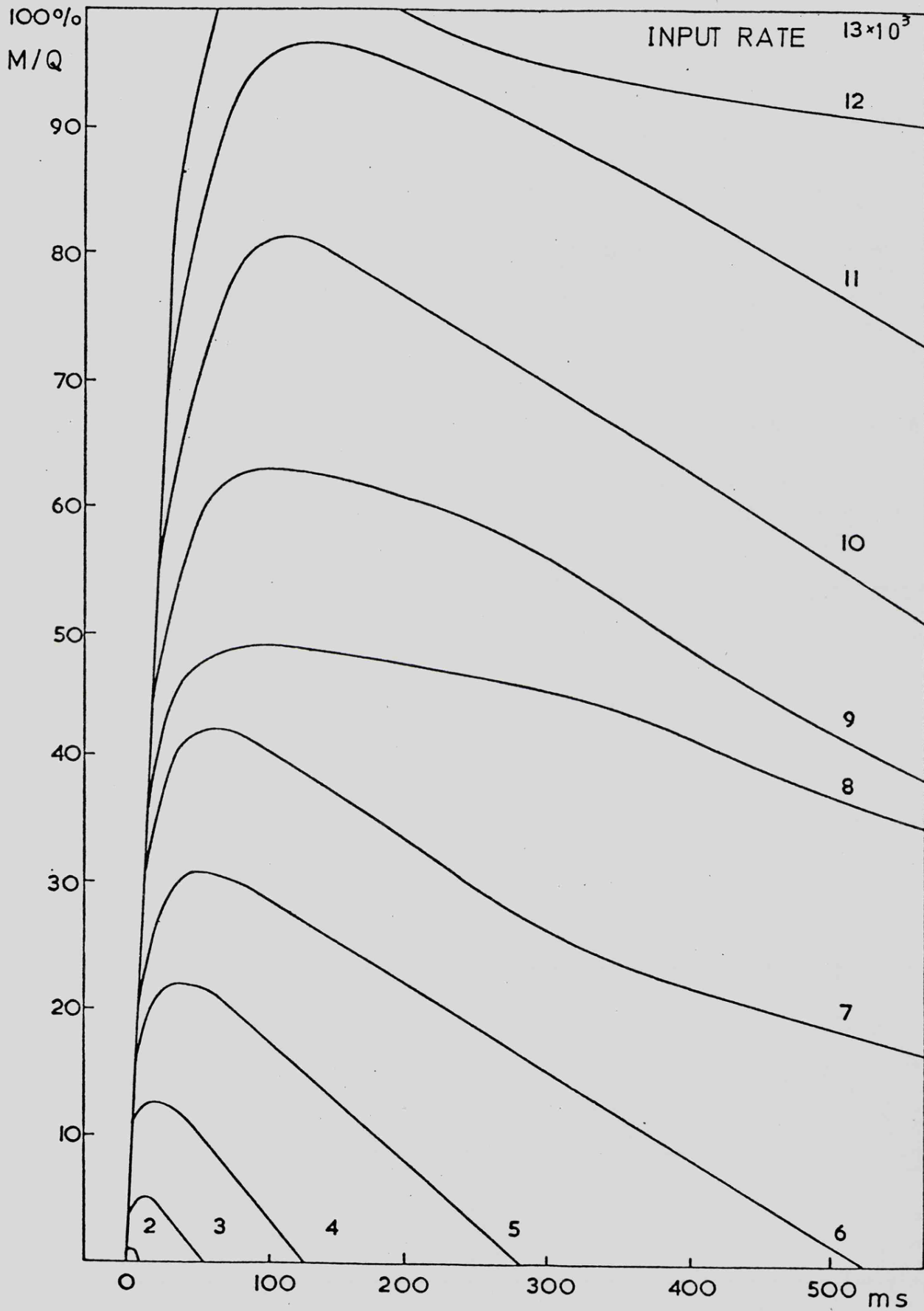


FIG. 4-9 MEMORY QUEUE LENGTH

observed by Rothschild (1974) in some 50 seconds of data. The time constant of this circuit is 0.5 sec so it should follow the course variations fairly well but will not reject an excessive fraction of energy words for a very fast millisecond burst. We can use the tables prepared by Chu (1970) to estimate the overflow probabilities for different mean detector rates and as expected these are exceedingly low until the word extraction frequency of 13,500 Hz is approached. In the steady state this corresponds to a detected EVENT rate of 12700 c/sec (fig. 2.15). Even at 99% of this rate the overflow probability is only  $10^{-9}$  since the store size is relatively large implying that only one OVERFLOW might occur in 20 hours of operation. A rapid increase to a higher mean rate may occur before the energy rejection takes much effect but the store will not be filled unless this new high mean level exceeds 6,000 c/sec.

4.4.4 Fast bursts and enhancements The rejection circuit will not respond at all to these events and a rapid growth in the queue size can be expected. Provided OVERFLOW does not occur we can write the following general expression for the number of words created by an enhancement.

$$1) \quad Q_L = N_O + N_O E_F + T - W$$

where  $Q_L$  = queue length increase

$N_O$  = number of events/mS

$E_F$  = energy fraction allowed

$W$  = words extracted from PCM frame

$T$  = number of time words

$N_T$  = duration of enhancement in mS

considering each term in equation 1 in turn we have:

#### Value of T

The value of T can be estimated using the Poisson distribution for the probability of getting no EVENTS in  $256 \mu S$  if  $N_O$  EVENTS occur in

time  $N_T$

$$P(r;\mu) = e^{-\mu} \mu^r / r!$$

where  $r = 0$  and  $\mu = N_O / 4NT$

2) We can however write  $P = N_O / N_T$

where  $P =$  burst mean rate in counts/mS

3)  $\therefore T = N_O e^{-P/4}$

We must allow also for the minimum rate of TIME update words at 122 Hz and can formulate the following approximate expression

4) IF  $Pe^{-P/4} < 0.122$ , THEN  $T = N_O / 8.2 P$

Value of W

Words are extracted from the store every  $74 \mu S$

5) 
$$W = \frac{N_T}{0.074} = \frac{N_O}{0.074 P}$$

Energy fraction  $E_F$

The energy fraction follows the profile shown in fig. 2.15 and appendix D, varying between 1 and 1/64, the lower limit being due to the nature of the integrated circuits used. For fast bursts we have already said that  $E_F$  is effectively constant but with a built in time constant of 500 mS any variations of this length or longer will need correction.

There is a limit to the size of  $Q_L$  at 1536 which is simply the number of words in the store. If we combine equations 1 - 5 we can form the following inequality for the queue length.

6) 
$$1536 \gg PN_T \left[ 1 + E_F + (e^{-P/4} \text{ or } \frac{1}{8.2P}) - \frac{1}{0.074P} \right]$$

There are two points to notice in this equation. Firstly, if the term in square brackets is negative the queue will normally be empty and secondly, since we are dealing with increases on a mean rate,  $E_F$  will decrease with time. We can now take any mean rate  $E_F$  and superimpose a

step function to mean intensity  $P$  and find the value of  $N_T$  at which the store will overflow. This will however be an underestimate since the value of  $E_F$  decreases. The true situation can be approximated by forming a summation of the equation increasing  $N_T$  in small steps and altering the value of  $E_F$  each time until the inequality is no longer true.

$$7) \quad 1536 \geq \sum_{m=1}^M P \left[ 1 + (E_F)_m + e^{-P/4} - \frac{1}{0.074P} \right]$$

$$\text{where } (E_F)_m = E_F + \left[ (E_F)_P - E_F \right] \left[ 1 - e^{-m/t} \right]$$

$E_F$  = energy fraction at mean initial density

$(E_F)_P$  = energy fraction at mean peak intensity

$m$  = time in milliseconds

$t$  = time constant of circuit = 500 mS

$M$  = maximum burst length in mS

Equation 7 was used to construct fig. 4.10 which shows contours of equal burst length that just reach the overflow condition. The initial intensity ( $E_F$ ) is plotted along the X axis and the increase in intensity ( $P-E_F$ ) along the Y axis, the graph dividing essentially into three regions.

I) This is the normal operating zone where the store is almost always empty with most source variations being below a maximum level of just over 6,000 c/sec.

II) Points in this shaded zone would in fact reach the overflow condition in a few seconds but this is avoided because the low intensity allows sufficient time for the energy fraction to be reduced. This zone would contain any large enhancements and really forms an extension of zone (I) since the overflow condition cannot be reached.

III) This last zone is where overflow can rapidly occur, the lower right hand side almost merging into regions I and II. The millisecond

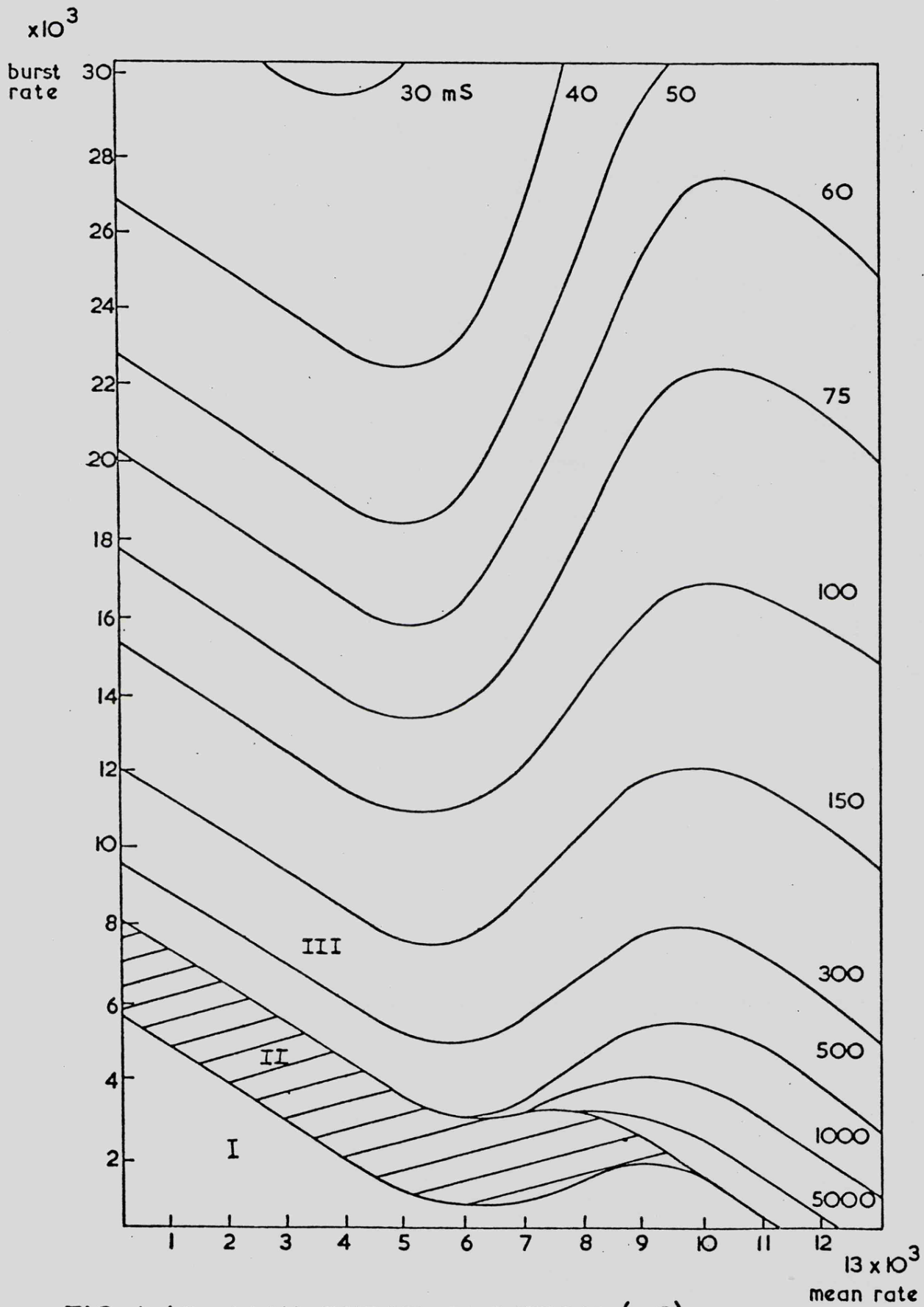


FIG.4-10 MAX BURST DURATION (mS)

bursts with an expected peak instantaneous rate of up to 28,000 c/sec will fall in this zone but due to their short duration should not reach the overflow mode.

CHAPTER 5

The flight of SL-1306 and an analysis of the non Cygnus X-1  
data

	Page
5.1 Summary of Flight and Source State	137
5.2 Attitude Solution and Scan Path	143
5.3 General Quality of Flight Data	149
5.4 Sensitivity of Scanning Observations and the Search for Other Sources	154

## 5.1 Summary of Flight and Source State

### 5.1.1

The integration and testing was satisfactorily completed and the round assembled in the launcher on 1st November, 1976. The time of launch chosen was 17.30 on 2nd November, this time corresponding to the mid-point of that day's slot as indicated by fig. 4.2. The Sun source distance was  $91.7^\circ$  and so wedges A and B had been placed beneath the fine eye prior to the round leaving the test shop. The weather had deteriorated rapidly, however, to produce complete cloud cover and very high winds that easily exceeded the safety margins for a Skylark. At -4 hr. the trial was discontinued with the intention to try again the following day. To this end part of the morning of 3rd November was spent on the novel procedure of removing the nose semi cones with the round in the launcher which was still swaying violently in the strong winds. With wedge B in place the trial was continued until -2 hours and was reluctantly withdrawn again due to the high winds. The following day with the A wedge in place the trial was still in doubt due to the cloud cover, the problem here being due to a possible reflection of the Sun off the top of the clouds. An approaching rain storm caused the launch time to be moved forwards 15 minutes and the round was successfully fired at 17.45 UT (fig. 5.1).

### 5.1.2

The general state of the source around the time of launch can be seen in fig. 5.2. This data was obtained by the All Sky Monitor (ASM) on Ariel 5 and was kindly telexed to Woomera by the Goddard Space Flight Centre team led by S. Holt, the data from October 29th onwards arriving after the firing. Each data point represents the summation of 3-7 orbits of observation in the 3-6 KeV energy range, the Crab Nebula

FIG. 5.1

THE LAUNCH OF SL-1306 FROM WOOMERA,  
AUSTRALIA, 7.45 UT 4th NOVEMBER, 1976



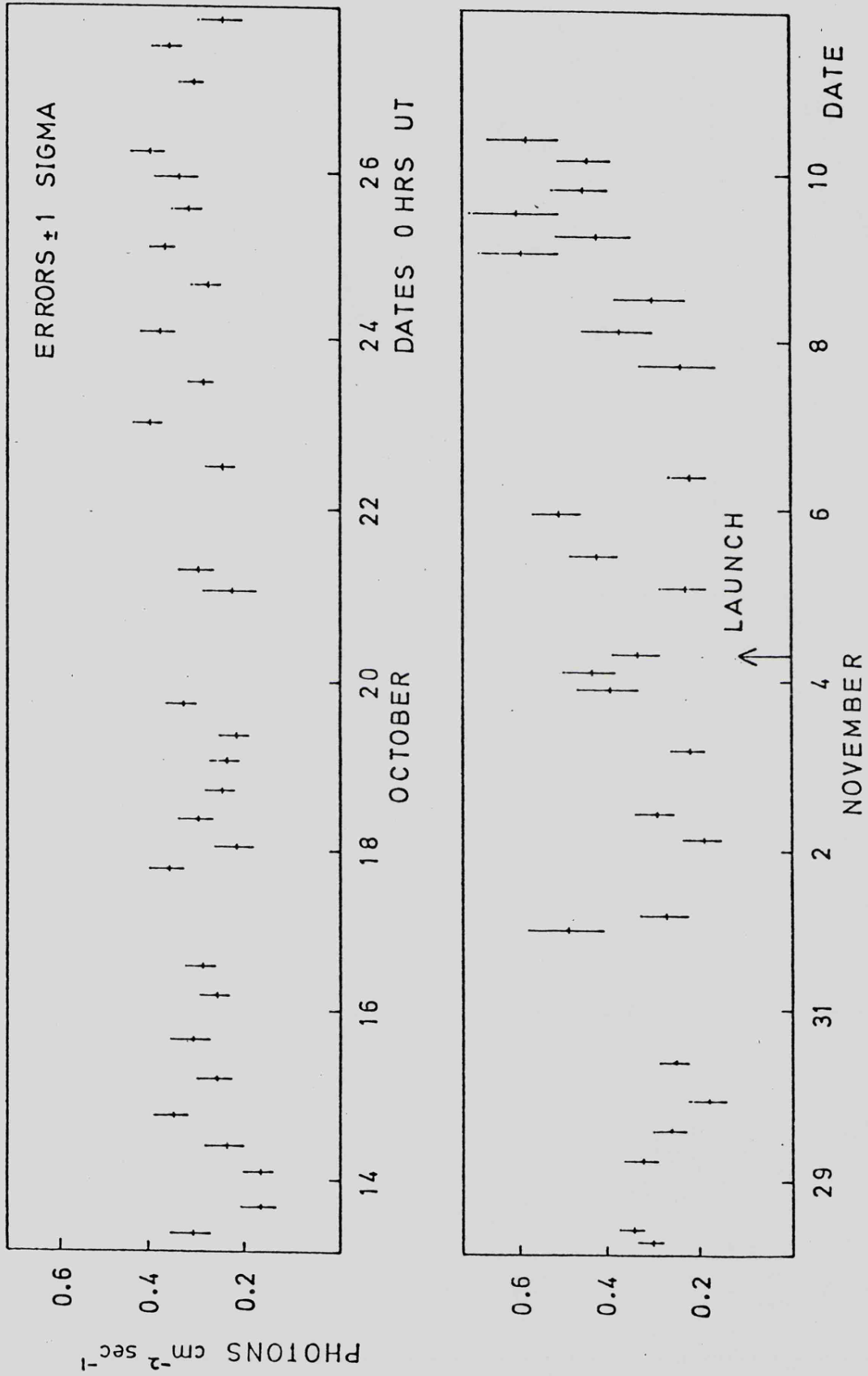


FIG 5.2 A.S.M. DATA COVERING LAUNCH PERIOD ( 3-6 KeV )

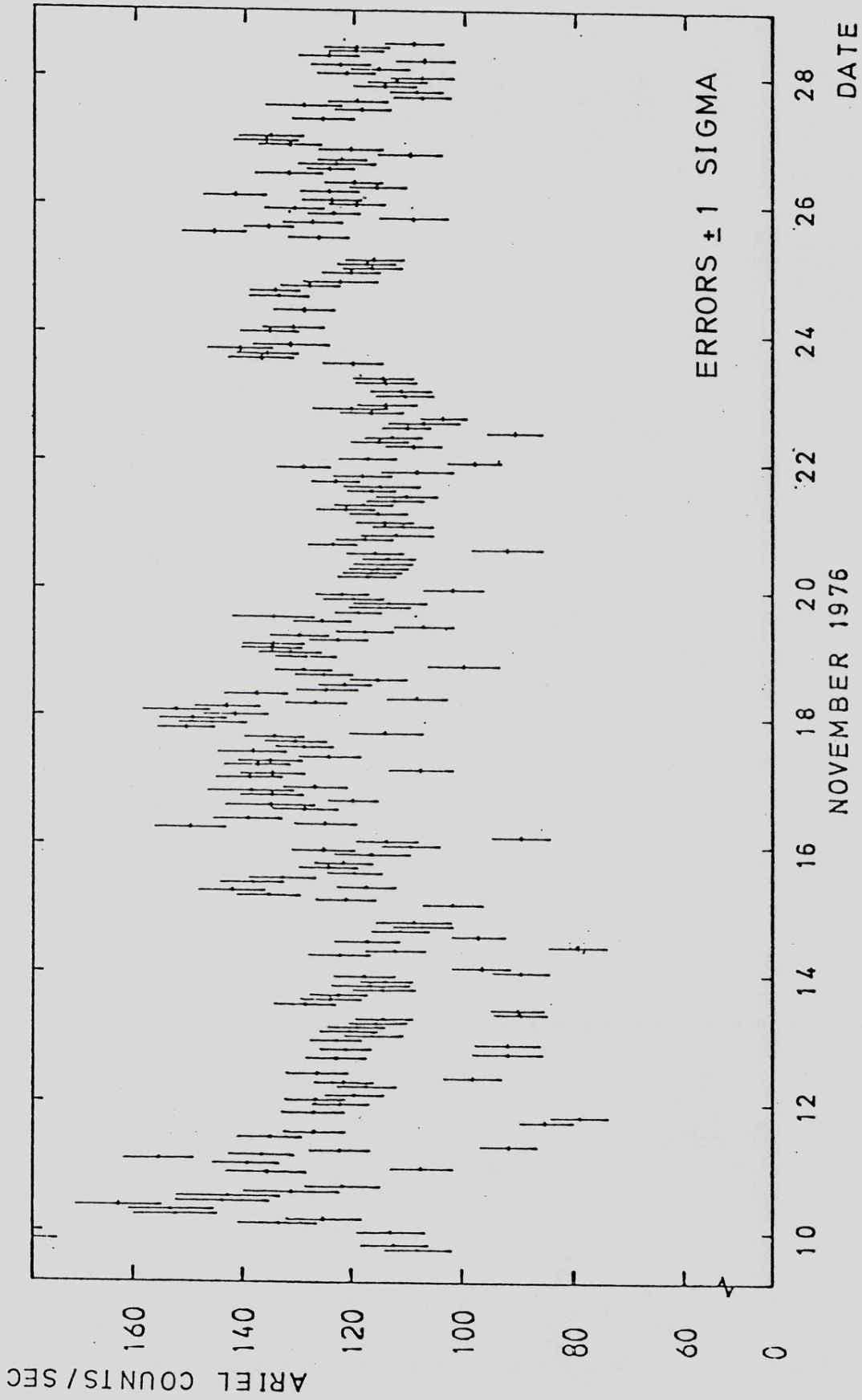


FIG 5.3 CYG X-1 AFTER LAUNCH FROM S.S.I. ON ARIEL 5 (2-18 KeV)

registering 1.1 units on the same intensity scale. The points from October 20th onwards are subject to large systematic errors since the source is then at the edge of the experiment field of view. At this time, however, the sky survey instrument (SSI) on Ariel 5 can monitor the source and fig. 5.3 shows the following 20 days, each data point corresponding to one orbit's integration which is approximately 90 minutes. Since one Ariel count is equivalent to three Uhuru counts the source appears to be more constant at around 350 Uhuru units than the preceding ASM data suggests. The SAS-3 spacecraft also observed Cygnus X-1 from 10-15th October (Canizares and Oda, 1977) and these higher time resolution results are discussed more fully in a later section.

### 5.1.3

A summary of the flight is given in fig. 5.4 and it was apparent from the real time display on the test gear that something had gone seriously wrong since the indicated count rate of 700/sec. was consistent with background only. The panels deployed successfully and all three detectors functioned correctly until re-entry caused the windows to fail. Subsequent analysis of the multiplexer record also showed that all the experiment monitors had the correct values. The outer panels became detached during re-entry as expected, the metal round the hinges having sheared due to the large aerodynamic forces. These two panels survived the free fall descent remarkably well and the rest of the payload was also in excellent condition, the parachute having deployed successfully.

The ACU performance data revealed the failure to be the gas jet on the +Z round axis which fired in an erratic fashion until +110 seconds when it failed completely. This was fortunately sufficient to

TIME (sec)	EVENT
0	Launch
57	HT on
75	Despin
77	Nose cone jettison
79	20" Bay jettison
80	CAL on
83	ACU gas on
91	coarse/fine change over
94	lateral acquire roughly
98	roll acquire exact
98	first camera frame (15 second intervals)
101	Deploy
108	roll acquire recovered
115	CAL off
130	coarse/fine drop out
156	closest approach to Vega
225	Apogee (190 Km)
274	detectors below horizon
343	detectors above horizon
353	last camera frame (no. 18)
358	CAL on
372	Pneumatics bay eject
373	detectors below horizon
377	CAL off
403	loss of detector gas
555	Parachute deploy
675	Impact (130 Km down range)

FIG 5.4 FLIGHT SUMMARY

bring the Sun within the  $10^{\circ}$  fine eye field of view enabling the deploy to occur. The quick look pen records revealed that Cygnus X-1 had briefly been observed before drifting out of the field of view and that no other individual bright sources were seen. Upon inspection after recovery the valve actuator mechanism was found to be jammed but was easily freed by hand and then continued to work perfectly. The circumstances surrounding the failure of this component have been extensively investigated but at the time of writing no satisfactory explanation has emerged.

The camera film was recovered the following morning and unfortunately did not provide much information due to fogging caused by reflected sunlight from the lens cone, although it has been possible to reconstruct accurately at least the first half of the flight. The remainder of the flight path has been reconstructed from the ACU magnetometer records, the attitude solution being presented in the next section.

The flight data presented in fig. 5.5 can be considered in four parts, namely:

- A) Cygnus X-1 data +101 to +120.
- B) Scan to horizon at +274.
- C) Scan below horizon to +343.
- D) Somewhat uncertain scan to +372.

Part A forms the contents of chapter 6 and the other three parts are discussed in detail in the remainder of this chapter.

## 5.2 Attitude Solution and Scan Path

### 5.2.1

The robot camera flown was powered by a clockwork mechanism

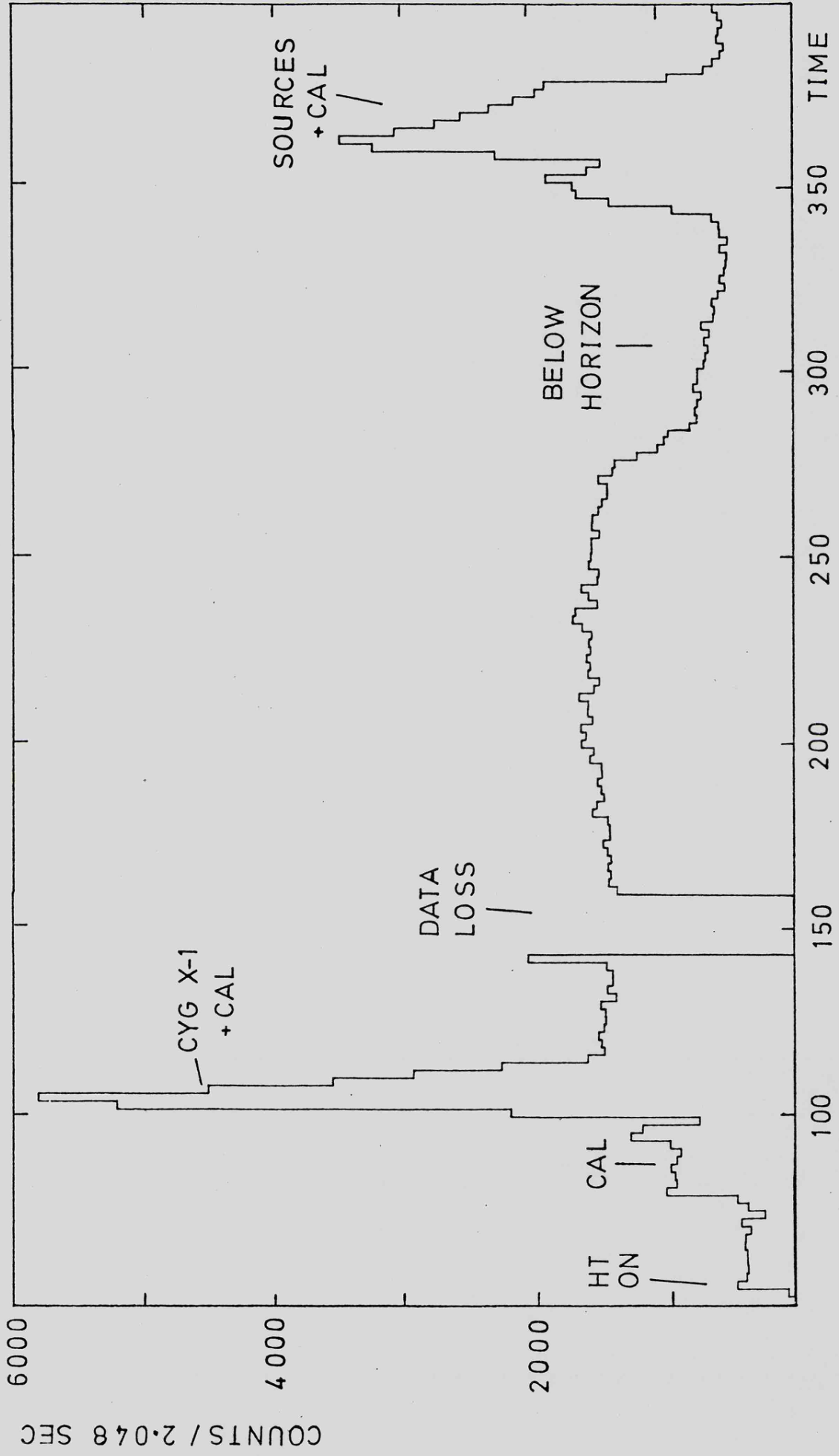
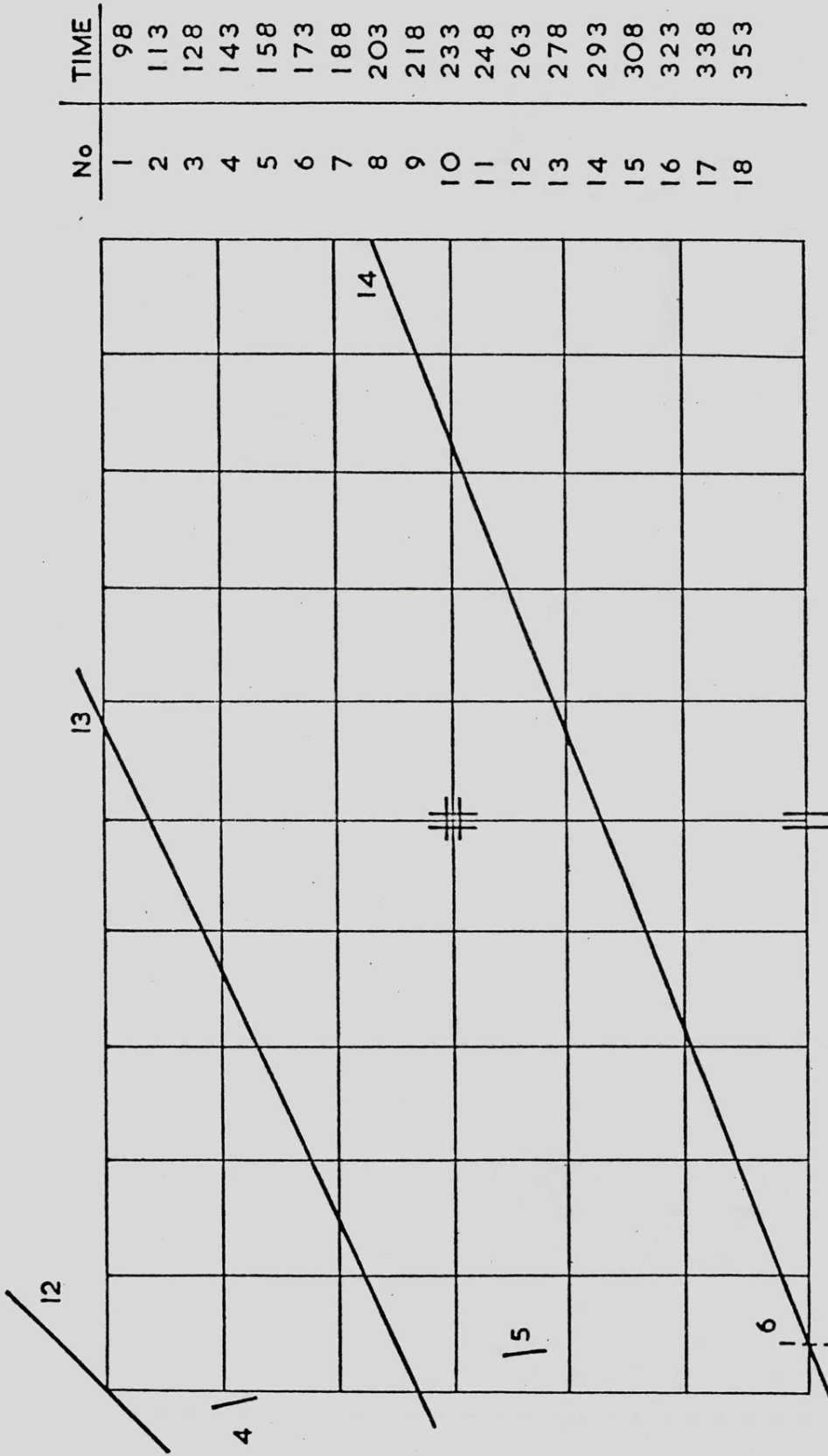


FIG 5.5 SL-1306 FLIGHT DATA

and the lens with a focal length of 86 mm produced a field of view of  $26^{\circ} \times 17^{\circ}$  on a standard 35 mm frame. A glass graticule at the focal plane had been engraved with a regular grid pattern to an accuracy of 10 microns, the side of the squares representing an angular distance of  $2^{\circ} 21'$ . This grid formed a reference frame from which to measure star images to determine the final pointing offset of the payload, the camera taking exposures of 2 second duration spaced 15 seconds apart from about +98 sec after launch. At the base of the lens cone 4 small lamps of variable intensity shone obliquely onto the front surface of the lens, to illuminate the graticule and overcome the "inertia" of the film to assist in the formation of faint star images. The intensity of the lamps was measured by means of a photoelectric cell placed over the camera lens cone and several test runs were carried out on selected star fields to optimise their effect. The camera alignment was checked by use of autocollimation techniques with a distant point light source, the round being placed on an air bearing for convenience.

### 5.2.2

The actual motion of the rocket is not trivial to analyse since the data available is somewhat limited as shown by fig. 5.6. Once the round no longer pointed at the Sun, reflections off the lens cone caused the film to become increasingly fogged as the camera axis drifted nearer the Sun (fig. 5.9). One star, however, is just visible on three frames enabling the drift rate to be calculated at  $0.52^{\circ}/\text{sec}$  which agrees with the ACU rate monitors. Camera frames 13 and 14 also show the Earth's horizon which confirms this drift rate as being constant up to +293 seconds. By considering the geometry of the failure as shown in fig. 5.7, we can plot the scan path by working back from the horizon after allowing for the  $12^{\circ}$  dip caused by the 160 Km altitude of



No	TIME
1	98
2	113
3	128
4	143
5	158
6	173
7	188
8	203
9	218
10	233
11	248
12	263
13	278
14	293
15	308
16	323
17	338
18	353

1 SQ = 2° 21'

FIG. 5-6 CAMERA DATA

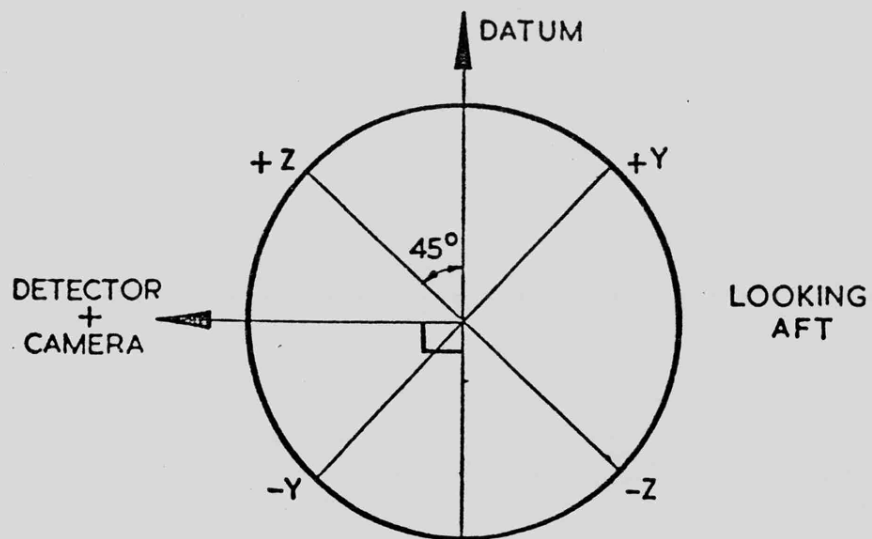
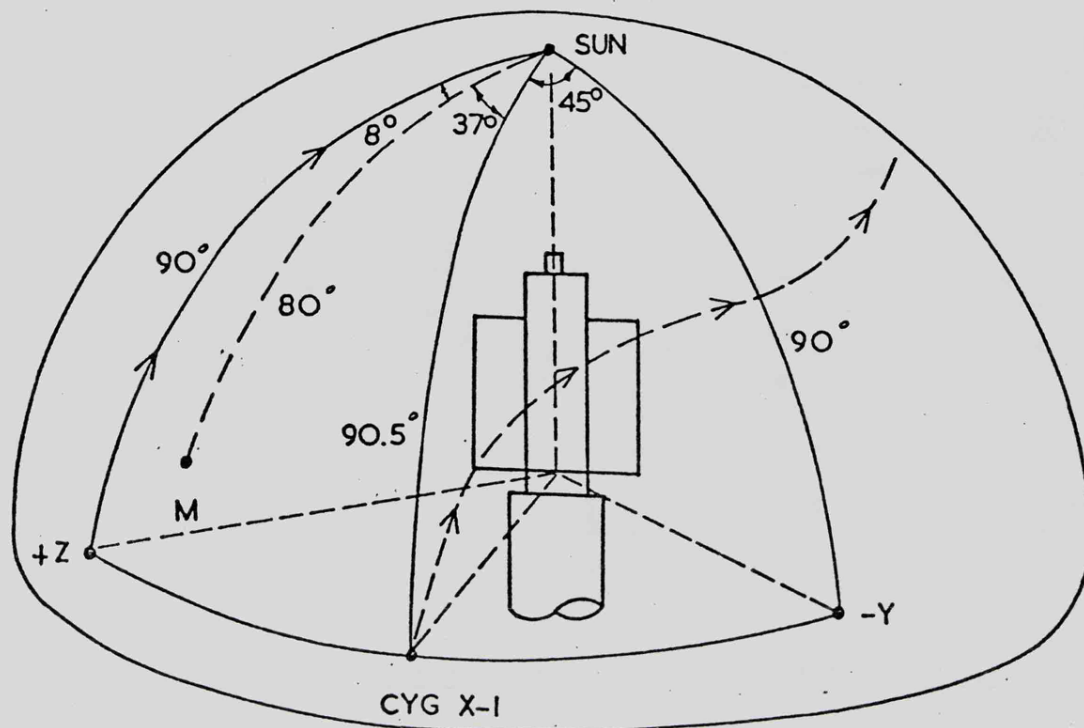


FIG. 5-7 GEOMETRY OF JET FAILURE

the experiment. This places the track near Vega and confirms this as the star seen by the camera since the measured minimum offset of  $11.08^\circ$  is correct. It is not surprising that other stars are not seen since the 2 second exposure produces streaks  $0.9^\circ$  long only allowing Vega at magnitude  $-0.6$  to show up, other nearby bright stars being typically 4 to 5 times fainter.

Considering the X-ray data, Cygnus disappears across half the narrow axis of the collimator ( $4^\circ$  FWHM) in 11 seconds corresponding to a drift rate of  $0.36^\circ/\text{second}$  roughly agreeing with the time of 29 seconds taken to reach the coarse/fine change over point at a distance of  $10^\circ$ . The ACU record shows that at this point the drift rate approximately doubles presumably due to the sudden firing of the jets since the coarse eye and fine eye null positions will not be exactly coincident. The precise motion during this interval cannot be confirmed from camera data but up to the change over point the roll angle will be maintained and the lateral axis not containing the failed jet will also be controlled. When the fine eye drops out the payload continues with its residual drift under the control of the coarse eyes and rate meters, the good axis still being maintained although small errors in roll of  $1 - 2^\circ$  are apparent.

A rough solution for this part of the flight is for the detectors to follow an arc radius  $45^\circ$  about the  $-Y$  axis at RA  $270^\circ$  DEC  $+70^\circ$  until the Z axis points at the Sun at about +295 seconds or just after the camera points below the Earth's horizon. At this point the round becomes unstable and control is lost in the Z axis causing the payload to revolve about this axis. From the ACU record this rotation increased to  $5^\circ/\text{sec}$  at +345 seconds corresponding roughly to the time when the detectors emerged from below the horizon. This rate then slows to zero by +360 when control is regained with the Sun once more

in the X-Z plane, the detector path during this time being an arc of radius slightly greater than  $45^\circ$  since the Z axis is itself rotating about the Sun.

### 5.2.3

The attitude solution for the flight has also been determined by B.A.C. based on the 3 magnetometer and vehicle angular rate monitors. These figures have been estimated to be accurate to within  $2^\circ$  and certainly agree with the camera data for the early part of the flight giving some confidence in their use for the last 40 seconds of observation. The attitude solution is tabulated in fig. 5.8 and has been used together with the camera data to produce the scan path shown in fig. 5.9. The camera time marks from frame 14 onwards have been taken from the attitude listing and are consistent with the fact that frame 17 at +338 sec was below the horizon and that frame 18 at +353 sec was above the horizon.

## 5.3 General Quality of Flight Data

### 5.3.1

The general performance of the experiment is best demonstrated in the following table:

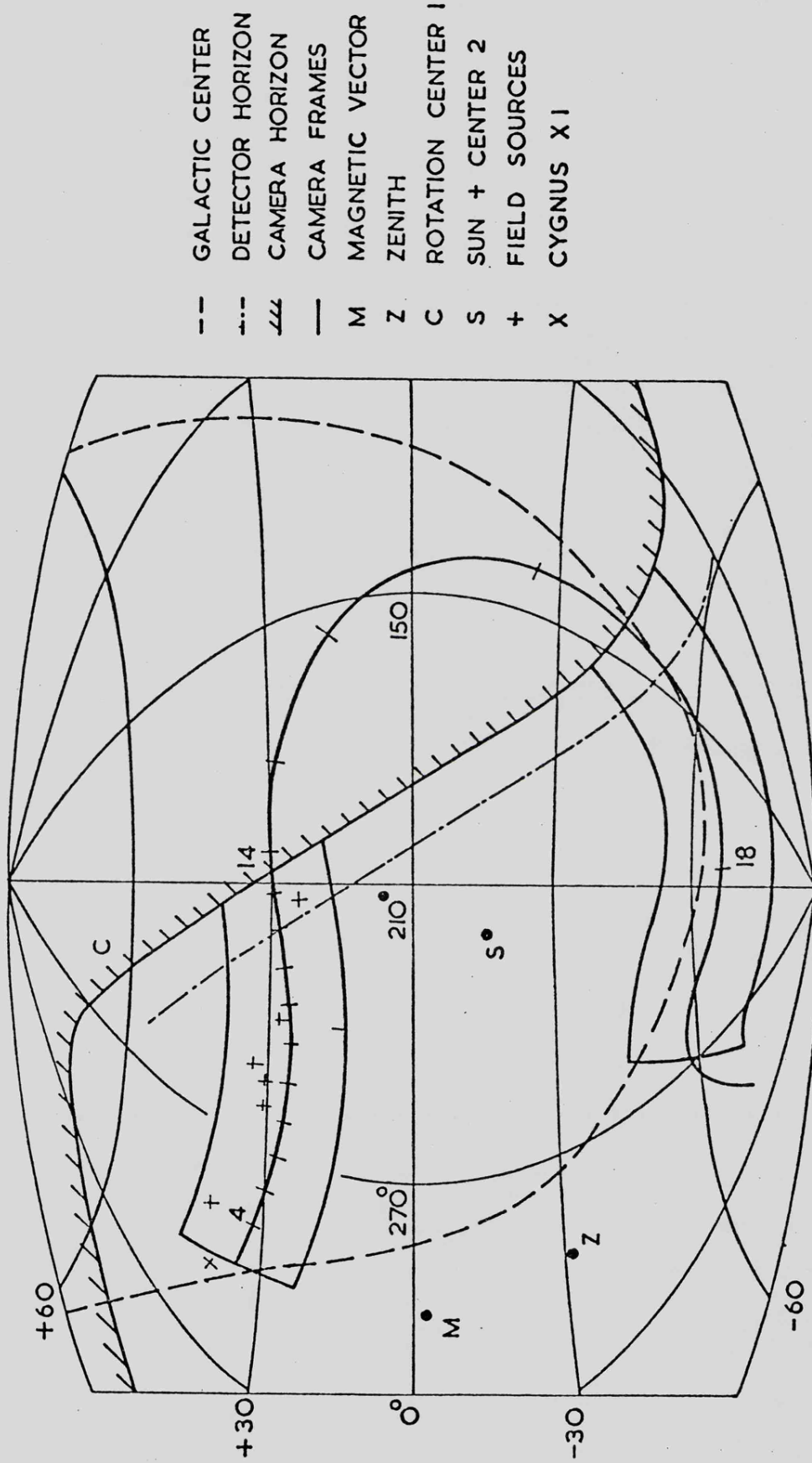
Type of signal	Count rate per second
Cosmic background	400
Diffuse background	350
Guard rate	2240
Calibration rate	550
Peak during Cyg X-1	3000
Mean rate for Cyg X-1	1700

This table shows that at best only 55% of counts are actually

Camera Frame No.	T+ Time (sec)	DET direction	
		RA hrs	DEC °
1	98.0	19.8	+ 35.1
	113.0	19.5	33.2
	128.0	19.4	32.9
	143.0	19.1	31.5
	158.0	18.7	31.0
	173.0	18.3	30.1
	188.0	17.7	28.0
	203.0	17.1	28.0
	218.0	16.6	28.7
	233.0	16.0	27.9
	248.0	15.6	29.1
	263.0	15.1	29.1
	278.0	14.5	30.1
14	293.0	13.8	31.0
15	308.0	12.8	30.0
16	323.0	10.5	17.2
	330.5	9.5	0.0
17	338.0	8.9	-28.6
	345.5	9.7	-59.8
18	353.0	13.8	-67.0
	360.5	15.5	-61.0
	368.0	16.1	-57.4
	375.5	18.9	-69.1

FIG 5.8 MAGNETOMETER ATTITUDE SOLUTION

FIG. 5-9 DETECTOR SCAN PATH



due to Cygnus X-1, this fraction decreasing to zero in roughly 10 seconds. This compares poorly with the 85% or greater expected from the original design. The guard efficiency is about 82% demonstrating an improvement over the 70% measured in the laboratory at ground level. The dead time was exceedingly small for such a low count rate and the HI rate indicates that 240 counts/sec were over the top of the PHA range at 13 KeV. These will be from both Cygnus X-1, the diffuse background and non vetoed cosmic primary events, the total representing some 14% of the actual Cygnus X-1 count rate.

### 5.3.2

The PHA calibration was obtained by background subtraction to produce the table below which indicates the deduced channel boundaries.

Counts/sec A+B+C		Channel Boundary KeV
1st CAL	2nd CAL	
		LL 1.3
39.6	31.1	2.11
45.6	64.1	3.04
56.0	87.0	4.21
126.9	129.7	5.62
261.6	264.8	7.18
114.2	112.7	8.97
3.0	19.0	10.92
7.7	24.6	HI 13.03

It is apparent that the detector gain remained very constant throughout the flight but the range itself falls somewhat lower than expected from the final launcher calibration. As previously mentioned in section 4.2.5 it had been intended to cover the range from 1.5 - 15 KeV.

## 5.3.3

It is apparent from the data in fig. 5.10 that the noise clearly visible to the left of the figure may not have entirely disappeared since some of the bins exceed 3 sigma variations from the mean. The cause of this noise is visible on a video monitor of the analog data tape and it is not surprising that the digitised tape is also corrupted. The noise is present throughout the record but gradually increases, being three times worse by the end of the flight. Visually the noise has a frequency of approximately 4 times the data rate and has a variable amplitude. Appleton Laboratory had considerable difficulty in digitising the analog tape due to the SYNC pattern itself being corrupted but this was finally accomplished by allowing the SYNC detection circuit in their PCM decomutator to search continuously. This allows the enormous noise spikes at +130 and +142 to occur since no dummy frames are inserted when SYNC is badly lost (Appendix F). It was not possible to filter out all this noise with the result that the digitised tape contains sequences of 1's of random length which also occur at random times giving a word error rate of approximately  $10^{-3}$  during the Cygnus observation. This situation is far from hopeless since visual inspection of part of the bulk data confirmed the above parameters allowing almost total correction by a combination of programming and manual checking, the key to this being the rigid structure of the PCM frame construction (fig. 2.14). The check code identifies faulty frames but cannot be used for correction since more than one bit is in error, and the check code itself may be corrupted. Examination of the word types (fig. 2.14) shows that strings of 1's will be interpreted as EVENT words occurring at regular intervals of  $256 \mu\text{s}$ . Since the count rate was so low, however, virtually every EVENT word should be accompanied by an ENERGY word which will clearly not be the

case for data strings allowing rejection of these events. The leading or trailing edges of the noise bursts occur at random within the words and these odd ambiguities can be picked up as sequence errors and empty errors in the software routines. Some data may be inevitably lost beneath the noise string but it is possible to check for TIME word discontinuities across the gap. Reprocessing the tape in this way to create the master (Pass 1 in Fig. 3.7) removes most invalid events and a check on the original error rate can be made by noting frame count discontinuities and obviously incorrect event counter contents.

Only the Cygnus data has been checked by hand to see that none of the potential millisecond bursts described in the next chapter can be explained in terms of remaining anomalies. Of the 120 odd false events on the first master tape during the Cygnus observation only 3 discrepancies remain.

The original noise appears to have been introduced in the receiver-recorder loop but at the time of writing no satisfactory explanation has been received. It has not been suggested that the telemetry signal received was exceptionally weak, indeed the 2.5 watt power should produce a 20 db signal to noise for the maximum range involved. The break present at +150 sec is present on both senders and is due to an unfavourable aspect of the vehicle aeri-als.

#### 5.4 Sensitivity of Scanning Observations and the Search for Other Sources

##### 5.4.1

We can represent the net detection rate at any given instant by the expression

$$R = \int_{j_s} f(\theta - \theta_0) + \frac{djd}{d\Omega} \delta\Omega + j b \int \mathcal{E} A \text{ c/sec}$$

where  $j_s$  = photon flux from the source  
 $f(\theta - \theta_0)$  = collimator transmission function  
 $\frac{djd}{d\Omega}$  = photon flux from diffuse background  
 $\delta\Omega$  = solid angle of collimator  
 $j_b$  = non X-ray background flux  
 $\xi$  = efficiency factor of detector  
 $A$  = area of detector.

The hexagonal collimator produces essentially a triangular response

$$\therefore f(\theta - \theta_0) = 1 - \frac{|\theta - \theta_0|}{\theta'} \quad \text{for } \theta - \theta_0 < \theta'$$

$$= 0 \quad \text{for } \theta - \theta_0 > \theta'$$

where  $\theta'$  is the FWHM of the collimator.

For a scanning instrument the rate obtained from the source is the integral of the transmission function over the field of view

$$N_s = \int_{\theta_1}^{\theta_2} j_s \xi A \frac{f(\theta - \theta_0)}{\omega} d\theta$$

where  $\omega$  is the rotation rate

$$\therefore N_s = j_s \xi A \left[ \frac{\theta'}{\omega} \right]$$

the term in brackets simply being the transit time between the FWHM points of the collimator. In the case of a weak source, the fluctuations originate entirely from the background counts, i.e.

$$\delta N_s = \sqrt{N_B} = \sqrt{\left[ \frac{djd}{d\Omega} \delta\Omega + j_b \right] \xi A t}$$

where the duration of the observation  $t$  can be expressed as

$$t = 2\theta' / \omega$$

The signal to noise ratio  $S/N$  is therefore

$$\sqrt{\frac{N_s}{N_B}} = j_s \sqrt{\epsilon A t / \left[ \frac{djd}{d\Omega} \delta\Omega + j_b \right]}$$

which if we express as a conventional  $3\sigma$  limit for the detection of a source leads to

$$j_s(\min) = 3 \sqrt{\left[ \frac{djd}{d\Omega} \delta\Omega + j_b \right] / A \epsilon t}$$

if we normalise the area to unity and convert to counts per second we have roughly

$$j_s = 3 \sqrt{\frac{400 + 350}{T}}$$

where T is the observing time of the sample. Using a nominal intensity for Cygnus X-1 based on fig. 5.2 and fig. 5.3 we can derive the table below which converts the  $3\sigma$  limit to Uhuru counts.

TABLE 5 A

Time sec.	fig. no.	$3\sigma$ counts/sec	Uhuru counts
0.2	5-11	178	35
0.4	5-10	126	25
2.0	5-5	57	11
15.0	max limit	21	4

When looking for significant detections the varying count rate has been allowed for by fitting a sinusoidal profile to the background in fig. 5.10 and fig. 5.5 and calculating the statistical deviation of the data points along the flat part of the scan.

The experiment was never designed for looking at weak sources particularly in a scanning mode since no great effort had been made to reduce the background. The actual background rate of approximately 750 counts/sec could have been reduced greatly by having a smaller field of view and by the inclusion of even a simple form of RTD.

## 5.4.2

The roughly sinusoidal change in background count rate visible in fig. 5.10 can be attributed partly to the varying rate in the guard channel which the sender 2 data shows to increase by a few percent between +160 and +240 seconds. The phase also correlates with the attitude of the panels the signal being a minimum when the round axis is in the horizontal plane. In this position the guard veto of the signal channel is most effective since the unprotected ends of the detector point towards the horizon. This is not unexpected since a similar effect was noted during laboratory testing with a strong  $\text{Co}^{60}$  source.

5.4.3 Data on other sources

From this aspect the flight is best divided into two sections, both of which unfortunately reveal very little in the way of information.

The first scan is shown in fig. 5.10 and covers the interval from +116 to +284. Apart from the large increases around +130 sec which are due to noise corrupted data, no obvious sources are visible. A search through the 3U, 4U and 2A catalogues reveals a number of objects to be within the scan path as deduced from the camera data. This list (table 5B) indicates the estimated offset from the 100% transmission track and the time at which each source is on the axis of the collimator. The insert in fig. 5.10 shows the profile expected for a point source based on the established drift rate of  $0.5^\circ/\text{sec}$ , the width of the triangle decreasing significantly for lateral offsets greater than  $6^\circ$ .

Unfortunately, Her X-1 was in its extended low state, this having commenced on November 1st  $\pm 0.5$  days. This lasts for 23 days of the 35 day period, the intensity during this phase having been

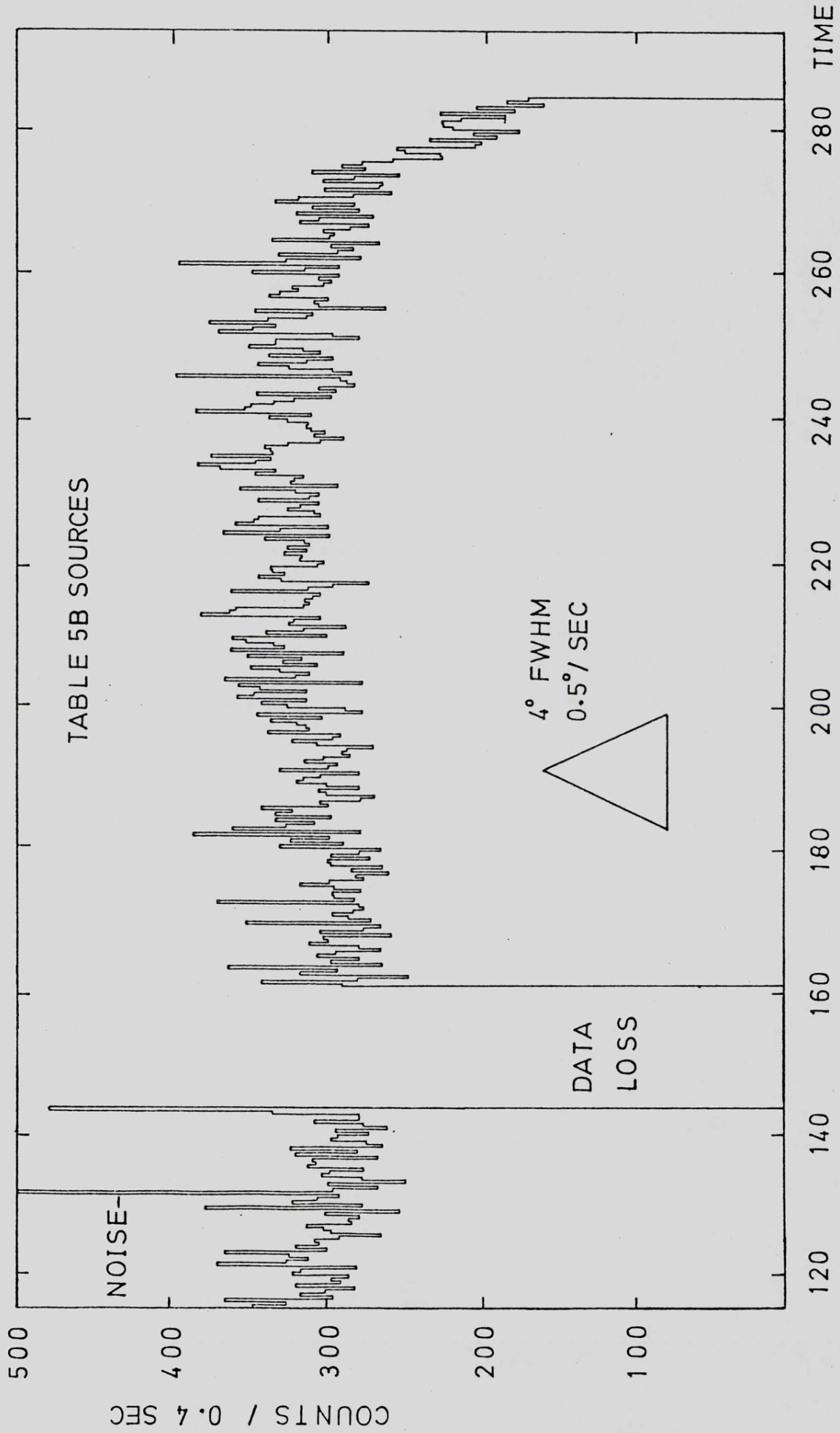


FIG 5.10 SCAN TO HORIZON

TABLE 5B

No.	Source	Details	Uhuru	Ariel	%	Time
1	2A1919+43	A2319 cluster	6.3	2.6	10	-
2	2A1721+32	-	5.1	1.5	75	198
3	2A1659+33	-	4.6	0.6	50	205
4	2A1655+35	Her X-1	100.0	55/5	35	210
5	2A1600+16	A2147/52	2.1	0.8	5	238
6	2A1556+27	A2142	5.1	1.4	100	241
7	2A1415+25	NGC 5548 (Seyfert)	-	0.8	60	281

TABLE 5C

8	4U0919-54	-	5.5	1.6	85	344
9	4U1118-60	Cen X-3	200.0	-	40	348
10	4U1137-65	-	9.6	-	75	349
11	4U1145-61	HD102567 ?	72.0	4.8	35	349
12	4U1210-64	-	5.2	1.0	75	350
13	4U1223-62	WRAY 977	40.0	10.30	40	350.5
14	4U1246-58	-	5.1	-	15	351
15	4U1254-69	-	23.0	10.14	95	351.5
16	4U1258-61	P = 272	55.0	3.15	40	351.5
17	4U1314-64	A1767	9.6	-	60	352
18	4U1323-62	-	4.2	-	50	352.25

TABLE 5D

19	4U1344-60	-	4.0	-	40	352.5
20	4U1416-62	-	7.6	-	75	354.5
21	4U1425-61	-	2.4	-	75	355
22	4U1436-56	-	3.8	-	60	356
23	4U1510-59	SNR	6	3.5	85	358
24	4U1516-56	Circ X-1	720	-	75	358.5
25	4U1538-52	Nor X-2	18	3.6	40	361
26	4U1543-62	-	19	10.15	85	363
27	4U1556-60	-	20	7	95	367
28	4U1624-49	Nor X-1	50	8.24	15	369
29	4U1626-67	P = 7.7 sec	18	8	40	369
30	4U1630-47	Tran	220	0.10	5	369.5
31	4U1631-64	-	5	3	50	369.5
32	4U1636-53	Bin	261	70.110	50	369.75
33	4U1658-48	-	344	40.75	15	371

measured at about 15 Uhuru units by the Ariel 5, SSI instrument. Although the data around +210 looks superficially interesting no evidence of the 1.24 sec period has been detected when folding the data from +205 to +215 about this period into bins. Her X-1 has been shown by Jones and Forman (1976) to continue pulsing at medium energies (2-6 KeV) through the low state, these observations being made by Uhuru in early January, 1972.

#### 5.4.4

Source number 7 in table 5B is particularly interesting since it is the Seyfert Galaxy NGC 5548 but although near the 100% transmission contour is unfortunately weak and close to the detector horizon. Fig. 5.5 shows an excess at +240 which is again associated with an interesting profile in fig. 5.10 but since this object is thought to be the Abell cluster A2142 it is unlikely to vary on a time scale of seconds.

#### 5.4.5

The remaining scan occurs when the detectors re-emerge from below the horizon but the scan rate is now considerably faster than before, being some  $6.7^{\circ}/\text{sec}$  at +340, slowing to  $0.9^{\circ}/\text{sec}$  at +367, and then increasing until +372 when the pneumatic bay was ejected. The magnetometer data allows the objects scanned during this interval to be determined but specific sources are not easily identifiable. This is due to the rapid motion and the general source confusion for such a large field of view while looking at the galactic equator region near the constellations of Crux, Centaurus and Circinus.

The scan itself is shown in fig. 5.11 and table 5C lists the

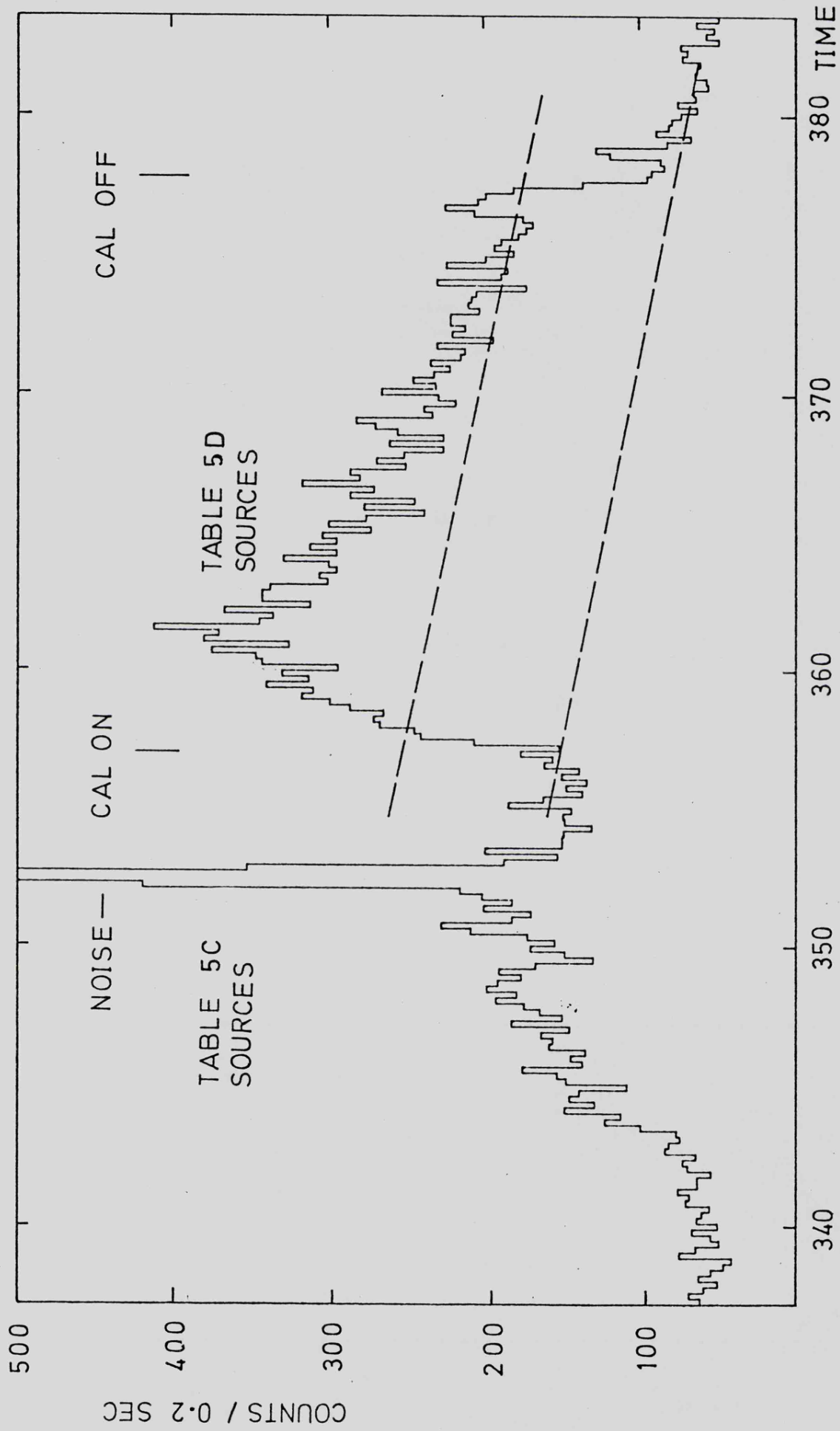


FIG 5.11 DATA FROM END OF FLIGHT

objects from +338 to +354, while table 5D lists those from +354 to +370. As shown in the figure the cal is on for a 20 second interval and a noise peak is evident at +352. At the time of the flight Cen X-3 was about 24 hours into the 'ON' state of its 2.087 day period and this source can just be seen at +348 in fig. 5.11, probably merged with a contribution from 4U1223-62. Superimposed with the noise spike at +352 is probably 4U1254-69 and 4U1258-61. The excess from +360 to +370 can be connected with sources 24-32 in table 5D, the major contribution probably being due to 4U1543-62.

CHAPTER 6

The analysis of the Cygnus X-1 data

	Page
6.1 Basic Observation and Spectral Data	164
6.2 Cygnus X-1 Shot Noise Time Structure	168
6.3 Millisecond Bursts	186
6.4 Statistical Aspects of Burst Identification	206
6.5 Discussion	212
6.6 Summary	218

## 6.1 The Analysis of the Cygnus X-1 Data

### 6.1.1 Basic Observation and Spectral Data

The brief observation of Cygnus X-1 visible in fig. 5.5 has been re-plotted in finer time bins in fig. 6.1. Deploy occurs approximately at the origin, the first brief increase being due to the front panel swinging outwards allowing more of the centre panel to see the source. At +103 however the round is no longer aligned on the source, the centre panel B viewing just the background with the CRI's on panel A and C having tripped out. At +104 the panels become locked and all three channels are clear but the round rolls on for an estimated  $6-7^\circ$  before being brought smoothly back to the correct roll attitude at +107. During this time the failed lateral jet allows the source to drift completely out of the field of view by +112.

It is immediately clear that the sensitivity of the observation is considerably less than anticipated, indeed at best only 40-50% of the count rate can be attributed to Cyg X-1. This poor signal to noise ratio is of considerable importance in the detection of millisecond bursts as shown by section 6.3. The highest mean rate from the source itself is about 1500 c/sec as compared to the prediction of  $\sim 6000$  c/sec.

This low rate was certainly not due to the experiment itself but must be due to small inaccuracies in pointing and a generally weak state of the source. Any small offset is not easy to determine due to the lack of camera data but the available records suggest that the source was within the 90% collimator transmission contour for several seconds.

Turning to the source state we see from fig. 5.2 and fig. 5.3 that the source was variable on a time scale of days and hours during November 1976. Cygnus X-1 was also observed by the spectrometer

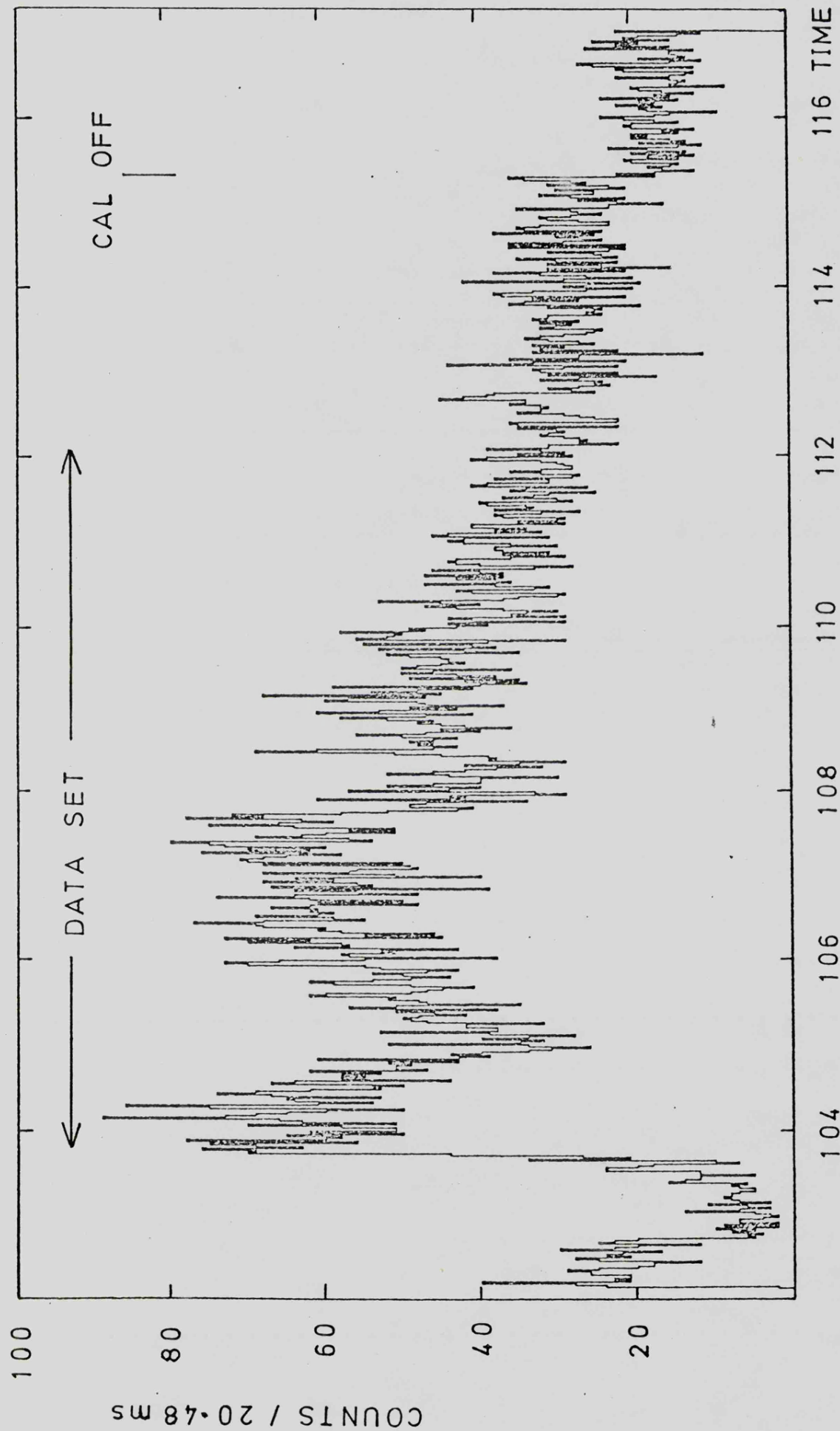


FIG 6.1 CYG X-1 DATA

on OSO-8 during November but unfortunately with a break from the 1st to the 7th (Dolan et al., 1977). A typical low rate from fig. 5.3 scaled up to the SL-1306 area gives a count rate around 1300 per second and so the 6 sec observation may have taken place during one of these intervals.

### 6.1.2 Spectrum of Cygnus X-1

The spectrum of Cygnus X-1 was obtained from the data between +104 and +110, the background subtraction being derived by three methods. The first of these was simply to use the counts between +113 and +115 and the second was to obtain the true background spectrum from +116 to +260, taking care to avoid the anomalies at +130 and +145 to +165, and combining it with the previously calibrated Fe<sup>55</sup> profile. The third method utilised the latter half of the second calibration interval from +370 to +376. The three results were found to be consistent and the normalised channel rates for Cygnus are shown in table 6A. This table also shows the diffuse background rates which were obtained by subtraction of the particle background rates obtained during the scan below the horizon.

TABLE 6A

KeV	PHA #	c/sec	
		Cyg X-1	Diffuse
1.30	1	109.6	55.0
2.11	2	205.0	84.8
3.04	3	217.2	83.0
4.21	4	168.5	74.9
5.62	5	137.8	56.7
7.18	6	53.9	32.9
8.97	7	41.4	26.9
10.92	8	7.4	21.0
13.03			

The spectral fitting program previously described produced a power law fit of

$$\frac{dN}{dE} \propto e^{-1.9 \pm 0.15}$$

with a hydrogen column density of  $23 \pm 7 \times 10^{21}$  atoms/cm<sup>2</sup>. The quoted uncertainties are 68% confidence limits calculated according to the method outlined by Lampton et al. (1976). These results are somewhat different to those of Rothschild et al. (1974, 1976) who obtained an index of -1.55 with  $H < 3.0 \times 10^{21}$ . Canizares and Oda (1977) describe five separate spectral observations from SAS-3 and these are shown below in table 6B. The SL-1306 index appears to be consistent with the more recent data particularly since they note that the fit is highly variable on a time scale of seconds and that the spectrum is harder when prominent flares are excluded from the data sample. Dolan et al. (1977) obtain  $\alpha = 2.05 \pm 0.03$  for their 1976 observations but this does not apply to a higher energy range (20 - 150 KeV).

TABLE 6B

DATE	INDEX
1975 June 21	- 1.8 $\pm$ 0.1
1975 Sept. 8-9	- 2 $\rightarrow$ - 3
1975 Oct. 15	- 1.8 $\pm$ 0.1
1976 Aug. 3-7	- 1.9 $\pm$ 0.1
1976 Oct. 10-15	- 1.5 $\pm$ 0.1

The SAS experiment was however not sensitive below 2 KeV and so the hydrogen column density near the time of the flight cannot be checked.

In view of the difference in hydrogen column density between the Rothschild and SL-1306 values the diffuse spectral data was

examined and as expected found to have  $H < 0.5 \times 10^{21}$ . The least well known factor in the detector response model appeared to be the window absorption and so a careful calibration using a 2 crystal spectrometer was performed. The mylar tested was identical to that used on the flight detectors and the absorption model was found to be accurate to within 5%. This implies that the absorption is astronomical in origin. An absorption of  $7.5 \pm 1.8 \times 10^{21}$  H atoms  $\text{cm}^{-2}$  has been obtained by Margon et al. (1973) based on line of sight extinction.

## 6.2 Cygnus X-1 Shot Noise Time Structure

The analysis of temporal data has been discussed by Rothschild (1977) and can be divided basically into studies of periodic and non-periodic structure. This section deals with both aspects for relatively long time scales and the next section deals with the search for the non-periodic millisecond bursts. It is important to bear in mind that the data sample obtained is not particularly suitable for investigating time scales  $> 0.5$  sec. The following presentation is included for completeness although the shot parameters would be relevant to the more rapid features.

### 6.2.1 Randomness of Data

A useful start is made by examining the data set shown in fig. 6.1 to see how random the rate is. This can easily be done by simply binning the intervals between counts to form a histogram plot and comparing this to the exponential profile one would expect from a truly random set of data. Since the rate varies considerably over the data set, this interval has been broken into 42 samples of 131 mS and the expected profile obtained by summation of the individual curves. Fig. 6.2 shows the results for  $6\mu\text{S}$  (the dead time limit) to  $200\mu\text{S}$  at which point the percentage of the total counts not included becomes

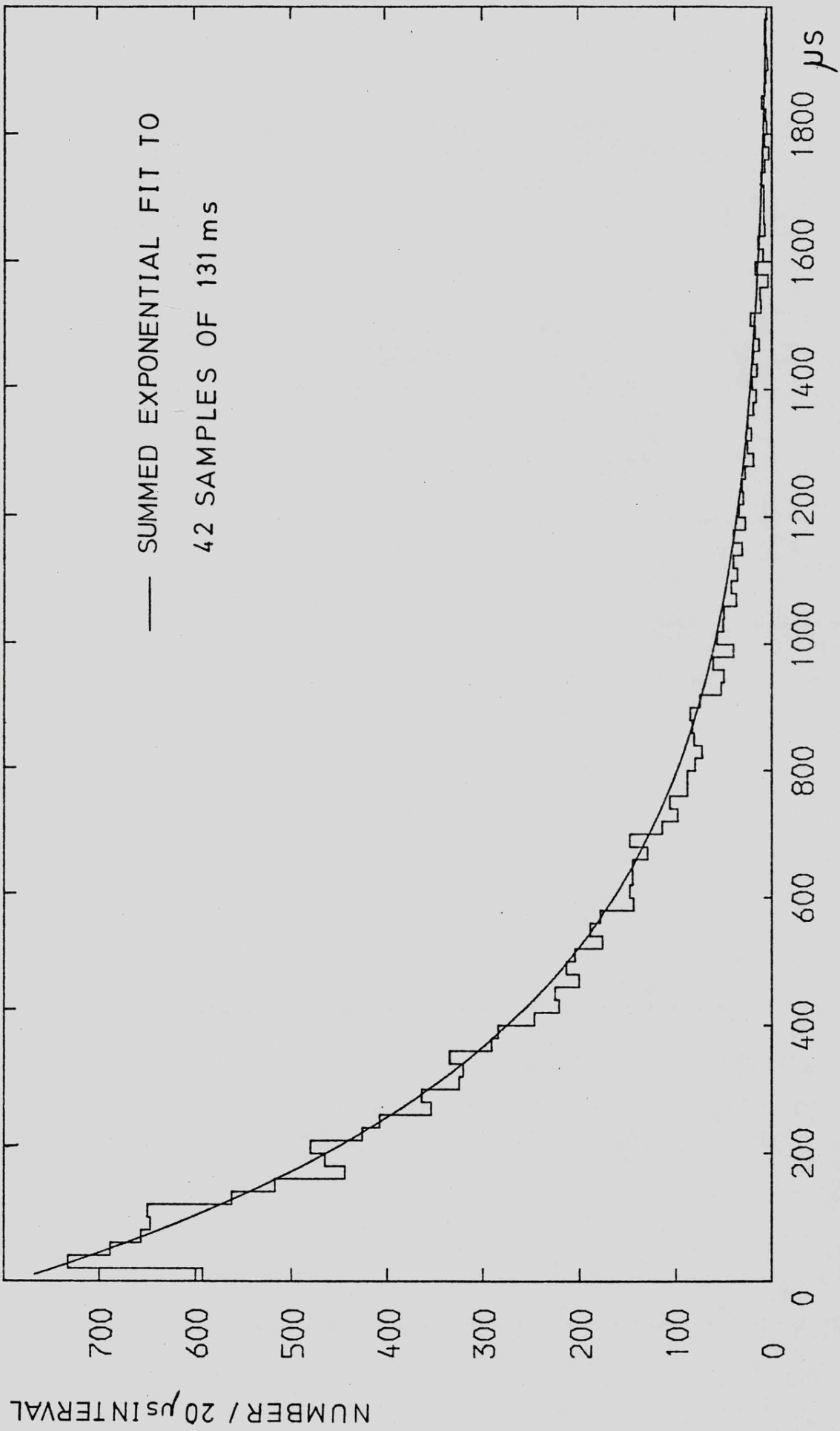


FIG 6.2 CYG X-1 COUNT INTERVAL TIME DISTRIBUTION

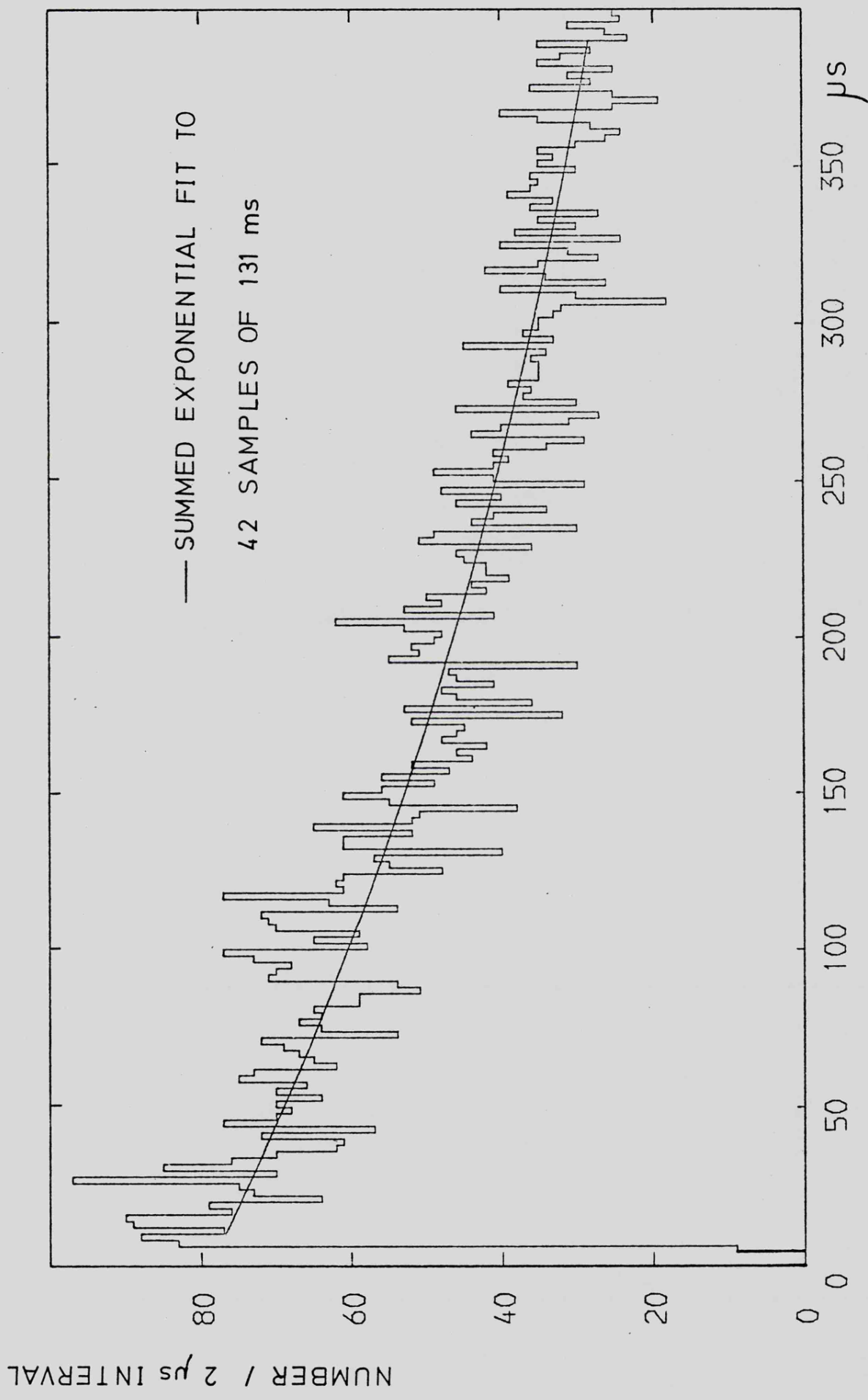


FIG 6.3 CYG X-1 COUNT INTERVAL TIME DISTRIBUTION

very low. As can be seen, the data is very consistent with a generally random rate but the resolution is only  $20\mu\text{S}$  per bin so the analysis was repeated at  $2\mu\text{S}$  per bin, the results being shown in fig. 6.3. The data is again consistent with the expected curve in terms of the statistical error alone, demonstrating that on a time scale of  $\sim 131$  mS (one telemetry block) the data contains no marked irregularities. Both these results reflect the fact that assuming the source itself is largely random, any small departures will be heavily masked by the greater than 50% truly random contribution from the calibration source and the background events.

#### Basic definitions

It is helpful at this stage to define a few equations.

$$\mu_x = \text{mean value of the observations}$$

$$\sigma_x^2 = \text{variance of } x(t)$$

$$\gamma_{xx}(\tau) = \text{autocovariance of } x(t)$$

$$\rho_{xx}(\tau) = \text{autocorrelation of } x(t)$$

$$\Gamma_{xx}(f) = \text{power spectrum of } x(t)$$

If the observations  $x(t)$  are in the form of a time series of  $N$  counts  $x_i$  then

$$\mu_x = \frac{1}{N} \sum_{i=1}^N x_i$$

$$\sigma_x^2 = \frac{1}{N} \sum_{i=1}^N (x_i - \mu_x)^2$$

$$\gamma_{xx}(\tau) = \frac{1}{N} \sum_{i=1}^N (x_i - \mu_x)(x_{i+\tau} - \mu_x)$$

$$\rho_{xx}(\tau) = \gamma_{xx}(\tau) / \sigma_x^2$$

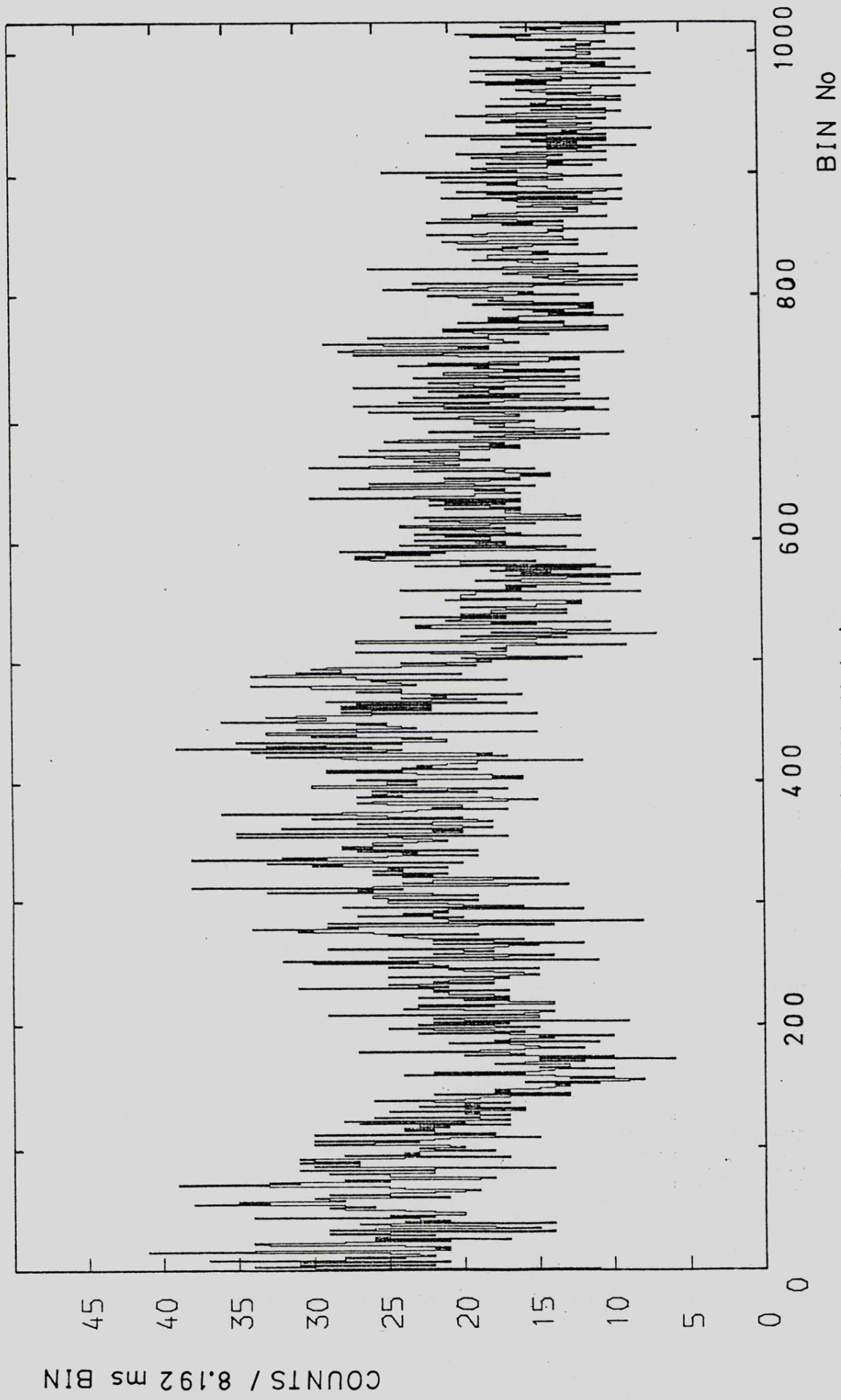


FIG 6.4 BASIC DATA SET ( CYG X-1 )

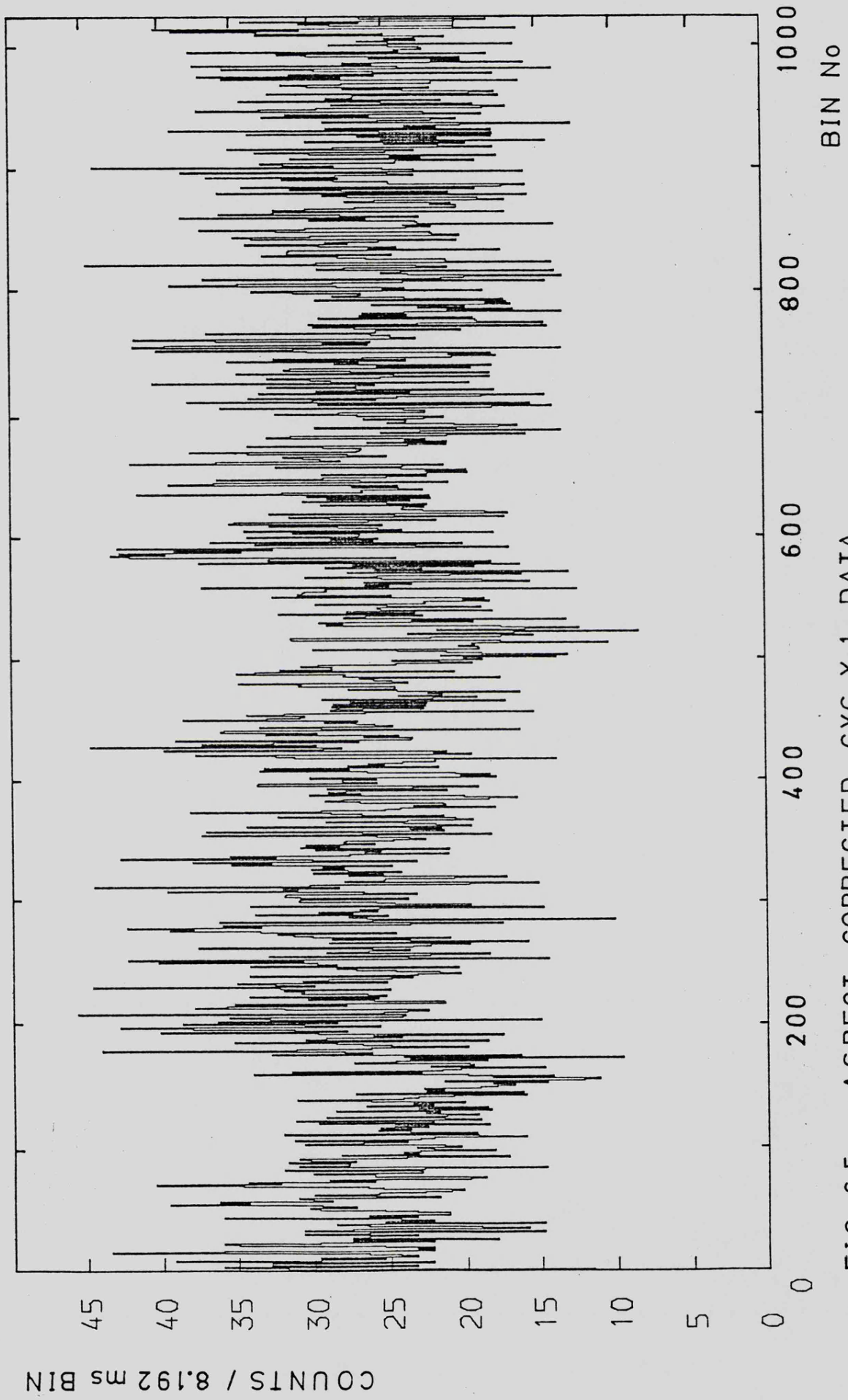


FIG 6.5 ASPECT CORRECTED CYG X-1 DATA

or 
$$\rho_{xx}(\tau) = \gamma_{xx}(\tau) / \gamma_{xx}(0)$$

$$\Gamma_{xx}(f) = \int_{-\infty}^{\infty} \gamma_{xx}(\tau) e^{i2\pi f\tau} d\tau$$

which is simply the Fourier transform of  $\gamma_{xx}(\tau)$ .

The data set marked in fig. 6.1 has been replotted in fig. 6.4 with finer resolution and forms the basic sample for subsequent analysis techniques. This data, however, still contains the unwanted profile of changing count rate due to the payload drift and this has been removed by applying a correcting factor based on smoothing the curve in fig. 6.4 over a running 0.5 sec interval. This aspect corrected curve is shown in fig. 6.5.

### 6.2.2 Autocorrelation

Even though the intensity of Cygnus X-1 displays no periodicities, there can still be an underlying structure. In the case of Cygnus X-1, there is the shot noise pattern first suggested by Terrell (1972) and the autocorrelation function is a powerful method for studying this type of structure. The data in fig. 6.4 has been analysed over several different time scales using two methods.

To take advantage of the exceedingly fine time resolution the following form was adopted.

$$\rho(\tau) = \sum_{i=1}^N x_i \cdot x_{i+\tau}$$

where  $x_i$  is a long sequence of  $2\mu\text{S}$  bins in which there is one count or no counts. This technique was used to produce three autocorrelation plots, the first of which is shown in fig. 6.6. This shows a statistically featureless, uniform, level function with  $2\mu\text{S}$  resolution

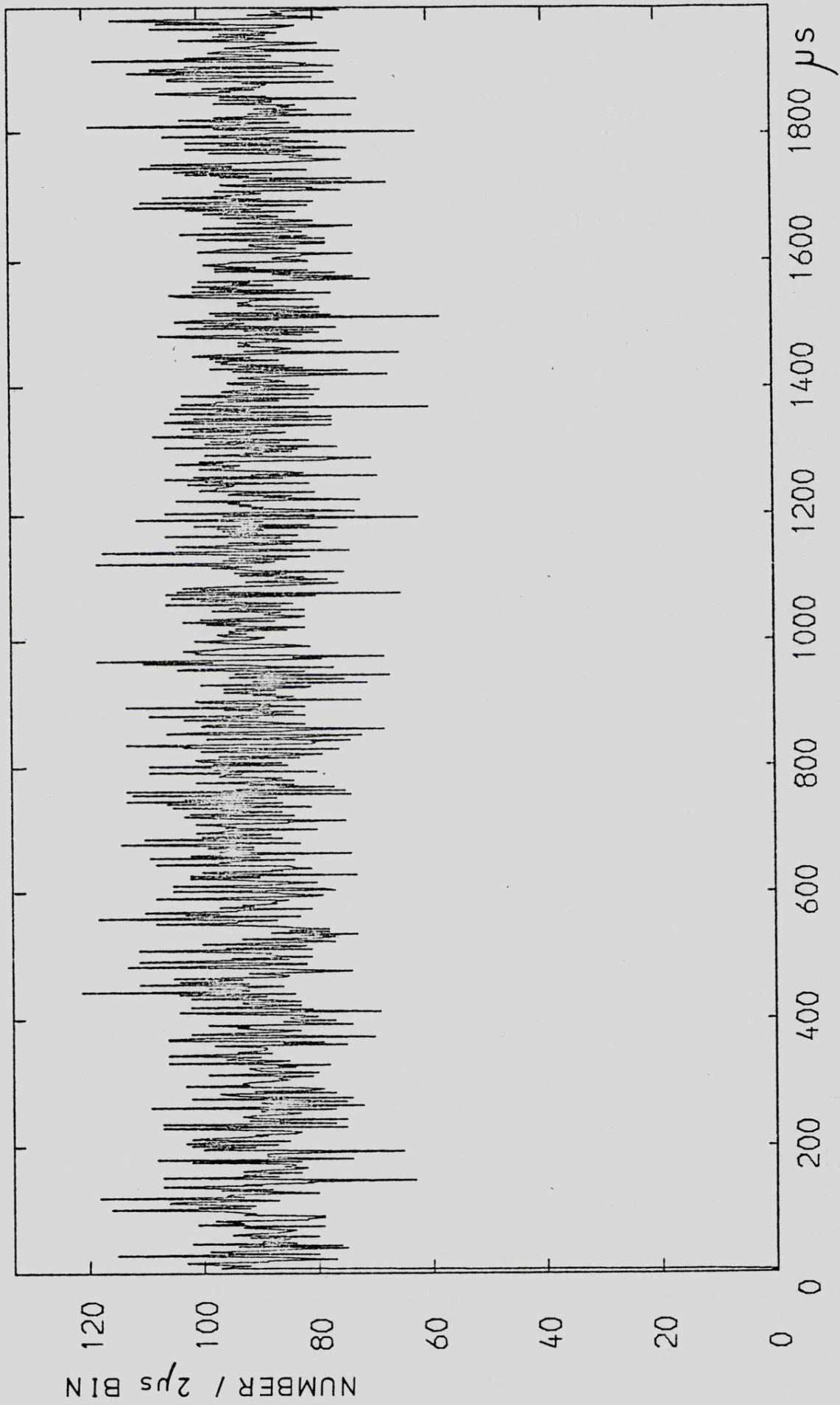


FIG 6.6 AUTOCORRELATION FOR CYG X-1 DATA

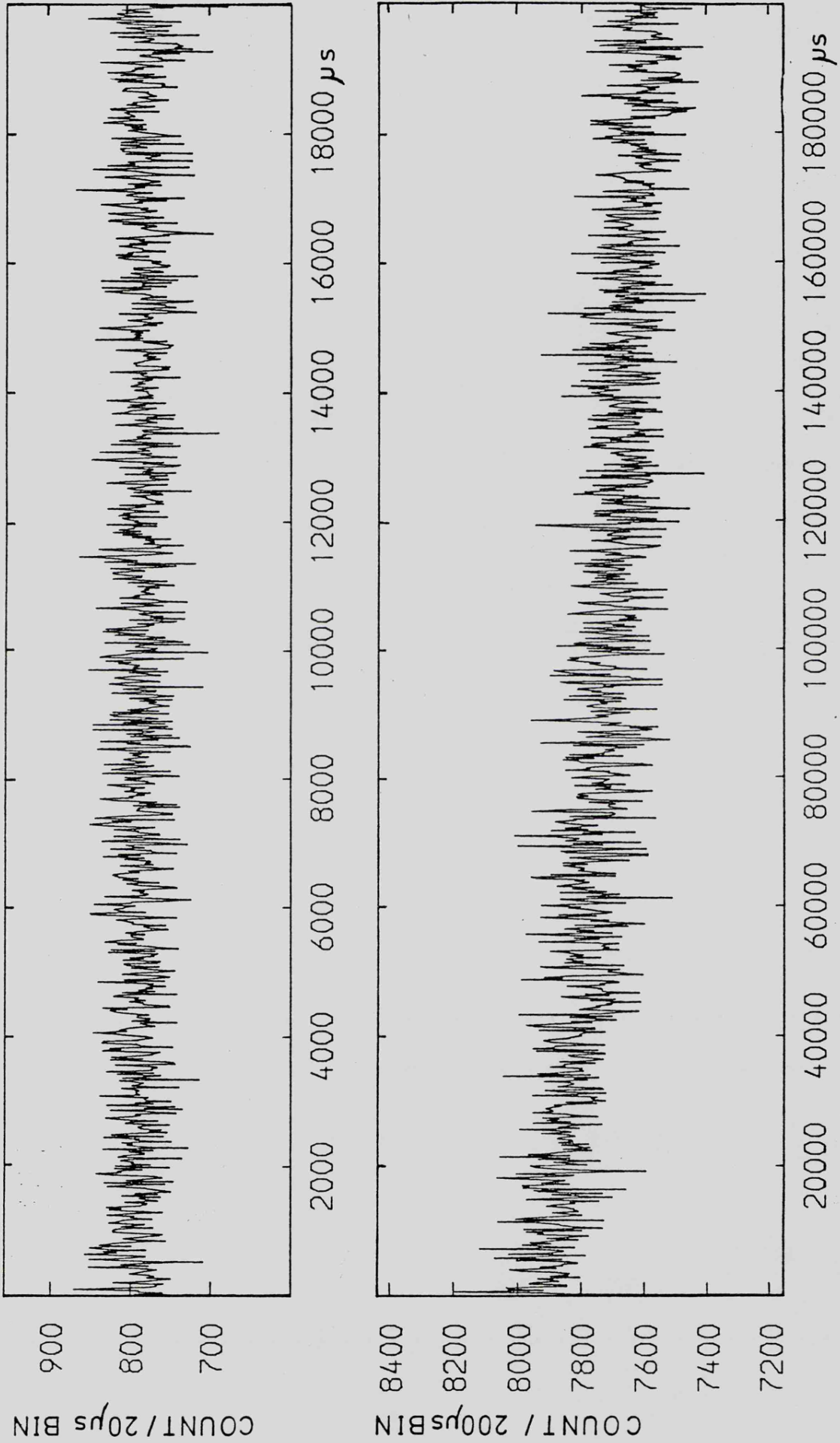


FIG 6.7 AUTOCORRELATION FOR CYG X-1 DATA

over the range up to  $2,000\mu\text{S}$ . Fig. 6.7 shows two plots, the top one representing the range up to  $20,000\mu\text{S}$  with  $20\mu\text{S}$  resolution and is again featureless but shows a very slight decline over the entire interval. The lower half of this figure, however, begins to show a large decline as would be expected from the shot noise model for Cygnus X-1, once such large time scales are reached. This plot actually extends to  $200,000\mu\text{S}$  ( $1/5$  sec) with  $200\mu\text{S}$  resolution. None of these plots indicate any unknown rapid shot or periodic features and have not been smoothed purely to retain clearly their inherent scatter.

For time scales greater than say 10 mS another form of the autocorrelation function (ACF) is convenient that can clearly show the exponential form of the shot noise pulses.

$$\rho_z(\tau) = \frac{\frac{1}{N} \sum_{i=1}^N (z_i - \mu_z)(z_{i+\tau} - \mu_z)}{\sigma_z^2}$$

It has been pointed out, however, by Weisskopf et al. (1975) that the measured ACF will be biased by the ratio of the source variance to the total variance and only when the counting statistics fluctuations are negligible will the ACF represent the true variability of the source. A correction can be made if we assume the signal and statistics can be separated.

$$z(t) = x(t) + y(t)$$

$$z(t) = \text{total signal}$$

$$x(t) = \text{source signal}$$

$$y(t) = \text{counting statistics}$$

It can be shown that

$$\rho_x(\tau) = 1 \quad \text{for } \tau = 0$$

$$\rho_x(\tau) = \frac{\sigma_z^2}{\sigma_z^2 - \sigma_y^2} \rho_z(\tau) \quad \tau \neq 0$$

where  $\sigma_y^2 = \mu$  and  $\sigma_z^2 = \delta(0)$

Fig. 6.8 shows a plot of  $\rho_x(\tau)$  obtained from the original data set (fig. 6.4) and the aspect corrected data set (fig. 6.5). It is clear that in removing the rocket motion by the use of a running average correction, over 0.5 sec intervals, the shot pulse has also been severely attenuated.

It is unfortunate that the characteristic rocket drift time scale is similar to that of the shots and it has proved impossible to effectively separate the two. Previous values for the decay time of the shots have varied between 0.24 and 1.4 sec in successive 20 sec intervals (Rothschild et al., 1977).

### 6.2.3 Energy Dependence of ACF

This analysis was attempted for two separate energy channels extracted from the basic data set in fig. 6.5. The low energy one (LE) was defined as PHA channels 1-3 (1.3-3.0 KeV) and the high energy one (HE) as 4-8 (3.0-13.0 KeV). The attenuation of the ACF was so bad that a meaningful comparison was not possible. Weisskopf et al. (1975) have shown for Uhuru data that when the right correction factor is applied to each channel the pulse profiles are, within the statistical limits, identical.

Any possible spectral variation with shot noise time variability can be examined by use of a Hardness Ratio for the two channels above

$$R_i = (L_i + H_i)/L_i$$

where  $L_i =$  LE count in bin  $i$

$$H_i =$$
 HE count in bin  $i$

Each series of bins was corrected for the large background rate and R showed a scatter that was consistent with Poisson statistics about a constant value. The corrected bins were also sorted into several intensity steps to search for any systematic trend of hardness with intensity, the data again being consistent with a constant R.

#### 6.2.4 Time Skewness

Since the autocorrelation function is time symmetric the data can be analysed to obtain the time skewness function to differentiate between the two possibilities

$$TS(\tau) = \frac{1}{T^3} \frac{1}{N} \sum \left[ (x_i - \mu_x)(x_{i+\tau} - \mu_x)^2 - (x_i - \mu_x)^2(x_{i+\tau} - \mu_x) \right]$$

$$TS(\tau) = -TS(-\tau) \quad T = \text{bin size}$$

$$\text{and } TS(0) = 0$$

In the limit of small bin size and large data set the time skewness for a falling exponential shot becomes

$$TS(\tau) = \frac{\lambda h^3 \tau_0}{3} e^{-\tau/\tau_0} (1 - e^{-\tau/\tau_0})$$

$$\tau_0 = \text{decay time}$$

$$\lambda = \text{mean rate } s^{-1}$$

$$h = \text{peak counting rate } c.s^{-1}$$

For rising shots  $TS(\tau)$  has the opposite sign.

#### 6.2.5 Cross-Correlation Analysis

The LE and HE data sets have also been examined using the cross correlation function (CCF).

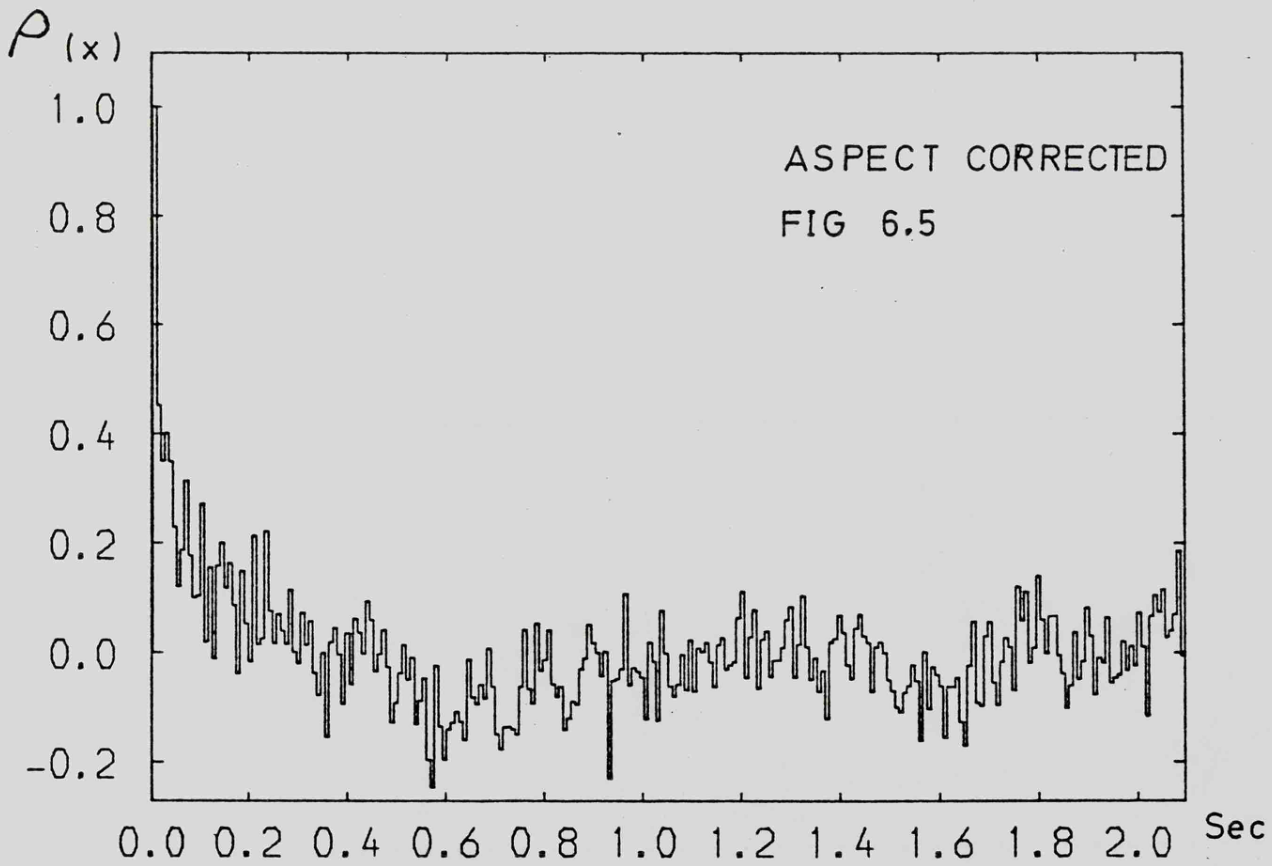
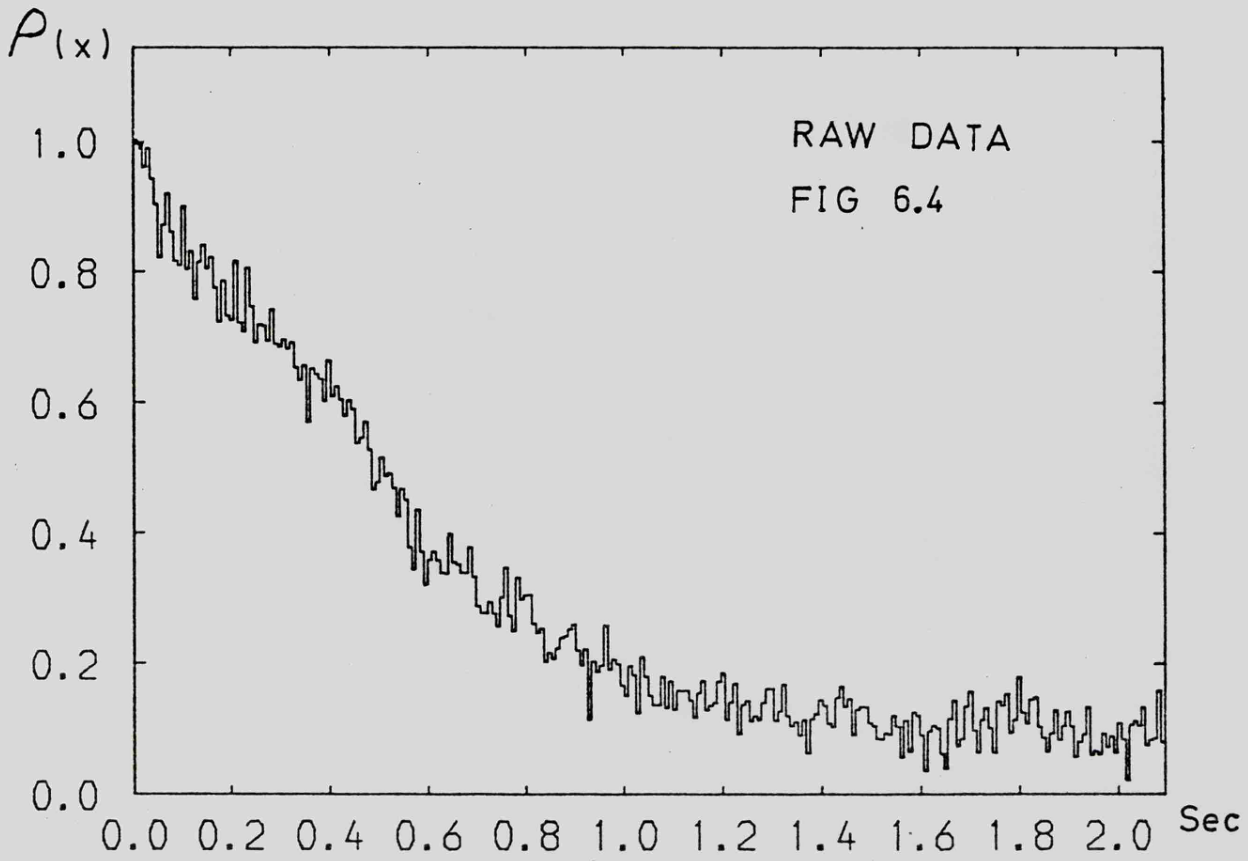


FIG 6.8 AUTOCORRELATION OF CYG X-1 DATA

If  $H_i$  = HE count in bin  $i$   
 and  $L_i$  = LE count in bin  $i$

the CCF is defined as

$$CC(\tau) = \frac{\frac{1}{N} \sum_{i=1}^N (L_i - \mu_L)(H_{i+\tau} - \mu_H)}{(\sigma_L^2 \cdot \sigma_H^2)^{\frac{1}{2}}}$$

As before, the CCF obtained from the data must be corrected so we write

$$H_Z(t) = H_X(t) + H_Y(t)$$

$$L_Z(t) = L_X(t) + L_Y(t)$$

It can be shown that

$$CC_X(\tau) = \left[ \frac{\sigma_{L,Z}^2 \cdot \sigma_{H,Z}^2}{(\sigma_{L,Z}^2 - \sigma_{L,Y}^2)(\sigma_{H,Z}^2 - \sigma_{H,Y}^2)} \right]^{\frac{1}{2}} CC(\tau)$$

or

$$CC_X(\tau) = \left[ \frac{\gamma(0)_L \cdot \gamma(0)_H}{(\gamma(0)_L - \mu_L)(\gamma(0)_H - \mu_H)} \right]^{\frac{1}{2}} CC(\tau)$$

Again this proved impossible to perform since one or other of the energy ranges produces a poor ACF depending on where the boundary is placed. Weisskopf et al. (1975) have shown that two such channels (2.1-5.2 KeV and 5.2-16.4 KeV) are effectively 100% correlated at least on time scales  $> 0.2$  sec. In addition to this, the profile obtained from  $-\tau$  to  $+\tau$  is symmetrical indicating that the HE counts neither lead nor lag the LE counts.

#### 6.2.6 Fourier Analysis

Obtaining the power spectra is a very powerful method of revealing even weak periodic signals in the presence of a strong random signal. The power spectrum will be digitised since the data itself is

and the Sampling Theorem states how the underlying continuous power spectrum can be calculated from the discrete one. In the case of X-ray Astronomy where the data is band limited in time we have

$$\Gamma_{xx}(f) = \frac{1}{2T_c} \sum_{n=-\infty}^{\infty} \Gamma_{xx} \left[ \frac{n}{2T_c} \right] \frac{\text{SIN} \left[ \frac{2 T_c (f - n/2T_c)}{\pi (f - n/2T_c)} \right]}{\pi (f - n/2T_c)}$$

where  $\Gamma_{xx}(f)$  is the continuous power spectrum

$\Gamma_{xx} \left[ \frac{n}{2T_c} \right]$  is the discrete power spectrum

The digitisation period  $T$  is chosen with  $T \leq \frac{1}{2} F_c$  so that aliasing overlap is minimised.

$f_c$  is defined as  $\Gamma(t) = 0$  for  $|f| > f_c$

which is analogous to  $x(t) = 0$  for  $t < 0$  and  $t > T_0$ . A finite length of exposure also creates a problem since if the exposure starts and stops instantaneously there will be a contribution or leakage to  $\Gamma_{xx}(f)$  at all frequencies. This effect from the start and end of the data can be significant for a short sample but can be minimised by using a non-rectangular interval window.

The power density spectrum (PDS) can also be calculated from the autocorrelation function  $\rho(K)$

$$P(f) = 2\Delta \left[ 1 + 2 \sum_{K=1}^{L-1} \rho(K) W(K) \cos [ 2\pi f(K) ] \right]$$

where  $0 < f < \frac{1}{2} \Delta$

$\Delta$  = sampling interval

$W(K)$  = smoothing interval

$\rho(K)$  = autocorrelation function

$L$  = truncation point

A suitable window function is the Tukey one

$$W(K) = 0.5 \left[ 1 + \cos (\pi K/L) \right]$$

Previous observations show that no particular frequency is evident and that the majority of the power occurs at frequencies less than 10 Hz as expected from a shot noise model with  $\tau \gg 0.1$  sec. Any pulsed component would support a neutron star as the collapsed object rather than a black hole.

### 6.2.7 Mean Variance

A further method described by Rothschild (1977) for identifying shot noise processes is to compute the mean variance of the data binned over intervals of duration  $\Delta T$  and plot  $(\delta N)^2/\Delta T$  against  $\Delta T$

$$\text{where } (\delta N)^2 = \frac{1}{N} \sum_{i=1}^N \left[ X_i - \mu(\Delta T) \right]^2$$

where  $N$  = number of bins of width  $\Delta T$

$X_i$  = counts in bin  $i$ .

$\mu(\Delta T)$  = mean of  $X_i$  for bins of width  $\Delta T$ .

It can be shown that

$$\frac{(\delta N)^2}{\Delta T} = \begin{matrix} R \left[ 1 + (1 - \epsilon)^2 \frac{R \Delta T}{\lambda \tau} \right] & \Delta T \ll \tau \\ R \left[ 1 + (1 - \epsilon)^2 \frac{R}{\lambda} \right] & \Delta T \gg \tau \end{matrix}$$

$R$  = mean rate per second on source

$\epsilon$  = background signal to total signal ratio

$\tau$  = shot pulse duration

$\lambda$  = shot pulse frequency

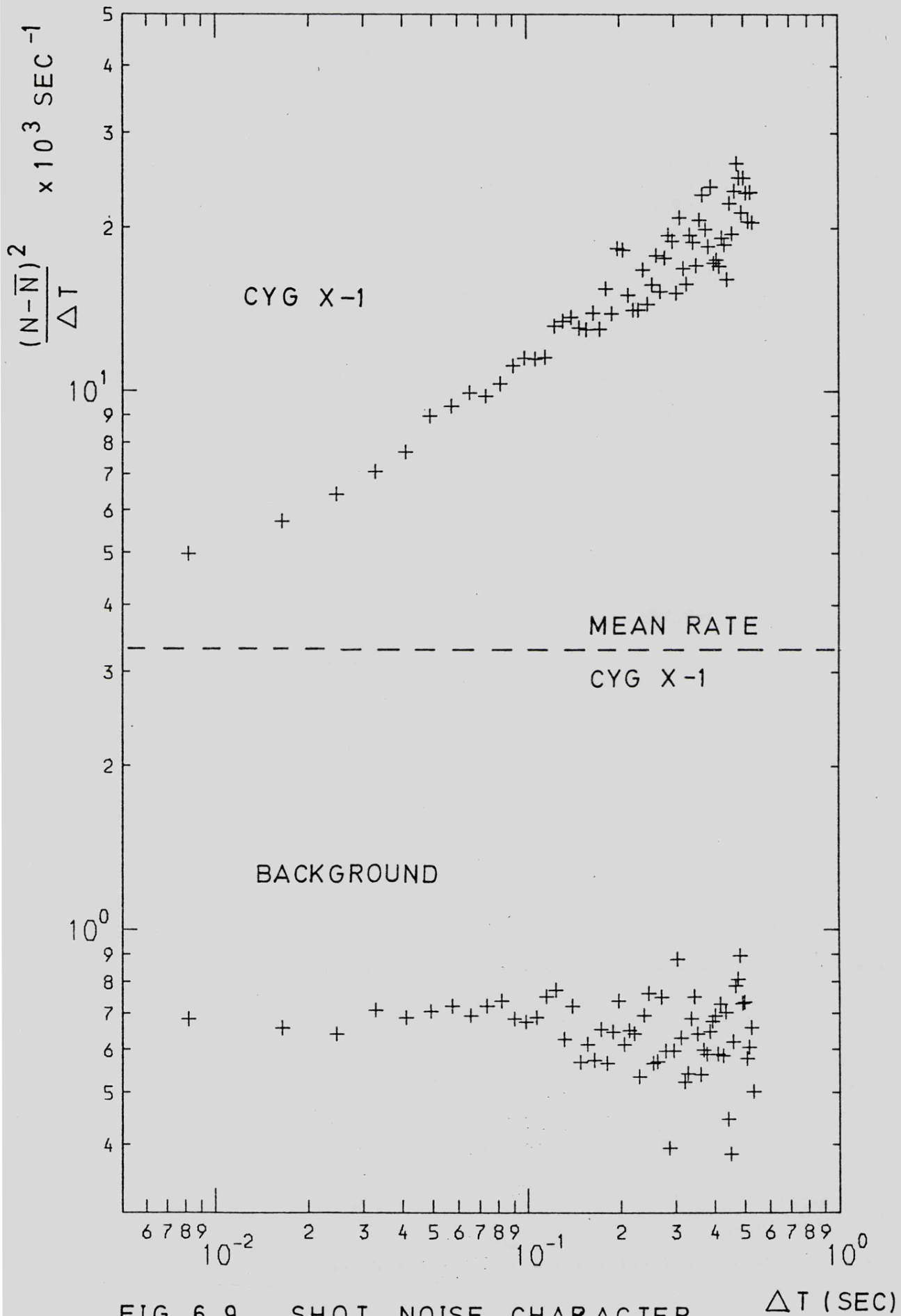


FIG 6.9 SHOT NOISE CHARACTER  
OF CYG X-1

$\Delta T \text{ (SEC)}$

This implies that shot noise, if present, will cause the mean square deviation (MSD) to increase linearly with  $\Delta T$  from the value  $\text{MSD} = R$ . Once  $\Delta T$  is large however, the MSD should be independent of  $\Delta T$  and elevated above the  $\text{MSD} = R$  level by an amount

$$(1 - \epsilon)^2 R^2 / \lambda$$

An attempt has been made to perform this analysis using the aspect corrected data in fig. 6.5, the results being shown in fig. 6.9. The data sample, although not really of sufficient length to determine  $\lambda$  accurately, does follow the trend expected from the theory and match the equivalent curve obtained by Rothschild et al. (1976). The statistical errors increase greatly to the right in the diagram, simply due to the limited number of intervals  $\Delta T$  in the data sample. The data points in fact are only plotted for  $N \gg 16$ . Larger values of  $\Delta T$  would also suffer disastrously in this case from the effects of smoothing the data.

Rothschild's data shows that  $\Delta T$  up to at least 5 seconds are required to really define a horizontal levelling off for the  $\Delta T \gg \tau$  condition which clearly has not been reached for the data in fig. 6.9. We can, however, obtain an upper limit for the observation of

$$\lambda \leq 100 \text{ sec}^{-1}$$

This analysis is based on the fact that the background and calibration rates are random and assumes that the entire Cygnus flux is in the shot noise pulses. Limiting Rothschild's data to  $\Delta T < 0.5 \text{ sec}$  leads to  $\lambda \leq 20$  suggesting the frequency of the shots was greater in 1976 than in 1975. This contrasts directly with the report by Canizares and Oda (1977) that SAS data from October 1976 shows timescales a factor 3 to 6 longer than previously reported values.

Fig. 6.9 also shows data points for a background sample of equivalent length. The data implies a horizontal fit as would be expected for a random background count rate with no shot noise present. In this case  $\tau = 0$  and therefore  $\Delta T \gg \tau$ . Also  $\lambda \tau$  must be constant, implying  $\lambda \rightarrow \infty$  or  $1/\lambda \rightarrow 0$  and therefore

$$(\delta N)^2 / \Delta T = R$$

The background data gives  $R \sim 700$  c/sec which agrees with the actual observed rate.

### 6.3 Millisecond Bursts

The millisecond bursts found by Rothschild et al. (1974, 1976) were obtained by binning counts into  $640 \mu\text{S}$  bins from the basic resolution of  $320 \mu\text{S}$  for the first flight and  $160 \mu\text{S}$  for the second. These bins were then taken in pairs as shown in fig. 1.4 to establish, over some interval, using Poisson statistics that high counts occurred more often than expected by chance. The same basic approach was used to examine the data obtained by SL-1306, the increased performance of the experiment introducing both improvements and additional complexities to the analysis.

#### 6.3.1 Basic Analysis

The counts were binned from an arbitrary start of uncertain position in time that was subsequently located exactly by use of the time code track. The bin size initially chosen was  $0.5$  mS to reflect the expected improvement in sensitivity. The probability of a bin containing  $n$  counts when the mean rate is  $\lambda$  is given by the Poisson function

$$P(n, \lambda) = e^{-\lambda} \lambda^n / n!$$

Fig. 6.4 clearly shows that  $\lambda$  is anything but constant so the observation must be split into short intervals of more nearly constant  $\lambda$ .

This however reduces the number of counts in each interval leading to greater statistical uncertainty so some compromise must be used. The balance used by Rothschild was to divide the entire observation into 120 intervals each of 409.6 mS, each interval containing 320 bins of 1.28 mS. Similarly, the 6.4 seconds of the SL-1306 observation was split into 40 intervals of 160 mS the statistical uncertainty on the predicted number of events per bin remaining at about 6%. In each interval the mean number of occurrences of each integer bin height (1  $\rightarrow$  n) were noted. These results were then compared with the expectation value  $N(n)$  for the number of 0.5 mS bins containing n counts as determined for each interval using the local mean and the Poisson function. Any excess to that expected was then easily found by a visual search through the print-out for the 40 intervals, although the technique used by Rothschild in which he pre-defined a probability limit of 0.01 per interval and searched for only bursts of greater significance is obviously more suitable for a larger number of intervals. The result of this analysis summed over all the intervals was that only two bursts with an expectation value  $< 0.02$  (both of height 8) were found when the total expectation value was 0.56. This compares to some 13 bursts, each with an expectation value  $< 0.01$ , observed by the two Rothschild flights when only 1.7 were expected by chance. These two bursts are shown in fig. 6.10 and fig. 6.11 together with their associated chance expectation value per 320 bin interval. Only the second (burst number 4) of these actually satisfies the probability limit defined by Rothschild.

A better impression of the 'bursts' discussed in this chapter

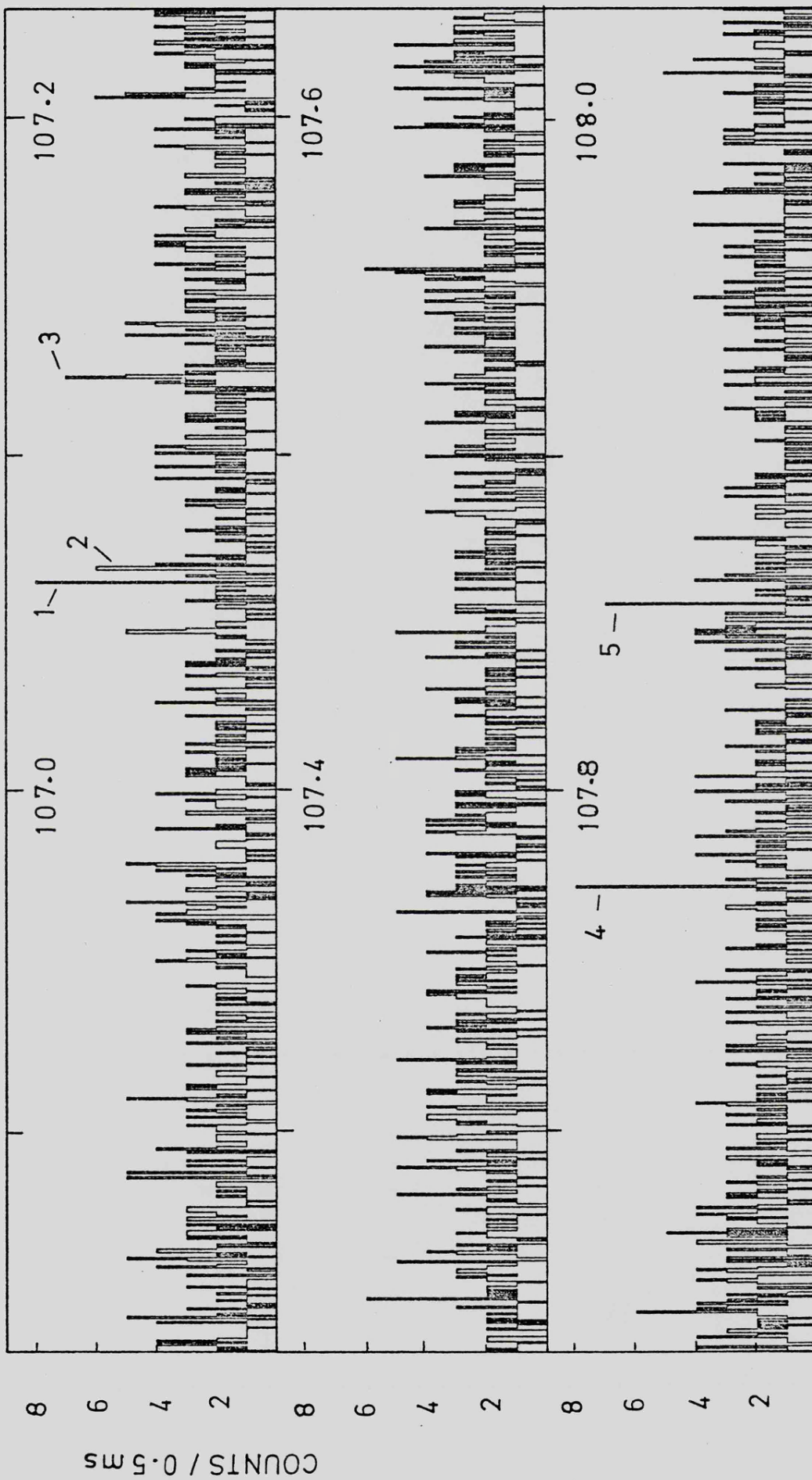


FIG 6.12 1.2 SECONDS OF DATA CONTAINING THE BURSTS

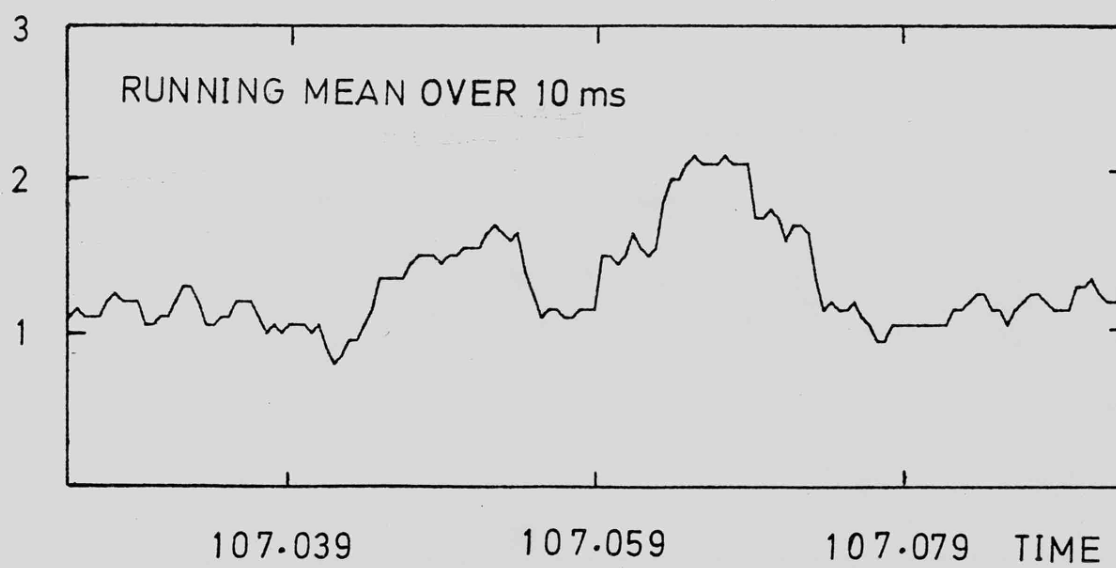
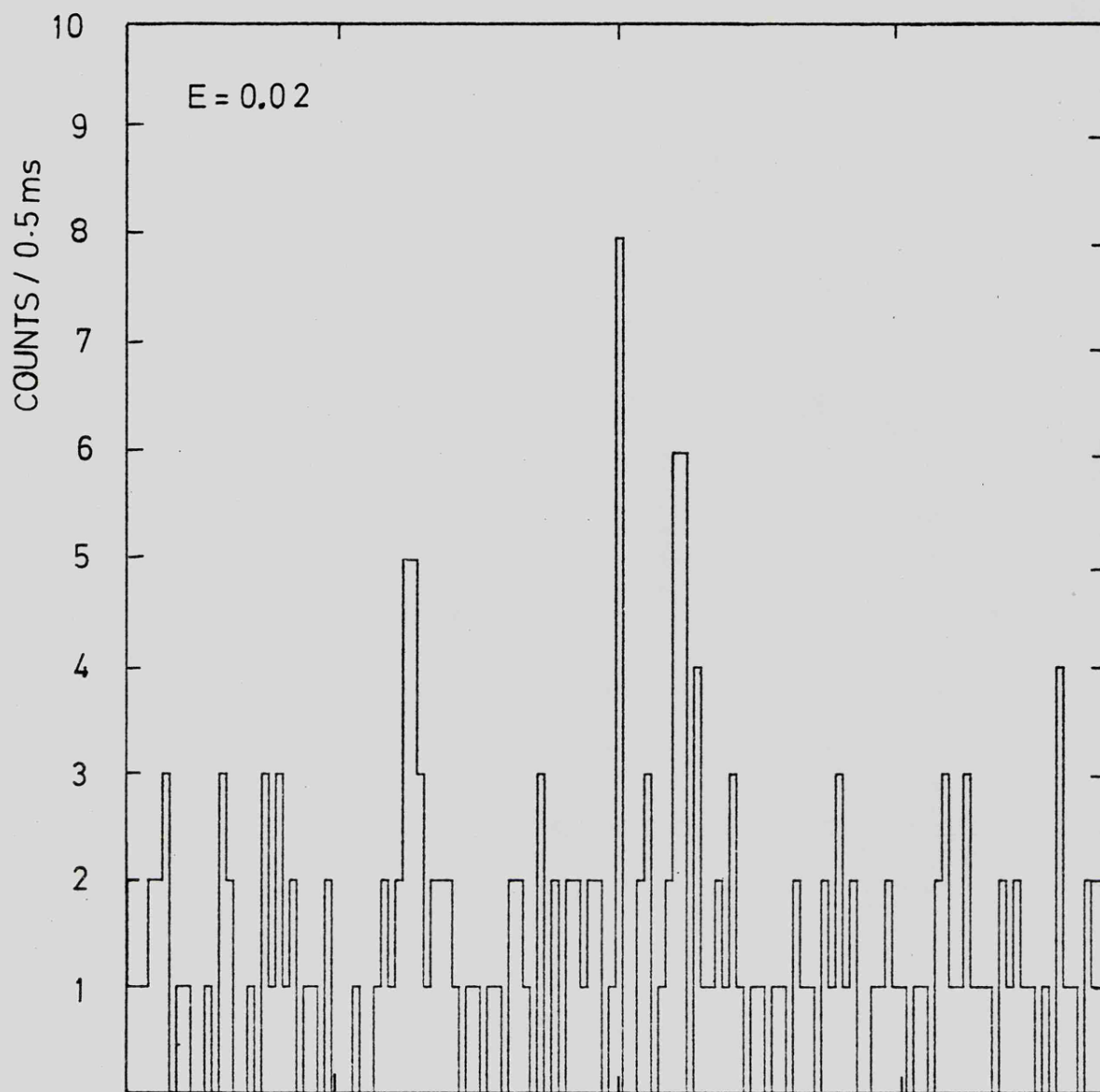


FIG 6.10 CYG X-1 BURST NO.1

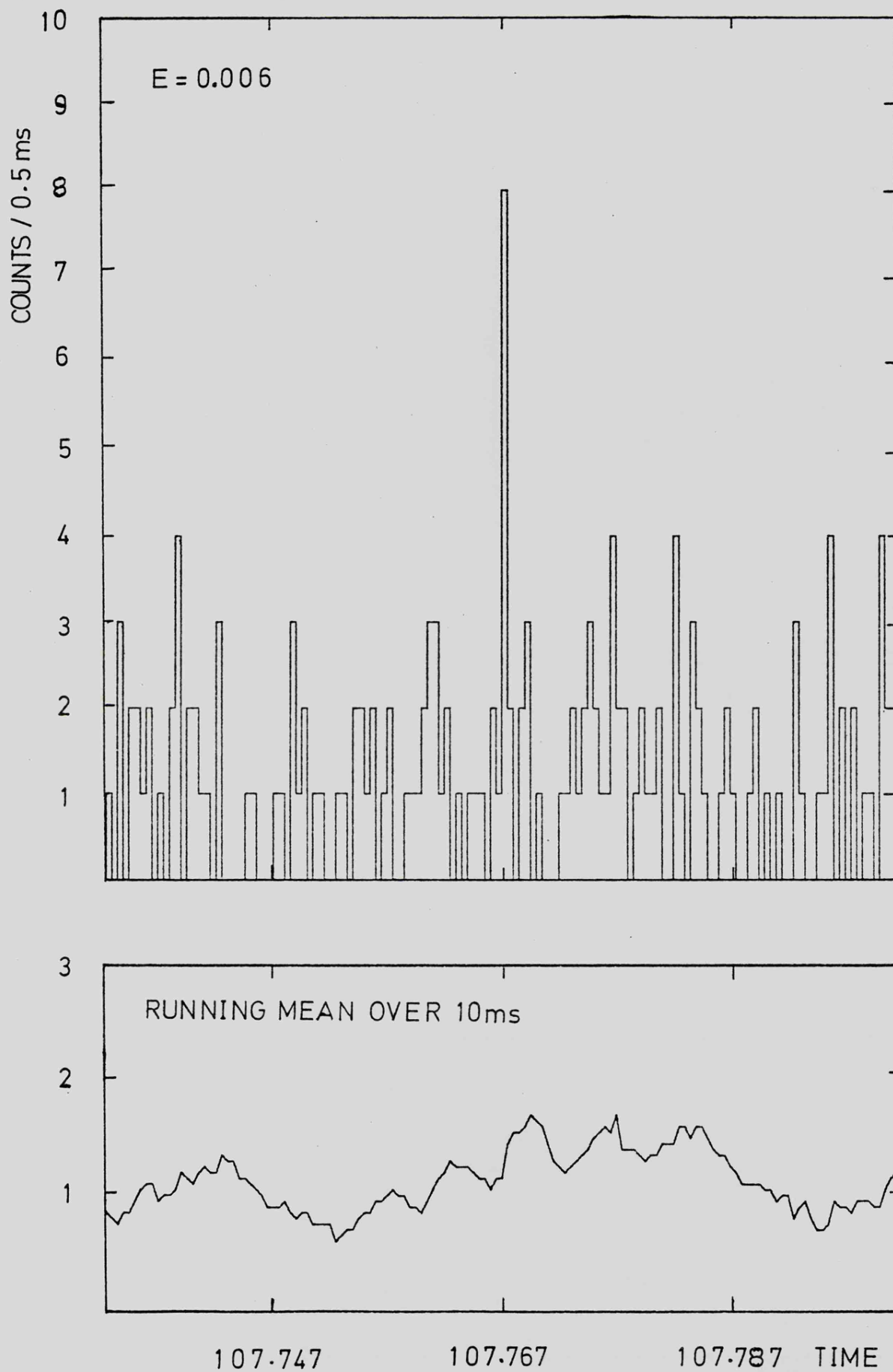


FIG 6.11 CYG X-1 BURST NO.4

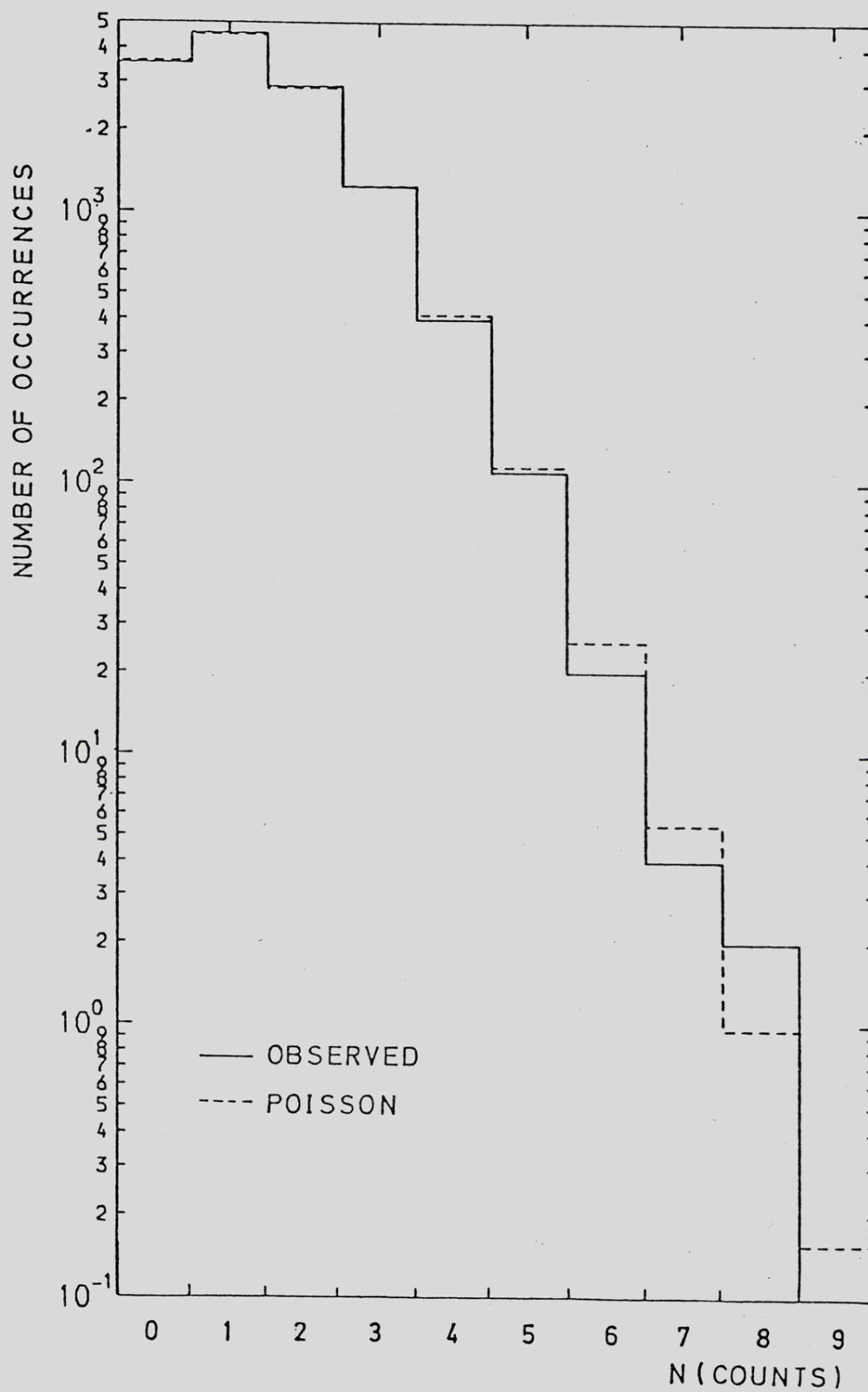


FIG 6.13 OBSERVED DISTRIBUTION OF COUNTS / 0.5 ms BIN

COUNTS / BIN	BIN SIZE mS					
	0.25	0.5*	1.0	2.0	4.0	8.0
0	0.99	0.98	1.00	1.03	1.27	-
1	1.01	1.02	0.99	1.02	1.15	3.32
2	1.01	1.00	1.00	0.98	0.92	0.73
3	0.92	1.00	1.00	0.98	0.97	1.03
4	0.87	0.98	0.99	1.01	1.10	1.53
5	0.96	0.90	0.97	1.04	0.86	0.73
6	0.55	0.77	1.11	0.96	1.07	0.66
7	-	0.70	0.92	1.02	1.00	1.30
8	-	1.95	1.00	0.92	0.93	0.76
9	-	-	0.84	1.09	1.07	0.93
10	-	-	1.10	1.02	1.13	1.21
(n) 11	-	-	-	1.06	0.89	0.98
12	-	-	-	0.96	0.90	1.15
13	-	-	-	0.78	0.95	0.66
14	-	-	-	1.04	0.97	0.92
15	-	-	-	0.65	1.07	1.06
16	-	-	-	1.70	1.18	1.17
17	-	-	-	4.70	0.87	0.94
18	-	-	-	-	0.84	0.97
19	-	-	-	-	1.12	1.11
20	-	-	-	-	1.61	0.89
21	-	-	-	-	1.07	0.92
22	-	-	-	-	0.77	1.10
23	-	-	-	-	1.44	0.97
24	-	-	-	-	1.40	1.09
25	-	-	-	-	-	1.23
26	-	-	-	-	-	0.88
27	-	-	-	-	-	0.60
28	-	-	-	-	27.3	0.96

FIG 6.14 RATIO OF OBSERVED/ EXPECTED N(n)

&gt;1.0 EXCESS &lt; 1.0 DEFICIT

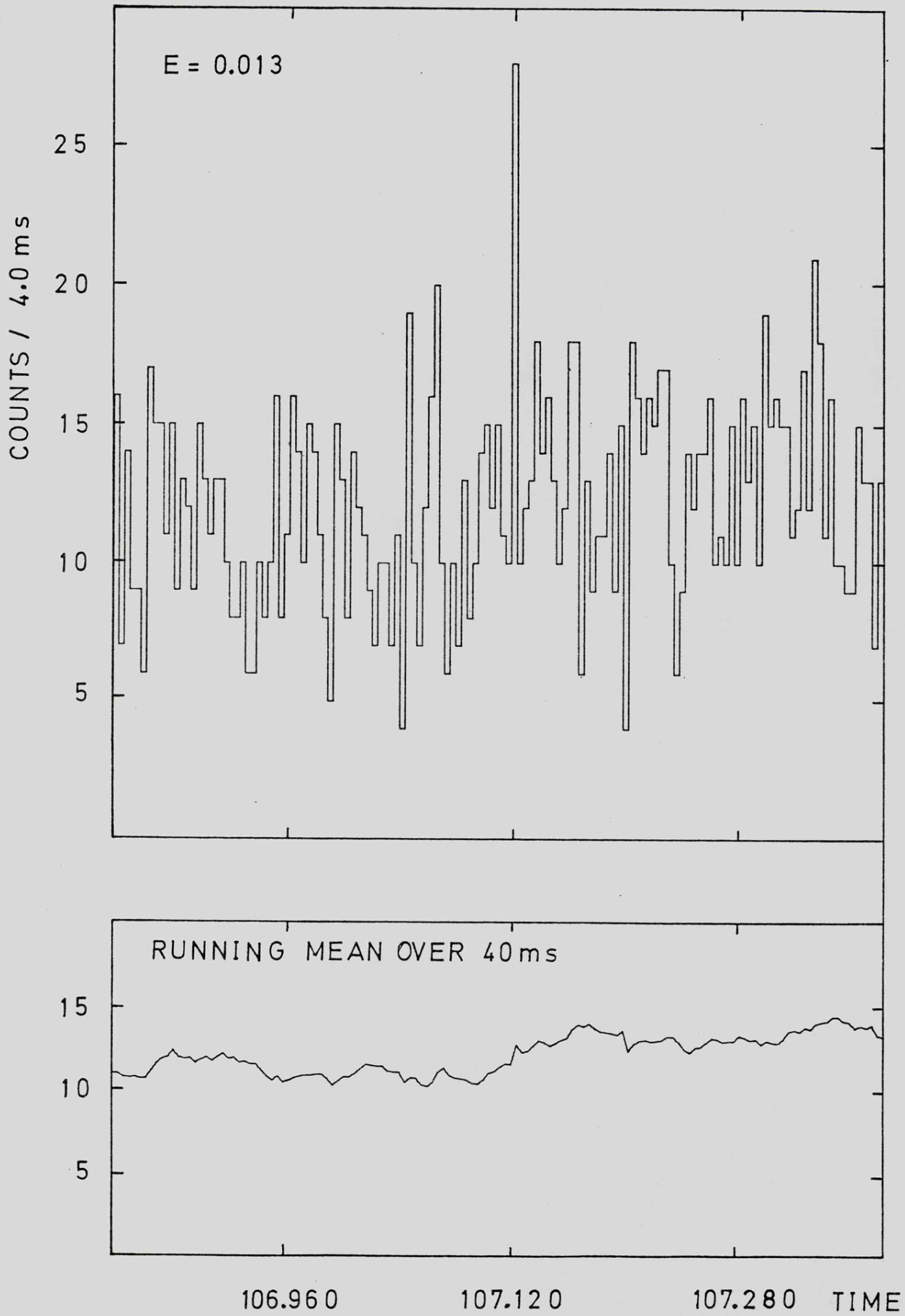


FIG 6.15 CYG X-1 4 ms BURST NO.3

is provided by fig. 6.12 which shows 1.2 seconds of data encompassing all the interesting features. The expectation value of each of these events is listed below in table 6C.

TABLE 6C

Feature	Counts/0.5 mS	Expectation/320 bins
1	8	0.02
2	6 each	0.68
	6+6 (1mS bin) uncorrected	0.009
	9 search	0.003
	9 corrected	0.019
3	7	0.37
	7+6 (1mS bin) uncorrected	0.009
	28 search (4mS bin)	0.013
4	3	0.006
5	7	0.045

Fig. 6.13 shows a comparison of the observed and expected bin heights summed over the entire exposure of 40 intervals, the difference being negligible.

A search for bursts of other durations was made by varying the bin widths from  $250\mu\text{S}$  to 8 mS. These results are tabulated in fig. 6.14 where values greater than one indicate an excess to that expected and values less than one a deficit. In fact, bins of 0.5 mS fortuitously appear to have a marginally higher chance of excess. The apparent 2 mS burst (17 counts) actually has a local expectation value of 0.034. The 4 mS burst (28 counts) however has an expectation value of 0.013 in its interval which is still less than 0.037 for the entire exposure. This feature shown in fig. 6.15 is therefore the most significant burst detected and is similar to the Toor (1976) detection of bursts from Circ X-1 in that it also contains evidence of more rapid internal structure (burst no. 3). Two 1 mS bursts with  $E \sim 0.01$  have been found but these are 'selected' pairings of 0.5 mS bins to which a

correction factor should be applied as described later. The interval over which the local mean was obtained was also varied by a factor of two either way but this made little difference to the expectation values.

### 6.3.2 Interpretation of Probability

The use of Poisson statistics in the case of Cyg X-1 has been questioned by Weisskopf et al. (1977) and this is discussed in the final part of this chapter. Leaving this point aside for now, it is very reasonable to ask if the analysis has been biased in any way, since the Poisson probability function varies rapidly around the range of values we are dealing with as is shown by the table in fig. 6.16. It was stressed earlier that the start point for the binning was completely arbitrary but having obtained some histogram plots we are in a position to shift the origin by  $-120\mu\text{S}$  and turn one of the features in fig. 6.10 into the peak of 9 in fig. 6.17. This is of course biasing the result but this origin could have been chosen quite by chance thereby dramatically decreasing the expectation value of the highest bin in the interval from 0.02 to 0.003. In fact, any shift from  $-96\mu\text{S}$  to  $-164\mu\text{S}$  will produce the same result and since the origin can be located to  $2\mu\text{S}$  relative to the  $500\mu\text{S}$  bin there was a 14% probability of obtaining the 9. All the bins can be moved about to an accuracy of 0.4% of their width, without an overlap condition if only the highest count examples are selected. This 'clustering' search method has also been used on the Cyg X-1 data and table 6D shows the relative bin count numbers for both this method and the arbitrary start case.

The results are now heavily biased and clearly Poisson statistics are no longer valid. The statistical treatment required has been described by Press and Schechter (1974) and results in a correction factor of order

COUNTS / BIN	(λ) MEAN RATE/DIN OVER INTERVAL									
	0.5	1.0	1.5	2.0	2.5	3.0	3.5	4.0		
0	194.1	117.7	71.4	43.3	26.3	15.9	9.7	5.9		
1	97.0	117.7	107.1	86.6	65.7	47.8	33.6	23.4		
2	24.3	58.9	80.3	86.6	82.1	71.7	59.2	46.9		
3	4.0	19.6	40.2	57.7	68.4	71.7	69.1	62.5		
4	0.51	4.9	15.1	28.9	42.8	53.8	60.4	62.5		
5	0.051	0.98	4.5	11.5	21.4	32.3	42.3	50.0		
6	0.004	0.16	1.13	3.85	8.9	16.1	24.7	33.3		
7	-	0.023	0.24	1.10	3.18	6.9	12.3	19.1		
8	-	0.003	0.045	0.28	0.99	2.59	5.40	9.5		
9	-	-	0.008	0.061	0.28	0.86	2.10	4.23		
10	-	-	0.001	0.012	0.069	0.26	0.73	1.69		
11	-	-	-	0.002	0.016	0.071	0.23	0.62		
12	-	-	-	-	0.003	0.018	0.066	0.21		
13	-	-	-	-	-	0.004	0.018	0.063		

FIG 6.16 EXPECTATION VALUE N(n) - 320 BIN INTERVAL

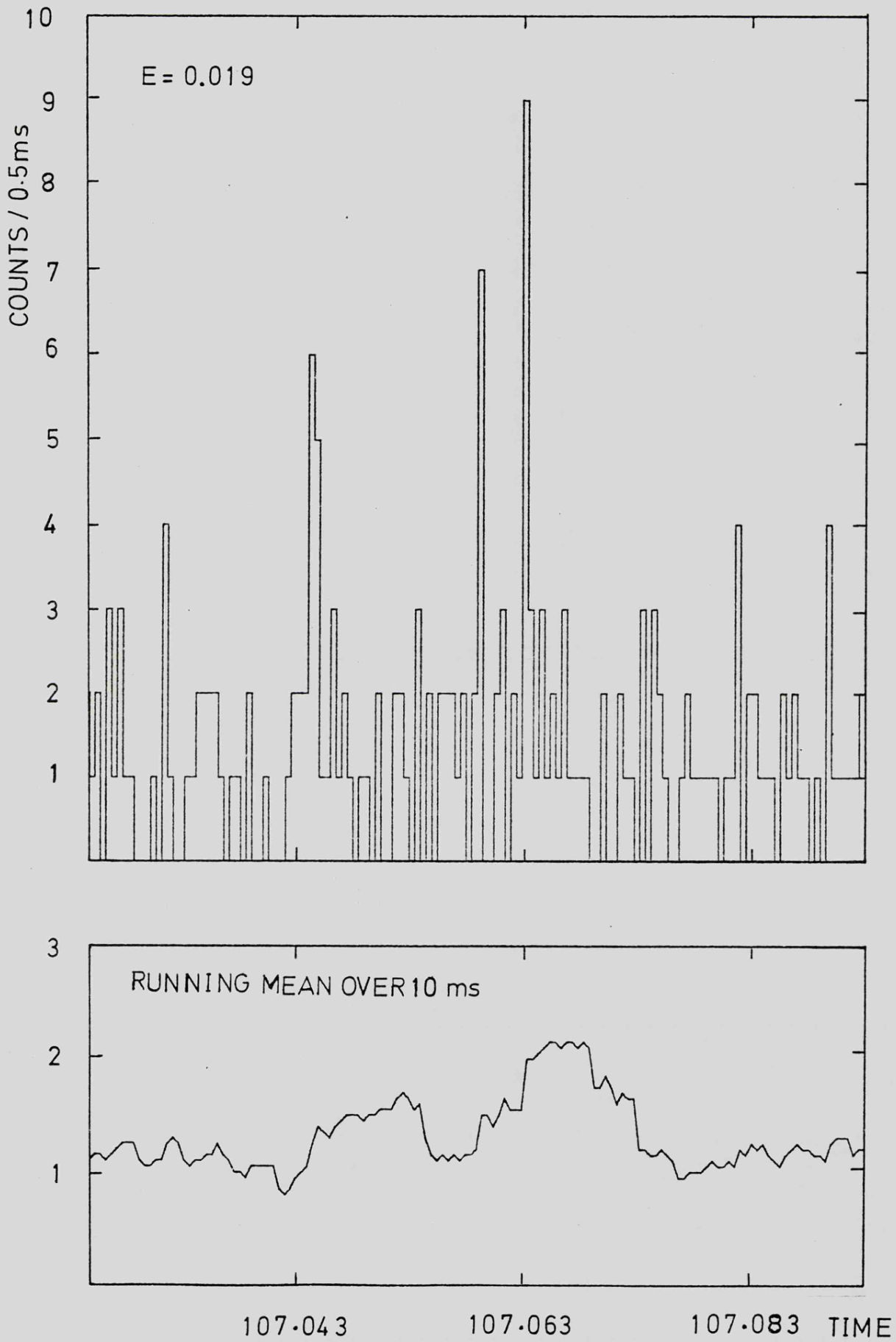


FIG 6.17 CYG X-1 BURST NO.2

TABLE 6D

Height(n)	Poisson Prediction	N(n) a priori	N(n) search	Search Corrected
6	24.2	20	78	22.7
7	5.5	4	19	4.3
8	1.0	2	4	0.8
9	0.15	0	1	0.16

$$K_o \left[ \frac{1 - \gamma^{-1} \exp(1 - \gamma^{-1})}{1 - \exp(-\gamma^{-1})} \right]$$

where  $K_o$  = counts in bin

$\gamma$  = overdensity =  $K_o / \text{mean counts per bin } (\lambda)$

For the height 9 bin in question the local mean is 1.34 which in the above equation gives a correction factor of 6.3. This factor measures the fraction of  $K_o$  flares which are lost in a priori binning but found in a continuous scanning (clustering search) of the data. In the routine a priori binning scheme not all  $K_o$  count flares will be found since some will straddle two bins, the resulting dilution preventing their discovery. For the example above, the simple expectation value for the  $K_o = 9$  flare of 0.003 becomes 0.019 since the bin position was defined after scanning the data.

The same effect reduces the search mode results in table 6D to be roughly equivalent to those of the a priori binning. In short nothing has been gained but the fact remains that quite by chance the single 9 that exists in the data may have occurred and significantly increased the probability of the 'burst'.

The above effect results from the ability to move the bins about at will rather than the a priori constraint imposed on Rothschild's data by the interfacing of the electronics to the telemetry system.

Individual resolution elements of  $320\mu\text{S}$  for 1974 or  $160\mu\text{S}$  for 1976 will obey Poisson statistics but how have these been combined to produce the  $640\mu\text{S}$  bins in fig. 1.4 and how were these combined to form the shaded bins of 1.28 mS? This is a simpler case of the freedom in binning the SL-1306 data, but such detailed information is not presented in Rothschild's papers. The bursts however are clearly not in a continuous set of 1.28 mS bins and therefore this 'selection' indicates that the assumption of simple Poisson statistics is no longer strictly correct.

### 6.3.3 Aligned Bursts

Although according to the Rothschild analysis method the 'bursts' are not significant it is still worthwhile to examine the count distribution within the bursts in the hope of finding some underlying pattern. A clustering search was repeated to extract the precise arrival time of each count contributing to the bursts together with those in the preceding and following few milliseconds. These counts can then be simply re-binned and summed to produce a composite burst profile since the shape of individual bursts is statistically meaningless. The problem here is how to align the bursts relative to each other, the actual summation being trivial since each count is effectively precisely located in time rather than pre-binned as in the Rothschild case. This has been done separately for bins of height 7 and 8+9 in the hope that the first represents generally random contributions and that the second will reflect a second class of events more attributable to Cygnus X-1. The flexibility of the data suggested three possible types of alignment, the results being shown in fig. 6.18.

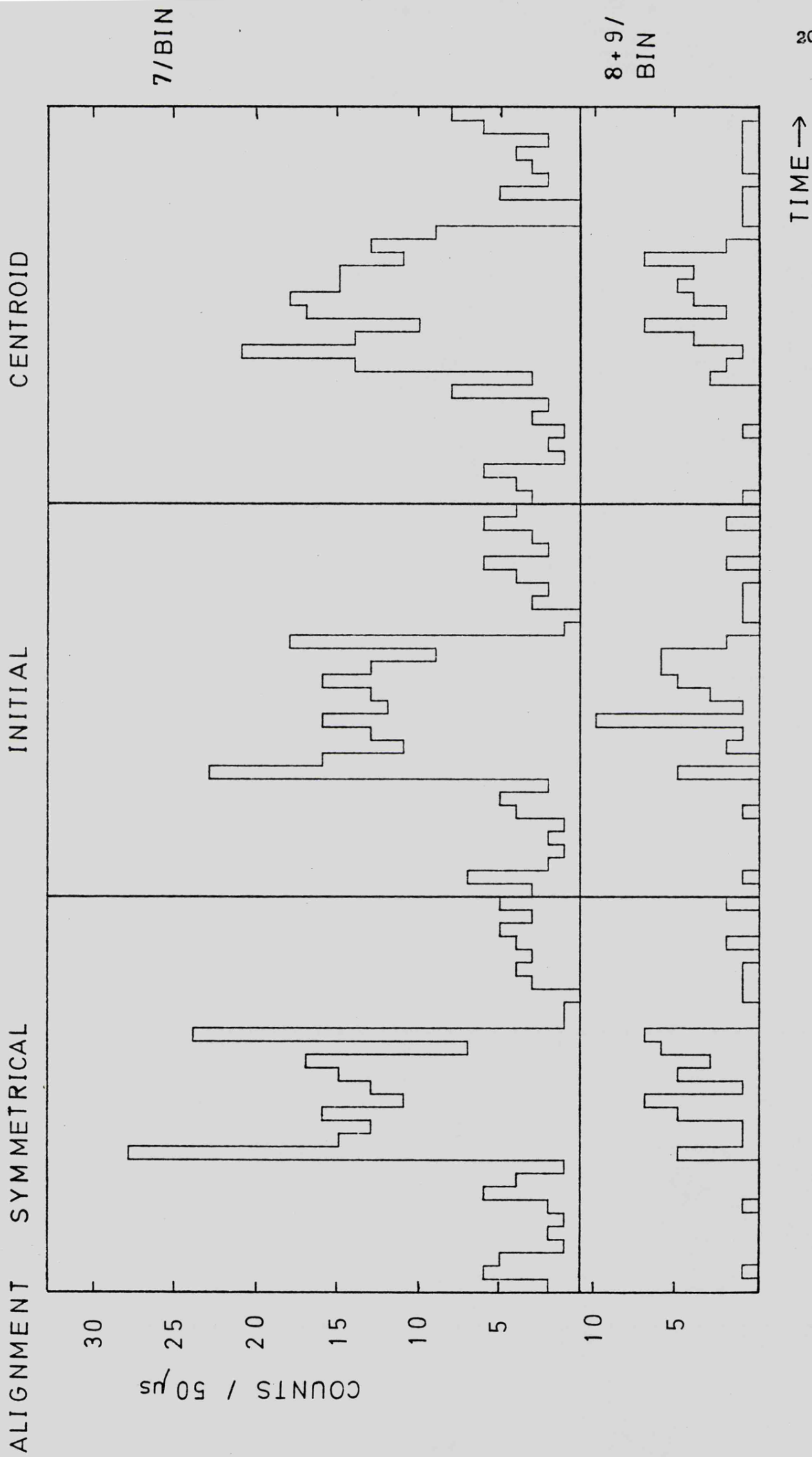


FIG 6.18 SUPERIMPOSED PROFILE OF SEARCHED FOR 0.5ms BURSTS

### Symmetrical

In this case each burst has been aligned symmetrically between its first and last count. Since as mentioned earlier there is a definite tendency for the clustering of events to occur over intervals of 0.5 mS this biases the first and last bin of the summed profile.

### Initial

In this case each burst is aligned from its initial event, thus biasing the first bin of the profile. There is also a tendency for a 'mirror' peak to occur, again due to the 0.5 mS clustering effect.

### Centroid

This method was used by Rothschild to produce the composite burst profile in fig. 1.4. The counts are simply binned about the centroid of the burst which does not produce the biases of the previous cases.

All three cases use precisely located counts and hence do not suffer the problem of aligning overlapping bins but what, if anything, do they reveal? All three methods for the height 7 bins seem consistent with a uniform random rate. The 8+9 cases, though appearing not to be random, are somewhat similar to each other and suggest a multiple peak structure.

#### 6.3.4 Energy Data

The PHA data is potentially useful in differentiating between the two classes of bin heights in fig. 6.18. Table 6E shows the energy distributions of these cases, together with those of the calibration source and the derived spectrum of Cygnus X-1.

TABLE 6E

PHA	Total c/sec	CAL c/sec	CYG c/sec	7+8+9 counts	8+9 counts	9 counts
1	1370	39.6	109.6	18	6	1
2	2131	45.6	205.0	34	6	3
3	2222	56.0	217.2	24	6	3
4	2292	126.9	168.5	28	10	1
5	2788	261.6	137.8	32	6	1
6	1452	114.2	53.9	21	5	0
7	648	3.0	41.4	11	1	0
8	517	7.7	7.4	6	1	0

Rothschild found the mean energy of the bursts  $2\frac{1}{2}\sigma$  below that of Cygnus X-1 in general with the exception of his one anomalous burst of higher mean energy. The results in table 6E, however, show the similarity between the 7+8+9 bins and the Fe<sup>55</sup> spectrum, reflecting the contamination of the Cygnus data by the random calibration events. The 8+9 bins appear much the same and although the statistics are very poor, the single 9 reflects the Cygnus peak between channels 2 and 3.

This does not really suggest that the located 'bursts' belong to a separate class of differing energy to the mean Cygnus spectrum.

#### 6.3.5 Autocorrelation of Bursts

A further method to demonstrate some peculiarity of the interval containing the bursts was to try an autocorrelation analysis. The 1.2 seconds of data in fig. 6.12 was processed for the interval up to  $2,000\mu\text{S}$  at  $2\mu\text{S}$  resolution and compared with the autocorrelation of the following 1.2 seconds of data. No difference was discernible and the spikes in fig. 6.19B near the  $400\mu\text{S}$  point did not disappear when

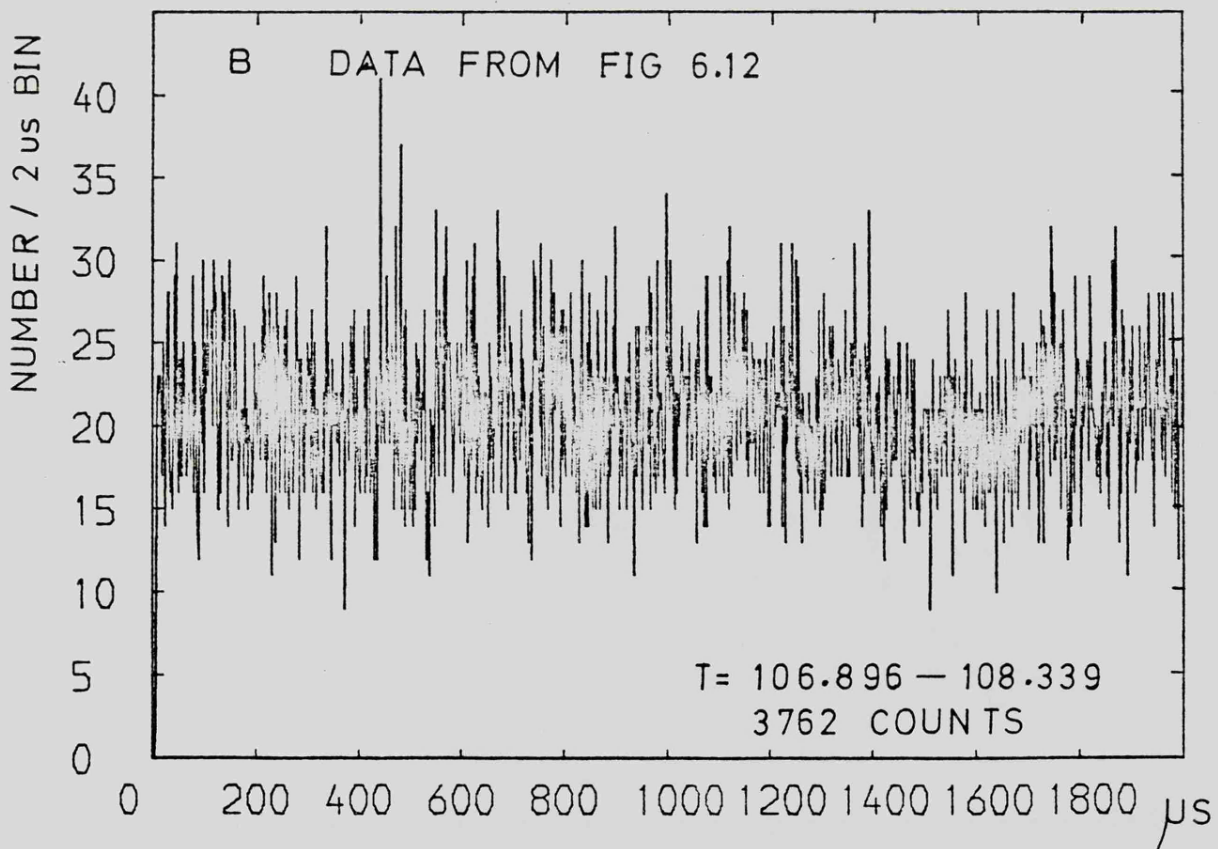
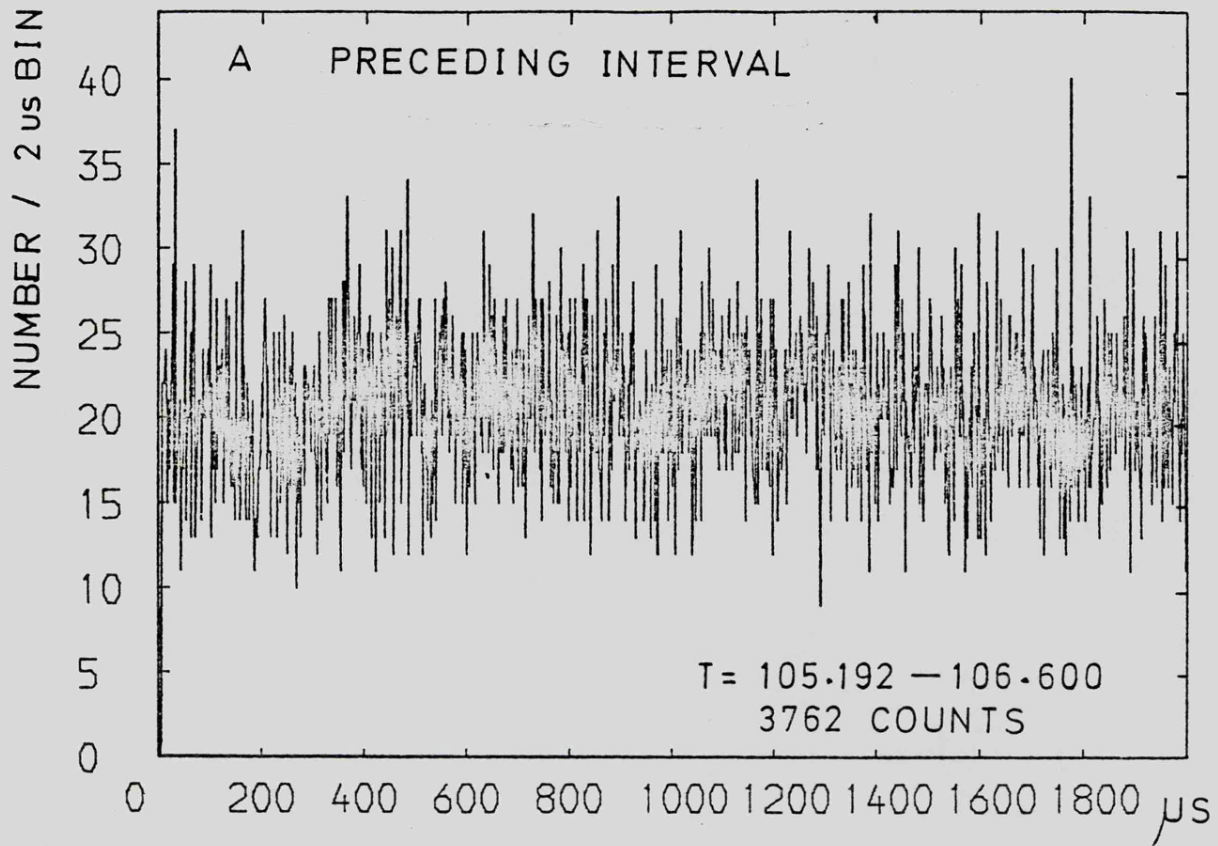


FIG 6.19 AUTOCORRELATION FOR CYG X-1 BURSTS

the individual counts contributing to the 8 and 9 height bins were removed.

#### 6.3.6 Ringling of Bursts

This really refers to the idea of the bursts coming in bunches or singly. Any such effects will be enhanced by combining all of the bursts in the same way as before but this time greatly increasing the time interval included on either side. This has been done for the 7+8+9 and the 8+9 cases, the time interval chosen being  $\pm 20$  mS. Fig. 6.20 shows the results, the noise on each side of the bursts being consistent with a constant rate. Since the number of counts in a peak goes as  $N$  and the scatter either side as  $\sqrt{N}$ , the 7+8+9 case shows a clearer peak simply because more events are included. There is no clear evidence of any multiple burst or ringing structure, the plot reflecting somewhat the data in fig. 6.10.

#### 6.3.7 Periodicity of Bursts

Recently it has been shown by Boldt (1977) that a basic 9.9 mS underlying period is present in parts of the G.S.F.C. data of 1974 and 1975 near to the most prominent millisecond bursts. This is interpreted as a disturbance in the accretion disc that is carried around inner Keplerian orbits for a fraction of a second at an essentially constant frequency. Radiation is not always emitted in our direction each time the disturbance comes round, the sequence finally ending after a particularly large burst (the millisecond burst). This feature was found by forming a composite burst profile as in fig. 6.20 but over an interval of  $\pm 1$  sec rather than  $\pm 20$  mS. A few small excesses were found away from the central millisecond burst which occurred nearly at multiples of a basic 9.9 mS period and these located

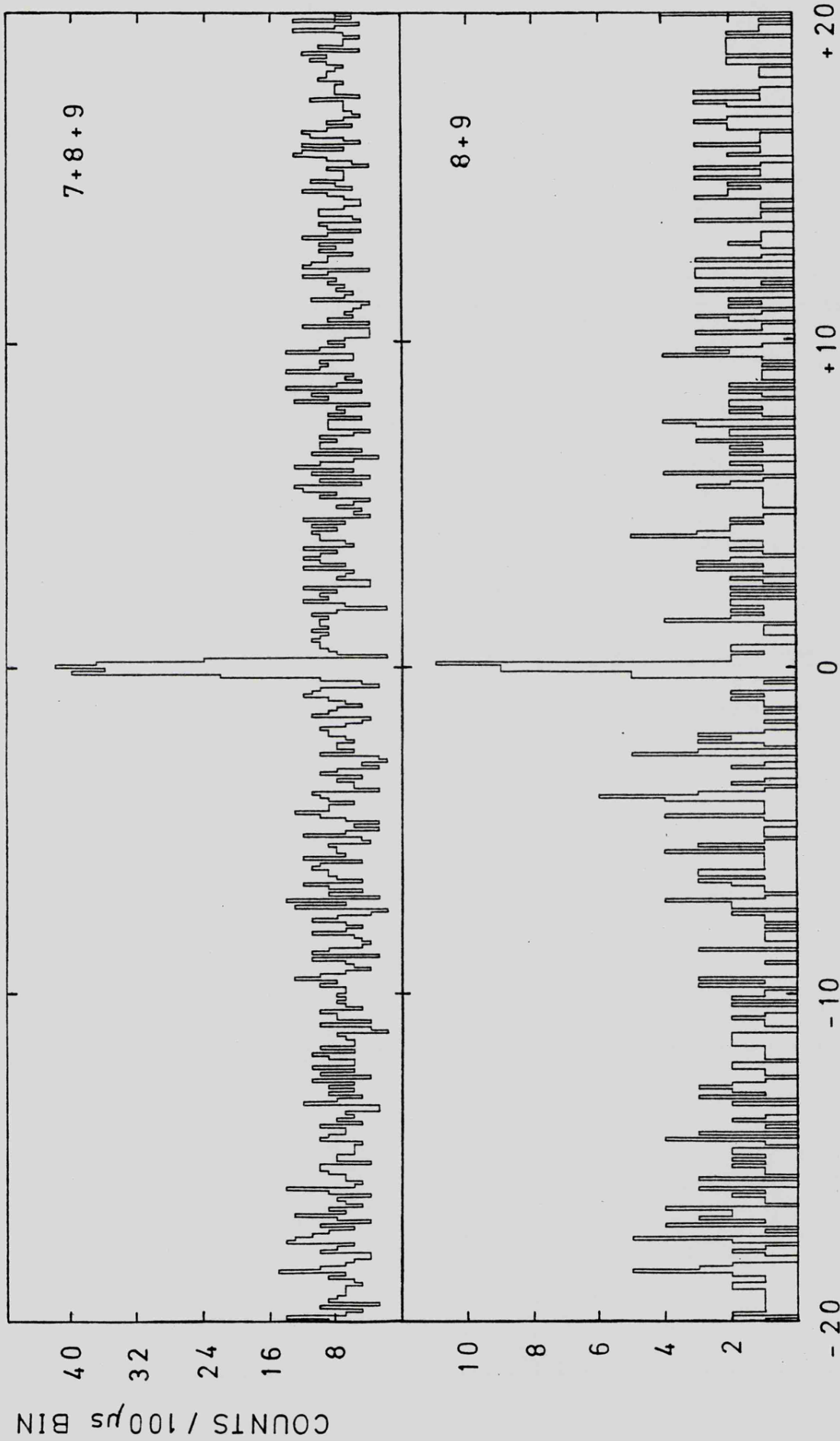


FIG 6.20 CENTROID ALIGNED BURST PROFILE ( RINGING )

segments were then summed with the data folded modulo a 9.946 mS period to statistically establish the accurate phasing of these excesses relative to the main burst. In all, 8 cases were found prior to the burst and 2 after the burst.

This analysis cannot be repeated exactly for the short SL-1306 data set but has been attempted for  $\pm 0.5$  sec. There is no indication of any similar type of periodicity, the summed data not allowing a first estimate period to be found.

#### 6.4 Statistical Aspects of Burst Identification

In dealing with the burst phenomena we have two basic questions to ask. Firstly, are the detected bursts real in terms of a statistical approach that allows for any selection effects and, in defining such a test, which must of course be chosen by the scientist, are the types of burst found actually reliant on the technique chosen? Secondly, believing the bursts found to be real and significant, do they really imply that such rapid variability exists in the source and are they the cause or effect of longer time scale features such as the shot pulses?

##### 6.4.1 Shot Model Interpretation

The concept of the bursts powering the shot noise model has been strengthened by the assertion of Weisskopf et al. (1977) that bursts of the observed size and rate are a basic consequence of the shot noise model. Previously, it has proved impossible to determine unambiguously the shot rate, intensity, decay time and fraction of total intensity due to all the shots but the recent mathematical technique of Sutherland et al. (1977) has solved this problem. They applied this to existing Uhuru data to yield the above parameters which appear to be

constant and independent of the source state. They obtain a value of 30% for the flux in the shots, a 0.5 sec decay time and a rate of about one per second.

These parameters have then been used by Weisskopf et al. (1977) in both a computer simulation and an analytical method, both of which yield an excess of large count bins to that expected from simple Poisson statistics. The prediction of the model can agree well with the observations of Rothschild et al. (1976) and also shows the same deficit of zero height bins. The actual pulse profile used in the simulations is apparently not too critical but an exponential pulse can be used to match the observed shot pulse shape.

These shots, however, have an instantaneous rise time and it is certainly open to question that any 'high frequency spikes' in the output of the simulation may be due simply to the unrealistic severity of the pulses. This provides an explanation for the bursts tendency to occur during enhancements which are interpreted as a piling up of the shot pulses. This correlation can, however, also be explained by another effect as described in section 6.5.4.

A similar simulation to that of Weisskopf has been set up by Gowan (1978) who, using the above parameters and the 1306 count rate, obtains the data in table 6F. This is compared with the simple Poisson expectation and the actual observed values.

The simulation result is less like the actual observed data than the simple Poisson prediction probably due to the large random background contribution in the data which makes the above comparison rather a poor test. The flux in the shots is  $\sim 12\%$  of the total flux rather than  $\sim 30\%$ .

TABLE 6F

N(n) a priori binning

n	Poisson	Simulation	Observed
0	3616	3225	3535
1	4496	4387	4566
2	2865	3036	2910
3	1264	1475	1240
4	417	567	401
5	115	194	110
6	24.2	46	20
7	5.5	12	4
8	1.0	1.75	2
9	0.15	0.88	0
10	0.02	-	0

#### 6.4.2 Multi Bin Flares

The treatment of this by Press and Schechter (1974) has been dealt with in section 6.3.2. Since the data in fig. 1.4 are 'selected' multi bin flares, some correction factor must also be applicable to them and may well increase the chance expectation of the 1.28 mS features to above 0.01.

#### 6.4.3 Locally Enhanced Mean ( $\lambda$ )

The problem of defining correctly the local mean has also been discussed by Press and Schechter (1974). The probability of a burst can depend on the time variability of the source over a much longer time scale than the actual burst since any broad small increase in  $\lambda$  can be statistically undetectable in the noise but will dramatically increase the local probability of a single bin excess.

A correction factor to the significance test is given by Press and Schechter (1974) as

$$\exp \left[ K_o (1 - \gamma^{-1}) \right] \Delta \lambda$$

where  $K_o$  = bin height  
 $\gamma$  =  $K_o$ /local mean ( $\lambda$ )  
 $\Delta \lambda$  = total uncertainty in local mean

#### 6.4.4 Interval for $\lambda$ itself

For detection of bursts the signal to noise ratio of the data ( $K_o/\lambda$ ) is crucial. The background contribution to  $\lambda$  will typically be much smaller ( $< 25\%$ ) than the mean flux from the source which may itself vary substantially. As noted previously, Rothschild et al. (1976) found the bursts to occur during enhancements but no such features are found in the SL-1306 data. The value of  $\lambda$  in any subset of the averaging interval is therefore more constant assuming that the subset is not so short that the statistical error is dominant. In Rothschild's data (fig. 1.4) the enhancements appear shorter than the chosen averaging interval and so the expectation value of the burst bin will decrease asymptotically as the  $\lambda$  is reduced by the inclusion of more bins. The actual chance of seeing the feature amongst the increased number of bins will however increase linearly and the product of these two factors for the overall chance expectation of the bin will pass through a minimum value. For a  $n = 12$  burst in fig. 1.4 this occurs for an interval of  $\sim 340$  bins which is remarkably close to the 320 actually used by Rothschild et al. (1974). To further demonstrate this aspect of the analysis the four cases shown in table 6G have been considered. The first example is the actual method employed by Rothschild et al. (1974) for the interval of 409.6 mS near

TABLE 6G

1)	409.6 mS	320 - 1.28 mS bins $\lambda = 2.80$ E(13) = 0.002 E(12) = 0.009 E(11) = 0.04	320 - 0.64 mS bins $\lambda = 1.40$ E(9) = 0.009 E(8) = 0.057 E(7) = 0.33
2)	81 mS	64 - 1.28 mS $\lambda = 4.08$ E(13) = 0.015 E(12) = 0.048 E(11) = 0.14	128 - 0.64 mS $\lambda = 2.04$ E(9) = 0.028 E(8) = 0.12 E(7) = 0.49
3)	409.6 mS at 81 mS rate	320 - 1.28 mS $\lambda = 4.08$ E(13) = 0.075 E(12) = 0.24 E(11) = 0.70	320 - 0.64 mS $\lambda = 2.04$ E(9) = 0.07 E(8) = 0.30 E(7) = 1.23
4)	16 mS	13 - 1.28 mS $\lambda = 6.46$ E(13) = 0.12 E(12) = 0.24 E(11) = 0.44	26 - 0.64 mS $\lambda = 3.23$ E(9) = 0.11 E(8) = 0.32 E(7) = 0.78

318.5 seconds after launch. The second case restricts the examination to the 80 mS enhancement actually shown in fig. 1.4, the following example extrapolating this rate back to a full 409.6 mS interval. Finally, the results for the central 16 mS of this figure from 318.484 to 318.510 are shown. The values indicate that the significance of the bursts decreases as the interval is reduced and none of the features in fig. 1.4 actually satisfies the  $E < 0.01$  limit when  $\lambda$  is determined only from this 80 mS sample. This interval contains 64 bins which allows a reasonable determination of the mean.

If we assume that the bursts had not occurred in an enhancement and simply use the mean  $\lambda$  for fig. 1.4 of 2.04 per 0.64 mS bin we find from table 6H that the SL-1306 features in fig. 6.10 are relatively more significant.

TABLE 6H

	n	SL-1306		GSFC	
		fig. 6.10		fig. 1.4	
		E(n)	N	E(n)	N
Basic Bin	9	0.003	0	0.07	1
	8	0.022	2	0.30	2
	7	0.13	0	1.23	0
Paired Bin	13	0.0013	0	0.075	1
No	12	0.006	1	0.24	2
correction	11	0.028	0	0.70	1
applied					

#### 6.4.5 Number of Bursts in Sample

If N intervals are searched for bursts of height n with  $E < E_L$  (where  $E_L$  is the chance expectation limit for defining a burst) then the total expected rate is given by

$$\sum_{1}^N \sum_{n=n^*}^{n^*+3} E(n)$$

where  $n^*$  = threshold for each interval and values beyond  $n^*+3$  are ignored. For the SL-1306 data we obtain the following table.

TABLE 6I

Bin size	N	$E < 0.01$	$E < 0.02$
0.5 mS	56	0.29	0.56
1.0 mS	28	0.19	0.33

Comparing the expected and observed bursts over the entire sample is however meaningless if the aperiodic bursts are naturally infrequent or if a combination of source count rate and statistical method conspire to make them appear so. This second important point is discussed in section 6.5.4.

## 6.5 Discussion

### 6.5.1 Shot Model

The shot noise model for Cygnus X-1 suggests the formation, emergence and decay of short-lived local 'hot' spots in the accretion disk. An alternative idea to this is that the 0.5 sec time scale of the shots is the result of reverberation of a millisecond pulse produced in the disc on the surrounding material (Canizares, 1976). The periodicity of millisecond bursts found by Boldt (1977) also occurs over timescales ( $\sim 0.7$  sec) much the same as that of the shots. This is also supported by Rothschild et al. (1974) who noted that the only instance of bursts bunching in their data (fig. 1.4) occurs during a peak of enhanced intensity where the increased X-ray flux possibly causes a local thinning of the disc. The actual data obtained by SL-1306 is not inconsistent with the well established shot noise model.

### 6.5.2 Bursts

Sunyaev (1973) has suggested that the turbulence in the accretion disc can lead to hot matter being convected out of the inner portions of the cloud, these spots existing for about one orbit. The duration therefore depends on the angular momentum of the collapsed object and shorter time structure may also be present due to a beaming effect of the radiation. It has been suggested by Canizares et al. (1976A), using SAS data, that millisecond aperiodic variability on a

smaller scale than seen by Rothschild may be a permanent feature of the source.

The information obtainable from observed bursts has been discussed by Rothschild et al. (1974). The loss of energy ( $U$ ) corresponding to a mass ( $M$ ) reaching the innermost stable orbit of a black hole is given by

$$U = \eta Mc^2$$

where  $\eta$  is the efficiency of gravitational energy release

and  $\eta = 0.06$  for the Schwarzschild metric

$\eta = 0.42$  for the Kerr metric.

The energy released by this mass in a burst of length  $\Delta t$  and luminosity  $\Delta L$  will be

$$\Delta t \Delta L = \epsilon U = \epsilon \eta Mc^2$$

where  $\epsilon$  is the efficiency of X-ray generation relative to other losses.

$\epsilon \rightarrow 1$  for thermal processes

$\epsilon = 10^{-5}$  for non-thermal processes

These two values define limits in the above equation and therefore the mass  $M$  associated with any observed burst is

$$1) \quad 10^5 > \frac{0.06 Mc^2}{\Delta L \Delta t} > 1 \quad \text{taking } \eta = 0.06$$

As has previously been mentioned the typical time  $\Delta t$  associated with the innermost stable orbit of a black hole is  $0.5 M_x/M_\odot$  for the Schwarzschild metric and  $0.06 M_x/M_\odot$  for the Kerr rotating case implying an expected  $\Delta t$  of 0.6 - 5.0 ms or less (Novakov and Thorne, 1972).

The various parameters deduced for the bursts seen by SL-1306 are shown below.

T	0.5 mS	4.0 mS
$\delta$	6.0	2.25
$M_x$	1 - 8 $M_\odot$	17 - 68 $M_\odot$
$M_{KERR}$	$4 \times 10^{19} > M > 4 \times 10^{14} \text{ g}$	$11 \times 10^{19} > M > 11 \times 10^{14} \text{ g}$
$M_{SCH}$	$6 \times 10^{18} > M > 6 \times 10^{13} \text{ g}$	$1.6 \times 10^{19} > M > 1.6 \times 10^{14} \text{ g}$

It is important to note that during the short observation of Cygnus X-1 no intervals of enhanced activity quite like those seen by Rothschild were observed.

If a periodicity is found for the bursts then in the case of a Schwarzschild metric

$$\frac{\Delta T}{\tau} \leq \left[ \frac{1.5}{R} \right] \left[ \frac{R_G}{R} \right]$$

where  $R_G = 2GM/c^2$  (Schwarzschild radius)

$\Delta T$  = burst duration

$\tau$  = burst period

$R$  = radius of burst disturbance

Further if the bursts are confined to a sharp period the mass of the black hole can be estimated from

$$\frac{M_x}{M_\odot} = \left[ \frac{\tau}{6 \times 10^{-4} \text{ s}} \right] \left[ \frac{R}{R_o} \right]^{-3/2}$$

where  $R_o = 3R_G$  (innermost stable orbit)

Boldt (1977) has found

$$M_x \gg 8 \pm 2 M_\odot$$

and  $\tau_{MIN} \gg 4 \pm 1 \text{ mS}$

### 6.5.3 Sensitivity to Bursts of Different Intrinsic Intensity

As stated previously the ratio  $K_0/\lambda$  is crucial for the detection of bursts. The background contribution to  $\lambda$  will typically be much smaller ( $< 25\%$ ) than the mean flux from the source so the rejection efficiency of the guard system is not too critical. The mean rate  $\lambda$  from the source will therefore be approximately proportional to the detector area as will the intensity of the bursts  $K_0$ . The expectation value however decreases very rapidly and only a modest increase in area takes bursts from being marginal cases to clear certainties.

To identify a burst some statistical analysis must be used and this will automatically define a clear division between detectable and undetectable features for any given detector area and source state. The analysis of Rothschild can conveniently be expressed in diagrammatical form as shown in fig. 6.21. Every feature seen must lie on one of the diagonal straight lines, only those above the centre dotted line being detectable as a burst at the  $E < 0.01$  limit for an averaging interval of 320 bins. If the source has a characteristic burst size of a particular  $\gamma$  value it is clear that small experiments with a low mean value  $\lambda$  per bin and low  $K_0$  are immediately at a disadvantage. A low mean per bin is inevitable since the bin size must be less than or equal to the time scale of interest. Doubling the detector area and observing the same  $\gamma$  flare with  $\lambda$  and  $K_0$  at twice the size may just be sufficient to cross the threshold line. Fig. 6.22 also shows the position of the individual bursts mentioned in the literature, the relevant data being shown below in table 6J. The Toor (1977) result for Circinus X-1 is also included for comparison.

Cygnus X-1 will presumably emit flares of varying  $\gamma$  but there may well be an actual characteristic value since large  $\gamma$  flares

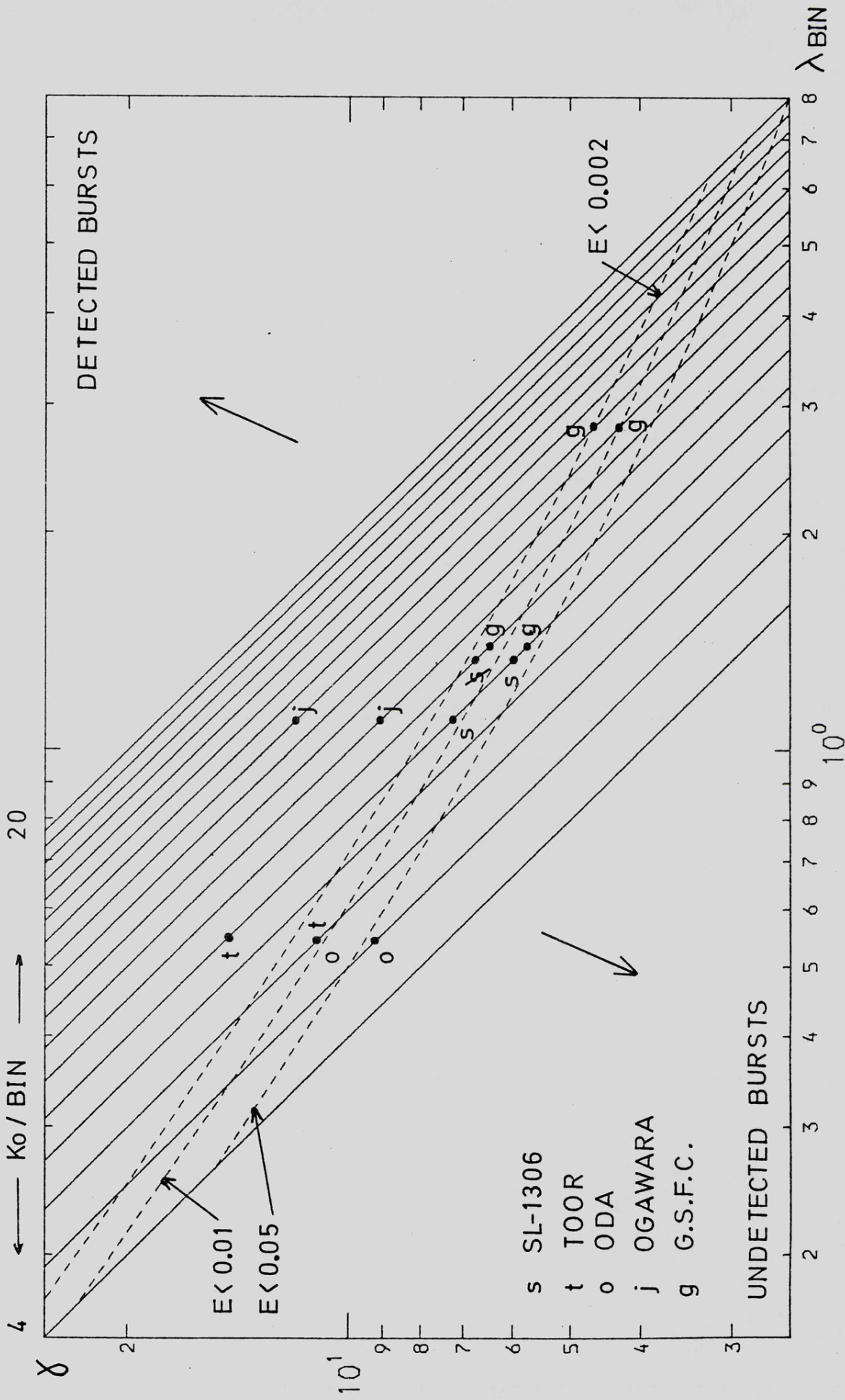


FIG 6.21 BURST LOCATION DIAGRAM ( 320 BIN INTERVAL )

TABLE 6J

Experiment	mean rate c/sec	$\frac{A}{A_{GSFC}}$	$\frac{I_x}{I_x GSFC}$	Bin mS	$\lambda$ /Bin	Burst $K_o$
SL-1306	1200	2.94	0.39	0.5	1.34	8
				1.0	2.68	12
Ogawara	650	0.5	1.28	1.25	1.1	10-13
G.S.F.C.	1020	1.0	1.00	0.64	1.4	8,9
				1.28	2.8	11-13
Oda	275	0.27	0.73	1.0	0.55	5,6
Toor	550	0.50	-	1.0	0.55	6,8

may be very rare and low  $\delta$  flares cannot be detected with small experiments.

The prominent bursts seen by several observers are certainly real and cannot be explained away entirely by the various factors discussed in section 6.4. The apparent occurrence of bursts only during intervals of enhanced activity also follows naturally from the limitations imposed by any reasonably competent statistical analysis. It is suggested that the number of bursts found simply depends on the ratio of the time the source is above the threshold statistical level (only during enhancements for small experiments) to that below. The flares seen by Rothschild ( $\delta = 3$ ,  $K_o = 8$ ) would not be seen for  $K_o = 4$  between enhancements and therefore these bursts are far more frequent than the observation immediately suggests and can be expected to occur all the time as has been tentatively suggested by Canizares et al. (1976A) using SAS 3 data. The above factor explains why bursts are not commonly seen from Cyg X-1 and indeed it is somewhat surprising that the relatively small detector system of Ogawara et al. (1977) located so many. This implies a higher characteristic  $\delta$  during this

particular observation. If bursts power the shots, since shots are present all the time bursts will also be and literally dozens per flight might exist just below previous detector area thresholds.

Again if we assume that burst intensity is proportional to source intensity (reasonable if bursts power the shots) then tripling the detector area can be approximately negated by halving or less the intrinsic source intensity. This is the case for SL-1306, bursts at approximately 1 per second being seen during a non-enhanced lowish intensity state. Presumably had the data been obtained for a full 240 sec then a whole series of bursts ranging from those actually seen up to several  $K_0 = 27$ ,  $\gamma = 6$  flares might have been detected. This represents a fundamental change in the certainty of the observation since the chance expectation value decreases from  $10^{-2}$  to  $\sim 10^{-9}$  for bursts such as those seen by Rothschild et al. (1974). Such an observation would also enable a clear study of the burst periodicity since many of the weaker preceding bursts would be individually detectable.

#### 6.6 Summary

The Cygnus X-1 data obtained at binary phase 0.25 by SL-1306 is consistent with the shot noise model first proposed by Terrell (1972).

Burst number 4 in fig. 6.12 is significant using the Rothschild analysis method but the others are not although two more are found with  $E < 0.02$ . It was shown in section 6.4.4 why the features in fig. 6.10, which are numerically similar to Rothschild's data in fig. 1.4, did not stand up to the  $E < 0.01$  acceptance limit, the reason being simply that the Rothschild bursts occurred during an enhancement of shorter duration than the averaging interval.

This interpretation suggests that the SL-1306 bursts scale

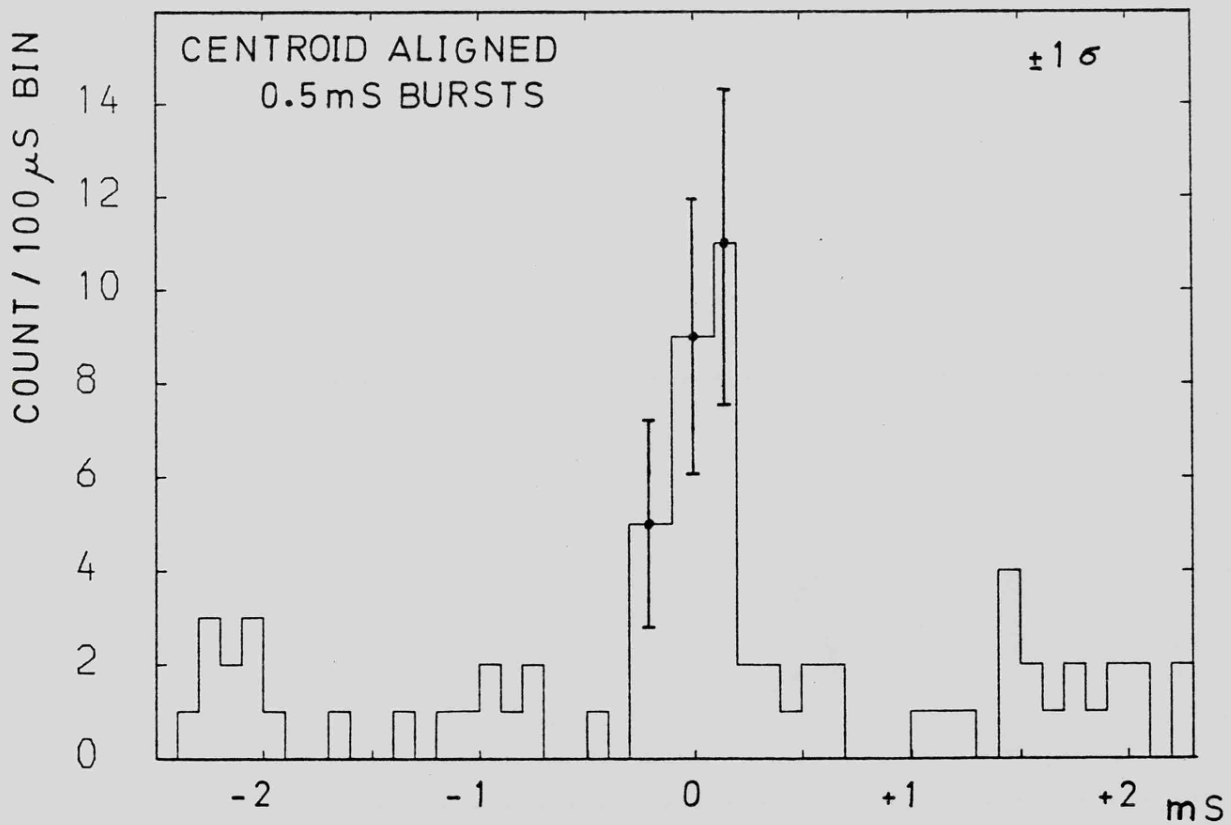
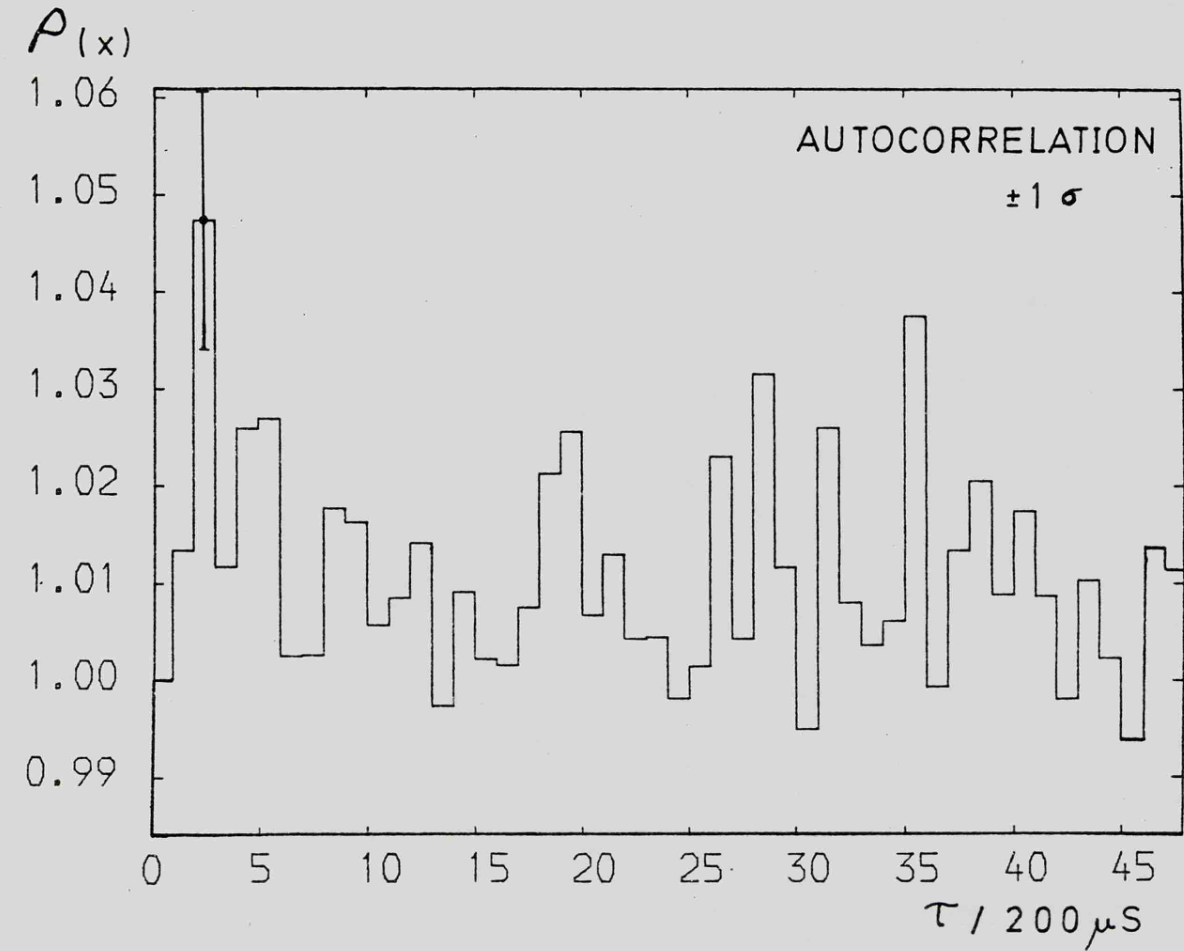


FIG 6.22 CYG X-1 BURSTS

to an intrinsic intensity  $\sim \frac{1}{3}$  of those seen by Rothschild et al. (1974) who note that their analysis method would have found none of the bursts they actually located if their detector had been only half the area (equivalent to a source of half the intensity). The aligned burst profile (fig. 6.22) may therefore be meaningful and suggests that the latter half of the 0.5 mS bursts are more intense than the first and end sharply. This time scale of 0.5 mS in November 1976 compares with 0.6 - 0.7 mS in September 1975 (Ogawara et al. 1977) and 1.0 mS in October 1973/74 (Rothschild et al. 1977). Three bursts have been found when less than 0.24 are expected by chance during the 3 sec in which the count rate is sufficient to detect these  $\delta \sim 6$  bursts at the  $E < 0.02$  significance level. This implies a rate of  $\sim 1$  sec which would appear to positively support the suggestion by Canizares et al. (1976A) that aperiodic millisecond structure is a constant feature of the source. The autocorrelation function in fig. 6.22 however indicates that any such activity cannot be enormously frequent, though there is a slight indication of an excess around  $500 \mu\text{S}$ .

Further study of millisecond bursts demands both a high data rate telemetry system and a detector area of order  $0.5 \text{ m}^2$  or greater. There can be no substitute for detector area and with the rapid demise of HEAO-A no such experiment exists in the near future.

Appendix AHoneycomb Transmission

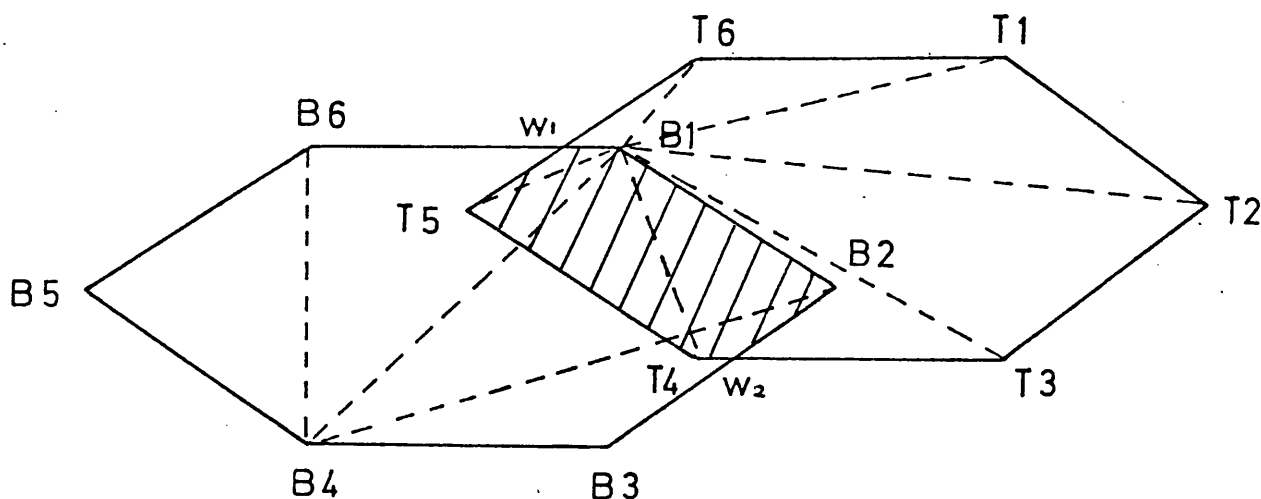
If we treat the collimator as a set of regular squashed hexagons we need only consider one cell and can represent its corners using cartesian co-ordinates in three dimensions. We can view this cell from any position in space by applying suitable rotational transformations about each axis in turn, such as about the Z axis.

$$x_1' = x_1 \cos \theta - y_1 \sin \theta$$

$$y_2' = x_1 \sin \theta + y_1 \cos \theta$$

where  $x_1$   $y_1$  are the old co-ordinates and  $x_1'$   $y_1'$  the new,  $\theta$  being the angle of rotation. Applying a typical set of transformations to all corners of a cell we get the plan view below where the subscript T denotes the top face and B the bottom face. The area of the B plane shape can be found by dividing it into triangles and summing the area of each one as given by the determinant

$$-\frac{1}{2} \begin{vmatrix} x_1 & y_1 & 1 \\ x_2 & y_2 & 1 \\ x_3 & y_3 & 1 \end{vmatrix}$$



This is then repeated for face T which in our case produces an identical result. We can now determine some of the vertices of the cross hatched section by taking each point in turn round the B plane, joining it to the 6 points in the T plane to create six triangles and summing the resultant areas. Clearly if we choose  $B_1$  we would get the same area as that of face T since that will be true for any point within shape T. However, for point  $B_6$  the area will naturally be greater than face T indicating  $B_6$  lies outside the shape. In this way we will obtain points  $B_1$  and  $B_2$  and by doing the opposite and considering each T point in turn within the B shape we shall find  $T_5$  and  $T_4$ . The remaining points  $w_1$  and  $w_2$  can be located by searching for intersections of the cell sides and for hexagonal cells there are always 2 of these together with 2 or 4 included corners. The order in which these points are obtained is quite arbitrary so to calculate the area of the shaded region by the method already described they must first be arranged into a clockwise angular sequence. The result is the actual geometrical area presented to a parallel beam of X-rays from the direction defined by the initial rotation transformations. This area can be expressed as a fraction of the normal incidence area and by taking many offset positions one can construct a complete transmission map such as in fig. 2.6. This method can be applied to any N sided semi-regular collimator cell and will also work for several layers of obstructing sections by redefining the effective shape at each level.

Appendix BField Theory

When a function  $U$  and its derivatives are single valued, finite and continuous functions of  $X$ , then by Taylor's theorem

$$1) \quad U(x + h) = U(x) + hU'(x) + \frac{1}{2} h^2 U''(x) + \frac{1}{6} h^3 U'''(x) + \dots$$

and

$$2) \quad U(x - h) = U(x) - hU'(x) + \frac{1}{2} h^2 U''(x) - \frac{1}{6} h^3 U'''(x) + \dots$$

adding 1) and 2) gives

$$U(x + h) + U(x - h) = 2U(x) + h^2 U''(x) + O(h^4)$$

where  $O(h^4)$  denotes terms containing fourth and higher powers of  $h$ .

Assuming these higher powers to be negligible

$$3) \quad U''(x) = \left[ \frac{d^2 U}{dx^2} \right] \approx \frac{1}{h^2} [U(x + h) - 2U(x) + U(x - h)]$$

If we now assume  $U$  is a function of the independent variables  $X$  and  $T$  we can sub-divide the  $X$ - $T$  plane as shown in fig. A.4 into sets of equal rectangles of sides  $\delta x = h$  and  $\delta t = k$ .

The co-ordinates of the representative mesh point  $P$  are  $x = ih$  and  $t = jk$  which we can denote as

$$U_p = U(ih, jk) = U(ij)$$

then by equation 3)

$$\left[ \frac{\partial^2 U}{\partial x^2} \right]_{ij} \approx \frac{U[(i+1)h, jk] - 2U(ih, jk) + U[(i-1)h, jk]}{h^2}$$

i.e.

$$4) \quad \left[ \frac{\partial^2 U}{\partial x^2} \right]_{ij} \approx \frac{U_{i+1,j} - 2U_{ij} + U_{i-1,j}}{h^2}$$

similarly

$$5) \quad \left[ \frac{\partial^2 U}{\partial t^2} \right]_{ij} \approx \frac{U_{i,j+1} - 2U_{ij} + U_{i,j-1}}{h^2}$$

Now in Poissons equation we have

$$6) \quad \frac{\partial^2 U}{\partial x^2} + \frac{\partial^2 U}{\partial t^2} + f(x,y) = 0$$

but as mentioned in chapter two all charges have been removed to the boundary therefore  $f(x,y) = 0$  and we have a simple hollow box the interior of which must satisfy Laplace's equation. Combining (4) and (5) in (6) we have

$$\frac{U_{i+1,j} - 2U_{ij} + U_{i-1,j}}{h^2} + \frac{U_{i,j+1} - 2U_{ij} + U_{i,j-1}}{h^2} = 0$$

which we can simplify to

$$7) \quad U_1 + U_2 + U_3 + U_4 - 4U_0 = 0$$

Every point in the mesh grid must satisfy this equation and the solution is obtained iteratively from a starting array of grid potentials derived from the boundary conditions of the box. The differences between the old value of  $U_0$  and the new value based on the four surrounding points should gradually decrease and the iteration can be stopped when sufficient accuracy has been obtained. The rate of convergence of this point relaxation method can be increased by over-relaxation, i.e. changing  $U$  by  $\frac{1}{4}$  to  $\frac{1}{2}$  more than is necessary to reduce the residual to zero

$$(V_1 + V_2 + V_3 + V_4) \frac{1}{4} = V_0 W$$

where  $W =$  relaxation factor.

Appendix CFIFO Tester

Shift register A presents 8 bit words to the FIFO down lines  $D_0$  to  $D_7$  and with the switch to earth each line will sequentially have 8 ones and zeros, the total period being 16 times that of the pulse generator. If, however, the switch is connected to 3 on shift register B a pseudo random sequence is presented to the input of shift register A. Control logic ensures that words are removed from the FIFO at the same rate as they are introduced, the comparator producing an error pulse if the FIFO output does not match the input data shifted by one bit, that is held in shift register C.

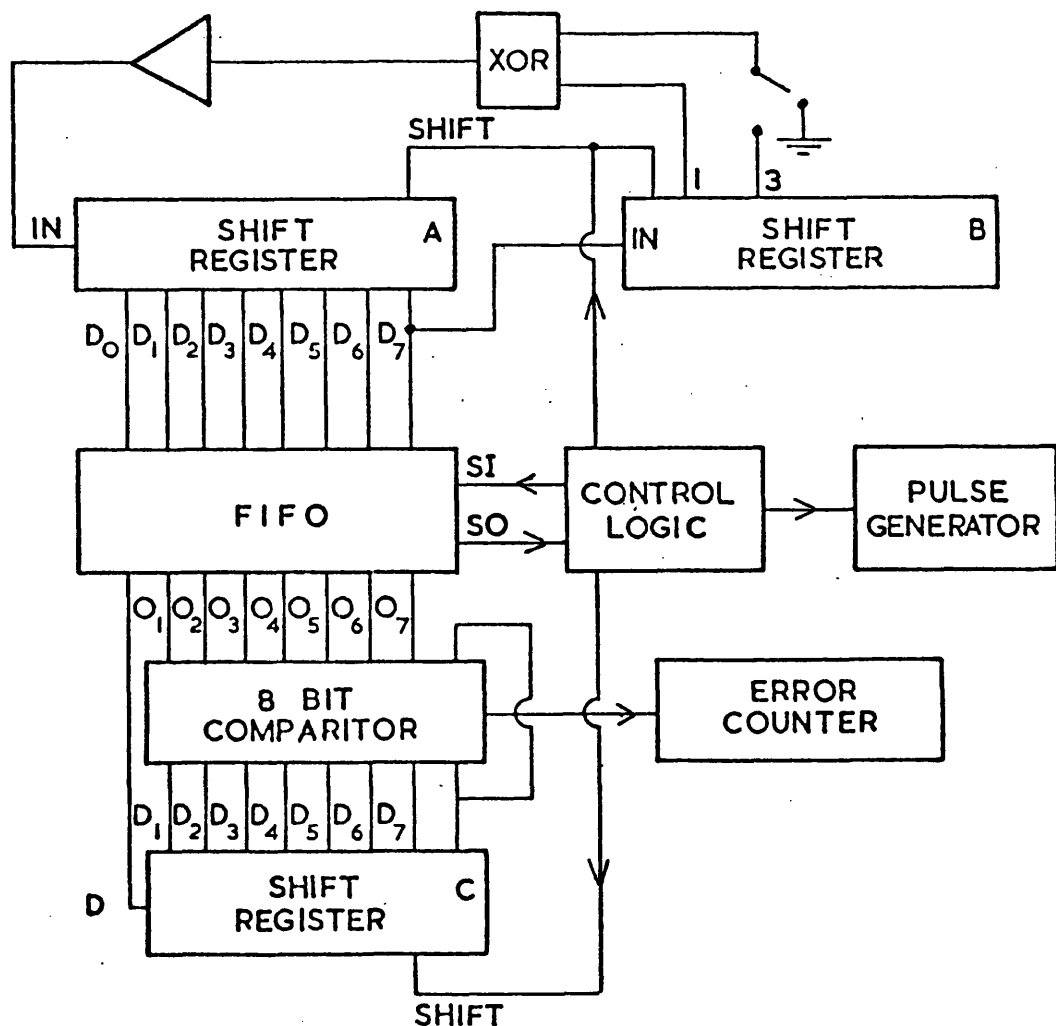


FIG. A-1 FIFO TEST BOX

Appendix DEnergy Fraction Circuit

The energy word flag generator circuit shown in fig. A.2 can be treated in two parts. The pre-set counter is re-loaded every  $2048 \mu\text{S}$  and every EVENT causes it to decrease in value by 1 until it is either loaded again or counts right down to zero producing an output pulse. The probability of an output pulse is given by summing the Poisson distribution

$$\sum_{j=0}^{j=N-1} e^{-x} x^j / j!$$

where  $N$  = pre-set value of counter (15 for flight)

$x$  = mean EVENT rate.

This can be evaluated directly or looked up in tables since it can be related to the incomplete gamma function

$$\frac{\Gamma(N, x)}{\Gamma(N)} = Q(\chi^2/\nu) = \sum_{j=0}^{N-1} e^{-x} x^j / j!$$

where  $\chi^2$  = chi-squared =  $2x$  and  $\nu$  =  $2N$ .

A plot of this function against count rate is shown in fig. A.3, the energy word curve in fig. 2.15 being derived from this.

The number of pulses to the UP input is given by  $fR$  where  $R$  is the clock rate (512 Hz) and  $f$  the above probability. The number of DOWN pulses is given by  $\alpha R$  where  $\alpha$  is the fraction allowed by rate multiplier  $A$ , so that the net change of the value in the counter in a small time is therefore

$$(fR - \alpha R) dt$$

Although the circuit varies in discrete steps it can be approximated to a continuous change so

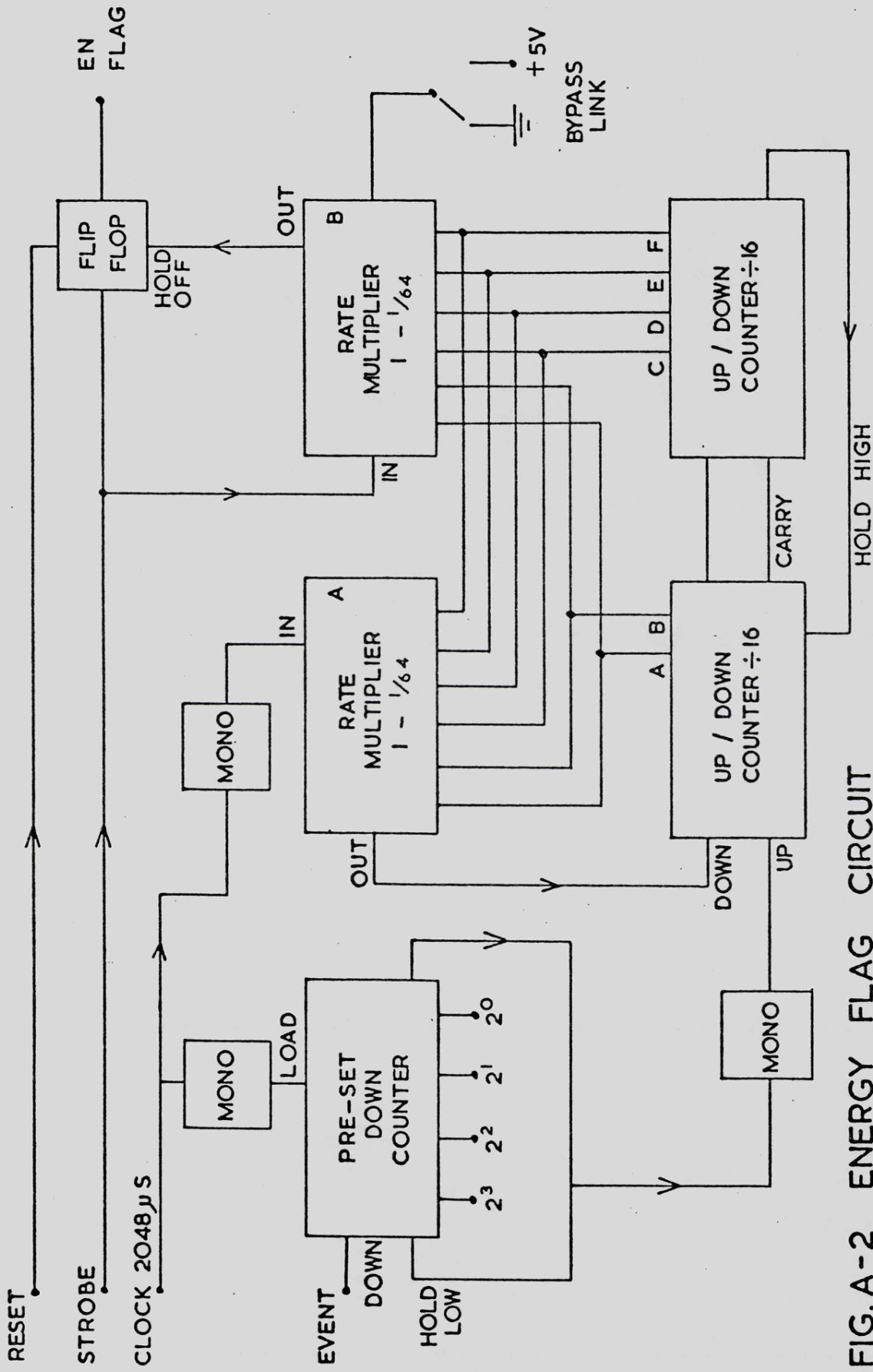


FIG. A-2 ENERGY FLAG CIRCUIT

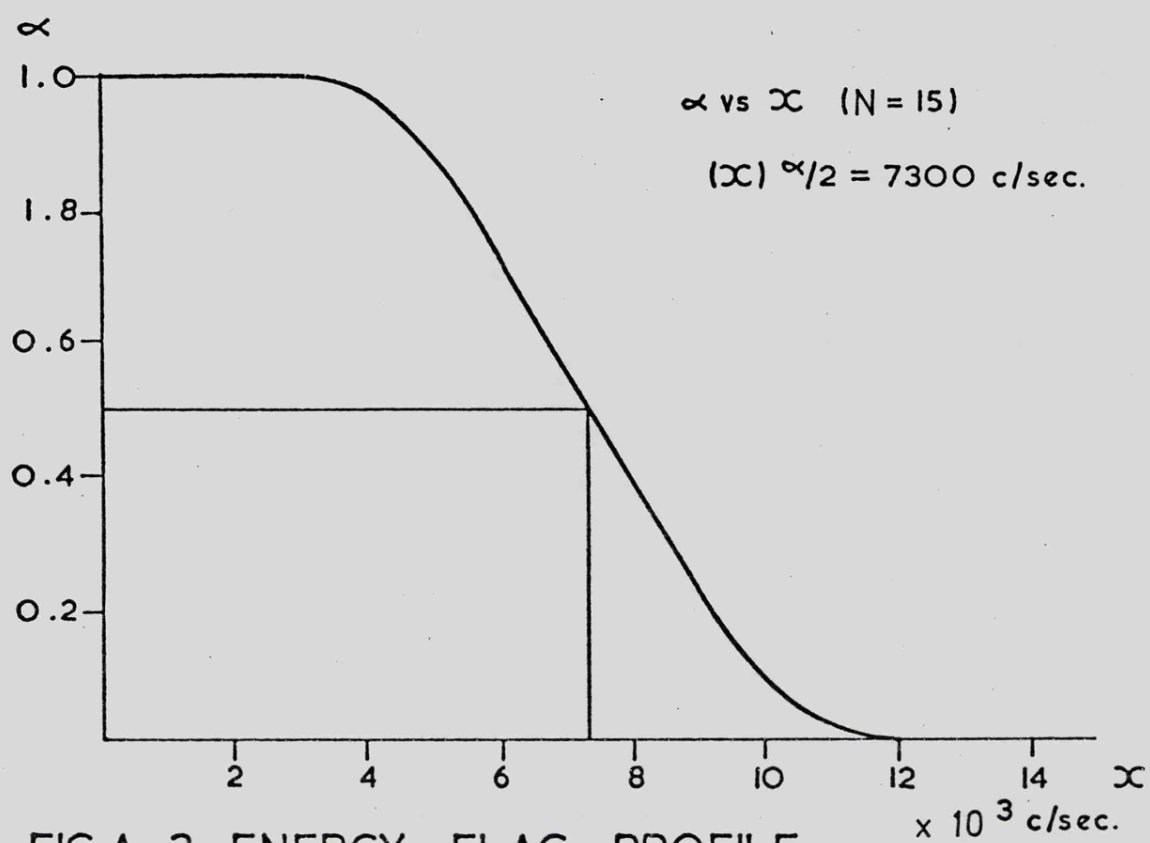


FIG.A-3 ENERGY FLAG PROFILE

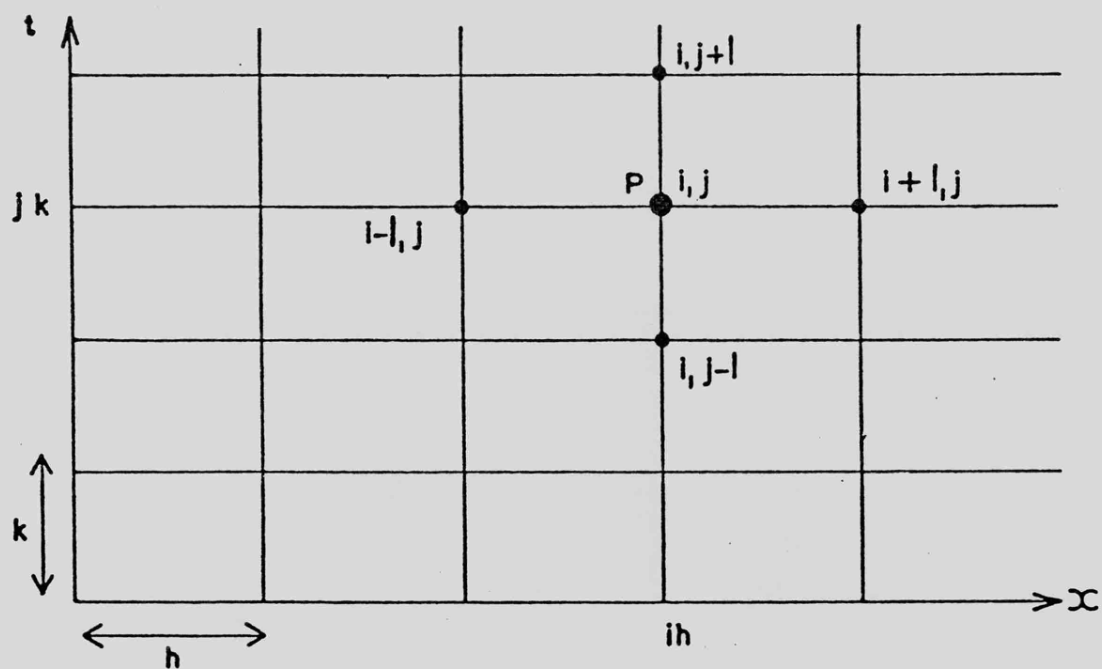


FIG. A-4 BOX GRID PATTERN

$$W \alpha = \int (fR - \alpha R) dt$$

where  $W$  is the maximum value of the counter (256)

$$\therefore \frac{d\alpha}{dt} + \frac{R}{N} \alpha = \frac{R}{N} f$$

which has the solution  $\alpha = K e^{-\frac{R}{N} t}$

This first order differential equation is like that of a simple RC integrator network so the second half of the circuit can be considered as a digital integrator. The time constant of the circuit is given by  $N/R$  and is 0.5 seconds. In the steady state

$$\frac{d\alpha}{dt} = 0 \quad \therefore \alpha = f$$

Rate multiplier B works in parallel with A and gradually inhibits more and more ENERGY flags as the incidence of pulses from the pre-set counter increases at higher mean EVENT rates.

The STROBE pulse is equivalent to EVENT but occurs on the following 4 MHz clock positive going edge with RESET immediately following to clear the flag.

Appendix ECheck Code Circuit

Error correcting codes were first described in detail in 1950 by R.W. Hamming (1950) and an extensive discussion can be found in Gallager (1968). In fig. A.6 the 8 shift register bits are combined within one chip but are drawn separately for clarity of operation and the mask pattern used is

$$1 \quad \vdots \quad 00011101$$

this being determined by the feedback paths of the 4 exclusive OR gates (XOR). This form of 8 bit mask when acting on a stream of up to 256 serially fed data bits forms a unique pattern at the output of each register cell. The pattern for the mask was selected from a compilation by Peterson (1968) and can be considered as the following degree 8 polynomial

$$X^8 + X^4 + X^3 + X^2 + 1 = P(X)$$

in which the roots are linearly independent.

The check code operation has been described for both the experiment and test gear but the software routine used the octal look up table in fig. A.5 which was constructed by simulating the flight circuit. This simplification is possible because the XOR and multiplication (AND) operations are both associative. The value of the check code registers (A to H) at any one time is easily extracted from the table by the following expression

$$CODE_{N+1} = \text{XOR}(\text{CODE}_N \cdot \text{DATA}) \cdot \text{AND} \cdot 377 \text{ ]} + 1$$

where the right hand side is the address 1 - 256 in the table of the new check code.

0				→				7
0	000	035	072	047	164	151	116	123
	350	365	322	317	234	201	246	273
	315	320	367	352	271	244	203	236
	045	070	037	002	121	114	153	166
	207	232	275	240	363	356	311	324
	157	162	125	110	033	005	041	074
	112	127	180	155	076	043	004	031
	242	277	230	205	326	313	354	361
	023	016	051	064	147	172	135	100
	373	346	301	334	217	222	265	250
	336	303	344	371	252	267	220	215
	066	053	014	021	102	137	170	145
	224	211	256	263	340	375	332	307
	174	141	106	133	010	025	062	057
	131	104	143	176	055	060	027	012
	261	254	213	226	305	330	377	342
	046	073	034	001	122	117	150	165
↓	316	323	364	351	272	247	200	235
	353	366	321	314	237	202	245	270
	003	036	071	044	167	152	115	120
	241	274	233	206	325	310	357	362
	111	124	163	156	075	040	007	032
	154	161	126	113	030	005	042	077
	204	231	276	243	360	355	312	327
	065	050	017	022	101	134	173	146
	335	300	347	372	251	264	223	216
	370	345	302	337	214	221	266	253
	020	015	052	067	144	171	136	103
	262	257	210	225	306	333	374	341
	132	107	140	175	058	063	024	011
	177	142	105	130	013	026	061	054
248	227	212	255	260	343	376	331	304

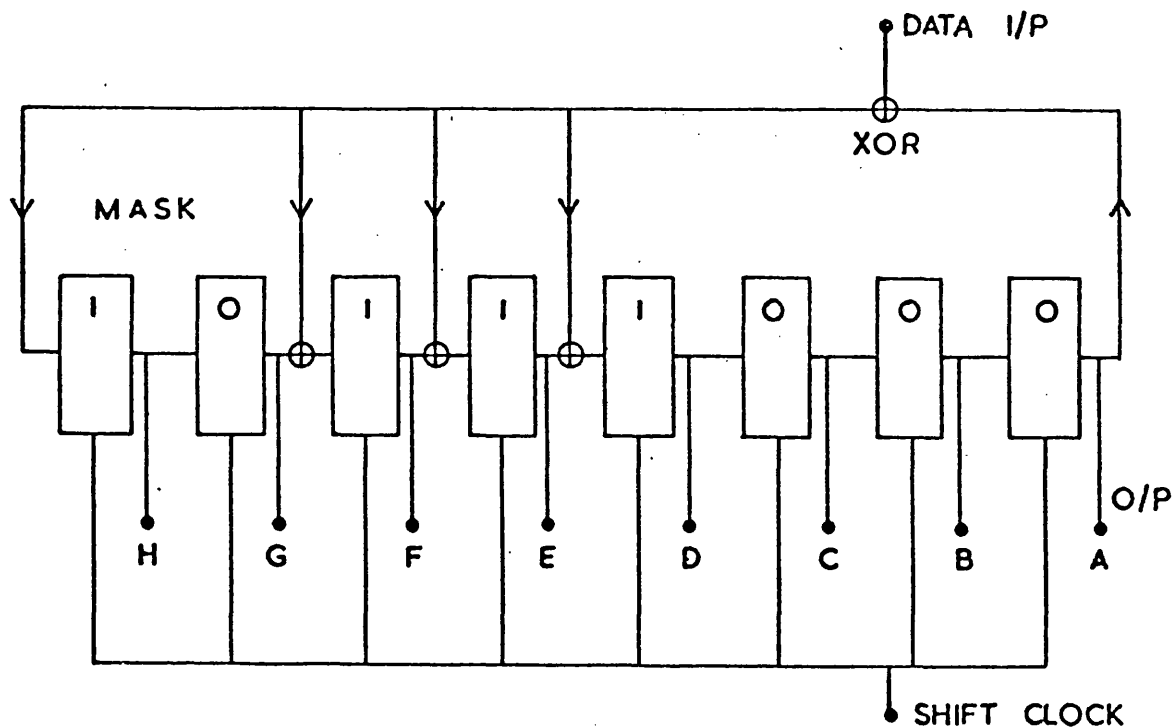
FIG.A-5 CHECK CODE TABLE (OCTAL)

DATA is the 8 bit data word

CODE<sub>N</sub> is the old check code value

This type of check code enables multiple errors to be detected but only single bit errors can actually be corrected. This can also be conveniently accomplished by means of a look up table.

FIG.A-6 FLIGHT CHECK CODE CIRCUIT



Appendix FAppleton P.C.M. Tape Format

The first block on the tape contains formatted descriptive text and the remaining blocks contain a block leader followed by a number of complete frames of digitised PCM data. Where data is missing due to SYNC being lost one or more dummy frames are inserted.

The descriptive text is simply various identification facts and is coded in ICL 1900 series character code which has to be corrected to CYBER 72 code for the University system. Each subsequent block has a data block header which contains 26 twelve bit words giving various status information such as the block number and length. Also available in this header is the date and time at the start of the block, this being obtained from the NASA 36 time code track and is expressed in days, hours, minutes, seconds and milliseconds. Each block contains 64 data frames so there are approximately 8 blocks for every second of data.

The actual data frames consist of 32 twelve bit words the first 2 containing special information and the other 30 containing words 3 - 32 of the PCM frame fig. 2.14. The first of these special words is known as a frame type word and identifies whether the frame contains data or is a dummy. If the frame is valid this word contains the time in milliseconds of the start of the frame. The second special word is known as a synchronisation word and contains the following three flag bits,  $B_0$  being the most significant.

$B_0$  - Set on detection of sync pattern

i.e. 1 for sync word

0 for data word

$B_1$  - Set when locked onto the sync pattern, i.e. the pattern is repeated after the correct number of data bits in the frame have been

detected.

$B_2$  - Set when checking the sync pattern, i.e. set when the first sync pattern has been detected after loss of data, but it has not been checked that the repeat interval is correct.

Bits  $B_4$  to  $B_{11}$  contain the trailing 8 bits of the sync pattern, the leading bits being examined but not output by the system. The remaining 30 data words are also preceded by the above flag bits  $B_0$  to  $B_3$  but bits  $B_4$  to  $B_{11}$  now contain the actual 8 bit data words we require.

REFERENCES

- Adams, D.J. and Ricketts, M.J.: 1973, *Astronomy and Space Science*, 24, 585.
- Aeroweb Information Sheet, Bonded Structures Division, CIBA-GEIGY (UK) Ltd.: 1973.
- Alme, M.L. and Wilson, J.R.: 1976, *Ap. J.*, 210, 233.
- Auriemma, G., Cardini, D., Costa, E., Giovannelli, F. and Ranieri, M.: 1976, NASA SP.389, p.485.
- Avni, Y., Fabian, A.C. and Pringle, J.E.: 1976, *M.N.R.A.S.*, 175, 297.
- B.A.C. Skylark Users Handbook, Space Systems Group: 1972.
- Bahcall, J.N., Rosenbluth, M.N. and Kulsrud, R.M.: 1973, *Nature*, 243, 27.
- Barlow, M.J. and Cohen, M.: 1977, *Ap. J.*, 213, 737.
- Basko, M.M. and Sunyaev, R.A.: 1976, *M.N.R.A.S.*, 175, 395.
- Basko, M.M. and Sunyaev, R.A.: 1977, *Soviet Astronomy*, 53, 537.
- Bath, G.: 1973, *Nature*, 246, 84.
- Batten, A.H.: 1973, *Binary and Multiple Systems of Stars*, (Oxford Pergamon Press).
- Becklin, E., Kristian, J., Neugebauer, G. and Wynn-Williams, C.: 1972, *Nature*, 239, 130.
- Boldt, E.: 1977, *Annals of the New York Academy of Sciences*, 302, 329.
- Bolton, C.T.: 1972, *Nature*, 240, 124.
- Bolton, C.T.: 1975, *Ap. J.*, 200, 269.
- Bowyer, S., Byram, E.T., Chubb, T.A. and Friedman, H.: 1964, *Science*, 146, 912.
- Braes, L. and Miley, G.: 1971, *Nature*, 232, 246.
- Bradt, H., Rappaport, S., Mayer, W., Nather, R., Warner, B., MacFarlane, M. and Kristian, J.: 1969, *Nature*, 222, 728.
- Brecher, K. and Morrison, P.: 1973, *Ap. J.*, 180, L107.
- Brecher, K., Morrison, P. and Sadun, A.: 1977, *Ap. J.*, 217, L139.
- Bregman, J., Butler, D., Kemper, E., Koski, A., Kraft, R.P. and Stone, R.P.S.: 1973, *Ap. J.*, 185, L117.
- Brinkman, A.C., Parsignault, D., Schreier, E., Gursky, H., Kellogg, E., Tananbaum, H. and Giacconi, R.: 1974, *Ap. J.*, 188, 603.
- Brown, W.K. and Jensen, T.H.: 1964, *Nuclear Instruments and Methods*, 27, 259.

- Brown, R.L. and Gould, R.J.: 1970, Physics Review D, 1, 2252.
- Brucato, R.J. and Kristian, J.: 1973, Ap. J., 179, L129.
- Burbidge, G.R.: 1972, Comments Astron. Astrophysics, 4, 105.
- Byram, E.T., Chubb, T.A. and Friedman, H.: 1966, Science, 152, 166.
- Castor, J.I., Abbott, D.C. and Klein, R.I.: 1975, Ap. J., 195, 157.
- Canizares, C.R.: 1976, Ap. J., 207, L101.
- Canizares, C.R., Bradt, H., Buff, J. and Laufer, B.: 1976, NASA SP.389, p.373.
- Canizares, C.R., Laufer, B. and Primini, F.: 1976A, Bull. Amer. Astron. Soc., 8, 439.
- Canizares, C.R. and Oda, M.: 1977, Ap. J., 214, L119.
- Charles, M.W. and Cooke, B.A.: 1968, Nuclear Instruments and Methods, 61, 31.
- Charles, M.W.: 1972, Journal of Physics, Scientific Instruments, 5, 95.
- Charpak, G.: 1970, Annual Rev. of Nuclear Science, 20, 195.
- Charpak, G., Rahm, D. and Steiner, H.: 1970, Nuclear Instruments and Methods, 80, 13.
- Chi Chao Wu, Van Duinen, R.J. and Hammerschlag-Hensberge, G.: 1976, NASA SP.389, p.529.
- Chu, W.W.: 1970, IEEE Transactions on Communication Technology, COM-18, No. 5, 613.
- Cocke, W.J., Disney, M.J. and Taylor, D.J.: 1969, Nature, 221, 525.
- Cooke, B.A., Griffiths, R.E. and Pounds, K.A.: 1969, Nature, 224, 134.
- Cooke, B.A., Griffiths, R.E. and Janes, A.F.: 1973, Nuclear Instruments and Methods, 106, 147.
- Cooke, B.A.: 1976, Nature, 261, 564.
- Cooke, B.A., Ricketts, M.J., Maccacaro, T., Pye, J.P., Elvis, M., Watson, M.G., Griffiths, R.E., Pounds, K.A., McHardy, I., Maccagni, D., Seward, F.D., Page, C.G. and Turner, M.J.L.: 1978, M.N.R.A.S., 182, 455.
- Cooper, R.D.: 1977, Electronic Engineering, May, p.17.
- Cowling, T.C.: 1938, M.N.R.A.S., 98, 448.
- Crawford, D.L., Barnes, J.V. and Warren, W.H.: 1974, Astron. Journal, 79, 623.
- Davidson, K. and Ostriker, J.P.: 1973, Ap. J., 179, 585.

- Deeter, J., Crosa, L., Gerend, D. and Boynton, P.: 1976, Ap. J., 206, 861.
- Diethorn, W.: 1956, US Atomic Energy Commission Report NYO-6628.
- Dolan, J.F.: 1976, NASA SP.389, p.493.
- Dolan, J.F., Crannell, C.J., Dennis, B.R., Frost, K.J. and Orwig, L.E.: 1977, G.S.F.C. Pre-Print X-682-77-83.
- Dor, M.N.: 1967, IEEE Transactions on Electronic Computers, EC16, 683.
- Elsner, R.F. and Lamb, F.K.: 1977, Ap. J., 215, 897.
- Elvis, M., Page, C.G., Pounds, K.A., Ricketts, M.J., Turner, M.J.L.: 1975, Nature, 256, 631.
- Fabian, A.C., Pringle, J.E. and Whelan, J.A.J.: 1974, Nature, 247, 351.
- Fabian, A.C., Pringle, J.E. and Rees, M.J.: 1976, M.N.R.A.S., 175, 43.
- Fano, U.: 1947, Physics Review, 72, 26.
- Fernice, J.D. and Hube, J.D.: 1968, Astron. Journal, 73, 492.
- Floyd, F.W.: 1969, Nature, 222, 967.
- Forman, W., Jones, C., Cominsky, L., Julien, P., Murray, S., Peters, G., Tananbaum, H. and Giacconi, R.: 1977, Center for Astrophysics Pre-Print, No. 763.
- Friedman, H., Byram, E.T. and Chubb, T.A.: 1967, Science, 156, 374.
- Gallager, R.G.: 1968, Information Theory and Reliable Communications, (J. Wiley, Inc.).
- Giacconi, R., Kellogg, E.M., Gorenstein, P., Gursky, H. and Tananbaum, H.: 1971, Ap. J., 165, L27.
- Giacconi, R., Murray, S., Gursky, H., Kellogg, E.M., Schrier, E., Matilsky, T., Koch, D. and Tananbaum, H.: 1974, Ap. J., (Supp), 237, 37.
- Glasby, J.S.: 1970, The Dwarf Novae, (Constable, London).
- Gnedin, Y.N. and Sunyaev, R.A.: 1973, Astron. Astrophysics, 25, 233.
- Gott, R. and Charles, M.W.: 1969, Nuclear Instruments and Methods, 72, 157.
- Gowan, R.A.: 1978, Private Communication.
- Griffiths, R.E.: 1971, Ph.D. Thesis, Leicester University.
- Grindley, J.E. and Gursky, H.: 1977, Centre for Astrophysics Pre-Print No. 829, (Cambridge, Mass.).
- Gursky, H., Giacconi, R., Paolini, F.R. and Rossi, B.: 1963, Phys. Rev. Lett., 11, 530.

- Gursky, H., Giacconi, R., Gorenstein, P., Waters, J.R., Oda, M.,  
Bradt, H., Garmire, G. and Sreekanton, B.V.: 1966, Ap. J.,  
146, 310.
- Gursky, H. and Gorenstein, P.: 1971, Ap. J., 167, L15.
- Hamming, R.W.: 1950, Bell System Technical Journal, Vol. XXVI.
- Harnden, F.R., Fabricant, D., Topka, K., Flannery, B.P., Tucker, W.H.  
and Gorenstein, P.: 1977, Ap. J., 214, 418.
- Harris, T.J. and Mathieson, E.: 1971, Nuclear Instruments and Methods,  
96, 397.
- Hatchett, S., Buff, J. and McCray, R.: 1976, Ap. J., 206, 847.
- Henry, P., Cruddace, R., Lampton, M., Paresce, F. and Bowyer, S.:  
1975, Ap. J., 195, 107.
- Hensberge, G. and Van Den Heuval, E.P.J.: 1974, Astron. Astrophysics,  
33, 311.
- Hiltner, W.A.: 1956, Ap. J., (Supp. 2), 389.
- Hjellming, R.M. and Wade, C.M.: 1971, Ap. J., 168, L21.
- Hoffman, J.A. and Giles, A.B.: 1974, Private Communication.
- Hoffman, J.A., Lewin, W.H.G., Brecher, K., Buff, J., Clarke, G.W. Joss,  
P.C. and Matilsky, T.: 1977, Nature, 261, 208.
- Holt, S.S., Boldt, E.A., Schwartz, D.A. and Serlemitsos, P.: 1971,  
Ap. J., 166, L65.
- Holt, S.S., Boldt, E.A., Serlemitsos, P.J. and Kaluzienski, L.J.:  
1976, Ap. J., 203, L63.
- Hoshi, R.: 1973, Prog. Theor. Physics, 49, 776.
- Hoyle, F. and Lyttleton, R.A.: 1939, Proc. Cambridge Phil. Soc., 35,  
405.
- Hutchings, J.B., Crampton, D., Glaspey, J. and Walker, G.A.H.: 1973,  
Ap. J., 182, 549.
- Hutchings, J.B.: 1974, Ap. J., 188, 341.
- Jackson, J.C.: 1975, M.N.R.A.S., 172, 483.
- Jones, C. and Forman, W.: 1976, Ap. J., 209, L131.
- Jones, C., Foreman, W., Tananbaum, H. and Turner, M.J.L.: 1976, Ap. J.,  
210, L9.
- Klebesadel, R.W., Strong, J.B. and Olson, R.A.: 1973, Ap. J., 182, L85.
- Kraft, R.P.: 1963, Advances in Astronomy, AP 2, 43.

- Kraft, R.: 1973, X-ray and  $\gamma$ -ray Astronomy, IAU Symp., 55, 36.
- Kristian, J. and Brucato, R.: 1971, Ap. J., 168, L91.
- Kopal, Z.: 1950, The Computation of Elements of Eclipsing Binary Systems, Harvard Obs. Monograph, No. 8.
- Kuiper, G.P.: 1938, Ap. J., 88, 472.
- Lamb, D.Q. and Van Horn, H.M.: 1973, Ap. J., 183, 959.
- Lamb, F.K., Pethick, C.J. and Pines, D.: 1973, Ap. J., 184, 271.
- Lamb, F.K., Fabian, A.C., Pringle, J.E. and Lamb, D.Q.: 1977, Ap. J., 217, 197.
- Lampton, M., Margon, B. and Bowyer, S.: 1976, Ap. J., 208, 177.
- Landau, L. and Lifshitz, E.: 1958, Statistical Physics, (Addison Wesley, Reading, Mass.).
- Leach, R. and Ruffini, R.: 1973, Ap. J., 180, L15.
- Lester, D.F., Nolt, I.G. and Radostitz, J.V.: 1973, Nature, 241, 125.
- Lewin, W.H.G., Doty, J., Clark, G.N., Rappaport, S.A., Bradt, H.V.D., Doxsey, R., Hearn, D.R., Hoffman, J.A., Jernigan, J.G., Li, F.K., Mayer, W., McLintock, J., Primini, F. and Richardson, J.: 1976, Ap. J., 207, L95.
- Lewin, W.H.G.: 1977, M.N.R.A.S., 179, 43.
- Li, F.K. and Clark, G.W.: 1974, Ap. J., 191, L27.
- Lightman, A.P., Rees, M.J. and Shapiro, S.L.: 1977, Proc. Enrico Fermi School on the Physics and Astrophysics of Neutron Stars and Black Holes.
- Liller, W.: 1976, NASA SP.389, p.513.
- Lin, D.N.C. and Pringle, J.E.: 1976, Structure and Evolution in Close Binary Systems, IAU Symposium, No. 73.
- Margon, B. and Ostriker, J.P.: 1973, Ap. J., 186, 91.
- Margon, B., Bowyer, S. and Stone, R.P.S.: 1973, Ap. J., 185, L113.
- Mason, K.O., Hawkins, F., Sanford, P.W., Murdin, P. and Savage, A.: 1974, Ap. J., 192, L65.
- Mason, K.O., Charles, P.A., Kahn, S.M., Thorstensen, J.R. and Walter, F.M.: 1977, BAAS, vol. 9, No. 4, Abst. 19.05.09, p.592.
- Mathieson, E. and Charles, M.W.: 1969, Nuclear Instruments and Methods, 72, 155.
- Mathieson, E. and Harris, T.J.: 1970, Nuclear Instruments and Methods, 88, 181.

- Matilsky, T., Gursky, H., Kellogg, E.M., Tananbaum, H., Murray, S. and Giacconi, R.: 1974, *Ap. J.*, 181, 753.
- Mauder, H.: 1973, *Astron. Astrophysics*, 28, 473.
- McCray, R.: 1976, Review IAU General Assembly, Grenoble, France.
- Merrill, J.E.: 1953, *Princeton Contr.*, No. 24.
- Merrill, J.E.: 1970, *Vistas in Astronomy*, Vol. 12, 43.
- Mewe, R., Heise, J., Gronenschild, E., Brinkman, A.C., Schrijver, H. and Den Bogge, A.J.F.: 1975, *Nature*, 256, 711.
- Mitchell, R.J., Culhane, J.L., Davison, P.J.N., and Ives, J.C.: 1976, *M.N.R.A.S.*, 175, 29p.
- Miyamoto, S., Fujii, M., Matsuoka, M., Nishimura, J., Oda, M., Ogawara, Y., Ohta, S. and Wada, M.: 1971, *Ap. J.*, 168, L11.
- McLintock, J.E.: 1975, *ESRO Colloquium SP110*.
- McLusky, G. and Kondo, Y.: 1971, *Astrophysics Space Sci.*, 10, 464.
- McMaster, W.H., Kerr Del Grande, N., Mallett, J.H. and Hubbil, J.H.: 1967, UCRL-50174, Sec. II, Rev. I, University California (Livermore).
- Moore, E.: 1973, *Publ. Astron. Soc. Pacific*, 85, 564.
- Morton, D.C.: 1969, *Astrophysics Space Sci.*, 3, 117.
- Munch, G.: 1968, *Stars and Stellar Systems*, Vol. 7, p.365.
- Murdin, P.: 1976, *NASA SP.389*, p.425.
- Novikov, I.D. and Thorn, K.S.: 1973, *Black Holes*, p.343, (eds. C. de Witt, B. de Witt, Gordon and Breach, New York).
- Oda, M., Gorenstein, P., Gursky, H., Kellogg, E., Schreier, E., Tananbaum, H. and Giacconi, R.: 1971, *Ap. J.*, 166, L1.
- Oda, M., Takagishi, K., Matsuoka, M., Miyamoto, S. and Ogawara, Y.: 1974, *Publ. Astron. Soc. Japan*, 26, 303.
- Oda, M., Doi, K., Ogawara, Y., Takagishi, K. and Wada, M.: 1975, *ISAS.RN3 Symposium, Varna, Bulgaria*.
- Ogawara, Y., Doi, K., Matsuoka, M., Miyamoto, S. and Oda, M.: 1977, *ISAS RN 26, University of Tokyo*.
- Paczynski, B.: 1967, *Acta. Astron.*, 17, 355.
- Paczynski, B.: 1971, *Ann. Rev. Astronomy and Astrophysics*, 9, 183.
- Paczynski, B.: 1972, Talk at VI Texas Symposium on Relativistic Astrophysics.

- Parsignault, D.R., Grindley, J.E., Schnopper, H., Schreier, E.J. and Gursky, H.: 1976, NASA SP.389, p.429.
- Peterson, W.W.: 1968, Error Correcting Codes, (M.I.T. Press).
- Press, W.H. and Scheckter, P.: 1974, Ap. J., 193, 437.
- Pringle, J.E. and Rees, M.J.: 1972, Astron. Astrophysics, 21, 1.
- Pringle, J.E.: 1973, Nature, 243, 90.
- Rappaport, S., Doxsey, S. and Zaumen, W.: 1971, Ap. J., 168, L17.
- Rappaport, S. and Joss, P.C.: 1977a, Nature, 266, 123.
- Rappaport, S. and Joss, P.C.: 1977b, Nature, 266, 683.
- Ricketts, M.J.: 1973, Ph.D. Thesis, Leicester University.
- Ricketts, M.J.: 1977, Private Communication.
- Ricketts, M.J., Turner, M.J.L., Page, C.G. and Pounds, K.A.: 1975, Nature, 256, 631.
- Ricketts, M.J.: 1978, Private Communication.
- Robinson, E.L., Nather, R.E., Africano, J. and Smith, B.: 1978, Nature, 271, 40.
- Rothschild, R.E., Boldt, E.A., Holt, S.S. and Serlemitsos, P.J.: 1974, Ap. J., 189, L13.
- Rothschild, R.E., Boldt, E.A., Holt, S.S. and Serlemitsos, P.J.: 1976, NASA SP.389, p.443.
- Rothschild, R.E., Boldt, E.A., Holt, S.S. and Serlemitsos, P.J.: 1977, Ap. J., 213, 818.
- Rothschild, R.: 1977, Recognition of Compact Astrophysical Objects, NASA SP.421, p.125.
- Ruffini, R.: 1973, Black Holes, eds. C. De Witt and B.S. De Witt (Gordon and Breach, New York).
- Russell, H.N. and Shapley, H.: 1912, Ap. J., 36, 243, 390.
- Russell, H.N. and Merrill, J.E.: 1952, Contr. Princeton Univ. Obs., 26, 1.
- Schrier, E., Gursky, H., Kellogg, E., Tananbaum, H. and Giacconi, R.: 1971, Ap. J., 170, L21.
- Schwarzschild, K.: 1900, Astronomische Nachrichten, 152, 65.
- Seward, F.D.: 1970, UCID Report No. 15622.
- Shapiro, S.L. and Lightman, A.P.: 1976, Ap. J., 204, 555.
- Shu, F.H.: 1976, Structure and Evolution of Close Binary Systems, IAU Symposium, No. 73.

- Shulman, S., Fritz, G., Meekings, J.F. and Freidman, H.: 1971, Ap. J., 168, L49.
- Shvartsman, V.F.: 1971, Astr. ZH, 48, 479.
- Smak, J.: 1972, Acta. Astron., 22, 1.
- Smith, A.: 1977, Ph.D. Thesis, Leicester University.
- Smith, H.E., Margon, B. and Conti, P.S.: 1973, Ap. J., 179, L125.
- Smith, J.F. and Coutier, G.M.: 1976, Proc. Royal Society, London, 350.
- Spada, G., Bradt, H., Doxsey, R., Levine, A. and Rappaport, S.: 1974, Ap. J., 190, L113.
- Staelin, D.H. and Riefenstein, E.C.: 1968, Science, 162, 1481.
- Stothers, R.: 1972, Ap. J., 175, 431.
- Sunyaev, R.A.: 1973, Soviet Astronomy, 16, 941.
- Sutherland, P.G., Weisskopf, M.C. and Kahn, S.M.: 1977, Columbia Pre-Print.
- Tananbaum, H., Gursky, H., Kellogg, E., Giacconi, R. and Jones, C.: 1972, Ap. J., 177, L5.
- Tarter, C.B. and Salpeter, E.C.: 1969, Ap. J., 156, 953.
- Terrell, N.J.: 1972, Ap. J., 174, L35.
- Timoshenko, S. and Woinoursky-Krieger, S.: 1959, Theory of Plates and Shells (McGraw-Hill).
- Tomitani, T.: 1972, Nuclear Instruments and Methods, 100, 179.
- Toor, A., Price, R., Seward, F. and Scudder, J.: 1971, Ap. J., 168, L15.
- Toor, A.: 1977, Ap. J., 215, L57.
- Trimble, V., Rose, W.K. and Weber, J.: 1973, M.N.R.A.S., 162, 1p.
- Trippe, T.: 1969, European Organisation for Nuclear Research, Report No. 69-18.
- Van Den Heuval, E.P.J. and Heise, J.: 1972, Nature, 239, 67.
- Van Den Heuval, E.P.J. and Ostriker, J.P.: 1973, Nature, 245, 99.
- Villa, G., Page, C.G., Turner, M.J.L., Cooke, B.A., Ricketts, M.J. and Pounds, K.A., 1976, M.N.R.A.S., 176, 609.
- Von Zeipel, H.: 1924, M.N.R.A.S., 84, 665.
- Walborn, N.R.: 1973, Ap. J., 179, L123.
- Waligórski, M.P.R.: 1973, Nuclear Instruments and Methods, 109, 403.

- Walker, E.N.: 1976, NASA SP.389, p.521.
- Walker, E.N. and Rolland-Quintanilla, A.: 1977, Private Communication.
- Warner, B.: 1974, M.N.R.A.S., 168, 235.
- Webster, B.L. and Murdin, P.: 1972, Nature, 235, 37.
- Weisskopf, M.C., Kahn, S.M. and Sutherland, P.G.: 1975, Ap. J., 199, L147.
- Weisskopf, M.C.: 1976, NASA SP.389, p.453.
- Weisskopf, M.C. and Sutherland, P.G.: 1977, Columbia Pre-Print.
- Whitford, C.H.: 1974, Private Communication.
- Wilson, R. and Devinney, E.: 1971, Ap. J., 166, 605.